

**STRUCTURE-PROPERTY RELATIONSHIPS AND ADHESION IN  
POLYIMIDES OF VARYING ALIPHATIC CONTENT**

Amy Elizabeth Eichstadt

Dissertation submitted to the Faculty of the  
Virginia Polytechnic Institute and State University  
in partial fulfillment of the requirements for the degree of

Doctor of Philosophy  
In  
Materials Engineering & Science

Dr. Thomas C. Ward, Chair

Dr. Richey M. Davis

Dr. David A. Dillard

Dr. John G. Dillard

Dr. Ronald G. Kander

July 16, 2002

Blacksburg, Virginia

Key words: polyimide; aliphatic diamine; structure-property relations; viscoelastic  
properties; dielectric properties; adhesion; shaft loaded blister test

Copyright © 2002, Amy Elizabeth Eichstadt

# STRUCTURE-PROPERTY RELATIONSHIPS AND ADHESION IN POLYIMIDES OF VARYING ALIPHATIC CONTENT

Amy Elizabeth Eichstadt

(ABSTRACT)

Aromatic polyimides have found widespread applicability which can be partially attributed to their thermal stability, chemical resistance, and high glass transition temperature. However, deficiencies in their processability, solubility, transparency, and relatively high dielectric constants do not always provide the optimum properties for many specialty microelectronics applications. The incorporation of aliphatic segments to form partially aliphatic polyimides, has been used to counteract these shortcomings. Many of the potential uses of partially aliphatic polyimides require them to adhere to ceramic substrates, a main topic of this research.

Polyimides and copolyimides that varied in chemical composition by their aliphatic content were characterized by their molecular weight, glass transition temperature, thermal stability, coefficient of thermal expansion, refractive index, dielectric behavior, and mechanical properties. Structure-property relationships were established. The  $\gamma$  and  $\beta$  sub- $T_g$  viscoelastic relaxations were investigated to understand their molecular origins.

The adhesion performance of a selected series of partially aliphatic polyimides to  $\text{SiO}_2/\text{Si}$  was examined using a shaft loaded blister test, which was designed and instrumented for use in a dynamic mechanical analysis instrument. The adhesion was studied at high and low percent relative humidities and for several temperatures to examine if adhesion strength is influenced by polymer chemical composition. The adhesion energy could not be quantified for the entire series of polyimides. It was possible to interpret the quantitative adhesive fracture energies along with the qualitative adhesion strength behaviors, the failure surface analyses, and to offer an understanding of the adhesive chemical structure-physical property relationships. These understandings provide a conclusion that the incorporation of aliphatic segments into the polyimide chemical structure improves the durability of the adhesive bond to  $\text{SiO}_2/\text{Si}$  under high percent relative humidities.

## ACKNOWLEDGEMENTS

I would like to extend my sincere appreciation to the following people and organizations who made this dissertation possible.

I acknowledge the Center for Adhesive and Sealant Science and the Adhesive and Sealant Council Education Foundation for financial support of this work.

I am grateful for the opportunity to work with Dr. Tom Ward over the years. He offered me the freedom and confidence to direct my project towards the topics I most enjoyed; from this experience my passion for science and learning has deepened. I would also like to thank my committee, Drs. Dave Dillard, John Dillard, Richey Davis, and Ron Kander for their guidance, and to Dr. Kai-tak Wan for helpful discussions. I extend a special thanks to both the Dillards for inviting me to participate in the various CASS activities and attend conferences. To, Dr. Jim McGrath for his involvement in my project, and his former students, Melanie Bagwell, Dr. Isaac Farr, and Dr. Debi Dunson, who synthesized the polyimides which were characterized in this dissertation.

I am indebted to TA Instruments, particularly Dr. Steve Aubuchon and Gary Mann, who donated two furnaces to be used for the shaft loaded blister test. I would like to thank the Physics Machine Shop (Melvin Shaver, John Miller, Scott Allen, and B.J. Evans) for their assistance in preparing the SLBT clamp and in drilling the holes in the DMA furnace. I also would like to acknowledge Frank Cromer for assistance and discussions on the XPS aspect of this work. And, Millie Ryan, Esther Brann, Laurie Good, Tammy Jo Hiner, and Linda Haney, from the NSF and CASS offices.

I also thank the past and present members of the PolyPkem research group for discussions, but mostly for their friendship, especially: Sandra Case, Emmett O'Brien, Jen Robertson, Jianli Wang, Mark Muggli, Kermit Kwan, Dave Porter, and Rob Jensen. And to: Ron DiFelice, Anders DiBiccari, Dave Godshall, Matt O'Sickey, Jody Krsmanovic, Matt Guzy, Dan Brannegan, and Randy McNally. I also must thank the chick posse: Maggie Bump, Sarah Finger, Kristen Wilson, Linda Harris, and Jen (Hoyt) Lalli, for all the fun memories from "chick nites" and conferences.

To my parents, Drs. Frank and Karen Eichstadt, and my brothers, Andrew and David, who have supported me with each endeavor and have been a constant source of love, laughter, and friendship. And finally to my boyfriend, Scott Waun...his love has inspired me each day.

**DEDICATION**

to

My parents

## TABLE OF CONTENTS

1.	Introduction .....	1
1.1	References .....	4
2.	Literature Review .....	6
2.1	Applications .....	6
2.2	Synthesis .....	6
2.2.1	Poly(amic acid) Method .....	6
2.2.2	Ester-acid Solution Imidization.....	9
2.2.3	Partially Aliphatic Polyimides .....	10
2.3	Charge Transfer Complexes .....	10
2.4	Thermal Properties .....	11
2.4.1	Thermal Stability .....	11
2.4.2	Coefficient of Thermal Expansion (CTE) .....	13
2.4.3	Viscoelastic Relaxations .....	14
2.4.3.1	The Glass Transition Temperature .....	14
2.4.3.2	Secondary Relaxations: General Definitions .....	15
2.4.3.3	Secondary Relaxations: Application to Polyimides .....	17
2.4.3.4	Role of $\beta$ Relaxation on Mechanical Properties .....	19
2.5	Water in Polyimides .....	22
2.6	Diffusion in Polyimides .....	25
2.6.1	Introduction to Diffusion .....	25
2.6.2	Diffusion Kinetics .....	26
2.6.3	Diffusion Kinetics via In situ Test Methods .....	28
2.7	Dielectric Properties .....	29
2.8	Mechanical Properties .....	32
2.9	Adhesion .....	33
2.9.1	Introduction .....	33
2.9.2	The Energy of Adhesion .....	33
2.9.3	Polyimide Adhesion .....	37
2.9.3.1	Polyimide-polyimide Adhesion .....	37
2.9.3.2	Polyimide-metal and Metal-polyimide Adhesion .....	38
2.9.3.3	Polyimide-ceramic Adhesion .....	40
2.10	Literature Review Conclusions .....	46
2.11	References .....	47
3.	Experimental .....	50
3.1	Aromatic Polyimides .....	50
3.1.1	Materials .....	50
3.1.2	Bilayer Sample Preparation .....	51
3.1.3	Characterization .....	52
3.2	The Effect of Moisture on the Mechanical and Dielectric Properties of Kapton <sup>®</sup> -E Polyimide Film .....	53

3.2.1	Humidity Environments .....	53
3.2.2	Saturated Environments .....	55
3.3	BPADA-based Partially Aliphatic Polyimides .....	56
3.3.1	Introduction .....	56
3.3.2	Materials .....	56
3.3.3	Synthesis .....	57
3.3.4	Film Preparation .....	59
3.3.5	Characterization .....	59
3.3.6	SLBT Sample Preparation .....	62
3.3.7	Additional Comments on SLBT Sample Preparation .....	65
3.3.8	SLBT Design .....	68
3.3.9	SLBT DMA Experimental Method .....	71
3.3.10	The Borescope and Blister Analysis .....	73
3.3.11	Surface Analysis – X-Ray Photoelectron Spectroscopy .....	76
3.4	References .....	79
4.	Aromatic Polyimide Viscoelastic Characterization .....	80
4.1	Introduction .....	80
4.2	Viscoelastic Characterization of Kapton <sup>®</sup> -E, KB and PI .....	80
4.2.1	Single Frequency DMA: Single Layer Films .....	80
4.2.2	Single Frequency DMA: Bilayer Composite Films .....	82
4.2.3	Multi-Frequency DMA .....	86
4.2.3.1	Introduction .....	86
4.2.3.2	Time-Temperature Superposition (tT-sp) .....	87
4.2.3.3	Activation Energy .....	92
4.2.3.4	Cooperativity Analysis .....	93
4.2.4	Conclusions .....	96
4.3	Effect of Moisture on the Mechanical and Dielectric Properties of Kapton <sup>®</sup> -E .....	97
4.3.1	Introduction .....	97
4.3.2	Weight Uptakes .....	98
4.3.3	Dynamic Mechanical Analysis .....	100
4.3.4	Stress-strain .....	105
4.3.5	Dielectric Analysis .....	106
4.3.6	Introduction to Activation Energy Calculations .....	107
4.3.6.1	Arrhenius Activation Energy .....	109
4.3.6.2	Starkweather-Eyring Activation Energy .....	111
4.3.6.3	Relaxation Distribution .....	112
4.3.7	In situ DMA .....	119
4.3.7.1	Coefficient of Thermal Expansion .....	121
4.3.8	Conclusions .....	123
4.4	References .....	124
5.	Characterization of Amorphous Partially Aliphatic Polyimides Based on Bisphenol-A Dianhydride .....	126
5.1	Introduction .....	126
5.2	Materials .....	126

5.3	Results and Discussion .....	126
5.4	Conclusions .....	143
5.5	References .....	144
6.	Structure-Property Relationships for the BPADA/ODA:DoDDA Series .....	146
6.1	Introduction .....	146
6.2	Materials .....	146
6.3	Results and Discussion .....	146
6.4	Relevance to Adhesion .....	168
6.5	Conclusions .....	169
6.6	References .....	169
7.	Adhesion .....	171
7.1	Introduction .....	171
7.2	Thermodynamic Work of Adhesion .....	171
7.3	The Shaft Loaded Blister Test: Background .....	174
7.3.1	Introduction and Theory .....	174
7.3.2	Experimental Parameters .....	176
7.4	The Shaft Loaded Blister Test: Results and Discussion .....	178
7.4.1	Introduction .....	178
7.4.2	Deviations from Theory .....	178
7.5	BPADA/ODA at High %RH .....	182
7.5.1	BPADA/ODA: SLBT Results .....	182
7.5.2	BPADA/ODA: Locus of Failure Analysis .....	189
7.6	BPADA/ODA:DoDDA, 75:25 at High %RH .....	195
7.6.1	BPADA/ODA:DoDDA, 75:25: SLBT Results .....	195
7.6.2	BPADA/ODA:DoDDA, 75:25: Locus of Failure Analysis .....	200
7.7	BPADA/ODA:DoDDA, 50:50 at High %RH .....	201
7.7.1	BPADA/ODA:DoDDA, 50:50: SLBT Results .....	201
7.7.2	BPADA/ODA:DoDDA, 50:50: Locus of Failure Analysis .....	205
7.8	BPADA/ODA:DoDDA, 25:75 and BPADA/DoDDA at High %RH .....	206
7.8.1	BPADA/ODA:DoDDA, 25:75 and BPADA/DoDDA: SLBT Results .....	206
7.8.2	BPADA/ODA:DoDDA, 25:75 and BPADA/DoDDA: Locus of Failure Analysis .....	210
7.9	Low %RH SLBT Experiments .....	211
7.10	Conclusions .....	213
7.11	References .....	216
8.	Conclusions .....	218
8.1	Aromatic Polyimides .....	218
8.2	Partially Aliphatic Polyimides .....	219
8.2.1	Structure-Property Relationships .....	219
8.2.2	Adhesion .....	220
9.	Suggestions for Future Work.....	222

## LIST OF FIGURES

Figure 2.1 Poly(amic acid) route for the synthesis of an aromatic polyimide Ar and Ar' denote aromatic moieties. ....	7
Figure 2.2 Acronyms, chemical structures, and chemical names of some common aromatic dianhydrides. ....	8
Figure 2.3 Acronyms, chemical structures, and chemical names of some common aromatic diamines. ....	8
Figure 2.4 Ester-acid solution imidization for the synthesis of aromatic or partially aliphatic polyimides Ar and Ar' designate aromatic moieties R designates an aliphatic moiety. ....	9
Figure 2.5 Examples of aliphatic and cycloaliphatic diamines.....	10
Figure 2.6 CTE comparison for microelectronics materials.....	13
Figure 2.7 General model of contribution to secondary relaxations.....	16
Figure 2.8 Crankshaft motion responsible for the $\gamma$ relaxation in many hydrocarbon based polymers.....	17
Figure 2.9 Phenyl ring torsional rotation in 4,4'-oxydianiline (ODA).....	18
Figure 2.10 Temperature dependence of deformation percent at break, $\epsilon_b$ %, and DMA $\tan \delta$ for two polyimides. The solid lines represent $\epsilon_b$ % and the dashed lines represent $\tan \delta$ .....	19
Figure 2.11 Relationship between the temperature of the polyimide $\beta$ relaxation and the strength of PI-epoxy molding compound adhesive bond.....	20
Figure 2.12 Relationship between the $\tan \delta$ magnitude of the polyimide $\beta$ relaxation and the strength of PI-epoxy molding compound (MC-A) adhesive bond.....	21
Figure 2.13 Temperature dependence of elongation at break and DMA $\tan \delta$ for PMDA/ODA with various degrees of stretching. The degree of stretching $\lambda$ is equal to 1 (curves 1, 1'), 2 (curves 2, 2'), and 5 (curves 3, 3'). Arrows indicate the maxima of $\beta$ losses at 72 Hz (a) and 01 Hz (b). ....	22
Figure 2.14 Dielectric analysis $\tan \delta$ displaying the effect of water on the gamma relaxation of Kapton-H (PMDA/ODA). Curves (a) to (d) correspond to 100% RH, 75% RH, 49% RH, and dry samples, respectively.....	24
Figure 2.15 Influence of Flexible Linkages on Dielectric Constant. ....	31
Figure 2.16 Peel strength of a 128 $\mu\text{m}$ thick Pyralin <sup>®</sup> 2555 polyimide film as a function of substrate temperature under high humidity condition (70 %RH) Peel rate = 0.5 mm/min. ....	42
Figure 2.17 Peel strength of a 143 $\mu\text{m}$ thick Pyralin <sup>®</sup> 2555 polyimide film with a peeling rate of 0.5 mm/min in an ambient of 125 %RH as a function of substrate temperature.....	43
Figure 2.18 Peel strength of 143 $\mu\text{m}$ thick Pyralin <sup>®</sup> 2555 polyimide film with a peeling rate of 0.5mm/min as a function of relative humidity. ....	44
Figure 2.19 Schematic drawing of a local dry atmosphere at the peel crack tip. ....	45
Figure 3.1 Monomers and polymer chemical structure for Kapton <sup>®</sup> -E. ....	50
Figure 3.2 Monomers and polymer chemical structure for KB. ....	51
Figure 3.3 Monomer chemical structures. ....	57

Figure 3.4 Ester-acid high temperature solution imidization scheme for the BPADA/ODA:DoDDA series.....	58
Figure 3.5 Precrack of BPADA/ODA-2. ....	63
Figure 3.6 BPADA/ODA:DoDDA, 50:50-4 prepared using the patch technique. ....	64
Figure 3.7 Shaft loaded blister test geometry within the TA Instruments DMA 2980. ....	69
Figure 3.8 TA Instruments DMA 2980 with a standard DMA furnace which was customized to accommodate the shaft loaded blister test. ....	71
Figure 3.9 Measurement of blister radius with Vision Gauge™ software (a) Blister of BPADA/ODA- 2 at 3 minutes (b) Blister radius at 3 minutes is 4.59 mm. ....	74
Figure 3.10 Correction for distortion for the borescope used at room temperature.....	75
Figure 3.11 Correction for distortion for the borescope used at high temperatures. ....	76
Figure 4.1 DMA response of Kapton®-E at 1 Hz. ....	81
Figure 4.2 DMA response of KB at 1 Hz. ....	81
Figure 4.3 DMA, 1 Hz for KB/PI bilayer. ....	83
Figure 4.4 DMA, 1 Hz for Kapton®-E/PI bilayer. ....	85
Figure 4.5 AFM Phase Image of the KB/PI bilayer With respect to the “seam” in the center of the image, KB and PI are left/right Scale is 10 x 10-µm. ....	86
Figure 4.6 Kapton®-E Storage Modulus Master Curve at 323 °C and Shift Factor Plot. ..	88
Figure 4.7 KB Storage Modulus Master Curve at 240 °C and Shift Factor Plot. ....	88
Figure 4.8 DMA, frequency dependence of the $\gamma$ , $\beta$ , and $T_g$ relaxations of KB. ....	90
Figure 4.9 Frequency dependence of the $T_g$ for PI, within KB/PI bilayer.....	91
Figure 4.10 PI Storage Modulus Master Curve for 179 °C and Shift Factor Plot. ....	91
Figure 4.11 DMA, frequency dependence of the $\gamma$ , $\beta$ , and $T_g$ of Kapton®-E. ....	93
Figure 4.12 Cooperativity plots for Kapton®-E, KB, and PI. ....	95
Figure 4.13 Cooperativity data and fit-line for (a) Kapton®-E, and (b) KB. ....	96
Figure 4.14 Weight percent uptake of moisture of Kapton®-E in different percent relative humidities.....	98
Figure 4.15 TGA, Weight % loss in air versus temperature of Kapton®-E conditioned in different percent relative humidities. ....	99
Figure 4.16 DMA, 1 Hz. Influence of moisture content on the $\beta$ relaxation of Kapton®-E. ....	100
Figure 4.17 DMA, 1 Hz. Influence of moisture content on the Storage Modulus ( $E'$ ) of Kapton®-E.....	101
Figure 4.18 DMA, 1 Hz. Three heating cycles of a Kapton®-E sample initially saturated with water. ....	103
Figure 4.19 DMA, 1 Hz. Influence of thermal conditioning on the $\beta$ relaxation of Kapton®-E Plot shows an unconditioned sample and 4 conditioned samples.....	104
Figure 4.20 Influence of relative humidity on the tensile modulus of Kapton®-E. ....	105
Figure 4.21 DEA, 1000 Hz. Influence of moisture content on the $\gamma$ relaxation of Kapton®-E. ....	106
Figure 4.22 DEA, 1 <sup>st</sup> Heating. Frequency dependence of the $\gamma$ relaxation of Kapton®-E conditioned at 98 %RH. ....	108
Figure 4.23 Arrhenius activation energy plot for the $\gamma$ relaxation of Kapton®-E as a function of % RH. ....	110

Figure 4.24 Argand diagram, Kapton-E 98% RH $\gamma$ relaxation. ....	115
Figure 4.25 Relaxation distribution, Kapton-E 98% RH $\gamma$ relaxation. ....	115
Figure 4.26 Argand diagram, Kapton-E 73% RH $\gamma$ relaxation. ....	116
Figure 4.27 Relaxation distribution, Kapton-E 73% RH $\gamma$ relaxation. ....	116
Figure 4.28 Argand diagram, Kapton-E 43% RH $\gamma$ relaxation. ....	117
Figure 4.29 Relaxation distribution, Kapton-E 43% RH $\gamma$ relaxation. ....	117
Figure 4.30 Argand diagram, Kapton-E 30% RH $\gamma$ relaxation. ....	118
Figure 4.31 Relaxation distribution, Kapton-E 30% RH $\gamma$ relaxation. ....	118
Figure 4.32 In situ DMA, Kapton <sup>®</sup> -E in water. Displacement versus immersion time for (a) 3 samples at 25 °C, 1 Hz, note that the curves overlay almost exactly, (b) 2 samples at 25 °C, 0.1 Hz, and (c) 1 sample at 60 °C, 1 Hz. ....	120
Figure 4.33 Weight % uptake of water by Kapton <sup>®</sup> -E at 25 °C and 60 °C. ....	120
Figure 4.34 In situ DMA, 1 Hz Influence of water temperature on the displacement of Kapton <sup>®</sup> -E Initial water temperature is 60 °C. ....	122
Figure 5.1 Dimension change versus temperature for BPADA/DCHM. ....	129
Figure 5.2 The dependence of the storage modulus on the percent aliphatic diamine DMA, 1 Hz. ....	131
Figure 5.3 Sub-Tg DMA responses at 1 Hz for BPADA/ODA, BPADA/HMDA:ODA, 75:25, BPADA/HMDA:DoDDA, 50:50, and BPADA/HMDA:DoDDA, 25:75. ....	132
Figure 5.4 Sub-Tg DMA response at 1 Hz for BPADA/DCHM. ....	133
Figure 5.5 DEA, 2 <sup>nd</sup> Heating The frequency dependence of the $\gamma$ and $\beta$ relaxations for BPADA/HMDA:ODA, 75:25. ....	135
Figure 5.6 DEA, 2 <sup>nd</sup> Heating The frequency dependence of the $\gamma$ relaxation for BPADA/HMDA:DoDDA, 25:75. ....	135
Figure 5.7 DEA, 2 <sup>nd</sup> Heating The frequency dependence of the sub-Tg relaxations for BPADA/DCHM. ....	136
Figure 5.8 Log frequency versus 1/T for the DEA $\gamma$ , $\beta$ , and T <sub>g</sub> relaxations of several BPADA-based polyimides. Note: the curves for the T <sub>g</sub> of HMDA/DoDDA, 50:50 and HMDA:DoDDA, 25:75 overlay almost exactly. ....	137
Figure 5.9 DEA, 2 <sup>nd</sup> Heating. Permittivity response for BPADA/HMDA:ODA, 75:25. ....	139
Figure 5.10 DEA, 2 <sup>nd</sup> Heating. Permittivity response of BPADA/DCHM. ....	140
Figure 5.11 TGA. The weight percent versus temperature for BPADA/HMDA:DoDDA, 25:75 conditioned at different relative humidities. ....	142
Figure 5.12 DEA, 1 <sup>st</sup> Heating, 1000 Hz. The effect of absorbed moisture on the low temperature tan $\delta$ response of BPADA/HMDA:DoDDA, 25:75. ....	143
Figure 6.1 Dimension change versus temperature for BPADA/ODA:DoDDA, 75:25. ...	148
Figure 6.2 The dependence of the glass transition temperature on the percent aliphatic diamine DMA, 1 Hz (a) Storage Modulus, E' b) Tan Delta. ....	150
Figure 6.3 Average Storage Modulus, E', at 25°C. ....	152
Figure 6.4 Sub-Tg DMA responses at 1 Hz. ....	153
Figure 6.5 Four replicate DMA experiments, 1 Hz, for BPADA/ODA:DoDDA, 75:25. Plot highlights the T <sub>g</sub> . ....	154

Figure 6.6 Four replicate DMA experiments, 1 Hz, for BPADA/ODA:DoDDA, 75:25 Plot highlights the $\gamma$ and $\beta$ sub- $T_g$ relaxations. ....	155
Figure 6.7 Example calculation of the $\beta$ relaxation peak area using a linear baseline. Sample is BPADA/ODA:DoDDA, 75:25 B. ....	156
Figure 6.8 $\beta$ relaxation tan delta peak area. ....	157
Figure 6.9 DEA, 2 <sup>nd</sup> Heating. The frequency dependence of the $\beta$ relaxation for BPADA/ODA. ....	158
Figure 6.10 DEA, 2 <sup>nd</sup> Heating. The frequency dependence of the $\gamma$ and $\beta$ relaxations for BPADA/ODA:DoDDA, 50:50. ....	158
Figure 6.11 DEA, 2 <sup>nd</sup> Heating. The frequency dependence of the $\gamma$ relaxation for BPADA/DoDDA. ....	159
Figure 6.12 DEA, 2 <sup>nd</sup> Heating. Frequency dependence of the $T_g$ for BPADA/ODA:DoDDA, 50:50. ....	159
Figure 6.13 DEA, 2 <sup>nd</sup> Heating. The frequency dependence of the $T_g$ for BPADA/DoDDA. ....	160
Figure 6.14 Log frequency versus $1/T$ for the DEA $\gamma$ , $\beta$ , and $T_g$ relaxations of several BPADA/ODA:DoDDA polyimides. ....	161
Figure 6.15 DEA, 2 <sup>nd</sup> Heating. Permittivity response for BPADA/ODA. ....	163
Figure 6.16 DEA, 2 <sup>nd</sup> Heating. Permittivity response for BPADA/ODA:DoDDA, 50:50. ....	164
Figure 6.17 Stress versus strain % for BPADA/ODA in tension. ....	165
Figure 6.18 Determination of the Young's Modulus for a BPADA/ODA sample. ....	166
Figure 6.19 Young's Modulus, $E$ , as a function of chemical composition. ....	167
Figure 6.20 Yield stress, $\sigma_y$ , as a function of chemical composition. ....	167
Figure 7.1 Blister growth of BPADA/ODA-2: (a) 3 minutes, radius = 4.59 mm, (b) 6 minutes, radius = 5.52 mm, (c) 9 minutes, radius = 6.73 mm. ....	176
Figure 7.2 Blister growth of BPADA/ODA:DoDDA, 25:75-1: (a) 14 minutes, radius = 4.79 mm, (b) 14.5 minutes, radius = 6.15 mm, (c) 15 minutes, radius = 6.94 mm. ....	177
Figure 7.3 Schematic of sample and change in adhesion. ....	179
Figure 7.4 Schematic of the variation in film thickness induced by the patch. ....	179
Figure 7.5 $P$ versus $w_o$ for the BPADA/ODA samples. For clarity, each successive curve is horizontally offset by 0.25 mm. ....	186
Figure 7.6 Linear fit of $P$ versus $w_o$ through the origin for ODA-3. ....	186
Figure 7.7 $P$ versus $a$ for the BPADA/ODA samples. ....	187
Figure 7.8 $G$ from the load-based equation versus $a$ . ....	187
Figure 7.9 $w_o$ versus $a$ for the BPADA/ODA samples. ....	188
Figure 7.10 $\text{Log}(da/dt)$ versus time for ODA-3, ODA-4, and ODA-5. ....	188
Figure 7.11 XPS wide-scan of the polyimide side of BPADA/ODA-2. ....	189
Figure 7.12 XPS wide-scan of silicon wafer ( $\text{SiO}_2/\text{Si}$ ) side of BPADA/ODA-2. ....	190
Figure 7.13 C 1s curve-fitted photopeak of cleaned ( $\text{SiO}_2/\text{Si}$ ) silicon wafer (not stored in water). ....	191
Figure 7.14 C 1s curve-fitted photopeak of the polyimide side of BPADA/ODA-2. ....	191
Figure 7.15 C 1s curve-fitted photopeak of the silicon wafer side of BPADA/ODA-2. ....	192
Figure 7.16 $P$ versus $w_o$ for BPADA/ODA:DoDDA, 75:25-1. ....	197

Figure 7.17 P versus $w_o$ for BPADA/ODA:DoDDA, 75:25-2. ....	198
Figure 7.18 P versus a for BPADA/ODA:DoDDA, 75:25-1 and 75:25-2. ....	198
Figure 7.19 G from the load-based equation versus a for 75:25-2. ....	199
Figure 7.20 $w_o$ versus a for BPADA/ODA:DoDDA, 75:25-1 and 75:25-2. ....	199
Figure 7.21 G from the displacement-based equation versus a for 75:25-1. ....	200
Figure 7.22 BPADA/ODA:DoDDA, 50:50-3 post-mortem specimen showing plastic yielding. ....	202
Figure 7.23 P versus $w_o$ for the BPADA/ODA:DoDDA, 50:50 SLBT samples. ....	203
Figure 7.24 P versus a for the BPADA/ODA:DoDDA, 50:50 SLBT samples. ....	204
Figure 7.25 $w_o$ versus a for the BPADA/ODA:DoDDA, 50:50 SLBT samples. ....	204
Figure 7.26 G determined by the displacement-based equation versus a for 50:50-4. ....	205
Figure 7.27 BPADA/DoDDA-1 post-mortem sample showing plastic yielding. ....	207
Figure 7.28 P versus $w_o$ for BPADA/ODA:DoDDA, 25:75 and BPADA/DoDDA. ....	208
Figure 7.29 P versus a for BPADA/ODA:DoDDA, 25:75 and BPADA/DoDDA. ....	208
Figure 7.30 $w_o$ versus a for BPADA/ODA:DoDDA, 25:75 and BPADA/DoDDA. ....	209
Figure 7.31 G from the displacement-based equation versus a for 25:75-2. ....	209
Figure 7.32 Load versus Shaft Displacement for BPADA/ODA in a low %RH environment at 25 °C, 38 °C, and 70 °C. ....	211
Figure 7.33 Load versus Shaft Displacement for BPADA/ODA:DoDDA, 50:50 in a low %RH at 70°C. ....	212

## LIST OF TABLES

Table 2.1 Dielectric Constants for Some Common Polymers. ....	30
Table 3.1 Humidity Environments.....	53
Table 3.2 Variables used in the harmonic mean method. ....	62
Table 3.3 XPS analysis of silicon wafers.....	77
Table 4.1 Glass transition temperatures for the neat and bilayer films.....	84
Table 4.2 DMA activation energies. ....	92
Table 4.3 Moisture contents of Kapton <sup>®</sup> -E determined gravimetrically and by TGA. ....	100
Table 4.4 T <sub>max</sub> for the $\gamma$ component of Tan $\delta$ at 1000 Hz as a function of % RH.....	107
Table 4.5 Coordinate pairs for activation energy calculations.....	109
Table 4.6 Arrhenius activation energies for the $\gamma$ relaxation of Kapton <sup>®</sup> -E. ....	110
Table 4.7 Starkweather-Eyring Activation Energies. ....	112
Table 5.1 Molecular Weight and Thermal Characterization of BPADA-based Polyimides. ....	127
Table 5.2 Linear Coefficients of Thermal Expansion. ....	129
Table 5.3 DMA Glass Transition Temperatures, 1 Hz. ....	132
Table 5.4 DEA Arrhenius Activation Energies. ....	137
Table 5.5 Refractive Index and Dielectric Constant. ....	138
Table 5.6 TGA Percent weight loss of BPADA/HMDA:DoDDA, 25:75 at 100 °C. ....	142
Table 6.1 Molecular Weight and Thermal Characterization of BPADA/ODA:DoDDA Series.....	147
Table 6.2 Linear Coefficients of Thermal Expansion. ....	149
Table 6.3 DMA Glass Transition Temperatures, 1 Hz. ....	151
Table 6.4 DEA Arrhenius Activation Energies. ....	161
Table 6.5 Refractive Index and Dielectric Constant. ....	162
Table 7.1 Contact angles and surface energies for the BPADA/ODA:DoDDA series.....	172
Table 7.2 Contact angles and surface energies for a cleaned silicon wafer (SiO <sub>2</sub> /Si). ....	172
Table 7.3 Thermodynamic work of adhesion for PI to SiO <sub>2</sub> /Si. ....	174
Table 7.4 Film Tensile Rigidity, <i>Eh</i> , of the BPADA/ODA:DoDDA series. ....	177
Table 7.5 Adhesion Energies of BPADA/ODA to SiO <sub>2</sub> at 25 °C and high %RH. ....	185
Table 7.6 Curve fit C 1s assignments for cleaned silicon wafer (SiO <sub>2</sub> /Si) and failure surfaces of BPADA/ODA-2.....	192
Table 7.7 XPS results for BPADA/ODA SLBT samples. ....	193
Table 7.8 Adhesion Energy of BPADA/ODA:DoDDA 75:25 to SiO <sub>2</sub> /Si at 25 °C and high %RH.....	197
Table 7.9 XPS results for BPADA/ODA:DoDDA, 75:25 SLBT samples. ....	201
Table 7.10 XPS results for BPADA/ODA:DoDDA, 50:50 SLBT samples. ....	206
Table 7.11 XPS results for BPADA/ODA:DoDDA, 25:75 and BPADA/DoDDA SLBT samples. ....	210

## 1. INTRODUCTION

Aromatic polyimides have found widespread applicability which can partially be attributed to their thermal stability, chemical resistance, high glass transition temperature, and mechanical integrity.<sup>1-3</sup> Many of their uses require them to adhere to various substrates, a main topic of this research. Wholly aromatic polyimides, however, do not always provide the optimum properties for many specialty applications due to deficiencies in processability, solubility, and transparency, as well as their relatively high dielectric constants. Fluorination, bulky substituents, asymmetric monomers, and flexible bridging groups have been added to counteract the polyimide shortcomings.<sup>2</sup> Another option for improvement has been the incorporation of aliphatic or cycloaliphatic monomers to form partially aliphatic polyimides.<sup>4-10</sup>

Polyimides containing aliphatic groups can be organized into three categories based on the combination and types of monomers used in their synthesis: (1) aromatic dianhydrides and aliphatic diamines, (2) aliphatic dianhydrides and aromatic diamines, and (3) aliphatic dianhydrides and aliphatic diamines (ie., fully aliphatic). To synthesize polymers from category (1), assuming the traditional two-step method for aromatic polyimide synthesis is employed, the basicity of the aliphatic diamine often results in the formation of insoluble intermediate salts with the carboxylic acid groups of the polyamic acid.<sup>4,5</sup> As a result, it is difficult to obtain high molecular weight polyamic acids. The deleterious salt formation can be reduced by adding the aliphatic diamine very slowly to the dianhydride<sup>4,6,7</sup> or by direct polycondensation in *m*-cresol at high temperatures.<sup>8,9</sup>

In this investigation, ester-acid high temperature solution imidization was employed by members of Professor J.E. McGrath's research group of Virginia Tech to prepare high molecular weight, fully-cyclized, soluble, amorphous, partially aliphatic copolyimides, without the problem of salt formation. Previously, this synthetic pathway had only been adopted to prepare aromatic polyimides.<sup>10-16</sup> Its implementation to prepare soluble, amorphous, partially aliphatic polyimides is a milestone, but it also yielded numerous novel materials for structure-property investigations. The latter are the basis of this dissertation, and to which the question "Is adhesion strength influenced by glassy polymer chemical composition?" is focused. Quantitative evaluation of the energy of adhesion in such mechanically complex polyimides represents a nontrivial problem in

fracture mechanics and became a further challenge for the investigation as will be seen. Also, the importance of moisture in any adhesion measurement is emphasized.

The chemical composition of a polymer influences (1) the types of physical and chemical bonding with the substrate, and (2) segmental mobility – cooperative and local viscoelastic relaxations which may dissipate energy as the adhesive is thermally or mechanically stressed. Both factors are intimately connected and contribute greatly to practical adhesion strength. Their roles are described by a general equation for adhesion energy:<sup>17-20</sup>

$$G = G_o + g(G_o) \cdot (\phi(R, T)) \quad \text{Equation 1.1}$$

where  $G$  is the practical adhesion energy,  $G_o$  is the intrinsic adhesion energy, and  $g(G_o) \cdot (\phi(R, T))$  is the energy dissipation term which depends on the intrinsic adhesion energy  $G_o$ , and on the loss function  $\phi$  which itself further depends on the test rate,  $R$ , and temperature,  $T$ . The term  $g(G_o)$  can be viewed as an activator for viscoelastic and plastic energy dissipation at a growing crack tip,  $(\phi(R, T))$ , during adhesive failure. The interaction of  $g(G_o)$  and  $(\phi(R, T))$  is not well understood and the exact relationship may be unique not only for every adhesive-substrate system, but also within the different regions of the viscoelastic spectrum of an adhesive-substrate system.

The concepts which embody equation 1.1 originated from observations made for model crosslinked elastomer adhesives bonded to rigid substrates.<sup>17-20</sup> These adhesive bonds were tested over wide ranges of temperatures and test rates to vary the amount of energy consumed by viscoelastic deformations at the growing crack tip. The two material responses, near-equilibrium and nonequilibrium, constitute the  $G_o$  and  $g(G_o) \cdot (\phi(R, T))$  terms, respectively. While the behaviors of several elastomer systems have been generally described by equation 1.1, its application to glassy adhesives in which plastic deformations at the crack tip occur, has not been demonstrated. Thus, for the glassy polyimide adhesives in this study, the validity of equation 1.1 is tested. Rigorous quantitative assignments were not possible, rather the terms are discussed conceptually as the central question is addressed. Part of the problem is embodied in the available experimental methods, of which one (the shaft loaded blister test) was extensively explored.

The present investigation features partially aliphatic copolyimides obtained from bis[4-(3,4-dicarboxyphenoxy)phenyl]propane dianhydride, or Bisphenol A dianhydride (BPADA), and four diamines: 4,4'-oxydianiline (ODA), 4,4'-diaminodicyclohexyl-methane (DCHM), hexamethylenediamine (HMDA), and dodecyldiamine (DoDDA). The combination and types of aromatic and aliphatic diamine monomers were selected according to anticipated structure-property relations. Cycloaliphatic diamines impart rigidity to the polymer backbone similar to that of aromatic diamines, but offer improvements in polymer transparency and dielectric constant partially due to the reduced formation of charge transfer complexes.<sup>5,7,21,22</sup> The linear aliphatic diamines are more flexible - the number of methylene units strongly influences the magnitude of the glass transition temperature, as well as, the crystalline/amorphous morphology of the polyimide. When the number of methylene units within the diamine was varied from 4 to 12, other research has found an “even-odd” propensity to crystallize.<sup>23,24</sup> Copolymerization of rigid plus flexible monomers (aromatic, cycloaliphatic, aliphatic) allows the thermal and mechanical properties of polyimides to be tailored to meet specific processing and property requirements.<sup>4</sup> Thus, an excellent series to correlate molecular and macroscopic data exists.

To address the central question of this dissertation, “Is adhesion strength influenced by glassy polymer chemical composition?” this investigation: (1) presents molecular weight, thermal, dielectric, and mechanical data to establish structure-property relationships, (2) discusses the molecular origins of the  $\gamma$  and  $\beta$  sub- $T_g$  viscoelastic relaxations, (3) describes the design and instrumentation of a shaft loaded blister test, (4) presents adhesion studies for selected polyimides to silicon wafers ( $\text{SiO}_2/\text{Si}$ ) using the shaft loaded blister test in high and low relative humidity, and high and low temperature environments, and (5) interprets the meaning of each property with respect to adhesion.

To facilitate the effort, this dissertation is organized into eight sections. Chapter 1 offers a general introduction and states the research objectives. Chapter 2 provides a literature survey of relevant physical properties of aromatic and partially aliphatic polyimides. Chapter 3 describes the sample preparations, various instrumental details, and the design and instrumentation of the shaft loaded blister test. Chapter 4 discusses the viscoelastic characterization of Kapton<sup>®</sup>-E, a commercially available aromatic polyimide, in dry, humid, and saturated water environments. Chapter 5 features the physical property characterization of BPADA-based polyimides containing a combination of rigid aromatic or cycloaliphatic diamines with flexible aliphatic

diamines.<sup>25</sup> Chapter 6 discusses the physical property characterization for BPADA/ODA:DoDDA, a series of five polyimides that vary in their molar ratio between a rigid aromatic and a flexible aliphatic diamine.<sup>26</sup> Chapter 7 presents the adhesive testing of the BPADA/ODA:DoDDA series of polyimides to silicon wafers (SiO<sub>2</sub>/Si) using the shaft loaded blister test. Chapter 8 summarizes the significant conclusions and offers suggestions for future research.

## 1.1. References

- <sup>1</sup> Bessonov, M.I.; Koton, M.M.; Kudryavtsev, V.V.; Laius, L.A. *Polyimides Thermally Stable Polymers*; Consultants Bureau: New York, 1987.
- <sup>2</sup> *Polyimides*; Wilson, D.; Stenzenberger, H.D.; Hergenrother, P.M., Eds.; Blackie: London, 1990.
- <sup>3</sup> *Polyimides Fundamentals and Applications*; Ghosh, M.K.; Mittal, K.L., Eds.; Marcel Dekker: New York, 1996.
- <sup>4</sup> Kreuz, J.A.; Hsiao, B.S.; Renner, C.A.; Goff, D.L. *Macromolecules* **1995**, *28*, 6926.
- <sup>5</sup> Volksen, W.; Cha, H.J.; Sanchez, M.I.; Yoon, D.Y. *Reactive Functional Polymers* **1996**, *30*, 61.
- <sup>6</sup> Jin, Q.; Yamahita, T.; Horie, K.; Yokota, R.; Mita, I. *J. Polym. Sci. Polym. Chem. Ed.* **1993**, *31*, 2345.
- <sup>7</sup> Jin, Q.; Yamahita, T.; Horie, K. *J. Polym. Sci. Polym. Chem. Ed.* **1994**, *32*, 503.
- <sup>8</sup> Koning, C.; Delmotte, A.; Larno, P.; Van Mele, B. *Polymer* **1998**, *39(16)*, 3697.
- <sup>9</sup> Korshak, V.V.; Babchinitser, T.M.; Kazaryan, L.G.; Vasilyev, V.A.; Genin, Ya. V.; Azriel, A. Ye.; Vygodsky, Ya.S.; Churochkina, N.A.; Vinogradova, S.V.; Tsvankin, D.Ya. *J. Polym. Sci. Polym. Phys. Ed.* **1980**, *18*, 247.
- <sup>10</sup> Moy, T.M., Ph.D. Dissertation, Virginia Tech, 1993.
- <sup>11</sup> Moy, T.M.; DePorter, C.D.; McGrath, J.E. *Polymer* **1993**, *34*, 819.
- <sup>12</sup> Tan, B., Ph.D. Dissertation, Virginia Tech, 1997.
- <sup>13</sup> Tan, B.; Vasudevan, V.; Lee, Y.J.; Gardner, S.; Davis, R.M.; Bullions, T.; Loos, A.C.; Parvatareddy, H.; Dillard, D.A.; McGrath, J.E.; Cella, J. *J. Polym. Sci. Polym. Chem. Ed.*, **1997**, *35*, 2943.
- <sup>14</sup> Farr, I.V.; Glass, T.E.; Ji, Q.; McGrath, J.E. *High Perform. Polym.* **1997**, *9*, 345.
- <sup>15</sup> Farr, I.V., Ph.D. Dissertation, Virginia Tech, 1999.
- <sup>16</sup> Farr, I.V.; Kratzner, D.; Glass, T.E.; Dunson, D.; Ji, Q.; McGrath, J.E. *J. Polym. Sci. Polym. Chem. Ed.* **2000**, *38*, 2840.
- <sup>17</sup> Gent, A.N.; Schultz, J. *J. Adhesion* **1972**, *3*, 281.
- <sup>18</sup> Andrews, E.H.; Kinloch, A.J. *Proc. R. Soc. Lond.* **1973**, *A.332*, 385.
- <sup>19</sup> Andrews, E.H.; Kinloch, A.J. *Proc. R. Soc. Lond.* **1973**, *A.332*, 401.
- <sup>20</sup> Ahagon, A.; Gent, A.N. *J. Polym. Sci., Polym. Phys. Ed.* **1975**, *13*, 1285.
- <sup>21</sup> Li, Q.; Horie, K.; Yokota, R. *Polym. J.* **1998**, *30(10)*, 805.
- <sup>22</sup> Chern, Y.T.; Shiue, H.C. *Macromolecules* **1997**, *30*, 5766.
- <sup>23</sup> Koning, C.; Delmotte, A.; Larno, P.; Van Mele, B. *Polymer* **1998**, *39(16)*, 3697.

---

<sup>24</sup> Korshak, V.V.; Babchinitser, T.M.; Kazaryan, L.G.; Vasilyev, V.A.; Genin, Ya. V.; Azriel, A. Ye.; Vygodsky, Ya.S.; Churochkina, N.A.; Vinogradova, S.V.; Tsvankin, D.Ya. *J. Polym. Sci. Polym. Phys. Ed.* **1980**, *18*, 247.

<sup>25</sup> Eichstadt, A.E.; Ward, T.C.; Bagwell, M.D.; Farr, I.V.; Dunson, D.L.; McGrath, J.E. *Macromolecules* accepted, 2002.

<sup>26</sup> Eichstadt, A.E.; Ward, T.C.; Bagwell, M.D.; Farr, I.V.; Dunson, D.L.; McGrath, J.E. *J. Polym. Sci. Polym. Phys. Ed.* **2002**, *40(15)*, 1503-1512.

## **2. LITERATURE REVIEW**

### **2.1 Applications**

Flexible printed circuits (FPC) are used as electronic interconnections for numerous applications encompassing: printer cartridges, hard disk drives, integrated circuit packaging, medical devices, and automotive devices. A FPC consists of a base dielectric layer or substrate on which a conductive pattern or circuit is deposited, then the pattern is protected by a top dielectric layer or coverlayer. Polyimides are used as substrates and coverlayers for FPC packaging due to their thermal and dimensional stability, chemical resistance, and electrical, mechanical, and adhesion characteristics. Copper is frequently used as a conductive layer for FPCs. Strong adhesion between all components is required to ensure device performance. FPCs are replacing traditional printed wiring boards, a composite composed of a thermosetting resin and glass cloth, in many applications because they offer improved shock and vibration absorption, provide flexural endurance for dynamic use, allow for dimensional variations between components, and easily accommodate three dimensional layouts. These improvements allow smaller devices to be made and reduce the weight and volume of devices.<sup>1</sup>

In addition to FPC, another major application of polyimides is as interlayer dielectrics within integrated circuits. Examples of integrated circuits include chip scale packaging for wireless electronics such as cellular telephones, pagers, and digital cameras. Integrated circuits are composed of layers of precisely patterned and positioned layers of dielectric (polyimide or silicon wafer) and conducting materials (metal) stacked upon each other.<sup>2</sup> The dielectric layer prevents electrical interference between metal layers and planarizes surface features. To achieve these performance demands, the dielectric must adhere strongly to metals, ceramics, and polyimides.

### **2.2 Synthesis**

#### **2.2.1 Poly(amic acid) Method**

Aromatic polyimides are often synthesized by a two step condensation reaction. Figure 2.1 provides a general reaction scheme.<sup>3</sup> By this method, an aromatic dianhydride is first reacted in a polar aprotic solvent, such as NMP or DMAc, with an aromatic diamine to form a soluble polyamic acid (PAA) precursor. The polar solvent dissolves intermediate products of the PAA and thus facilitates the polymerization.<sup>2</sup> For PAAs which may precipitate upon imidization, the

PAA solution is then cast onto a substrate to form a film. Upon heating, the PAA undergoes ring closing or imidization, during which water is simultaneously lost. Formation of the polyimide using heat is called thermal imidization. The thermal imidization step involves a multi-temperature procedure.<sup>2</sup> Typically, the PAA film first is “soft baked” to remove the casting solvent. The temperature is low enough such that little imidization occurs. The film is then “hard baked” at higher temperatures, 200°C or greater, to initiate bulk imidization. Temperatures greater than the ultimate glass transition temperature are used to enable enough chain mobility to complete the imidization.

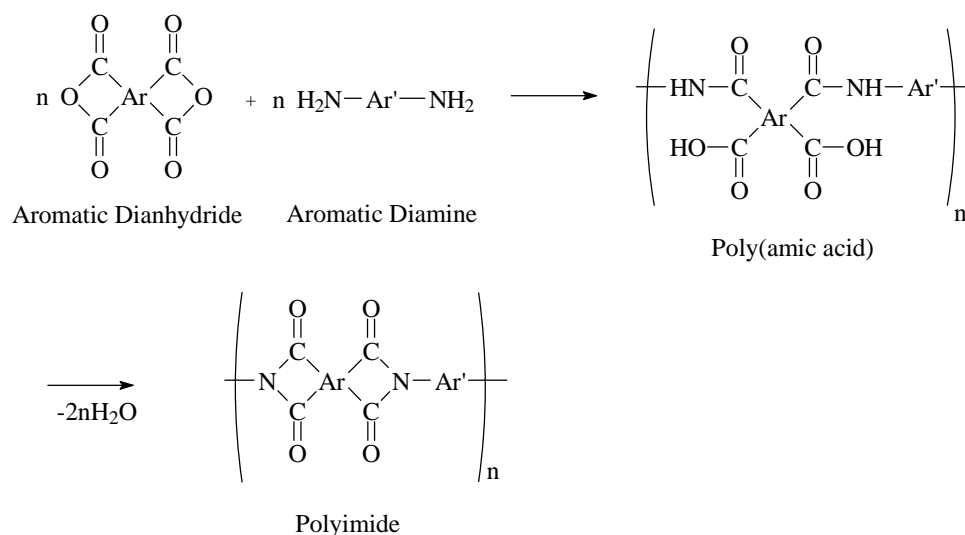


**Figure 2.1. Poly(amic acid) route for the synthesis of an aromatic polyimide. Ar and Ar' denote aromatic moieties.**

Aromatic polyimides that vary in chain linearity and rigidity can be synthesized by combination of different monomers. Polyimides are usually called by the acronyms of their monomers. Some common aromatic dianhydrides and aromatic diamines are presented in Figure 2.2 and Figure 2.3, respectively.

Acronym	Chemical Structure	Name
PMDA		pyromellitic dianhydride
BPDA		3,3',4,4'-biphenyltetracarboxylic dianhydride
BTDA		3,3',4,4'-benzophenonetetracarboxylic dianhydride
OPDA		4,4'-oxydiphthalic dianhydride
BPADA		bisphenol-A dianhydride

**Figure 2.2. Acronyms, chemical structures, and chemical names of some common aromatic dianhydrides.**

Acronym	Chemical Structure	Name
p-PDA		<i>para</i> -phenylene diamine
m-PDA		<i>meta</i> -phenylene diamine
ODA		4,4'-oxydianiline

**Figure 2.3. Acronyms, chemical structures, and chemical names of some common aromatic diamines.**

Since many aromatic polyimides are insoluble, determination of the molecular weight by a standard technique such as Gel Permeation Chromatography is not possible. A well-defined, high molecular weight PAA can be attained by using pure monomers, moisture free reaction conditions, the proper choice of solvent, and a low to moderate reaction temperature such that side reactions are prevented.<sup>4,5</sup> Using infrared spectroscopy, the imidization reaction can be followed by monitoring the disappearance of the amine (N-H) absorption bands and the

appearance of the aromatic imide (C-N) absorption band.<sup>6</sup> Upon conversion of the PAA to the polyimide, there is an improvement in the intermolecular and intramolecular order which enhances the overall thermal and mechanical integrity of the film.<sup>7</sup>

One limitation of polyimide synthesis via the PAA method is that the PAA precursor is sensitive to hydrolysis reaction based depolymerization. This sensitivity limits its “shelf life” and is a drawback in manufacturing processes in which the environment is difficult to control.<sup>2</sup>

### 2.2.2 Ester-acid Solution Imidization

Aromatic polyimides can also be synthesized via an ester-acid precursor. This method involves the prereaction of aromatic dianhydrides with ethanol and a tertiary amine catalyst to form ester-acids, followed by the addition of diamines. Subsequent thermal reaction forms a high molecular weight, fully-cyclized polyimide.<sup>4</sup> Figure 2.4 shows a general reaction scheme.

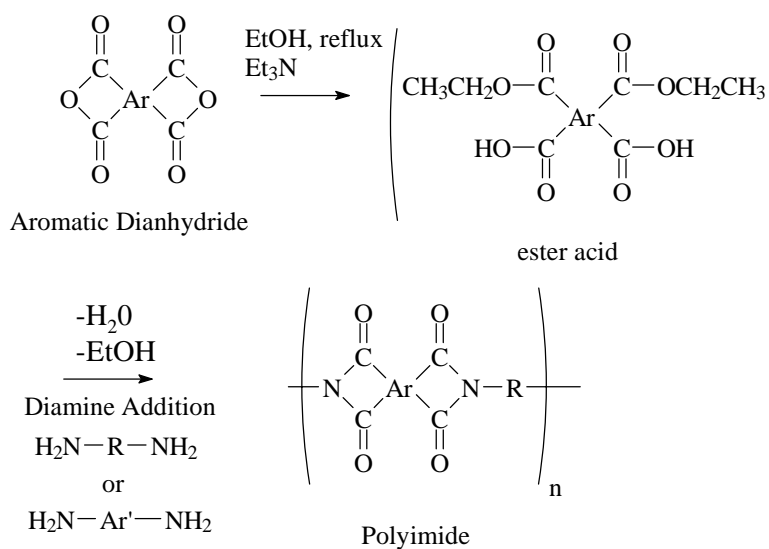


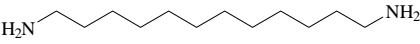
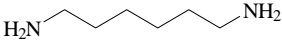
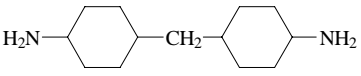
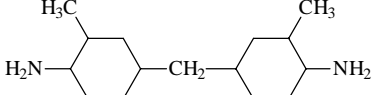
**Figure 2.4. Ester-acid solution imidization for the synthesis of aromatic or partially aliphatic polyimides. Ar and Ar' designate aromatic moieties. R designates an aliphatic moiety.**

The aromatic monomers may include any of those presented in Figure 2.2 and Figure 2.3. Some common aliphatic diamines monomers are presented in Figure 2.5.

An advantage of using the ester-acid method over the PAA method is that the ester-acid is more hydrolytically stable. This quality allows a longer shelf life and easier use within manufacturing processes.<sup>2</sup>

### 2.2.3 Partially Aliphatic Polyimides

Much of the published literature for polyimides discusses the synthesis and physical properties of wholly aromatic polyimides. Another class of polyimides which is used as interlayer dielectric materials for microelectronics applications and as color filters and liquid crystal orientation layers in display applications, is partially aliphatic polyimides.<sup>8-11</sup> This class of polyimides can be subdivided into three categories: (1) aromatic dianhydrides and aliphatic diamines, (2) aliphatic dianhydrides and aromatic diamines, and (3) aliphatic dianhydrides and aliphatic diamines (ie. fully aliphatic). Partially aliphatic polyimides from category (1) are the most prevalent. The chemical structures of some common aliphatic and cycloaliphatic diamines are shown in Figure 2.5.

Acronym	Chemical Structure	Name
DoDDA		1,12-dodecyl diamine
HMDA		1,6-hexamethylene diamine
DACH		1,4-diaminocyclohexane
DCHM		4,4'-diamino-dicyclohexylmethane
DMDHM		Bis(4-amino-3-methyl-cyclohexyl)methane

**Figure 2.5. Examples of aliphatic and cycloaliphatic diamines.**

A thorough survey of the literature for partially aliphatic polyimides is presented in the Introduction and in Chapters 5 and 6 so this will not be reiterated here.

### 2.3 Charge Transfer Complexes

One of the distinguishing characteristics of aromatic polyimide films is their color. The color ranges from pale yellow to deep orange depending on the dianhydride and diamine chemical structures. Charge transfer complexes (CTC) form between electron donor (diamine) and electron acceptor (dianhydride) groups. The strength of these complexes is determined by

the ionization potential of the diamine and the electron affinity of the dianhydride.<sup>12,13</sup> As the strength of the CTC increases, the color intensity increases.

The ionization potential of the diamine, the electron affinity of the dianhydride, the cut-off wavelength (absorption edge,  $\lambda_0$ ) in optical absorption spectra, and <sup>15</sup>N NMR chemical shifts ( $\delta_N$ ) have been used as evidence to correlate polyimide color to chemical structure. Ando et al. provide a thorough literature survey on the topic and show the agreement of conclusions regardless of the technique.<sup>13</sup> Some conclusions included: the higher the ionization potential of the diamine, the more intense the yellow color; however, incorporating electron withdrawing groups such as  $-\text{SO}_2-$  and  $-\text{C}(\text{CF}_3)_2-$  or groups that altered the backbone linearity such as  $-\text{O}-$  or *meta*-linked structures, reduced CTC interactions and weakened the intensity of the yellow color. Generally, the higher the electron affinity of the dianhydride, the more intense the yellow color. PMDA showed the most intense color. The incorporation of additional benzene rings or flexible bridging units isolated the electron withdrawing anhydride groups from each other and interrupted the backbone linearity. As a result, CTC interactions were reduced and the yellow color was less intense.

It is hypothesized that CTC interactions influence the physical properties of aromatic polyimides. St. Clair observed that when CTC interactions were reduced, in addition to reducing the film color, the solubility and melt processability increased and the dielectric constant decreased.<sup>12</sup> Fryd commented on CTC interactions to explain a trend between chemical structure and the glass transition temperature.<sup>14</sup> Tamai et al. suggested that the thermo-oxidative stability of some aromatic polyimides was improved due to CTC interactions.<sup>15</sup>

## 2.4 Thermal properties

### 2.4.1 Thermal Stability

The thermal stability of aromatic polyimides favors their use versus other polymers for high temperature applications. The thermal stability of aromatic polyimides, particularly above 300 °C, arises from the high primary bond strengths of the phenyl and imide ring structures, intermolecular interactions among the polymer chains, resonance stabilization, and molecular symmetry.<sup>2-4</sup> Increasing the flexibility<sup>16</sup> or aliphatic character<sup>5</sup> decreases thermal stability due to the presence of weaker primary and secondary interactions.

Aromatic polyimide thermal and thermo-oxidative stability are influenced by the synthetic route, chemical structure, residual solvent, and absorbed moisture.<sup>17</sup> Thermal stability and thermo-oxidative stability refer to resistance to degradation in an inert (N<sub>2</sub>, Ar) and air atmosphere, respectively. Thermogravimetric analysis (TGA) and/or infrared analysis (TGA-FTIR), gas chromatography (GC) and/or mass spectrometry (GC-MS) are a few of the techniques employed for investigating the kinetics and mechanisms of polyimide degradation.<sup>17</sup>

Although no single grand scheme for thermal degradation can be drawn for aromatic polyimides, insight to the degradation pathways is gained from a few examples. For PMDA/ODA at 600 °C, 33 volatile compounds were identified by mass spectrometry.<sup>17</sup> Scission reactions of the heterocyclic ring of the imide were evidenced by decomposition products such as benzonitrile, aniline, dicyanobenzene, and p-aminophenol. Scission within ODA resulted in phenol and benzene. In addition, water, carbon monoxide, and carbon dioxide were produced. The water was attributed to that absorbed from the atmosphere and the cyclization of yet uncyclized amic acid units. The carbon dioxide was assigned to the rupture of very weak bonds, the hydrolysis of yet uncyclized amic acid units, and the thermal breakdown of isoimide rings. The carbon monoxide evolved increased substantially above 400 °C and was attributed to the decomposition of the chemical structure.

Several researchers have correlated dianhydride and diamine chemical structure to thermal and thermo-oxidative stability.<sup>12,17</sup> The results generally agreed that the stability for dianhydrides followed the order: PMDA > BTDA > OPDA. The stability for diamines of structure H<sub>2</sub>N-C<sub>6</sub>H<sub>4</sub>-X-C<sub>6</sub>H<sub>4</sub>-NH<sub>2</sub> followed the order: X = -S- ≥ -SO<sub>2</sub>- > -CH<sub>2</sub>- > -CO- > -SO- ≥ -O-. When compared, the diamine was more susceptible to oxidation than the dianhydride.

A study presented in the text by Bessonov related thermal stability determined by TGA to stress-strain behavior measured using a tensile tester for several aromatic polyimides.<sup>3</sup> The authors conditioned the tensile test specimens under the same heating rate (5 °C/min) and temperatures used within the TGA experiments. It was observed that the stress at break ( $\sigma_b$ ) and strain at break ( $\epsilon_b$ ) were dependent on chemical structure and the mechanical integrity was maintained within specimens until they were conditioned at temperatures corresponding to 10% weight loss within the TGA. At higher weight losses,  $\sigma_b$  and  $\epsilon_b$  were low. Processes such as cross-linking, chain scission, and re-packing of chains were hypothesized to cause these deleterious effects.

### 2.4.2 Coefficient of Thermal Expansion (CTE)

The CTE is a material property that is indicative of the extent to which a material expands upon heating.<sup>18</sup> The linear coefficient of thermal expansion is defined as the relative change in length divided by the change in temperature:<sup>18</sup>

$$\alpha = \frac{1}{l_o} \left( \frac{\Delta l}{\Delta T} \right) \quad \text{Equation 2.1}$$

where  $\alpha$  is the linear CTE,  $l_o$  is the initial sample length,  $\Delta l$  is the change in sample length, and  $\Delta T$  is the change in temperature. From an atomic perspective, the CTE reflects an increase in the average distance between atoms with increasing temperature. The greater the atomic bonding energy, the less the interatomic distance will increase with temperature. Due to their atomic bonding energy, ceramics exhibit low CTEs, metals exhibit intermediate values, and polymers exhibit high CTEs. Figure 2.6 compares a few CTEs from these classes of materials.

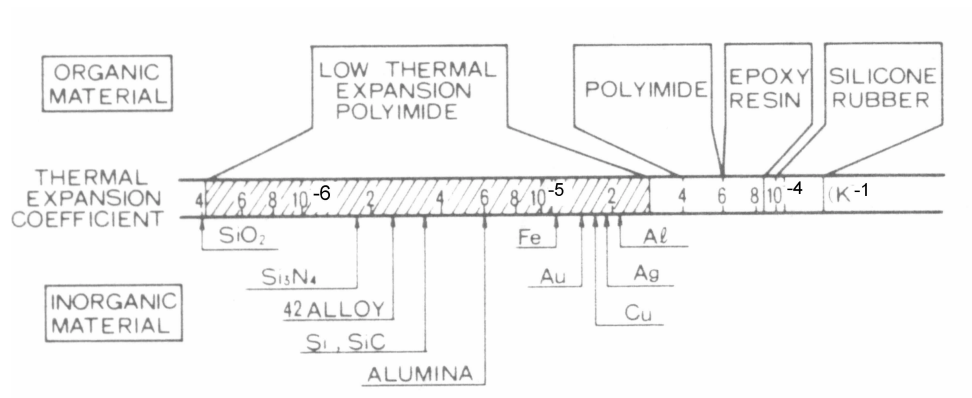


**Figure 2.6. CTE comparison for microelectronics materials.**<sup>19</sup>

A CTE mismatch between adjoining materials can contribute to adhesive bond failure. In microelectronics applications, control of the CTE is also desirable to maintain alignment of through-holes between layers, maintain alignment of component interconnections, and reduce thermal stresses which could lead to fracture of wire leads. For FCP, polyimides are adhered to silicon chip surfaces, copper within the conductive pattern, solder alloys (Au, Au plated Cu, Al, Cu), and polymer adhesives (die attach adhesive and the encapsulant). Thus, the polyimide CTE

must be designed to create the least amount of thermal mismatch between interfaces. Although polyimides display higher coefficients of thermal expansion (CTEs) than metals or ceramics, their CTEs can be lowered to better match that of such substrates by increasing the chain stiffness, chain linearity, and intermolecular interactions.<sup>2,19-22</sup>

Numata et al. extensively studied the relationship between the chemical structure of aromatic polyimides and their CTEs. The experiments encompassed polyimides synthesized from three aromatic dianhydrides and twenty one aromatic diamines.<sup>19,20,22</sup> The authors termed the polyimides exhibiting CTEs lower than  $2 \times 10^{-5}/^{\circ}\text{Kelvin}$  as *low-thermal-expansion* polyimides. All low-thermal-expansion polyimides contained diamines with only benzene or pyridine rings fused at the *para* position, and dianhydrides with linear or almost linear linkages. The high thermal expansion polyimides contained diamines with bent structures such as a benzene ring bonded at the *meta* position, or flexible bridging units. The authors then suggest that the CTE is a function of the linearity of the chemical structure. The significance of the low-thermal-expansion polyimides lies in their close match to the CTEs of inorganic materials. Numata et al. did not explore the effect of aliphatic diamines on the CTE. It is expected, however, that aliphatic sequences will increase the CTE of the polyimide since these units act as flexible spacers which increase the mobility of the chain and decrease or dilute the strength of intermolecular interactions among chains.<sup>23</sup>

Inoue et al. and Fay et al. synthesized a series of aromatic copolyimides and measured the resulting  $T_g$ , thermal stability, CTE, modulus of elasticity, and percent elongation.<sup>24,25</sup> Their conclusions illustrate how properties can be tailored by varying the chemical structure. As suggested by Numata et al., the presence of flexible linkages greatly affects physical properties.

## **2.4.3** Viscoelastic Relaxations

### **2.4.3.1** *The Glass Transition Temperature*

The glass transition temperature ( $T_g$ ) is the temperature at which large scale, cooperative segmental motion onsets. The  $T_g$  is a non-equilibrium process, and as such the detected  $T_g$  depends on the heating/cooling rate and the direction which it is approached. The temperature dependence of many physical properties, such as coefficient of thermal expansion, heat capacity, and modulus, change in the vicinity of the  $T_g$  due to the change in molecular motion.<sup>26</sup> Polymer chemical structure affects the glass transition due to its influence on internal mobility. Internal

mobility describes the ease at which the backbone bonds rotate about one another and is determined by the activation energy for internal rotation as well as by steric hindrance introduced by substituents.<sup>26</sup> In addition, chemical composition, stereochemistry, and molecular weight all impact the  $T_g$ . The presence of plasticizers within a polymer also influences the  $T_g$  by altering intermolecular interactions among chains and the amount of free volume.

The high glass transition temperatures of aromatic polyimides have been attributed to their chain stiffness, chain linearity, and to a lesser degree, intermolecular interactions.<sup>3</sup> The chain stiffness can be decreased by the incorporation of flexible bridging units such as ethers, methylenes, and ketones, within the dianhydride and/or diamine. Linearity can be disrupted by the use of *meta* rather than *para* alignment of monomers. Intermolecular interactions in the form of charge transfer interactions result between electron donor (diamine) and electron acceptor (dianhydride) groups.<sup>12</sup> The strength of these complexes is determined by the ionization potential of the diamine and the electron affinity the dianhydride.<sup>12,13</sup> Incorporating electron withdrawing groups or groups that decrease the backbone linearity within either monomer decreases the strength of the complexes. The amount or distribution of intermolecular interactions within the polyimide can be altered by the size of the dianhydride or diamine unit. Variation in the chain stiffness, linearity, and intermolecular interactions allows modification of the glass transition temperature.

#### **2.4.3.2 Secondary Relaxations: General Definitions**

At temperatures below the  $T_g$ , large scale conformational rearrangements of a polymer's backbone atoms are frozen; however, smaller scale motions can still occur. These smaller scale motions initiate secondary relaxations such as the  $\beta$  relaxation and the  $\gamma$  relaxation. The  $T_g$  is usually called the  $\alpha$  relaxation and secondary relaxations are labeled using successive letters of the Greek alphabet,  $\beta$ ,  $\gamma$ ,  $\delta$ , etc. as the temperature decreases. A general model elucidating the contributions to the  $\beta$  or  $\gamma$  relaxation was depicted by Heijboer and is reconstructed in Figure 2.7.<sup>27</sup>

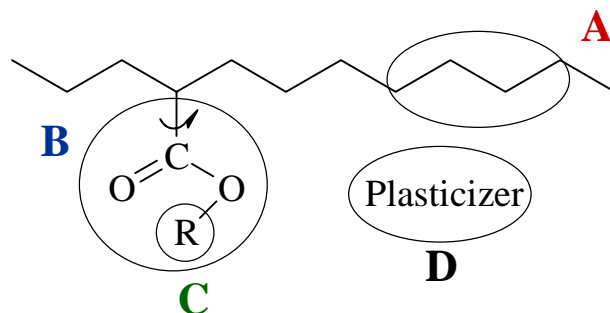


**Figure 2.7. General model of contribution to secondary relaxations.**<sup>27</sup>

Four general motions contribute to secondary relaxations: **A**. local motion within the polymer backbone, **B**. rotation of a side group about the bond connecting it to the backbone, **C**. internal motion within the side group, and **D**. motion of, or within, a plasticizer or small molecule absorbed or dissolved in the polymer.<sup>27</sup> The number of possible sources points to the complexity of secondary relaxations. To determine the exact source of a secondary relaxation for a polymer, a systematic series of chemical structures must be evaluated. Examples of the type **A** motion include the  $\beta$  relaxation for polycarbonate and polysulfone, in which the motion of the *p*-phenylene unit in the main chain was assigned.<sup>27</sup> Examples of the type **B** motion include the  $\beta$  relaxation for poly(alkyl methacrylates).<sup>27</sup>

At temperatures below the  $\beta$  relaxation, even smaller scale motions contribute to the  $\gamma$  relaxation. The  $\gamma$  relaxation arises from internal motions within a side group (type **C** motion of Figure 2.7). Heijboer showed that for polymethacrylates, the appearance of a mechanical  $\gamma$  relaxation between  $-100$  and  $-200^\circ\text{C}$  was due to motions in R of the  $-\text{COOR}$  group; for example, the *n*-butyl group on poly(*n*-butyl methacrylate) and the cyclohexyl group in poly(cyclohexyl methacrylate).<sup>27</sup>

However, for polymers containing linear  $(\text{CH}_2)_n$  sequences of  $n = 4$  or greater, the  $\gamma$  relaxation is often attributed to a “crankshaft” motion within the main chain (type **A** motion), as shown in Figure 2.8.<sup>27,28</sup>

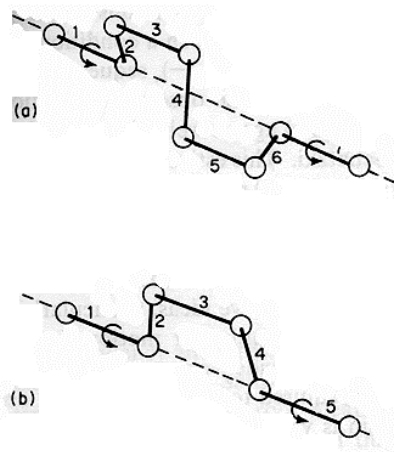


**Figure 2.8. Crankshaft motion responsible for the  $\gamma$  relaxation in many hydrocarbon based polymers.<sup>28</sup>**

Mechanical relaxations for hydrocarbon polymers near  $-150\text{ }^{\circ}\text{C}$  are attributed to crankshaft motions.<sup>28</sup> The mechanical  $\gamma$  relaxation for dry nylon 6,6 shows the same temperature and frequency dependence as the  $\gamma$  relaxation for polyethylene.<sup>28</sup> Thus the mechanical  $\gamma$  relaxation for dry nylon 6,6 was attributed to motions of the  $-(\text{CH}_2)_n-$  units between the amide groups. Polyimides containing long aliphatic sequences should also display the crankshaft motion.

Secondary relaxations may also result from motions associated with absorbed penetrants (type **D** motion of Figure 2.7). Since secondary relaxations are controlled by local intramolecular bond rotation potentials, the presence of a penetrant and its intermolecular interaction with the polymer does not change these local rotation potentials.<sup>27</sup> As a result, absorbed penetrants influence the magnitude of secondary relaxations, but not their temperature ranges. For example, when dry nylon 6,6 was exposed to moisture, its mechanical  $\beta$  relaxation, viewed through  $\tan \delta$ , increased in magnitude with increasing water content.<sup>28</sup> Upon drying the exposed nylon 6,6 samples, the  $\beta$  relaxation disappeared. The  $\beta$  relaxation of a polyurethane showed the same water dependence.<sup>27</sup>

#### **2.4.3.3. Secondary Relaxations: Application to Polyimides**

Applying Heijboer's general model to polyimides, sources of secondary relaxations may include local motions within the diamine, local motions within the dianhydride, if substituted, the motion of the substituent, or from motions associated with absorbed penetrants. In the 1970s,

researchers deduced that for aromatic diamines containing phenyl rings joined by an ether group, the  $\beta$  relaxation for aromatic polyimides was the torsional rotation of the phenyl rings, as schematically shown in Figure 2.9. However, acknowledging the complexity of the relaxation these researchers also proposed a small contribution from rotations of benzimide rings of the dianhydride.

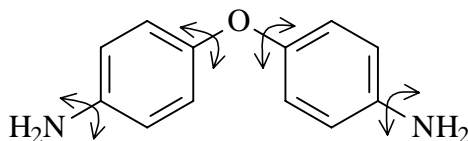


**Figure 2.9. Phenyl ring torsional rotation in 4,4'-oxydianiline (ODA).**

Recently, comprehensive studies to elucidate the source of the  $\beta$  relaxation within aromatic polyimides were reported by Coburn et al. and Cheng et al.<sup>29-32</sup> Both authors also concluded that the  $\beta$  relaxation arises from torsional rotations of the phenyl rings of the diamine. Coburn et al. arrived at the conclusion by first holding the diamine structure constant and varying the dianhydride; the  $\beta$  relaxations all occurred within the same temperature range.<sup>29</sup> Next, Coburn et al. held the dianhydride structure constant and varied the diamine by substitution of its phenyl rings; the temperature ranges of the  $\beta$  relaxations differed because the substituents altered the rotation potential of the phenyl rings. Small substituents, such as -Cl, -CH<sub>3</sub>, and -OCF<sub>3</sub>, created lower rotation potentials and thus, these polymers displayed  $\beta$  relaxations at lower temperatures than those with bulky, hindering, substituents, such as -CF<sub>3</sub>, p-phenyl, and p-terphenyl. Coburn et al. calculated rotational barriers and activation energies for the  $\beta$  relaxation to confirm their dynamic mechanical analysis results.

Cheng et al. similarly held the diamine or dianhydride structure constant, and varied the other monomer chemical structure.<sup>30-32</sup> Cheng et al. also concluded that the  $\beta$  relaxation mainly arises from rotations of the phenyl rings of the diamine. Cheng et al. also attributed a second, higher temperature  $\beta$  relaxation, observed when the diamine structure was held constant, but the dianhydride structure was varied with substituents, to local motion of the dianhydride. Coburn et al. and Cheng et al.'s results provide further and more conclusive documentation for the sources of the  $\beta$  relaxation within aromatic polyimides.

Numerous studies have measured a moisture dependent  $\gamma$  relaxation at temperatures below the  $\beta$  relaxation for aromatic polyimides.<sup>33-37,43-45</sup> The intermolecular interactions involved in this relaxation will be discussed in a later section.

#### 2.4.3.4. Role of $\beta$ Relaxation on Mechanical Properties

The  $\beta$  relaxation influences mechanical properties, such as stress-strain behavior and impact strength, of polymers. A polymer may exhibit either tough or brittle response depending on the temperature. For polyimides, upon entering the temperature range of the  $\beta$  relaxation (as determined from  $\tan \delta$  by DMA), mechanically there is a corresponding increase in deformation percent at break ( $\epsilon_b$  %).<sup>3</sup> Figure 2.10 illustrates this behavior for polyimides DPO and BZP (structures shown). The solid lines represent the deformation percent at break ( $\epsilon_b$  %, left axis). The dashed lines represent  $\tan \delta$  obtained via dynamic mechanical analysis (right axis).

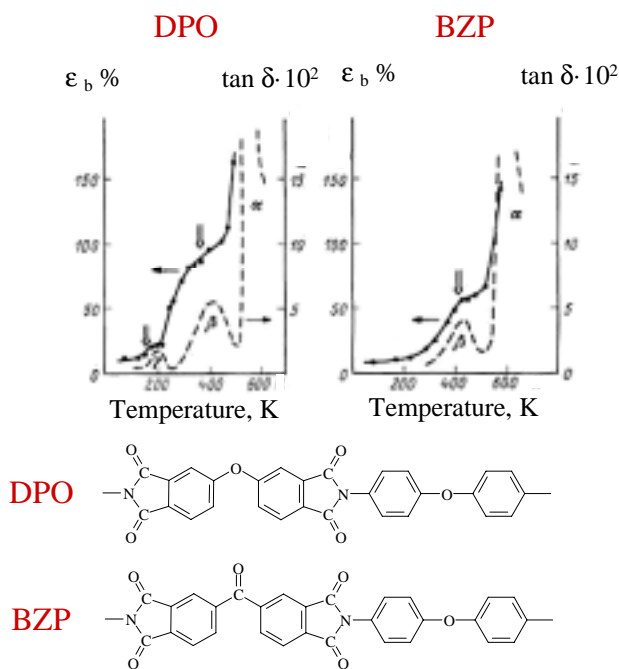


**Figure 2.10.** Temperature dependence of deformation percent at break,  $\epsilon_b$  %, and DMA  $\tan \delta$  for two polyimides. The solid lines represent  $\epsilon_b$  % and the dashed lines represent  $\tan \delta$ .<sup>3</sup>

Tomikawa et al. investigated the role of the polyimide  $\beta$  relaxation in polyimide-epoxy molding compound adhesive bond strength.<sup>38</sup> Figure 2.11 illustrates the lap shear adhesive strength versus the temperature maximum of the polyimide  $\beta$  relaxation for 3 different epoxies (MC-A, MC-B, MC-C). The epoxies possessed similar mechanical properties ( $T_g$ , modulus, CTE) and were cured at 170 °C against films of 12 different polyimides. Each point represents a polyimide-epoxy combination.

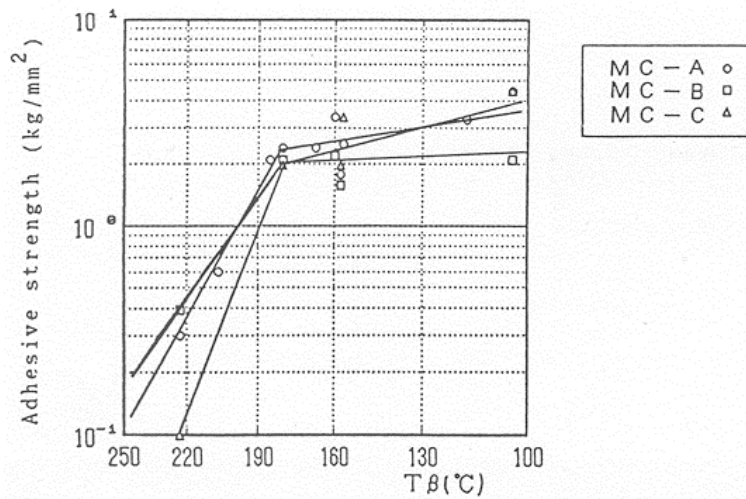


**Figure 2.11. Relationship between the temperature of the polyimide  $\beta$  relaxation and the strength of PI-epoxy molding compound adhesive bond.**<sup>38</sup>

From these experiments, Tomikawa et al. noted that when the epoxy cure temperature overlapped with the polyimide  $\beta$  relaxation, adhesive bond strength increased. When the polyimide  $\beta$  relaxation occurred in a temperature range higher than the epoxy cure temperature, adhesive bond strength was poor.

In the same study, Tomikawa et al. also noted that when the epoxy cure temperature overlapped with the polyimide  $\beta$  relaxation, the higher the  $\tan \delta$  magnitude of the  $\beta$  relaxation, the greater the adhesion strength. Figure 2.12 illustrates this trend for epoxy MC-A and several polyimides.

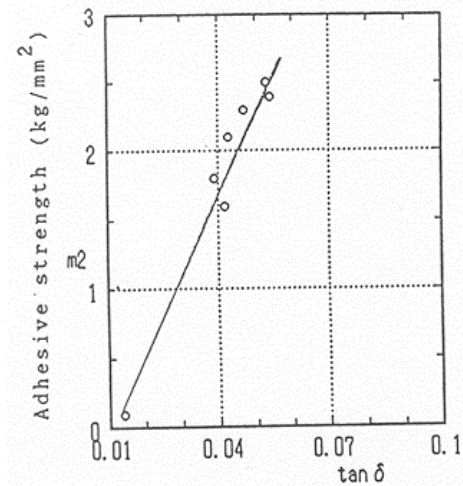


**Figure 2.12. Relationship between the  $\tan \delta$  magnitude of the polyimide  $\beta$  relaxation and the strength of PI-epoxy molding compound (MC-A) adhesive bond.<sup>38</sup>**

Many commercial aromatic polyimide films used as substrates for flexible circuitry are biaxially oriented. The deformation induced during the orientation process changes the supermolecular morphology formed by the molecules.<sup>39</sup> As a consequence, the resulting film exhibits an increased tensile modulus and a balance in properties within the plane of the film compared to the unoriented film. In addition, secondary relaxations can be influenced. Bessonov et al. have cited the work of Knznetsov, who showed that orientation stretching in PMDA/ODA equally affects the  $\beta$  relaxation (as determined from  $\tan \delta$  by DMA) and the strain percent at break ( $\epsilon_b$ , %) of the polymer.<sup>3</sup> Figure 2.13 displays the correlation. Upon stretching, the magnitude of the  $\beta$  losses decrease and the peak maximum shifts to higher temperatures. Likewise the strain percent at break also decreases and shifts to higher temperatures.<sup>3</sup>

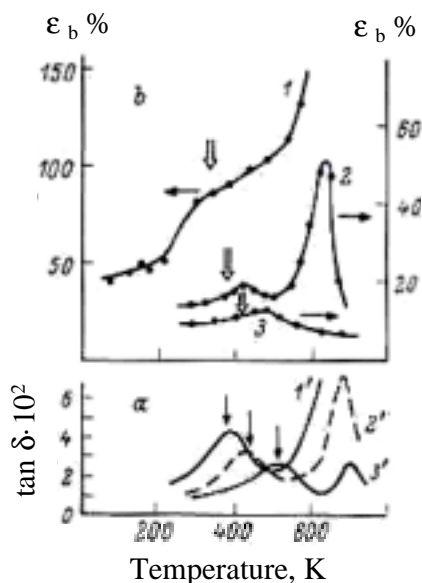


**Figure 2.13. Temperature dependence of elongation at break and DMA  $\tan \delta$  for PMDA/ODA with various degrees of stretching. The degree of stretching  $\lambda$  is equal to 1 (curves 1, 1'), 2 (curves 2, 2'), and 5 (curves 3, 3'). Arrows indicate the maxima of  $\beta$  losses at 72 Hz (a) and 0.1 Hz (b).<sup>3</sup>**

Eashoo et al. investigated the influence of drawing on the DMA  $\tan \delta$  magnitude of the  $T_g$  and  $\beta$  relaxation for aromatic polyimide fibers.<sup>40</sup> Wide angle x-ray scattering was used to monitor changes in percent crystallinity. The as-spun fibers were amorphous and the  $\beta$  relaxation and  $T_g$  displayed high  $\tan \delta$  values. As the draw ratio increased, the percent crystallinity increased, the magnitudes of the  $\beta$  relaxation and  $T_g$  decreased. In addition, the activation energy for the  $\beta$  relaxation increased. Eashoo et al. concluded that the  $\beta$  relaxation occurred within the amorphous regions and motion became more cooperative upon orientation.

These specific polyimide examples demonstrate the role of the  $\beta$  relaxation in their mechanical and adhesive properties. The limited literature studies allow for more expanded studies involving new polyimides and more advanced adhesive tests.

## 2.5 Water in Polyimides

Study of the intermolecular interactions between water and polyimide has been a widely researched topic due to the interest in achieving low moisture uptake properties in polyimides for microelectronics applications. Low moisture absorption by polyimides is desirable to maintain a low dielectric constant, prevent corrosion of metal components, and prevent short circuits within

a device. The following is a brief summary of literature discussing the location where moisture absorbs within the bulk polyimide and how the absorbed moisture interacts with the polyimide.

At temperatures below the  $T_g$ , free volume provides sites where moisture can absorb. Moisture can also absorb into interstitial sites within the bulk polymer matrix. Dlubek et al. used positron annihilation lifetime spectroscopy (PALS) to study the effect of water uptake on the free volume of the fluorinated aromatic polyimide 6FDA-ODA, as well as draw conclusions on the nature of the free volume filling process as a function of relative humidity.<sup>41</sup> PALS is a very sensitive and well established technique for studying the sub-nanometer sized regions of free volume. For polymers, positrons that are injected into a sample form a bound state called positronium (Ps).<sup>41</sup> The Ps appears either as para- or ortho-positronium, p-Ps or o-Ps, respectively, with a relative abundance of 1:3.<sup>41</sup> When injected into an amorphous polymer, the density of the Ps is largely restricted to the free volume holes.<sup>41</sup> The o-Ps typically has a lifetime in the nanosecond range, which is suitable for evaluating the size of free volume holes.<sup>41</sup> The o-Ps decay lifetimes will vary for different sized free volume holes. In the experiments by Dlubek et al, the positrons were generated using a  $2 \times 10^6$  Bq ( $^{22}\text{Na}$ ) positron source and injected into 6FDA-ODA samples that were preconditioned under different levels of percent relative humidity, and the o-Ps decay lifetimes were measured. The authors observed that the o-Ps decay lifetimes and the number of unoccupied holes decreased with increasing humidity; that is, free volume sites were filled by absorbed water molecules. In the early and medium stages of water sorption, water first occupied the larger regions of free volume and only one water molecule would absorb per hole. At higher humidities (RH of 30% and higher), hole filling proceeded slower. Two mechanisms were proposed to explain the decrease: (1) water began to occupy sites other than preexisting holes, e.g. interstitial sites or (2) water began to absorb into a hole already occupied by another water molecule to form a “cluster.” Dlubek et al. conclusively shows that water occupies free volume, as well as bulk interstitial sites, in 6FDA-ODA. Their observation on the change in absorption mode at the high humidities corresponds well with the well established ideas of “bound” and “clustered” water in polymer science.

Bound water is water associated with the polymer chain by some type of specific interaction such as dipole-dipole interaction or hydrogen bonding.<sup>42</sup> Bound water can reside within interstitial sites in the bulk polymer or in the free volume.<sup>41</sup> Bound water can be difficult to evaporate from interstitial sites depending on the chemical structure and morphology of the

polymer. Clustered water, or free water, is formed by 2-3 water molecules that are not associated with the polymer by secondary interactions.<sup>42</sup> Clustered water resides within free volume regions and can be easily absorbed or desorbed.

Noting the moisture dependent, low temperature, mechanical  $\gamma$  relaxation for aromatic polyimides, several authors employed dielectric and NMR techniques to determine the molecular sites where water molecules accumulated in PMDA/ODA.<sup>37,43-45</sup> Due to its sensitivity to dipole moments, dielectric analysis revealed that the single mechanical  $\gamma$  relaxation contained two components: a high temperature component ( $\gamma_1$ ), and a low temperature component ( $\gamma_2$ ). An example dielectric plot is shown in Figure 2.14.<sup>37</sup>

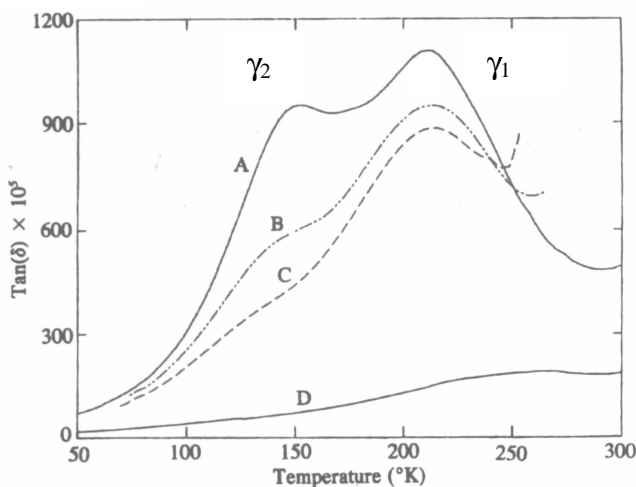


**Figure 2.14. Dielectric analysis  $\tan \delta$  displaying the effect of water on the gamma relaxation of Kapton-H (PMDA/ODA). Curves (a) to (d) correspond to 100% RH, 75% RH, 49% RH, and dry samples, respectively.<sup>37</sup>**

Figure 2.14 illustrates that as the %RH increases the low temperature component,  $\gamma_2$ , increases in magnitude more than the high temperature component,  $\gamma_1$ . The authors suggested that water molecules enter at random sites at low relative humidity to contribute to  $\gamma_1$ , but undergo clustering at high relative humidity to contribute to  $\gamma_2$ . A cluster of 2-3 water molecules will have a greater dipole moment than a single free molecule which is reflected in the higher  $\tan \delta$  signal.<sup>37</sup> Combined dielectric<sup>37</sup> and NMR<sup>45</sup> results suggest that the increased magnitude of  $\gamma_1$  may arise from hydrogen bonding of water to the carbonyl of the imide ring, and the increased magnitude of  $\gamma_2$  may result from clusters of 2-3 water molecules at undetermined positions along

the polymer chain. By NMR, Xu et al. likewise noted that the water in films containing less than 2 wt. % absorbed moisture was less mobile than the water in saturated films (3.1 wt. % water).<sup>44</sup> Xu et al. explained that the more mobile water aggregated in free volume areas.<sup>44</sup>

## 2.6 Diffusion in Polyimides

### 2.6.1 Introduction to Diffusion

The diffusion of small molecules in and through polymers is an important phenomenon. The presence of absorbed molecules can alter molecular motions, energy of deformation, viscoelastic properties, mechanical properties, and adhesive properties of polymers.

Diffusion kinetics can be determined gravimetrically by direct weighing of the polymer specimen using an analytical microbalance. By this method, the specimen is kept in a constant environment, such as at a constant vapor pressure or immersed in a fluid, but is periodically removed, blotted dry, and weighed. Upon weighing, the specimen is returned to its environment. The procedure is repeated until the weight of the specimen becomes constant. The analytical microbalance is a very simple and reliable instrument for the study of diffusion kinetics provided the sample is large enough. As sample size decreases, error increases. Error is of particular concern for films (less than 50 $\mu$ m in thickness) throughout all steps of the procedure for several reasons.<sup>46,47</sup> First, absorbed penetrant may desorb simply due to the removal of the specimen from its constant environment. Second, during blotting, a significant amount of absorbed penetrant may desorb. Third, the thinner the film, the higher the diffusion rate; the specimen must be weighed rapidly and often. Repeated handling of the specimen can result in erroneous weight uptake values. Finally, the percent weight change may be small and consequently, beyond the detection limits of the balance.

To circumvent these experimental problems, *in-situ* test methods such as bending beam, dielectric analysis, and dynamic mechanical analysis, can be employed. These test methods offer the added benefit of allowing the correlation of weight uptake to a material property such as solvent induced stress, solvent induced strain, electric permittivity or expansion. FTIR-ATR is another *in-situ* test method; FTIR-ATR can be used to associate mass uptake with intermolecular interactions.

### 2.6.2 Diffusion Kinetics

The diffusion kinetics of penetrant uptake in thin films can be described by Fick's second law. For the film geometry, it is assumed that diffusion occurs only through the thickness of the film (perpendicular to the film surface), that is, diffusion is negligible through the film edges. After applying the appropriate boundary conditions, the solution to Fick's second law for diffusion into a semi-infinite slab that is exposed to an infinite bath of penetrant is:<sup>48,49</sup>

$$\frac{M_t}{M_\infty} = 1 - \sum_{n=0}^{\infty} \frac{8}{(2n+1)^2 \pi^2} \exp\left[\frac{-\pi^2 (2n+1)^2 Dt}{4L^2}\right] \quad \text{Equation 2.2}$$

Equation 2.2 describes the fraction of mass absorbed at time  $t$ ,  $M_t$ , relative to the amount absorbed at infinite time,  $M_\infty$ . The sample is modeled as a composite of many layers,  $n$ , and the diffusion coefficient,  $D$ , is assumed constant.  $2L$  is the film thickness. The diffusion coefficient reflects the rate at which the penetrant enters and traverses the film. At short times,  $M_t / M_\infty \leq 0.5$ , Equation 2.2 simplifies to:<sup>48,49</sup>

$$\frac{M_t}{M_\infty} = \frac{2}{L} \left( \frac{Dt}{\pi} \right)^{1/2} \quad \text{Equation 2.3}$$

By plotting  $M_t / M_\infty$  versus the square root of time, from the linear portion of the curve:

$$D = \frac{\pi}{4} (\text{Slope})^2 \quad \text{Equation 2.4}$$

When  $M_t / M_\infty$  is plotted versus either time or square root of time, the shape of the curve is indicative of the type of diffusion. Diffusion behavior in polymers can generally be defined as Case I (Fickian), Case II or Anomalous (Non-Fickian). The classification criteria for each are outlined below.

For Case I Fickian absorption, the penetrant diffuses "freely" within the polymer because the rate of mechanical relaxation,  $\tau_m^{-1}$ , is rapid compared to the rate of diffusion.<sup>50,51</sup> When a

penetrant is introduced and begins to diffuse into the polymer, the polymer segments achieve an equilibrium conformation instantaneously; the time dependence of the diffusion coefficient associated with conformational arrangements of the polymer segments disappears. For Case I Fickian absorption,  $M_t/M_\infty$  versus  $t^{1/2}$  is initially linear.

For Case II absorption, when a penetrant is introduced and begins to diffuse into the polymer, the polymer segments cannot rearrange themselves to achieve an equilibrium conformation instantaneously;<sup>48</sup> the rate of mechanical relaxation,  $\tau_m^{-1}$ , is slow compared to the rate of diffusion.<sup>50,51</sup> The absorbed penetrant must relax the polymer segment or swell the polymer before diffusion can proceed. Chain relaxation is the diffusion rate limiting step. The time dependence of the diffusion for Case II,  $M_t/M_\infty$  versus time is initially linear. The features of Case II absorption often arise due to inhomogeneity, anisotropy or non-equilibrium characteristics of polymers.<sup>52</sup>

For anomalous or non-Fickian diffusion, the rate of penetrant diffusion is comparable with the rate of mechanical relaxation,  $\tau_m^{-1}$ .<sup>50,51</sup> Anomalous diffusion represents transport behavior through a combination of Case I and Case II diffusion. For anomalous diffusion,  $M_t/M_\infty$  versus  $t^{1/2}$  is sigmoidal.

An easier way to determine the type of diffusion, is through the use of the following time power law equation:<sup>52</sup>

$$\frac{M_t}{M_\infty} = K t^n \quad \text{Equation 2.5}$$

when linearized:

$$\log\left(\frac{M_t}{M_\infty}\right) = \log K + n \log(t) \quad \text{Equation 2.6}$$

where  $K$  is a constant that depends on the structural characteristics of the polymer and its interaction with the solvent. The exponent  $n$  indicates the nature of the transport mechanism. The value  $n$  is the slope of the log-log plot according to Equation 2.6. For  $n = 0.5$ , Fickian transport is present.<sup>52</sup> For  $n = 1$ , Case II transport is present. For  $0.5 < n < 1$ , anomalous transport is present.<sup>52</sup>

### 2.6.3 Diffusion Kinetics via In-situ Test Methods

Equations 2.2 and 2.3 were derived to relate the change in mass of a polymer upon exposure to a penetrant to diffusion. To apply the solution of Fick's second law to experiments with parameters other than mass, it may be necessary to modify the solution depending on the relationship between mass and the new experimental parameter. A common and widely accepted example of this modification is for FTIR-ATR.<sup>47</sup> In FTIR-ATR, changes in infrared absorbance band intensity due to intermolecular interactions of the penetrant with the polymer are monitored with time. The solution of Fick's Second law is modified for this experiment since absorbance and concentration are related through the Beer-Lambert Law thus allowing the generation of sorption curves and the calculation of diffusion coefficients. Van Alsten and Coburn used FTIR-ATR to determine the diffusion coefficients of deuterated water (D<sub>2</sub>O) in the polyimides BPDA/PPD, BTDA/PPD, PMDA/ODA, and BTDA/ODA/MPD.<sup>53</sup> The diffusion coefficients were all on the order of 10<sup>-9</sup> cm<sup>2</sup>/sec, and as the polyimide chain stiffness increased, the diffusion coefficient decreased, and the activation energy for diffusion increased. In addition, Van Alsten and Coburn observed that as the immersion temperature increased, so did the diffusion coefficient.

Sorption kinetics have also been investigated using mechanics based experiments. One example is the bending beam technique which correlates the kinetics of bending curvature of a beam to a solution of Fick's second law of diffusion through linear elasticity theory. Jou et al. measured diffusion coefficients on the order of 10<sup>-9</sup> cm<sup>2</sup>/sec for room temperature water in PMDA/ODA, PMDA/PDA, and BPDA/ODA using the bending beam technique.<sup>54,55</sup>

Dielectric analysis has also been implemented to measure sorption kinetics. Pethrick et al. have compared sorption kinetics of water in epoxies determined gravimetrically to those measured using an *in-situ* dielectric technique.<sup>56</sup> The authors justified the use of the solution of Fick's second law by stating that the increase in permittivity ( $\epsilon' - \epsilon'_0$ ) is proportional to the number of water dipoles in the system. However, they did mention that some discrepancies in this correlation exist within the literature. In Pethrick et al.'s study, the *in-situ* dielectric absorption curve and subsequent diffusion coefficient depended on the applied frequency due to the different states of water that can form (bound versus clustered water). For the analysis, a frequency that measured the response representative of both types of water was selected. They concluded that the sorption curves and diffusion coefficients for the gravimetric and *in-situ*

dielectric technique correlated reasonably well and provided information about the sorption kinetics and the development of molecular interactions during the sorption process.

*In-situ* dynamic mechanical analysis has also been used to simultaneously investigate diffusion kinetics and the effect of the absorbed penetrant on polymer mechanical properties. McPeak utilized *in-situ* DMA to study diffusion and solvent induced crystallization in PEEK (poly(etheretherketone)).<sup>57</sup> McPeak used relative changes in the storage modulus to calculate a diffusion coefficient using a solution of Fick's second law. Gravimetric mass uptake measurements, wide angle x-ray diffraction, and differential scanning calorimetry were used to interpret the *in-situ* DMA response and justify the substitution of relative modulus change into Fick's second law. Bao et al. utilized *in-situ* DMA to study the mechanical properties of poly(vinyl alcohol) hydrogels used in biomedical purposes.<sup>58</sup> In an application, hydrogels function in a constant fluid environment, thus *in-situ* DMA is an ideal test method for these materials.

The FTIR-ATR, bending beam, *in-situ* dielectric analysis, and *in-situ* DMA examples illustrate that sorption kinetics can be measured by methods other than gravimetric mass uptake.

## 2.7 Dielectric Properties

The insulative or dielectric properties of a material refer to the material's ability to be polarized by an electric field. Polarization is the alignment of permanent or induced atomic or molecular dipole moments with an externally applied electric field.<sup>18</sup> Sources of polarization include dipoles, ions, and electrons. All materials possess electronic polarization, but contributions by dipoles, ions or both, will depend on the material's chemical structure.

The relative dielectric constant,  $\epsilon_r$ , is defined as the ratio of the dielectric constant of the material to that of free space; its value varies with frequency, temperature, and water content within the material.<sup>59</sup> At low frequencies, dipoles, ions, and electrons all contribute to  $\epsilon_r$ . As the frequency is increased to above the microwave region,  $10^8$  Hz, the dipole contribution vanishes because the frequency is too high for the dipole to follow the field and the dipole remains stationary.<sup>59</sup> Above the infrared region,  $10^{14}$  Hz, the ion contribution vanishes for the same reason.<sup>59</sup> At frequencies within the visible and ultraviolet region, only electrons contribute to the dielectric constant. In this region, the dielectric constant is proportional to the optical refractive index squared ( $\epsilon = n^2$ ).<sup>59</sup> For viscoelastic materials,  $\epsilon_r$  contains contributions from an elastic component called the permittivity,  $\epsilon_r'$ , and a viscous component called the loss factor,  $\epsilon_r''$ . The

ratio between the loss factor and the permittivity ( $\epsilon_r''/\epsilon_r'$ ) is called  $\tan \delta$ , which is indicative of the energy dissipation by a material. The permittivity and  $\tan \delta$  at a particular frequency and temperature are commonly used to state a material's dielectric properties.

Dry polymers are poor conductors of electricity because of the unavailability of large numbers of free electrons to participate in the conduction process.<sup>18</sup> Thus, polymers are classified as insulators. Polymers with more polarizable atoms or functional groups, such as oxygen, nitrogen, and aromatic rings will display a higher relative dielectric constant in all frequency ranges, than polymers with fewer polarizable groups. Absorbed water will also increase the relative dielectric constant. Table 2.1 provides dielectric constants for some common polymers.<sup>18</sup>

**Table 2.1. Dielectric Constants for Some Common Polymers.<sup>18</sup>**

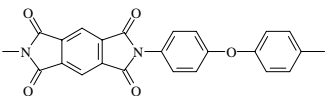
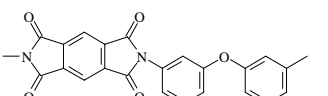
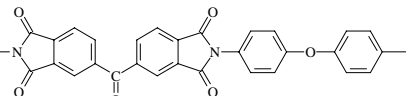
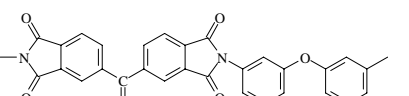
<i>Polymer</i>	<i>Dielectric Constant (1 MHz)</i>
Phenol-formaldehyde	4.8
Nylon 6,6	3.6
Polyimide (PMDA/ODA)	3.2 (10 GHz)*
Polystyrene	2.6
Polyethylene	2.3
Polytetrafluoroethylene	2.1

\*Ref. 60

Polyimides with low dielectric constants are desirable to increase the efficiency at which a microelectronics device transmits signals.<sup>61</sup> The  $\epsilon_r$  of aromatic polyimides typically lies between 2.5 and 3.5 and polyimides with more polarizable atoms or functional groups display a higher relative dielectric constant,  $\epsilon_r$ , in all frequency ranges than polyimides with fewer polarizable groups.

Several authors have investigated structure-property relationships to tailor  $\epsilon_r$  of polyimides.<sup>62-65</sup> Eftekhari et al. and Simpson and St. Clair investigated the relationship among polyimide backbone linearity, free volume, and  $\epsilon_r$ .<sup>62, 63</sup> The authors introduced free volume to the polyimides by using dianhydrides and diamines which reduced the chain packing efficiency. For

example, the monomers contained *ortho*- or *meta*- linkages along the backbone, flexible bridging units or pendant groups. Figure 2.15 shows two pairs of polyimides investigated and their measured  $\epsilon_r$ .

		$\epsilon$ (10 GHz)
PMDA/4,4' ODA		3.22
PMDA/3,3' ODA		2.84
BTDA/4,4' ODA		3.15
BTDA/3,3' ODA		3.09

**Figure 2.15. Influence of Flexible Linkages on Dielectric Constant.**<sup>63</sup>

Positron Annihilation Lifetime Spectroscopy (PALS) was used to measure the free volume for pairs of polyimides, such as those in Figure 2.15, which differed only in backbone linearity.<sup>62,63</sup> PALS indicated that higher amounts of free volume were present for the polyimides with the less linear backbone structure. Lower  $\epsilon_r$  values were correlated to the increased free volume for these polyimides.

Hougham et al. studied the effect of fluorine substitution within a polyimide on the dielectric constant, water absorption, and optical properties.<sup>64,65</sup> In general, increasing the fluorine content decreased the dielectric constant and the percent water sorption, and improved optical properties. Hougham et al. attributed decreased water sorption to the hydrophobicity of fluorine, a characteristic which also decreased the dielectric constant. However, the decrease in  $\epsilon_r$  was also related to an increase in free volume due to the fluorine substitution. Hougham et al.'s results correlate well with Eftekhari et al. and Simpson et al.

Absorbed moisture substantially increases the  $\epsilon_r$  at low frequencies for polyimides. For PMDA/ODA,  $\epsilon_r$  at 1 MHz increases 14% as the relative humidity increases from 30% to 100%.<sup>2</sup>

Fluorinated polyimides are much more hydrophobic and  $\epsilon_r$  increases approximately 1-2 % as the relative humidity increases from 30% to 100%.<sup>2</sup>

## 2.8 Mechanical Properties

As discussed in Section 0 regarding the role of the  $\beta$  relaxation in mechanical properties, mechanical properties such as deformation percent at break,  $\epsilon_b$  %, or stress at break,  $\sigma_b$ , at a given temperature often reflect underlying viscoelastic relaxations. Bessonov et al. provide several such examples for aromatic polyimides in their text.<sup>3</sup> These examples correlate microscopic behavior to macroscopic behavior, thus justifying the need to measure tensile modulus,  $\epsilon_b$  %,  $\sigma_b$ , fracture toughness, creep compliance, hygrothermal expansion, etc., when investigating the reliability and lifetime of electronics packaging.

Bessonov et al. provide numerous tables displaying the tensile modulus,  $\epsilon_b$  %, and  $\sigma_b$  for aromatic polyimides.<sup>3</sup> More recent studies conducted by Inoue et al. and Ree et al. also discuss trends among chemical structure, tensile modulus, and  $\epsilon_b$  %.<sup>24, 66</sup>

Hinkley et al. and Klemann et al. conducted single edge notch (SEN) fracture experiments in the tensile geometry to evaluate the resistance to crack growth of several aromatic polyimide films.<sup>67, 68</sup> Both authors found that the polyimide critical fracture toughness for crack initiation,  $K_{Ic}$ , showed some dependence on chemical structure and film thickness.

Kapton<sup>®</sup> (DuPont) is a biaxially oriented aromatic polyimide film used as substrates and coverlayers in flexible printed circuitry. Popelar et al. published a series of papers assessing the time-dependent structural integrity of several formulations of Kapton<sup>®</sup>-H (PMDA/ODA).<sup>69,70, 71</sup> Popelar et al. performed creep compliance tests and SEN fracture experiments at several temperatures and relative humidities and then constructed master curves for the two experiments using time-temperature, crack growth rate-temperature, and crack growth rate-humidity superposition. The master curves and corresponding shift factor plots were generated according to the Williams-Landel-Ferry (WLF) equation to predict creep compliance or crack growth behavior at untested temperatures or relative humidities. Popelar et al. made several conclusions from their SEN experiments. First, for Kapton<sup>®</sup>-300H film, the fracture resistance did not depend on whether the crack growth rate was measured parallel or perpendicular to the machine direction.<sup>69</sup> The fracture resistance decreased with decreasing film thickness.<sup>69</sup> The fracture resistance decreased with increasing temperature and relative humidity.<sup>70</sup>

Popelar et al. also measured the length change Kapton<sup>®</sup>-300H film upon exposure to relative humidity using an LVDT.<sup>70</sup> Samples were subjected to increasing levels of relative humidity such that a hygral coefficient of expansion (HCE) could be measured. At 25°C, the HCE was 25ppm/%RH. The authors compared the HCE to the coefficient of thermal expansion of Kapton<sup>®</sup> (20ppm/°C) and stated that a 1% increase in the relative humidity at 25°C produces the same expansion as a 1.25°C change in temperature.<sup>70</sup>

## 2.9 Adhesion

### 2.9.1 Introduction

The measured adhesion strength of an adhesive bond arises from intrinsic bonding forces, such as covalent bonds or secondary interactions, between the adhesive and the adherend, plastic and/or viscoelastic energy dissipation at the crack tip, and from plastic and/or viscoelastic energy dissipation within the bulk of the adhesive and adherend.

Separation of the intrinsic bonding forces and the various energy dissipation components from the measured adhesion strength is difficult; however, several researchers have shown that by approaching the problem from chemical and mechanical perspectives the influence of each on adhesion performance can be investigated. The next section discusses these approaches.

### 2.9.2 The Energy of Adhesion

The thermodynamic work of adhesion,  $W_A$ , is defined as the work required to separate a unit area of a solid and a liquid phase forming an interface across which secondary forces are acting.<sup>79</sup> Thus,  $W_A$  is a measure of the intrinsic bonding forces between a liquid adhesive and a solid substrate. Van der Waals secondary bonding forces, include Keesom forces, Debye forces, and London dispersion forces and the strength of these secondary forces decreases with  $1/r^6$  distance ( $r$ ) between them, intimate molecular contact across the interface must be present.<sup>72</sup> The  $W_A$  can be calculated from the polar and dispersion surface free energies of the adhesive and the substrate using the following relation:<sup>72</sup>

$$W_A = 2\sqrt{\gamma_a^d \gamma_s^d} + 2\sqrt{\gamma_a^p \gamma_s^p} \quad \text{Equation 2.7}$$

where the subscripts  $a$  and  $s$  represent the adhesive and the substrate, respectively, and the superscripts  $d$  and  $p$  represent the dispersion and polar components of the surface free energy  $\gamma$ , respectively. While  $W_A$  is often of the order of  $1 \text{ J/m}^2$ , intimate molecular contact between the adhesive and the substrate is a necessary requirement for the development of strong adhesive joints.<sup>72</sup>

Mechanically, the intrinsic bonding forces can be measured if the adhesive joint is tested to failure under near equilibrium conditions, that is, at slow testing rates and at high temperatures, such that plastic and/or viscoelastic dissipation at the crack tip and within the bulk adhesive and adherend are minimized.<sup>76</sup> Under near equilibrium conditions, the intrinsic adhesion energy,  $G_o$ , represents the energy required to propagate a crack through a unit area of interface.<sup>79</sup>  $G_o$  should agree with  $W_A$  if only secondary bonding forces across the interface are present and if *strictly* interfacial failure occurs. If a discrepancy between  $G_o$  and  $W_A$  exists, covalent bonding may be present, near equilibrium conditions may not have been achieved or partial cohesive failure may have occurred.<sup>76</sup> Regardless of the types of chemical bonding,  $G_o$  mechanically represents a threshold adhesion energy below which no failure should occur.

Mechanically, when the adhesive joint is tested to failure under non-equilibrium conditions, that is, at fast testing rates and at low temperatures, intrinsic bonding forces and plastic and/or viscoelastic energy dissipation at the crack tip can contribute to the measured adhesion energy. Under non-equilibrium conditions, the practical adhesion energy is then described by the following relation:<sup>73-79,82</sup>

$$G = G_o + g(G_o) \cdot (\phi(R, T)) \quad \text{Equation 2.8}$$

where  $G$  is the practical adhesion energy,  $G_o$  is the intrinsic adhesion energy, and  $g(G_o) \cdot (\phi(R, T))$  is the energy dissipation term which depends on the intrinsic adhesion energy  $G_o$ , and on the loss function  $\phi$  which itself further depends on the test rate  $R$  and temperature  $T$ .

Equation 2.8 shows that  $G_o$  contributes to the adhesion energy in two ways. First,  $G_o$  contributes a small amount of energy ( $\approx 1 \text{ J/m}^2$ ) from intrinsic bonding forces across the interface. Second, within the energy dissipation term,  $g(G_o) \cdot (\phi(R, T))$ ,  $G_o$  can be viewed as an “activator” for plastic and/or viscoelastic dissipation which occurs at the crack tip. This effect

arises because the adhesive can only be subjected to stress, and thus to energy dissipation, if the interface itself is capable of withstanding stress.<sup>74</sup> If  $G_o$  is small, then the contribution of energy dissipation in the adhesion energy decreases. If  $G_o$  is large, then  $G_o$  “activates” the energy dissipation to be the dominant component of the adhesion energy, such that  $g(G_o) \cdot (\phi(R, T)) \gg G_o$ . The adhesion energy,  $G$ , can increase by as much as  $1000 \times G_o$  near the glass transition temperature due to energy dissipative processes.<sup>78</sup>

The influence of the energy dissipation ( $\phi(R, T)$ ) which occurs at the crack tip must also be recognized. Its dependence on test rate and temperature reflects the viscoelastic properties of the adhesive. At slow test rates and high temperatures, near-equilibrium conditions are approached and the dissipation term has little impact on the magnitude of the adhesion energy ( $G \approx G_o$ ). At fast test rates and low temperatures, non-equilibrium conditions are present and as a result, the dissipation term dominates the adhesion energy. Another important point is that the dissipation term is independent of the substrate; the polymer will exhibit the same viscoelastic response regardless of the surface to which it adheres.<sup>76,82</sup> Yet, without  $G_o$ , the energy dissipation cannot be “activated”. Once activated though, the greater the energy dissipation as stresses are applied, the greater the adhesion energy.

Plastic and/or viscoelastic energy dissipation within the bulk of the adhesive and adherend can also increase the measured adhesion energy; however, these contributions depend on variables within the experiment, such as thickness of the adhesive, thickness of the adherend, and the mode of loading (tension, shear, peel), rather than on the true adhesion described by Equation 2.8. Plastic and/or viscoelastic energy dissipation within the bulk of the adhesive and adherend can be reduced by careful adhesive joint design.

Much of the general interpretation associated with Equation 2.8 arose from the work of Gent, Andrews, Kinloch, and Kendall. Gent published a series of papers investigating the adhesion between elastomers as measured using a T-Peel test.<sup>77, 78, 80, 81</sup> The experiments studied the separation of elastomers adhered together by only secondary forces and the separation of elastomers with various degrees of covalent bonding across the interface. In the former, Gent showed that at near equilibrium conditions  $G_o \approx W_A$ . In the latter, Gent showed that at near equilibrium conditions  $G_o > W_A$ . The relationship among viscoelastic properties, test rate, test temperature, and adhesion energy was also investigated. Under non-equilibrium conditions, it was observed that the magnitude of the dissipation term ( $\phi(R, T)$ ) was mainly governed by the

test rate and the temperature difference ( $T-T_g$ ).  $G$  increased by as much as  $1000 \times G_o$  near the glass transition temperature due to dissipative processes.<sup>78</sup> Similarly, Andrews and Kinloch investigated the adhesion between an elastomer and a rigid polymeric substrate in simple tension, pure-shear, and peel geometries.<sup>74,75</sup> The results of Andrews and Kinloch correspond well with the work of Gent.

Kendall sought to experimentally distinguish the surface ( $G_o$ ) and bulk viscoelastic dissipation contributions to the energy of adhesion using a peel test.<sup>82</sup> To isolate surface effects two experiments were performed. In the first, a rubber adhesive with a small bulk relaxation (low loss) was peeled from the substrate. In the second, the substrate was treated with a monolayer of a surface active material, then the same low loss rubber adhesive was applied and peeled from the substrate. To isolate bulk, viscous effects two different experiments were performed. In the first, a rubber adhesive with a large bulk relaxation (high loss) was peeled from the substrate. In the second, different thickness' of the high loss rubber adhesive were peeled. The results of the four experiments were interpreted using an energy balance approach. Kendall's conclusions are in accordance with our general discussion of Equation 2.8.

The concept of a threshold adhesion energy,  $G_o$ , closely ties to the threshold tear energy,  $T_o$ , described by Lake and Thomas<sup>83</sup> and Lake.<sup>84</sup> Values of  $T_o$  which were determined experimentally and theoretically were compared. Experimentally, tensile test strips of an elastomer (natural rubber) containing a crack were repeatedly deformed to fixed maximum strains (ie. fatigue crack growth). A crack growth rate per cycle versus tearing energy curve was generated and from which  $T_o$  was estimated ( $\approx 4 \times 10^4$  ergs/cm<sup>2</sup>). Theoretically, an approximate  $T_o$  value ( $\approx 2 \times 10^4$  ergs/cm<sup>2</sup>) was calculated from chemical structure considerations, such as chemical bond dissociation energies, the length of the monomer unit, and the number of chains per unit volume. The authors suggested that the agreement between the  $T_o$  values was reasonable, and attributed the discrepancy to energy losses due to secondary bonding forces and the relaxation of unbroken chains in the vicinity of the crack tip which were not accounted for in the theoretical calculation. Also, the theoretical calculation applied to an atomically sharp crack, which was not experimentally attainable. By the same procedure, several elastomers that differed in their degree of crystallinity and their viscoelastic behavior were evaluated by Lake and Thomas. The experimental values of  $T_o$  were relatively constant and this observation led Lake and Thomas to conclude that (1)  $T_o$  is governed by the chemical structure and (2)  $T_o$  provides a

threshold energy below which crack growth will not occur (in the absence of chemical corrosion). Again, these are similar to the earlier discussion on  $W_A$  and  $G_o$ .

Lake and Thomas<sup>83</sup> and Lake<sup>84</sup> also noted that when  $T_o$  was exceeded, catastrophic failure of the test sample did not typically occur; this observation was associated with the viscoelastic behavior or energy dissipation properties of the elastomer. The authors described this phenomena conceptually by stating that as the crack begins to grow, there is relaxation of the highly strained material around the crack tip. The relaxation depends on the viscoelastic properties or energy dissipation of the material, and the greater the energy dissipation, the more difficult it is for the crack to propagate. To investigate these ideas, the authors performed stress-strain experiments for each of the elastomers to determine their tensile strengths. The tensile strength is a property which depends on the viscoelastic properties of a material. For all elastomers, (1) the tensile strength values were much greater than the corresponding  $T_o$  values and (2) the slight differences in  $T_o$ , due to the chemical structures, could not be related to the tensile strengths, ie. the differences in viscoelastic behavior. The conclusions by Lake and Thomas are similar to the earlier discussion that the practical adhesion energy,  $G$ , which contains viscoelastic contributions, can be as much as  $1000 \times G_o$  and as a result it can be difficult to discern the contribution or role of  $G_o$  in the practical adhesion energy.

### 2.9.3 Polyimide Adhesion

Within microelectronic devices, strong adhesion between a polyimide and its substrate is critical to ensure device performance, particularly in high temperature, high humidity or liquid environments. Polyimides must adhere to other polyimides, metals, and ceramics. The adhesion energy for these systems has been measured using traditional peel and blister geometries.

#### 4.1.1.1 *Polyimide-polyimide adhesion*

Polyimide to polyimide self-adhesion is of interest because in multi-chip modules, multiple polyimide layers are cast and cured successively. The strength of adhesion between layers depends on the interdiffusion of the latter-cast polyamic acid into the prior-cast film. Brown et al. has shown that the greater the interdiffusion length, the greater the T-peel strength between two layers of polyimide.<sup>85</sup> Greater interdiffusion lengths were achieved by only partially curing the first layer of polyimide. Variables such as the cure temperatures and cure times for the layers, casting solvent, polymer miscibility, and polymer chemical structure influenced the

interdiffusion length.<sup>85</sup> Jou et al. also investigated the effect of cure temperatures of multiple polyimide layers on their peel strength.<sup>98</sup>

#### 4.1.1.2 *Polyimide-metal and metal-polyimide adhesion*

Within microelectronics devices, polyimides must adhere to metals such as copper, chromium, aluminum, and magnesium. Copper is the most desirable metal due to its low resistivity and cost. The polyimide/metal interface and adhesion strength are strongly dependent on the method of preparation. The interface can be formed two ways: (1) casting the PAA onto the metal, followed by imidization, ie. polymer-on-metal, or (2) vapor deposition of the metal onto the fully cured polyimide, ie. metal-on-polymer. The adhesion strength of polymer-on-metal is generally much higher than metal-on-polymer.

Kim et al investigated the adhesion strength of PMDA/ODA to Cr, Ni, and Cu using a 90° peel test.<sup>86</sup> The adhesion strength was highest to Cr (1146 J/m<sup>2</sup>), followed by Ni (842 J/m<sup>2</sup>) and then Cu (715 J/m<sup>2</sup>). Kim et al also noted several interesting observations on the peel failure surfaces. Due to the solubility of Cu oxide in acidic solutions, the Cu oxide reacts with the PAA to form an insoluble salt. Consequently, Cu-rich particles were observed in the PMDA/ODA film near the metal interface. The distance the Cu-rich particles migrated from the metal interface into the bulk of the polyimide was dependent on the cure schedule. The oxide of Cr, however, is very resistant to acids. No Cr particles were observed within the PMDA/ODA film. The corrosion resistance of Ni lies between that of Cu and Cr. A few Ni-rich particles were observed within the PMDA/ODA layer. The presence of these metal particles within the polyimide film has been shown to increase the dielectric constant of the polyimide, which is an obvious shortcoming. The study by Kim et al demonstrates that although Cu is desirable electrically, polyimide adhesion to Cu is weak and the Cu oxide is reactive towards the PAA thus creating Cu-rich particles within the polyimide film. The deposition of a thin “adhesion promoter” layer of Cr to the Cu surface to form a Cu/Cr film, has been effective in counteracting the PI to Cu adhesion shortcomings.<sup>87</sup>

Allen et al. measured the adhesion strength of PMDA/ODA to SiO<sub>2</sub>, Al, Cr, and Au using the island blister test. The adhesion strength to Au was 57 J/m<sup>2</sup> and the locus of failure, determined using XPS, was essentially interfacial. The adhesion strengths to SiO<sub>2</sub>, Al, and Cr were 93 J/m<sup>2</sup>, 91 J/m<sup>2</sup>, and 126 J/m<sup>2</sup>, respectively. The error (15%) of the experiments, lead the authors to conclude that the adhesion strength of PMDA/ODA was constant over the substrates studied. For these samples, the locus of failure was either in the bulk of the polyimide or in a

region near the interface. It is interesting to compare adhesion value for PMDA/ODA to Cr measured using the 90° peel test by Kim et al<sup>86</sup> to the value reported by Allen et al. These are 1146 J/m<sup>2</sup> and 126 J/m<sup>2</sup>, respectively. While a direct comparison may not be appropriate because of differences in the PMDA/ODA cure conditions and films thicknesses, it is probably true to state that the value reported from the blister test contains less plastic deformation than the 90° peel test, and thus may be more representative of the intrinsic adhesion.

Metal-on-polyimide adhesion strength has been investigated by numerous authors. During vapor deposition, a reactive state of the metal is deposited on a relatively inert, fully cured polyimide. The practical adhesion strength has been correlated to the degree of reactivity of the metal with the carbonyl groups of the dianhydride moiety. Cr and Ni react with the carbonyl groups to form chemical bonds at the interface, resulting in good adhesion.<sup>88,89</sup> Whereas, Cu weakly interacts with the carbonyl groups through van der Waals forces, resulting in poor adhesion.<sup>90</sup>

Metal-on-polyimide adhesion can be improved by surface modification of the polyimide, for example, by reactive ion etching or physical bombardment. These treatments can remove weak boundary layers (WBL) at the surface of the polyimide film. Pappas et al improved the 90° peel strength of Cu/Cr films to PMDA/ODA by exposing the PMDA/ODA to low energy Ar<sup>+</sup> and/or O<sub>2</sub><sup>+</sup> ions.<sup>87</sup> Peel strengths were 235 J/m<sup>2</sup> to the untreated polyimide, and 519 J/m<sup>2</sup>, 480 J/m<sup>2</sup>, and 588 J/m<sup>2</sup> to the Ar<sup>+</sup>, Ar<sup>+</sup>/O<sub>2</sub><sup>+</sup>, and O<sub>2</sub><sup>+</sup> treated polyimides, respectively. Locus of failure analysis indicated that the samples failed within the polyimide, near the boundary of the modified and unmodified polyimide.

Buchwalter et al measured the 90° peel strength of Cu/Ta and Cu/Cr on BPDA/PDA films that had been etched with either CF<sub>4</sub> reactive ion etching or Ar sputtering physical bombardment.<sup>91,92</sup> The two treatments altered the surface roughness of the BPDA/PDA, with the former increasing the roughness and the latter decreasing the roughness, with respect to the virgin polyimide. The change in roughness did not, however, correlate with the peel strength and within the error of the experiments, Cu/Ta did not differ from Cu/Cr. The peel strengths were: virgin polyimide ≈ 100 J/m<sup>2</sup>, Ar sputter ≈ 600 J/m<sup>2</sup>, and CF<sub>4</sub> RIE ≈ 1100 J/m<sup>2</sup>. For all samples, although the locus of failure occurred within the unmodified polyimide, the peel strengths differed. The virgin polyimide-metal sample failed within a WBL close to the metal interface. The surface treatments removed the WBL of the other specimens and thus the differences in peel

strengths were attributed to changes in the polyimide toughness induced by the surface treatments.

Kim et al. measured the peel strength of a 500 Å layer of chromium, backed with various thicknesses of copper, to a polyimide.<sup>93</sup> By increasing the thickness of copper, the modulus of the Cu/Cr layer changed which in turn altered the plastic deformation contribution to the peel strength. The peel strength was plotted versus copper thickness, and then by extrapolation to zero copper thickness, the intrinsic bonding adhesion for the 500 Å Cr layer to polyimide was determined to be  $\approx 6 \text{ J/m}^2$ .

#### 4.1.1.3 *Polyimide-ceramic adhesion*

Another very important interface in microelectronics is polyimide to ceramic. Oh et al investigated the role of the acid-base properties of polyimide precursors and ceramic substrates on their 90° peel strength.<sup>94</sup> PMDA/ODA derived from two precursors, a polyamic acid and a polyamic ethyl ester, which are acidic and neutral, respectively, was spin coated onto the ceramic substrates, SiO<sub>2</sub>/Si, Al<sub>2</sub>O<sub>3</sub>, and MgO, and then thermally converted to the polyimide. The films of both the acid and ester precursors, showed much higher 90° peel strengths to SiO<sub>2</sub>/Si and Al<sub>2</sub>O<sub>3</sub> than to MgO. The ester showed better adhesion to all surfaces than the acid. The improved adhesion of the ester to SiO<sub>2</sub>/Si and Al<sub>2</sub>O<sub>3</sub> was attributed to its ductility. For these samples failure occurred within a weak boundary layer of the polyimide. The improved adhesion of the ester to MgO, however, was attributed to its neutral interaction with the basic MgO surface. The acid precursor interacts strongly with the basic MgO, which degrades the MgO interface. As a result, during peel testing the MgO failed rather than the polyimide. This difference in the locus of failure demonstrates that acid-base interactions can dramatically influence adhesion strengths.

Paek et al. utilized a pressurized blister test to measure the adhesion energy of PMDA/ODA to silicon wafers in the presence of water or water/methanol solutions.<sup>95</sup> Paek et al. initiated a debond by injecting water or water/methanol solutions at a constant rate into the blister. The pressure inside the blister was then recorded with injection time after the first debonding. The slope of the (pressure)<sup>3</sup> versus injection time plot, injection rate, film thickness, and film modulus were next used to calculate the critical strain energy release rate,  $G_c$ . The authors found that the adhesion strength and debonding pattern were greatly influenced by the injection liquid. Pure water and the 10% methanol solution initiated a continuous debond pattern of the PMDA/ODA from the silicon wafer. Higher methanol contents initiated slip-stick

debonding due to crack tip blunting. The strain energy release rate could only be calculated for the samples with continuous debond patterns. The strain energy release rate of the PMDA/ODA-silicon samples exposed to water increased from 9.84 J/m<sup>2</sup> for an injection rate of 0.01 ml/min, to 23.05 J/m<sup>2</sup> for an injection rate of 5 ml/min.

Hu et al. employed a 90° peel test to measure the adhesion energy of an aromatic polyimide, BTDA/ODA/*m*-PDA (DuPont Pryalin 2555), to silicon as a function of the variables: polyimide film thickness (7, 12.8, 23.3, 18.7, and 28.6 μm), peel rate (0.25, 0.5, 1, 2, 5, and 10 mm/min), percent relative humidity (2 to 98 %RH), and temperature (20-95 °C).<sup>96,97</sup> A hydrofluoric acid cleaning step was employed to remove the native oxide layer from the wafer, then the wafers were immediately spin coated with the polyamic acid precursor. Samples were then thermally cured. The main conclusion was that “the peel behavior of polyimide film at the elevated temperature is almost the same as peeling at room temperature in a low humidity environment.”<sup>97</sup> The experiments of Hu et al. are organized in the following paragraphs as “Study 1, 2 etc.”

Hu et al., Study 1:<sup>96</sup> for 70 %RH and 20 °C, the peel strength as a function of PI thickness and peel rate was measured. At high peel rates, 5 and 10 mm/min, as the thickness increases, the peel strength increased due to an increase in plastic deformation. At low peel rates, 0.5 and 0.25 mm/min, as the thickness increased, the peel strength increased, reached a maximum, then decreased. The decrease in the peel strength for large thicknesses was attributed to the fact that the films were too stiff to yield plastically.

Hu et al., Study 2:<sup>96</sup> for 70 %RH, 12.8 μm thick film, and 0.5 mm/min peel rate, the peel strength was measured as a function of peel test temperature, as shown in Figure 2.16.

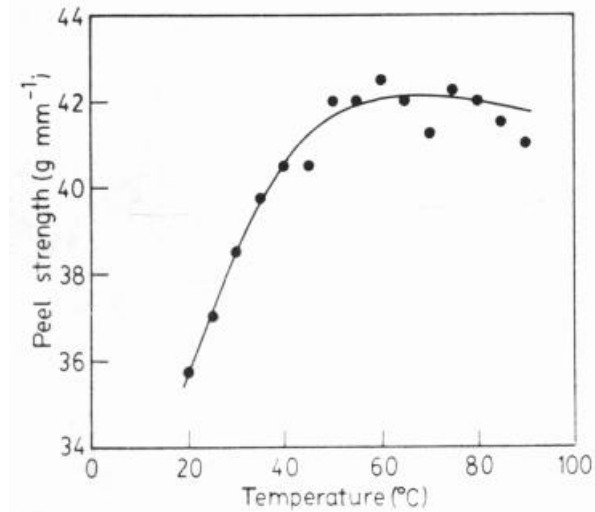


**Figure 2.16 Peel strength of a 12.8 mm thick Pyralin<sup>®</sup> 2555 polyimide film as a function of substrate temperature under high humidity condition (70 %RH). Peel rate = 0.5 mm/min.<sup>96</sup>**

Figure 2.16 illustrates that the peel strength in the 70 %RH environment improved by 15 % as the test temperature increased from 20 to 60 °C. No further improvement in the peel strength was observed for testing at temperatures above 60°C, ie. 60 to 95 °C. The authors suggested that the PI reached “low moisture condition”  $\approx$  60 °C which resulted in an increased peel strength to silicon. The low moisture condition is reached above 60 °C even though the tests are in a 70 %RH environment.

Hu et al., Study 3:<sup>97</sup> for 12.5 %RH, 12.8  $\mu$ m thick film, and 0.5 mm/min peel rate, the peel strength was measured as a function of peel test temperature. The results of Hu et al are shown in Figure 2.17.

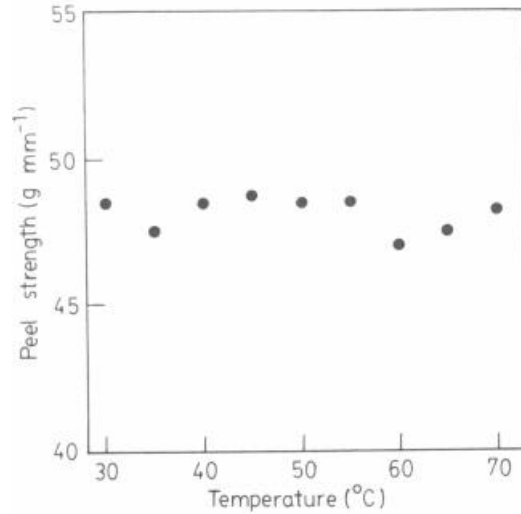
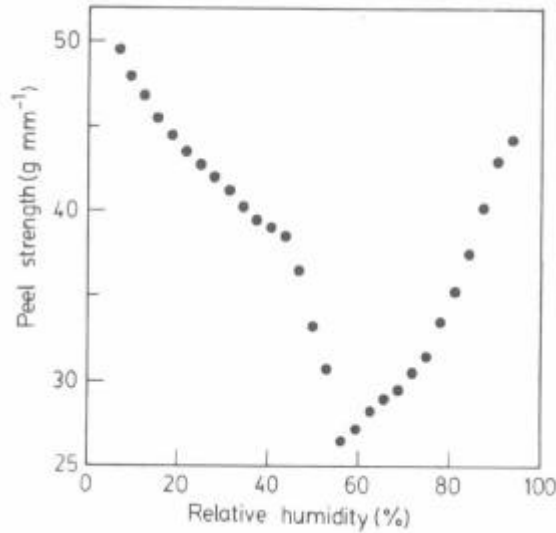


**Figure 2.17. Peel strength of a 14.3 mm thick Pyralin<sup>®</sup> 2555 polyimide film with a peeling rate of 0.5 mm/min in an ambient of 12.5 %RH as a function of substrate temperature.<sup>97</sup>**

From Figure 2.17, the authors concluded that at 12.5 %RH, no apparent difference in the peel strength was observed as the test temperature increased from 30 to 70 °C. This is in contrast with Figure 2.16 presented in “Study 2.”

Hu et al. Study 4:<sup>96</sup> for 23.3 μm-thick PI, tested at 70 %RH, at 20 °C and 80 °C, the peel strength was measured as a function of peel rate. The PI is in a “low moisture condition” when tested at 80 °C. For both temperatures, the peel strength increased as the peel rate increased. At each test rate, the peel strength for the 80 °C sample was higher than that of the 20 °C sample. The authors suggested that this effect is related to moisture.

Hu et al. Study 5:<sup>97</sup> for a 14.3 μm-thick PI film, a 0.5 mm/min peel rate, and at 20 °C, the peel strength was measured as a function of %RH. The results of Hu et al are presented in Figure 2.18.



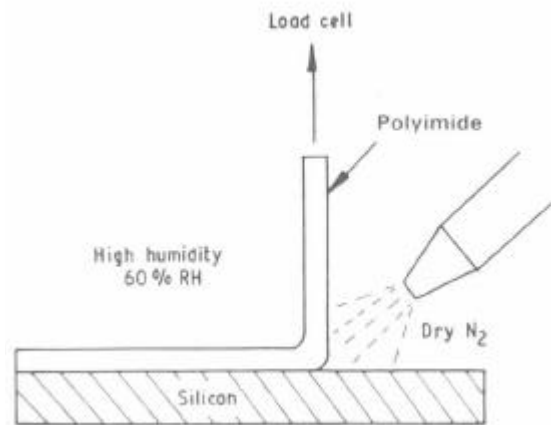
**Figure 2.18. Peel strength of 14.3 mm thick Pyralin<sup>0</sup> 2555 polyimide film with a peeling rate of 0.5mm/min as a function of relative humidity.<sup>97</sup>**

Figure 2.18 illustrates that as the %RH increases, the peel strength steadily decreases until it reaches a minimum strength at  $\approx 55$  %RH. As the %RH is further increased above 55 %RH, the peel strength rises. This observation was substantiated by experiments which showed that the effect was reproducible and independent of the test procedure. SEM of a peeled polyimide film for 12.5 %RH showed striations which are indicative of plastic deformation. SEM of a peeled polyimide film for 50-60 %RH did not show any striations. The latter observation was attributed to the low interfacial strength in which the bond breaking occurred before the development of plastic hinges. The authors hypothesized that that rise in the adhesion strength at high %RH occurred because the water absorbed by the polyimide film formed bridges of hydrogen bonds among the polyimide weak boundary layers near the PI/silicon interface.

Hu et al, Study 6:<sup>97</sup> To investigate the rise in the peel strength at conditions above 55 %RH, the peel strength was measured as a function of peel rate. Experiments were performed at 23 °C, for 30, 40, 51, 60 70 and 80 %RH and the peel rates: 0.25, 0.5, 1, 2, 5, and 10 mm/min. For 30, 40, and 51 %RH, the peel strengths increased linearly as the peel rate increased. For 60, 70, and 80 %RH, the initial peel strengths (at 0.25 mm/min) were lower than that for the 30, 40, and 51 %RH at this test rate. This is in agreement with Hu et al.'s observation as described in "Study 4." For these humidities, the peel strength remained at a low and fairly constant value

until the 5 mm/min test rate, at which the peel strength then increased. The authors then concluded that a low peel rate is needed to observe the humidity effect at 55 %RH.

Hu et al., Study 7:<sup>97</sup> The authors next investigated the modes which moisture may attack the PI/silicon adhesive bond. They suggest that moisture may attack the interface (1) directly at the peel crack tip, and (2) by diffusion through the polyimide film. To investigate the effect of each, Hu et al created a locally dry atmosphere ( $\approx 8$  %RH) by blowing dry nitrogen at the crack tip, but then exposed the bulk film to various %RH. The test set-up is shown schematically in Figure 2.19.



**Figure 2.19. Schematic drawing of a local dry atmosphere at the peel crack tip.<sup>97</sup>**

Comparison of the peel strength versus peel rate for a sample conditioned entirely at 12.5 %RH to that of a sample where the crack tip was dried locally to 8 %RH, by the method shown in Figure 2.19, revealed almost no difference in the adhesion behavior. Thus, the authors concluded that the most important path of moisture attack is at the crack tip and also proposed that moisture weakens the adhesion by displacing hydrogen bonds and van der Waals interactions.<sup>97</sup>

Jou et al. similarly applied a 90° peel test to investigate the effect of polyimide chain flexibility on adhesion to SiO<sub>2</sub>/Si in dry and humid environments.<sup>98</sup> Adhesion performance in humid environments was correlated to the percentage of moisture absorbed by the bulk polyimide. In humid conditions, the adhesion strengths for polyimides that absorbed high moisture contents were significantly lower than their dry adhesion strengths. The adhesion

strengths for polyimides that absorbed low moisture contents were only slightly lower than their dry adhesion strengths. Jou et al's observation that in a humid environment, the adhesion strength decreases is consistent with the results of Hu et al. Jou et al, however, did not discuss the possibility of moisture attack at the crack tip.

Miwa et al. employed a 90° peel test to investigate the effect of aromatic polyimide backbone flexibility on the adhesion energy to SiO<sub>2</sub>/Si.<sup>99</sup> No adhesion promoter was used. The authors concluded that under dry, ambient conditions, the more flexible the polyimide backbone, the greater the adhesion strength. Values ranged from  $\approx 25 \text{ J/m}^2$ , for polyimides with no flexible linkages, to  $\approx 640 \text{ J/m}^2$ , for polyimides containing flexible linkages, such as ether or ketone groups, in both the diamine and the dianhydride. The improvement was attributed to the increase in dipole-dipole interactions and the ability of the flexible segments to change their conformation to maximize intermolecular bonds with the surface. In a high humidity environment, the adhesion to SiO<sub>2</sub>/Si was weak,  $\approx 25 \text{ J/m}^2$ , regardless of the flexibility of the backbone.

Both Miwa et al. and Jou et al. attributed the weakened adhesion in the high humidity environments to water invading the interface and displacing hydrogen bonds and van der Waals interactions.

## 2.10 Literature Review Conclusions

As evidenced from the preceding literature review, much groundwork has been laid in the understanding of chemical structure-property relationships in fully aromatic polyimides. These provide a good resource for interpreting the thermal, viscoelastic, dielectric, and mechanical properties of the BPADA-based partially aliphatic polyimides in the present investigation. The literature review also described several aromatic polyimide-substrate adhesion studies. These demonstrate the importance of surface treatments, chemical structure, cure temperature, humidity, and the adhesive test geometry. These highlight the complexity of adhesive testing and reinforce the importance of sample preparation in attaining meaningful results.

## 2.11 References

- <sup>1</sup> Stearns, T.H. *Flexible Printed Circuitry*; McGraw-Hill: New York, 1995.
- <sup>2</sup> *Electronic Materials Chemistry*; Pogge, H.B., Ed.; Marcel Dekker: New York, 1996.
- <sup>3</sup> Bessonov, M.I.; Koton, M.M.; Kudryavtsev, V.V.; Laius, L.A. *Polyimides Thermally Stable Polymers*; Consultants Bureau: New York, 1987.
- <sup>4</sup> Farr, I.V. Ph.D. Dissertation, Virginia Tech, 1999.
- <sup>5</sup> *Polyimides: Synthesis, Characterization and Adhesion*; CASS Review Series Volume 1; McGrath, J.E.; Taylor, L.T.; Ward, T.C.; Wightman, J.P., Eds.; 1992.
- <sup>6</sup> Echigo, Y.; Iwaya, Y.; Tomioka, I.; Yamada, H. *Macromolecules* **1995**, *28*, 4861.
- <sup>7</sup> Ojeda, J.R.; Mobley, J.; Martin, D.C. *J. Polym. Sci., Polym. Phys. Ed.* **1995**, *32*, 559.
- <sup>8</sup> Jin, Q.; Yamashita, T.; Horie, K.; Yokota, R.; Mita, I. *J. Polym. Sci., Polym. Chem. Ed.* **1993**, *31*, 2345.
- <sup>9</sup> Jin, Q.; Yamashita, T.; Horie, K. *J. Polym. Sci., Polym. Chem. Ed.* **1994**, *32*, 503.
- <sup>10</sup> Hsiao, B.S.; Kreuz, J.A.; Cheng, S.Z.D. *Macromolecules* **1996**, *29*, 135.
- <sup>11</sup> Yi, M.H.; Huang, W.; Choi, K.Y. *Pure Appl. Chem.* **1998**, *A35(12)*, 2009.
- <sup>12</sup> St. Clair, T.L. In *Polyimides*; Wilson, D.; Stenzenberger, H.D.; Hergenrother, P.M., Eds.; Blackie: London, 1990; pp 58-78.
- <sup>13</sup> Ando, S.; Matsuura, T.; Sasaki, S. *Polym. J.* **1997**, *29(1)*, 69.
- <sup>14</sup> Fryd, M. In *Polyimides: Synthesis, Characterization, and Applications Volume 1*; Mittal, K.L., Ed.; Plenum: New York, 1982; pp 377-383.
- <sup>15</sup> Tamai, S.; Yamashita, W.; Yamaguchi, A. *J. Polym. Sci., Polym. Chem. Ed.* **1998**, *36*, 1717.
- <sup>16</sup> Gillham, J.K.; Hallock, K.D.; Stadnicki, S.J. *J. Appl. Polym. Sci.* **1972**, *16*, 2595.
- <sup>17</sup> Wright, W.W. In *Developments in Polymer Degradation, Volume 3*; Grassie, N., Ed.; Applied Science: London, 1981; pp 1-26.
- <sup>18</sup> Callister, W.D. Jr. *Materials Science and Engineering: An Introduction*, 3rd ed.; Wiley: New York, 1994.
- <sup>19</sup> Numata, S.; Kinjo, N. *Polym. Eng. Sci.* **1988**, *28(14)*, 906.
- <sup>20</sup> Numata, S.; Oohara, S.; Fujisaki, K.; Imaizumi, J.; Kinjo, N. *J. Appl. Polym. Sci.* **1986**, *31*, 101.
- <sup>21</sup> Arnold, F.E.; Cheng, S.Z.D.; Hsu, S.L.C.; Lee, C.J.; Harris, F.W. *Polymer* **1992**, *33(24)*, 5179.
- <sup>22</sup> Numata, S.; Fujisaki, K.; Kinjo, N. *Polymer* **1987**, *28*, 2282.
- <sup>23</sup> Liou, H. C.; Ho, P.S.; Stierman, R. *Thin Solid Films* **1999**, *339*, 68.
- <sup>24</sup> Inoue, H.; Sasaki, Y.; Ogawa, T. *J. Appl. Polym. Sci.* **1996**, *62*, 2303.
- <sup>25</sup> Fay, C.C.; St. Clair, A.K. *J. Appl. Polym. Sci.* **1998**, *69*, 2383.
- <sup>26</sup> Aklonis, J.J.; McKnight, W.J. *Introduction to Polymer Viscoelasticity*, 2nd ed.; Wiley: New York, 1983.
- <sup>27</sup> Heijboer, J. In *Molecular Basis of Transitions and Relaxations*; Meier, D.J., Ed.; Gordon and Breach Science: New York, 1978; pp 75-102.
- <sup>28</sup> McCrum, N.G.; Read, B.E.; Williams, G. *Anelastic and Dielectric Effects in Polymeric Solids*; Dover: New York, 1991.
- <sup>29</sup> Coburn, J.C.; Soper, P. D.; Auman, B.C. *Macromolecules* **1995**, *28*, 3253.
- <sup>30</sup> Arnold, F.E.; Bruno, K.R.; Shen, D.; Eashoo, M.; Lee, C.J.; Harris, F.W.; Cheng, S.Z.D. *Polym. Eng. Sci.* **1993**, *33(21)*, 1372.

- 
- <sup>31</sup> Li, F.; Fang, S.; Ge, J.J.; Honigfort, P.S.; Chen, J.C.; Harris, F.W.; Cheng, S.Z.D.; *Polymer* **1999**, *40*, 4987.
- <sup>32</sup> Li, F.; Fang, S.; Ge, J.J.; Honigfort, P.S.; Chen, J.C.; Harris, F.W.; Cheng, S.Z.D. *Polymer* **1999**, *40*, 4571.
- <sup>33</sup> Bernier, G.A.; Kline, D.E. *J. Appl. Polym. Sci.* **1968**, *12*, 593.
- <sup>34</sup> Butta, E.; DePetris, S.; Pasquini, M. *J. Appl. Polym. Sci.* **1969**, *13*, 1073.
- <sup>35</sup> Lim, T.; Frosini, V.; Zaleckas, V.; Morrow, D.; Sauer, J.A. *Polym. Eng. Sci.* **1973**, *13*(1), 51.
- <sup>36</sup> Melcher, J.; Daben, Y.; Arlt, G. *IEEE Transactions on Electrical Insulation* **1989**, *24*(1), 31.
- <sup>37</sup> Li, S.Z.; Chen, R.S.; Greenbaum, S.G. *J. Polym. Sci., Polym. Phys. Ed.* **1995**, *33*, 403.
- <sup>38</sup> Tomikawa, M.; Eguchi, M.; Asano, M.; Hiramoto, H. In *Polymers for Microelectronics: Science and Technology*; Tabata, Y.; Mita, I.; Nonogaki, S.; Horie, K.; Tagawa, S., Eds.; VCH: Tokyo, 1989; pp 655-664.
- <sup>39</sup> Hedvig, P. *Dielectric Spectroscopy of Polymers*; Adam Hilger: Bristol; 1977.
- <sup>40</sup> Eashoo, M.; Shen, D.; Wu, Z.; Lee, C.J.; Harris, F.W.; Cheng, S.Z.D. *Polymer* **1993**, *34*(15), 3209.
- <sup>41</sup> Dlubek, G.; Buchhold, R.; Hubner, C.; Nakladal, A. *Macromolecules* **1999**, *32*(7), 2348.
- <sup>42</sup> Deodhar, S.; Luner P. In *Water in Polymers*; Rowland, S.P., Ed.; ACS Symposium Series 127; American Chemical Society: Washington, D.C., 1980; p 273.
- <sup>43</sup> Lim, B.S.; Norwick, A.S.; Lee, K-W.; Viehbeck, A. *J. Polym. Sci., Polym. Phys. Ed.* **1993**, *31*, 545.
- <sup>44</sup> Xu, G.; Gryte, C.C.; Norwick, A.S.; Li, S.Z.; Pak, S.; Greenbaum, S.G. *J. Appl. Phys.* **1989**, *66*(11), 5290.
- <sup>45</sup> Waters, J.F.; Likavec, W.R.; Ritchey, W.M. *J. Appl. Polym. Sci.* **1994**, *53*, 59.
- <sup>46</sup> McKnight, A.H.; Gillespie, J.W., Jr. *J. Appl. Polym. Sci.* **1997**, *64*, 1971.
- <sup>47</sup> Linossier, I.; Gaillard, F.; Romand, M.; Feller, J.F. *J. Appl. Polym. Sci.* **1997**, *66*, 2465.
- <sup>48</sup> Crank, J. *Diffusion in Polymers*; Academic: London; 1968.
- <sup>49</sup> Vieth, W.R. *Diffusion In and Through Polymers*; Hanser: New York; 1991.
- <sup>50</sup> Sammon, C.; Yarwood, J.; Everall, N. *Polymer* **2000**, *41*, 2521.
- <sup>51</sup> Chin, J.W.; Nguyen, T.; Aouadi, K. *J. Appl. Polym. Sci.* **1999**, *71*, 483.
- <sup>52</sup> *Diffusion in Polymers*; Neogi, P., Ed.; Marcel-Dekker: New York; 1996.
- <sup>53</sup> Van Alsten, J.G.; Coburn, J.C. *Macromolecules* **1994**, *27*(14), 3746.
- <sup>54</sup> Jou, J.H.; Huang, R.; Huang, P.T.; Shen, W.P. *J. Appl. Polym. Sci.* **1991**, *43*, 857.
- <sup>55</sup> Jou, J.H.; Hsu, L.; Huang, R.; Huang, P.T.; Shen, W.P. *Polym. J.* **1991**, *23*(9), 1123.
- <sup>56</sup> Grave, C.; McEwan, I.; Pethrick, R.A. *J. Appl. Polym. Sci.* **1998**, *69*, 2369.
- <sup>57</sup> McPeak, J.L. Ph.D. Dissertation, Virginia Tech, 1999.
- <sup>58</sup> Bao, Q.B.; Bagga, C.S. *Thermochemica Acta* **1993**, *226*, 107.
- <sup>59</sup> Omar, M. A. *Elementary Solid State Physics: Principles and Applications*, Revised Printing; Addison-Wesley: New York, 1993.
- <sup>60</sup> Boston, H.G.; St.Clair, A.K.; Pratt, J.R. *J. Appl. Polym. Sci.* **1992**, *46*, 243.
- <sup>61</sup> *Electronic Materials Handbook, Volume 1 Packaging*; Minges, M.L., Ed.; ASM International: Materials Park, Ohio, 1989.
- <sup>62</sup> Eftekhari, A.; St. Clair, A.K.; Stoakley, D.M.; Sprinkle, D. R.; Singh, J.J. In *Polymers for Microelectronics: Resists and Dielectrics*; Thompson, L.F.; Wilson, C.G.; Tagawa S., Eds.; ACS Symposium Series 537; American Chemical Society: Washington, D.C., 1994; pp 535-545.
- <sup>63</sup> Simpson, J.O.; St. Clair, A.K. *Thin Solid Films* **1997**, *308-309*, 480.

- 
- <sup>64</sup> Hougham, G.; Tesoro, G.; Viehbeck, A.; Chapple-Sokol, J.D. *Macromolecules* **1994**, *27*, 5964.
- <sup>65</sup> Hougham, G.; Tesoro, G.; Viehbeck, A. *Macromolecules* **1996**, *29*, 3453.
- <sup>66</sup> Ree, M.; Kim K.; Woo S.H.; Chang, H. *J. Appl. Phys.* **1997**, *81*(2) 698.
- <sup>67</sup> Hinkley, J.A.; Mings, S.L. *Polymer* **1990**, *31*, 75.
- <sup>68</sup> Klemann, B.M.; DeVilbiss, T. *Polym. Eng. Sci.* **1996**, *36* (1), 126.
- <sup>69</sup> Popelar, S.F.; Chengalva, M.K.; Popelar, C.H.; Kenner, V.H. AMD-Vol.155, *ASME*, **1992**, 15.
- <sup>70</sup> Popelar, S.F.; Popelar, C.H.; Kenner, V.H. EEP-Vol.4-1, *Advances in Electronics Packaging, ASME*, **1993**, 287.
- <sup>71</sup> Popelar, S.F.; Popelar, C.H.; Kenner, V.H. *Transactions of the ASME* **1993**, *115*, 264.
- <sup>72</sup> Owens, D.K.; Wendt, R. *C. J. Appl. Polym. Sci.* **1969**, *13*, 1741.
- <sup>73</sup> Gent, A.N.; Schultz, J. *J. Adhesion* **1972**, *3*, 281.
- <sup>74</sup> Andrews, E.H.; Kinloch, A.J. *Proc. R. Soc. Lond.* **1973**, A.332, 385.
- <sup>75</sup> Andrews, E.H.; Kinloch, A.J. *Proc. R. Soc. Lond.* **1973**, A.332, 401.
- <sup>76</sup> Ahagon, A.; Gent, A.N. *J. Polym. Sci., Polym. Phys. Ed.* **1975**, *13*, 1285.
- <sup>77</sup> Gent, A.N.; Lai, S.-M. *J. Polym. Sci., Polym. Phys. Ed.* **1994**, *32*, 1543.
- <sup>78</sup> Chun, H.; Gent, A.N. *J. Polym. Sci., Polym. Phys. Ed.* **1996**, *34*, 2223.
- <sup>79</sup> Kinloch, A.J. *Adhesion and Adhesives, Science and Technology*; Chapman Hall: New York; 1987; pp 83-86, 264-271.
- <sup>80</sup> Chang, R.J.; Gent, A.N. *J. Polym. Sci., Polym. Phys. Ed.* **1981**, *19*, 1619.
- <sup>81</sup> Chang, R.J.; Gent, A.N. *J. Polym. Sci., Polym. Phys. Ed.* **1981**, *19*, 1635.
- <sup>82</sup> Kendall, K.; *J. Adhesion* **1973**, *5*, 179.
- <sup>83</sup> Lake, G.J.; Thomas, A.G. *Proc. R. Soc. Lond. A Mat.* **1967**, *300*, 108.
- <sup>84</sup> Lake, G.J. *Rubber Chemistry and Technology* **1995**, *68*(3), 435.
- <sup>85</sup> Brown, H.R.; Yang, A.C.M.; Russell, T.P.; Volksen W.; Kramer, E.J. *Polymer* **1988**, *29*, 1807.
- <sup>86</sup> Kim, Y.-H.; Kim, J.; Walker, G.F.; Feger, C.; Kowalczyk, S.P. *J. Adhesion Sci. Technol.* **1988**, *2* (2), 95.
- <sup>87</sup> Pappas, D.L.; Cuomo, J.J.; Sachdev, K.G. *J. Vac. Sci. Technol. A* **1991**, *9* (5), 2704.
- <sup>88</sup> Chou, N.J.; Dong, D.W.; Kim, J.; Liu, A.C. *J. Electrochem. Soc.* **1984**, *131*(10), 2335.
- <sup>89</sup> Chou, N.J.; Tang, C.H. *J. Vac. Sci. Technol. A* **1984**, *2* (2), 751.
- <sup>90</sup> Ho, P.S.; Hahn, P.O.; Bartha, J.W.; Rubloff, G.W.; LeGoues, F.K.; Silerman, B.D. *J. Vac. Sci. Technol. A* **1985**, *3* (3), 739.
- <sup>91</sup> Buchwalter, L.P.; Saraf, R. *J. Adhesion Sci. Technol.* **1993**, *7* (9), 925.
- <sup>92</sup> Buchwalter, L.P. *J. Adhesion Sci. Technol.* **1993**, *7* (9), 941.
- <sup>93</sup> Kim, K.S.; Kim, J. *ASME J. Eng. Mater. and Technol.* **1988**, *110*, 266.
- <sup>94</sup> Oh, T.S.; Buchwalter, L.P.; Kim, J. *J. Adhesion Sci Technol.* **1990**, *4*(4), 303.
- <sup>95</sup> Paek, S.H.; Lee, K.W.; Durning, C.J. *J. Adhesion Sci. Technol.* **1999**, *13*(4), 423.
- <sup>96</sup> Hu, D.C.; Chen, H.C. *J. Adhesion Sci. Technol.* **1992**, *6*(5), 527.
- <sup>97</sup> Hu, D.C.; Chen, H.C. *J. Mater. Sci.* **1992**, *27*, 5262.
- <sup>98</sup> Jou, J.H.; Liu, C.H.; Liu, J.M.; King, J.S. *J. Appl. Polym. Sci.* **1993**, *47*, 1219.
- <sup>99</sup> Miwa, T.; Tawata, R.; Numata, S. *Polymer* **1993**, *34*(3), 621.

### 3. EXPERIMENTAL

#### 3.1 AROMATIC POLYIMIDES

##### 3.1.1 Materials

The aromatic polyimides investigated included Kapton<sup>®</sup>-E, PMDA-ODA-BPADA, and a generic polyimide of unknown chemical structure that was called PI.

Kapton<sup>®</sup>-E is a commercial oriented polyimide film from DuPont with superior thermal and dimensional stability, a CTE close to copper, a high modulus, and low moisture absorption.<sup>1</sup> Much of the literature regarding Kapton film is for Kapton<sup>®</sup>-HN, which is an aromatic polyimide derived from pyromellitic dianhydride (PMDA) and oxydianiline (ODA). Kapton<sup>®</sup>-E was invented by the systematic introduction of stiff cosegments of pyromellitic dianhydride (PMDA) and para-phenylene diamine (p-PDA), into the classic PMDA/ODA polyimide.<sup>1</sup> The monomers and polymer chemical structure for Kapton<sup>®</sup>-E are presented in Figure 3.1.

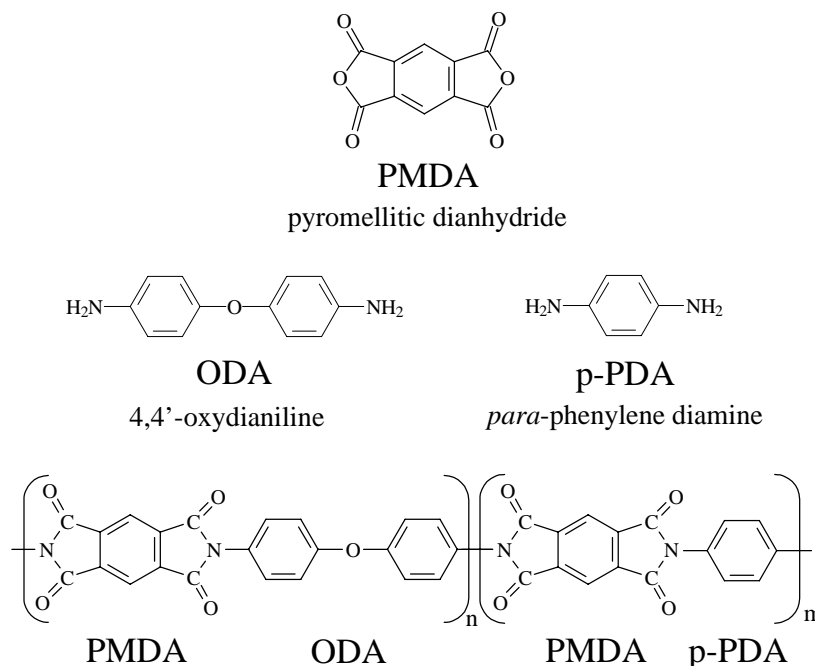


**Figure 3.1. Monomers and polymer chemical structure for Kapton<sup>®</sup>-E.**

(PMDA/ODA)-co-(BPADA/ODA) or “KB” is a random aromatic copolyimide synthesized from pyromellitic dianhydride (PMDA), 4,4'-oxydianiline (ODA), and bisphenol A dianhydride (BPADA). The molar ratio of the dianhydrides is 50:50, and the polyimide had a target molecular weight of  $M_n \approx 40,000$  g/mol. KB was synthesized and 40  $\mu\text{m}$  thick films were cast and cured by a former student, Dr. Isaac Farr, of Professor James E. McGrath’s research group at Virginia Tech. The monomers and polymer chemical structure for KB are presented in Figure 3.2.

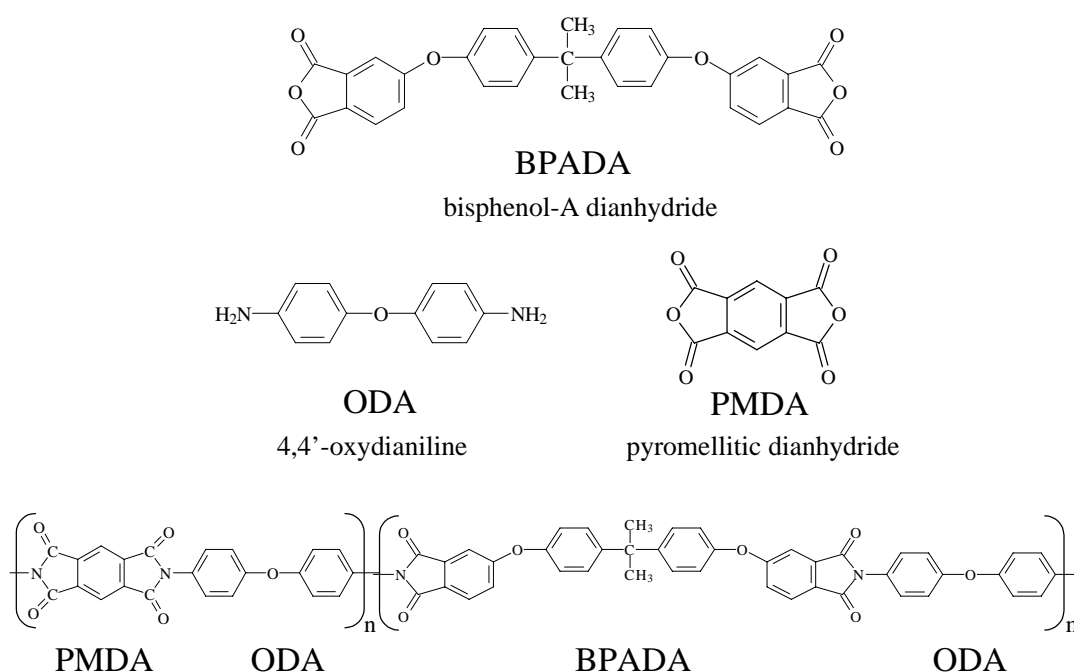


**Figure 3.2. Monomers and polymer chemical structure for KB.**

The chemical structure of the third material, PI, characterized within this study is unknown. The viscoelastic properties of PI films, 20  $\mu\text{m}$  thick, were examined using a unique sample preparation technique.

### 3.1.2 Bilayer Sample Preparation

Due to the low mechanical strength of the PI films, films of PI were thermally bonded to Kapton<sup>®</sup>-E or KB to form a bilayer. The bilayer was then characterized to obtain the viscoelastic

properties of PI. Vacuum dried Kapton<sup>®</sup>-E, KB, and PI films were sandwiched between thin Teflon<sup>®</sup> sheeting and clean, flat, aluminum plates and then thermally bonded together using a Tetrahedron MTP-13 Compression-Lamination Press. KB/PI, was bonded at 240 °C for 20 minutes at 700 psi, then quenched to room temperature. Kapton<sup>®</sup>-E/PI was bonded at 300 °C for 10 minutes at 700 psi, then quenched to room temperature. Bonding times were arbitrarily selected, however, Kapton<sup>®</sup>-E/PI bonding times were shorter to limit the extent of PI degradation.

### 3.1.3 Characterization

Dynamic Mechanical Analysis (DMA) was utilized to determine the viscoelastic relaxation transition temperatures of the three polyimides. A TA Instruments DMA 2980 was operated in the film tension geometry. Films were vacuum dried overnight and then tested at a frequency of 1 Hz and an oscillation amplitude of 25  $\mu\text{m}$ . Strips, 25 x 5 x 0.05 mm, of Kapton<sup>®</sup>-E were cut along the machine direction from a roll. Samples of KB were cut to 25 x 5mm strips from a 0.04 mm thick film. For each, a heating rate of 1 °C/min from -110 °C to 70 °C above the  $T_g$  was utilized. For the PI film investigations, 25 x 6 x 0.06 mm bilayer samples were heated at 2 °C/min from 25 °C to 270 °C for KB/PI, and from 25 °C to 245 °C for Kapton<sup>®</sup>-E/PI. For the latter, the  $T_g$  of Kapton<sup>®</sup>-E was not exceeded because of the thermal stability of PI.

The frequency dependence of the sub- $T_g$  and  $T_g$  viscoelastic relaxations of Kapton<sup>®</sup>-E and KB was also measured by DMA. To investigate the sub- $T_g$  relaxations, a step-isothermal path was adopted with 3 °C increments from -120 °C to 380 °C for Kapton<sup>®</sup>-E, and from -120 °C to 325 °C for KB. At each step, the response to 0.1, 1, and 10 Hz was measured. To generate master curves for the  $T_g$  of Kapton<sup>®</sup>-E and KB, a step isothermal temperature path was used with 3 °C increments from approximately 80 °C below to 80 °C above the respective glass transition temperature. At each step, the response to 12 frequencies, ranging from 0.03 to 30 Hz, was measured.

To generate a master curve for the  $T_g$  of PI, a KB/PI bilayer was tested. A 15  $\mu\text{m}$  oscillation amplitude and a step-isothermal temperature path, with 3 °C increments from 140 °C to 225 °C, were utilized. At each step, the response to 6 frequencies, ranging from 0.33 Hz to 10 Hz, was

measured. A master curve for the  $T_g$  of PI within a Kapton<sup>®</sup>-E/PI bilayer was not prepared due to overlap of the  $T_g$  of PI with the  $\beta$  transition of Kapton<sup>®</sup>-E.

Atomic Force Microscopy (AFM) was adopted to examine for an interphase region in KB/PI bilayer films. A small piece of the bilayer film was embedded in epoxy, then a microtome was used across the cross-section to prepare a flat surface for AFM analysis. A Digital Instruments Corporation AFM was used in Tapping Mode<sup>™</sup> and the cantilever probe was etched silicon.

### 3.2 THE EFFECT OF MOISTURE ON THE MECHANICAL AND DIELECTRIC PROPERTIES OF KAPTON<sup>®</sup>-E POLYIMIDE FILM.

#### 3.2.1 Humidity Environments

Six humidity environments, listed in Table 3.1, were prepared from saturated salt solutions.<sup>2</sup>

**Table 3.1. Humidity Environments.**

Salt	Relative Humidity
Vacuum oven	0%
LiCl	8%
KOOCCH <sub>3</sub> <sup>a</sup>	21%
CaCl <sub>2</sub>	29%
Ca(NO <sub>3</sub> ) <sub>2</sub>	43%
NH <sub>4</sub> Cl	73%
d H <sub>2</sub> O <sup>b</sup>	98%

<sup>a</sup> Potassium Acetate

<sup>b</sup> Deionized water

For each, the salt was added to  $\approx$  20 ml of distilled water until undissolved crystals remained. The saturated salt solutions were placed at the bottom of glass desiccators which were then sealed and stored at room temperature ( $\approx$  23 °C). A General Eastern Model 800B Humidity Indicator was periodically used to monitor the humidity in the desiccators through a septum in the lid.

Tensile test, DMA, and Dielectric Analysis (DEA) samples, 152.4 x 12.7 x 0.05 mm, 25 x 6.5 x 0.05 mm, and 25.4 x 25.4 x 0.05 mm, respectively were cut from the machine direction of

a 14-inch wide, 50  $\mu\text{m}$  thick roll of the Kapton<sup>®</sup>-E film. The samples were dried in a vacuum oven at  $\approx 150\text{ }^{\circ}\text{C}$  for 24 hours, weighed using a Mettler AE200 analytical microbalance ( $\pm 0.1\text{ mg}$ ), and then placed in the humidity environments on a platform suspended  $\approx 2$  inches above the salt solutions. The samples were equilibrated for at least 3 days, weighed to determine the percent moisture uptake, and returned to the humidity environments. The samples were stored in the humidity environments until immediately prior to tensile testing, DMA, and DEA. The samples defined as “vacuum” were dried at  $150^{\circ}\text{C}$  for 24 hours; then, the oven was turned off and the samples were held under vacuum for 4 days. After the 4 day period the samples were immediately weighed and then characterized. The weights of the tensile test samples were used for the weight uptake calculations because these were the largest samples and weight changes could be more easily detected.

Thermogravimetric Analysis (TGA) was used to confirm the percent moisture uptake. A TA Instruments TGA 2950 was operated using a heating rate of  $10\text{ }^{\circ}\text{C}/\text{min}$  from  $25\text{ }^{\circ}\text{C}$  to  $700\text{ }^{\circ}\text{C}$ . The purge gas was air. The percent moisture absorbed was determined from the change in weight at  $100\text{ }^{\circ}\text{C}$ .

The tensile test samples were characterized using ASTM D882 on an Instron 1123 mechanical tester. A 200 lbs. load cell and pneumatically actuated grips with steel faces were used. The distance between the grips was  $\approx 100\text{ mm}$  and paper was interposed between the Kapton<sup>®</sup>-E and the grip surface to reduce stress and prevent sample failure within the grips. Using this technique, the strips yielded within the gage length. The tests were performed at a strain rate of  $10\text{ mm}/\text{min}$  and five samples were tested for each humidity.

A TA Instruments DMA 2980 was operated in the film tension geometry at a frequency of 1 Hz and an oscillation amplitude of  $25\text{ }\mu\text{m}$ . A  $2\text{ }^{\circ}\text{C}/\text{min}$  heating rate from  $-25\text{ }^{\circ}\text{C}$  to  $380\text{ }^{\circ}\text{C}$  was used.

Dielectric Analysis experiments were performed using a TA Instruments DEA 2970. Films were sputter coated with gold to improve their contact with the electrodes. A mask overlay was used to assist in sputtering a  $285.05\text{ mm}^2$  circle of gold on each side of the film and the sputtering time was set to coat  $200\text{ }\text{\AA}$  of gold. The DEA ram force and minimum spacing were set to 150 N and 0 mm, respectively. A heating rate of  $2\text{ }^{\circ}\text{C}/\text{min}$  from  $-150\text{ }^{\circ}\text{C}$  to  $275\text{ }^{\circ}\text{C}$  was utilized and seven decades of frequency, 0.1 Hz to 100,000 Hz, were scanned. The time required

to scan all the frequencies was less than 1 minute. Only the temperature range of the sub- $T_g$  transitions was studied because ionic conductivity disrupted the signal near the  $T_g$ .

### 3.2.2 Saturated Environments

Weight uptake samples, 76.2 x 25.4 x 0.05 mm, were cut from the machine direction of a 14-inch wide, 50  $\mu\text{m}$  thick roll of the Kapton<sup>®</sup>-E film. Five samples were cut for the 25 °C weight uptake experiments and three samples were cut for the 60 °C experiments. The samples were dried in a vacuum oven at  $\approx$  150 °C for 24 hours. Initial “dry” sample weights were measured using Mettler AE200 analytical microbalance ( $\pm$  0.1 mg) and then the each sample was placed in a different jar of water. For the 60 °C uptakes, the water was preheated to 60 °C and the jars were kept in an oven for the duration of the experiment. Samples were periodically removed from each water environment, blotted dry, weighed, and returned to the water environment. For each measurement, the sample was out of the environment for approximately 30 seconds. For the 25 °C uptakes, the measurements were first made in 15 minute intervals, then the interval was lengthened to 30 minutes and 60 minutes as saturation was approached. For the 60 °C uptakes, the measurements were first made in 5 minute intervals, then the interval was lengthened to 15 minutes, 30 minutes, and 60 minutes as saturation was approached.

A TA Instruments DMA 2980 was operated using the Submersion Film/Fiber Tension geometry to study the physical properties of Kapton<sup>®</sup>-E in situ upon exposure to water. Specifically, the geometry was used to examine the change in sample length of Kapton<sup>®</sup>-E as water absorbs. This technique is particularly appropriate for thin films since the diffusion process usually reaches equilibrium within 24 hours. Samples, 20 x 6 x 0.05 mm, were dried in a vacuum oven and then immediately placed within the DMA. Sample placement is crucial for meaningful results. In this geometry, films have the tendency to buckle when the mechanical oscillation is applied. If the sample buckles during oscillation, the viscoelastic properties of the film are not measured. Thus, upon sample loading, the initial storage modulus, loss modulus, and  $\tan \delta$  values were checked; if the values were in the range observed using the Film Tension geometry, water was then pipetted into the fluid container and the experiment was started. An oscillation amplitude of 25  $\mu\text{m}$  and frequency of 1 Hz were used. Samples were pretensioned, initially, to 150 % strain under 5 N static force. If buckling of the film was observed, the % strain was increased until the sample was taut and an appropriate modulus was measured.

Since the furnace of the DMA cannot be closed when the Submersion Film/Fiber Clamp is in use, TA Instruments designed an external temperature controller for the fluid container. The temperature of the liquid within the fluid container can be controlled for isothermal in situ measurements, provided the temperature remains below the boiling temperature of the liquid in question. The length change of Kapton<sup>®</sup>-E was monitored for 25 °C and 60 °C water temperatures. For both test temperatures, the water was  $\approx$  25 °C when it was pipetted into the fluid container. For the 60 °C test temperature, the controller was used to heat the water to 60 °C; this was typically achieved within  $\approx$  4 minutes.

### **3.3 BPADA-BASED PARTIALLY ALIPHATIC POLYIMIDES**

#### **3.3.1 Introduction**

The BPADA-based polyimides were synthesized by former students, Melanie Bagwell, Dr. Isaac Farr, and Dr. Debra Dunson, of Professor James E. McGrath's research group at Virginia Tech. An outline of the synthetic procedure is provided in a following section to provide context for their physical property and adhesive characterization.

#### **3.3.2 Materials**

*N*-methyl-2-pyrrolidone (NMP), triethylamine (TEA), *o*-dichlorobenzene (*o*-DCB), ethanol, and methanol were used as-received without further purification. The bis[4-(3,4-dicarboxyphenoxy)phenyl]propane dianhydride, or Bisphenol A dianhydride (BPADA), was donated by General Electric. The aromatic diamine, 4,4'-oxydianiline (ODA), was purchased from Allco. The linear aliphatic diamines, hexamethylenediamine (HMDA) and dodecyldiamine (DoDDA), and the cycloaliphatic diamine, isomeric 4,4'-diaminocyclohexylmethane (DCHM), were purchased from Aldrich. The monomer chemical structures are shown in Figure 3.3.

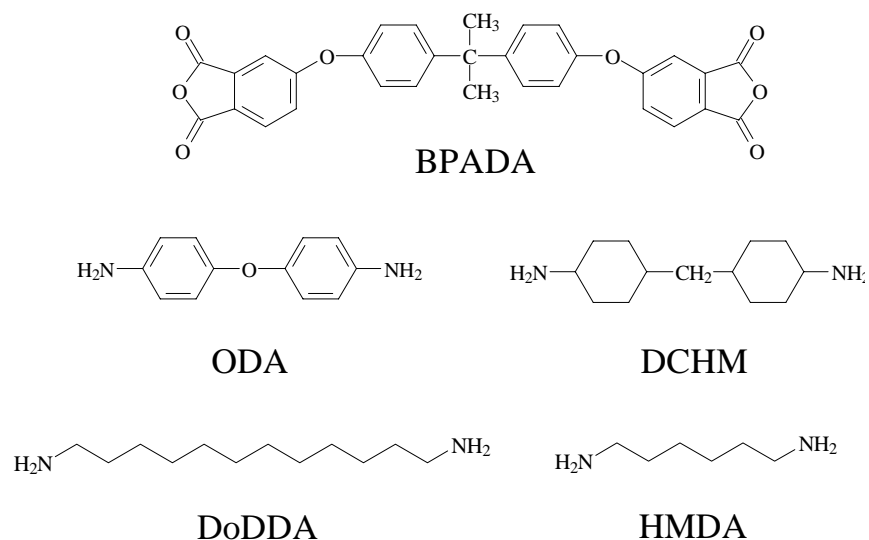


**Figure 3.3. Monomer chemical structures.**

The monomers were purified by sublimation or recrystallization prior to use to ensure proper stoichiometry. After recrystallization, the BPADA was dried under vacuum at 120 °C to cyclize possible diacid moieties. The ODA was dried under vacuum at 100 °C and the HMDA and DoDDA were dried under vacuum at room temperature.

Nine BPADA-based polyimides were synthesized by combination of the diamines in Figure 3.3. These were divided into two groups for physical property characterization. Group 1, discussed in Chapter 5, included BPADA/ODA, BPADA/HMDA:ODA, 75:25, BPADA/HMDA:DoDDA, 50:50, BPADA/HMDA:DoDDA, 25:75, and BPADA/DCHM. Group 2, discussed in Chapters 6 and 7, included a series of BPADA/ODA:DoDDA polyimides where the ODA:DoDDA diamine molar ratio was varied 100:0, 75:25, 50:50, 25:75, and 0:100.

### 3.3.3 Synthesis

A number of aromatic polyimides<sup>3-9</sup> have been prepared at Virginia Tech using ester-acid high temperature solution imidization. The same approach was applied in the present study to prepare high molecular weight, soluble, amorphous, partially aliphatic polyimides. This method involves the prereaction of aromatic dianhydrides with ethanol and a tertiary amine catalyst to form ester-acids, followed by the addition of diamines. Subsequent thermal reaction forms high molecular weight, fully-cyclized polyimides. Unlike the poly(amic acid) route, the aliphatic

diamines are added to the ester-acid rather than to the dianhydride, thus eliminating the undesirable “gel-like” intermediate salt formation. A general reaction scheme for the preparation of the BPADA/ODA:DoDDA series is shown in Figure 3.4.

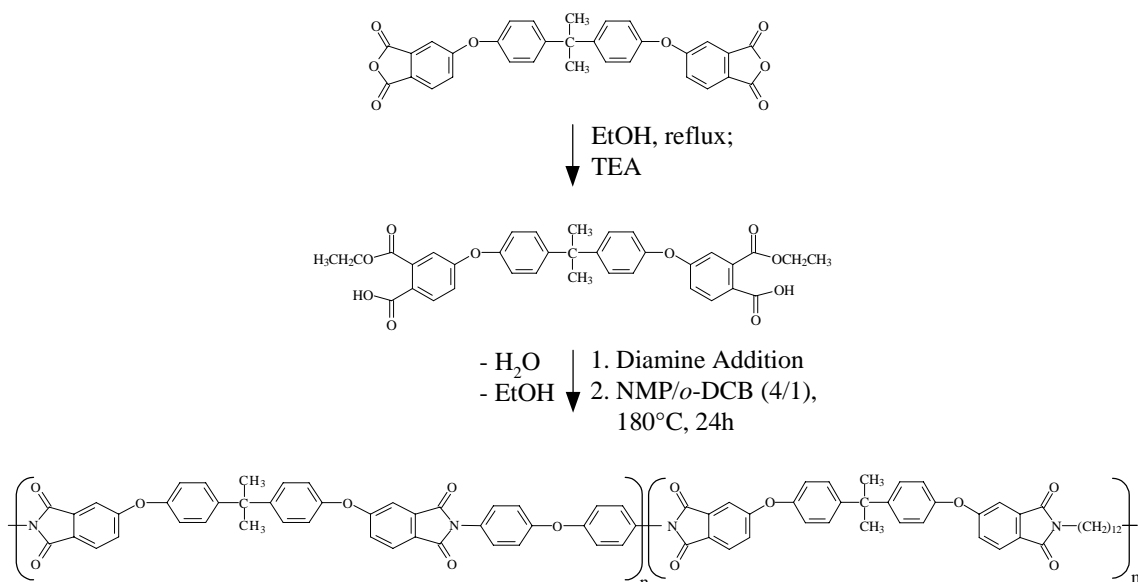


**Figure 3.4. Ester-acid high temperature solution imidization scheme for the BPADA/ODA:DoDDA series.**

ODA:DoDDA diamine molar ratios of 100:0, 75:25, 50:50, 25:75, and 0:100 were used. Thus, the series includes both the homopolymers BPADA/ODA and BPADA/DoDDA, and random copolyimides from the intermediate molar ratios.

The synthesis of BPADA/ODA:DoDDA, 50:50 is described as follows to illustrate the steps used in the ester-acid method. A three-necked round-bottomed flask was equipped with a mechanical stirrer, nitrogen inlet, and a reverse Dean-Stark trap fitted with a condenser. To the flask, 10 g (19.2 mmol) of BPADA were charged and rinsed in with 100 ml of ethanol and 3 ml of TEA. Under refluxing conditions, the ethyl ester-acid of the dianhydride was formed. After approximately 1 hour, the excess ethanol was distilled from the solution leaving a viscous yellow ester-acid solution. An equimolar amount of the diamines, (DoDDA, 1.923 g (9.605 mmol); ODA, 1.924 g (9.605 mmol)), was added into the ester-acid solution with NMP and *o*-DCB, an azeotropic solvent, to give 10 wt% solids. The solution was refluxed at 180 °C for 24 hours to

obtain fully cyclized imide linkages. The viscous solution was cooled and then added to stirring methanol. The white, fibrous material was isolated, washed with methanol, and dried under vacuum at 150 °C for 24 hours.

### 3.3.4 Film Preparation

To fabricate films, the polyimides were dissolved in NMP to prepare 5-10% (w/v) solutions, filtered under pressure (argon, 60-80 psi) to remove impurities, and then degassed in a vacuum oven (air, 25 psi). The solutions were cast onto clean glass substrates using a doctor blade with a 25 mil clearance. The glass substrates were immediately placed onto a temperature programmable hot plate, covered, and exposed to a gentle flow of nitrogen. The temperature was gradually increased from 30 °C to ( $T_g + 10^\circ\text{C}$ ) over 8 hours. Since the polyimides were fully imidized, the long heating cycle removed the NMP slowly enough to prevent the formation of bubbles within the films. Upon completion of the heating cycle, the films were removed from the glass substrates using a razor blade to lift an edge of the film, followed by applying several drops of water at the exposed interface to induce delamination. The resulting films were approximately 0.03 mm thick.

### 3.3.5 Characterization

Gel Permeation Chromatography (GPC) was conducted using a Waters GPC/ALC 150C chromatograph equipped with a differential refractometer detector and a differential viscometer detector (Viscotek 150R). Waters  $\mu$ Styragel HT3 + HT4 columns maintained at 60 °C were used. NMP, which contained 0.02 M  $\text{P}_2\text{O}_5$ , was the mobile phase (0.1 ml/min flow rate). A universal calibration curve was generated using a series of polystyrene standards with narrow molecular weight distributions such that absolute values of  $\langle M_n \rangle$ ,  $\langle M_w \rangle$ , and  $\langle M_v \rangle$  could be calculated.<sup>10,11</sup>

Degradation temperatures of the polyimides were found by heating 10-mg samples at 10 °C/min to 900 °C in air using a Perkin Elmer TGA 7 instrument.

A Perkin Elmer DSC 7 instrument was used to determine the glass transition temperature. Samples (10 mg) were heated at 10 °C/min to 300 °C under a nitrogen purge. Two heating cycles were performed, with the  $T_g$  reported obtained on the second scan.

Dynamic Mechanical Analysis (DMA) was utilized to determine the viscoelastic relaxation transition temperatures. A TA Instruments DMA 2980 was operated in the film tension geometry. Films, 20 x 5 x 0.03 mm, were tested at a frequency of 1 Hz and an oscillation amplitude of 20  $\mu\text{m}$ . A heating rate of 2  $^{\circ}\text{C}/\text{min}$  over the temperature range of interest was utilized. For the BPADA/ODA:DoDDA series, four replicate experiments were performed for each polyimide.

A TA Instruments DMA 2980 in the film tension geometry, creep mode was utilized to measure the linear coefficient of thermal expansion (CTE). The dimension change of films, 20 x 5 x 0.03 mm, under 0.05 N of static force was monitored as a function of temperature. Multiple heating and cooling cycles, in which the temperature was ramped at 2  $^{\circ}\text{C}/\text{min}$  from 25  $^{\circ}\text{C}$  to just below the  $T_g$  or vice versa, were performed. The  $T_g$  of the sample was not exceeded to prevent sample deformation during the temperature cycles. Liquid nitrogen was used to mediate the heating or cooling rate.

Dielectric Analysis (DEA) experiments were performed using a TA Instruments DEA 2970. Films, 25.4 x 25.4 x 0.03 mm, were sputter coated with gold to improve their contact with the electrodes. A mask overlay was used to assist in sputtering a 285.05  $\text{mm}^2$  circle of gold on each side of the film and the sputter time was set to coat 200  $\text{\AA}$  of gold. The DEA ram force and minimum spacing were set to 150 N and 0 mm, respectively. A heating rate of 2  $^{\circ}\text{C}/\text{min}$  over the temperature range of interest was utilized and seven decades of frequency, 0.1 Hz to 100,000 Hz, were scanned. Two heating cycles were performed.

A Metricon Corporation Model 2010 prism coupler was used to measure the in-plane refractive index. The instrument utilizes a 200-P-4 prism and a He-Ne laser light source at a 632.8 nm wavelength. The index accuracy is  $\pm 0.001$  and the index resolution is  $\pm 0.0005$ . Films, 20 x 5 x 0.03 mm, were tested at 25  $^{\circ}\text{C}$  and five measurements were made for each sample.

The yield stress,  $\sigma_y$ , was measured using an Instron 1123 mechanical tester equipped with a 200 lbs. load cell and pneumatically actuated grips with steel faces. Rectangular strips, 101.6 x 12.5 x 0.04 mm, were tested in tension at 12.5 mm/min. Samples were loaded such that the distance between the grips was 50.8 mm. Four or five samples were tested per polyimide, depending on the quantity of film available.

A Rame-Hart, Inc., optical goniometer with a camera attachment was used to measure the contact angles of two probe liquids against films of the BPADA/ODA:DoDDA series and a cleaned silicon wafer. The polyimide films were wiped with isopropyl alcohol prior to the measurements. The silicon wafer was cleaned as described in the SLBT sample preparation section. Measurements were performed at room temperature using deionized water and methylene iodide. The drop volume was 5  $\mu\text{l}$  and the angle from both sides of the drop was measured. An average of the angles for five drops was taken. From the average angle of each probe liquid on the given surface, the polar and dispersive components of the surface energy,  $\gamma_s^p$  and  $\gamma_s^d$ , were calculated by a harmonic-mean method in which two equations were solved simultaneously:<sup>12</sup>

$$(1 + \cos \theta_1) \gamma_1 = 4 \left( \frac{\gamma_1^d \gamma_s^d}{\gamma_1^d + \gamma_s^d} + \frac{\gamma_1^p \gamma_s^p}{\gamma_1^p + \gamma_s^p} \right)$$

$$(1 + \cos \theta_2) \gamma_2 = 4 \left( \frac{\gamma_2^d \gamma_s^d}{\gamma_2^d + \gamma_s^d} + \frac{\gamma_2^p \gamma_s^p}{\gamma_2^p + \gamma_s^p} \right)$$

where the variables were assigned as listed in Table 3.2.

**Table 3.2. Variables used in the harmonic mean method.**

Variable	Symbol	Value <sup>a</sup>
Contact angle of H <sub>2</sub> O	$\theta_1$	-
Surface energy of H <sub>2</sub> O	$\gamma_1$	72.8 dyne/cm
Polar component of the surface energy of H <sub>2</sub> O	$\gamma_1^p$	50.7 dyne/cm
Dispersive component of the surface energy of H <sub>2</sub> O	$\gamma_1^d$	22.1 dyne/cm
Contact angle of CH <sub>2</sub> I <sub>2</sub>	$\theta_2$	-
Surface energy of CH <sub>2</sub> I <sub>2</sub>	$\gamma_2$	50.8 dyne/cm
Polar component of the surface energy of CH <sub>2</sub> I <sub>2</sub>	$\gamma_2^p$	6.7 dyne/cm
Dispersive component of the surface energy of CH <sub>2</sub> I <sub>2</sub>	$\gamma_2^d$	44.1 dyne/cm
Polar component of the surface energy of substrate	$\gamma_s^p$	-
Dispersive component of the surface energy of substrate	$\gamma_s^d$	-

<sup>a</sup> Reference 12.

### 3.3.6 SLBT Sample Preparation

One inch diameter, 300  $\mu$ m thick, test-grade silicon wafers were purchased from Wafer World, Inc. Wafer specifications were: p-type, (100) orientation, 1-10 ohm/cm resistivity, no flats, and one side polished. To prepare the blister specimens for the BPADA/ODA:DoDDA series the following procedure was used:

1. Drill a 3 mm diameter hole through the thickness of the silicon wafer using a Dremel<sup>®</sup> tool with a diamond bit. A one inch diameter aluminum disk with a 4 mm diameter hole was used as a guide. The Dremel<sup>®</sup> was not used like a traditional drill-press. Rather, the silicon was slowly drilled away with gentle pressure over a period of 15 minutes to ensure that the wafer did not fracture.

2. Clean the silicon wafer using the RCA Standard Clean - a procedure based on hot alkaline and acidic hydrogen peroxide solutions.<sup>13,14</sup> Step 1. Boil wafer in a 1:1:5 (v/v/v) mixture of hydrogen peroxide (30%), ammonium hydroxide, and purified water, at 90 °C for 1 hour. Step 2. Rinse wafer with 2 L of purified water. Step 3. Boil wafer in a 2:5 (v/v) mixture of hydrogen peroxide (30%) and sulfuric acid at 100 °C for 1 hour. Pour the sulfuric acid into the hydrogen peroxide slowly because the addition is exothermic. Step 4. Rinse wafer with 2 L of purified water. Typically seven wafers were cleaned at a time. The native silicon dioxide layer of the silicon wafer cleaned by this procedure is wet completely by water, indicating a hydrophilic

surface. Wafers were stored in purified water for 0-5 hours prior to film casting. Step 5. Dry wafer in a stream of purified nitrogen immediately prior to casting the polyimide film.

For BPADA/ODA, then:

3. Cast the polyimide film onto the cleaned wafer and transfer sample to a hot plate which is preheated to  $\approx 100$  °C. Cover sample with an evaporating dish, introduce an argon purge, and hold for 1 hour. Remove sample from hot plate and place in a 190 °C vacuum oven for 12 hours. The film was cast by pipetting 1 ml of solution (10% (w/v) in NMP) near an edge of the wafer, then a doctors blade with an 8 mil clearance was used draw the solution uniformly over the surface. Since the solution was cast directly over the hole in the wafer, the solution filled the wafer hole. Upon drying, this resulted in a continuous  $\approx 17$   $\mu\text{m}$ -thick film over the wafer surface. Small defects in the film were observed around the perimeter of the drilled hole.

4. Precrack the sample and then dry at 100 °C overnight. During the film casting step, polyimide solution filled the wafer hole. Upon drying, this resulted in a continuous 10  $\mu\text{m}$ -thick film over the wafer surface, however, the film also adhered to the interior walls of the hole. The film within the hole was loosened using a combination of microliter-size drops of water and gentle pressure to create a precrack which facilitated blister testing. Without a precrack, the blister samples would puncture. Samples were dried at 100 °C overnight to evaporate water absorbed by the film during precracking. The precrack for BPADA/ODA-2 is illustrated in Figure 3.5.



**Figure 3.5. Precrack of BPADA/ODA-2.**

5. SuperGlue<sup>®</sup> the sample to an aluminum disk. Place in desiccator for 1 hour. The aluminum disk was 25.4 mm in diameter, 1 mm in thickness, and had a 4 mm diameter hole in the center. The aluminum disk provides support for the fragile silicon wafer during blister testing.

6. Test the adhesion within a TA Instruments DMA 2980 in a modified penetration clamp geometry, ie. a shaft loaded blister test, at 0.5 N/min. Further details are provided in a later section.

For BPADA/ODA:DoDDA, 75:25, 50:50, 25:75, and BPADA/DoDDA a “patch” technique was used to prepare blister specimens. In the patch technique, a 4 mm diameter circle of free film (prepared for DMA and DEA property characterization) was cut from each polyimide. The film patch film thickness was  $\approx 30 \mu\text{m}$  and the properties of the patch, such as modulus and yield strength, are reported in Chapter 6. This circle of film was used to cover the wafer hole, such that during film casting the polyimide solution would not enter. The patch then later served as the precrack during blister testing.

3. Place clean, dry wafer on a hot plate preheated to a temperature just below the glass transition temperature of the polyimide in question. Preheat wafer for 15 minutes, then place a circle of film of the polyimide in question over the hole. Since the wafer is preheated to a temperature near the  $T_g$ , within seconds the circle of film will adhere to the wafer surface surrounding the hole, thus sealing off the hole. Immediately remove wafer from hot plate, allow to cool for 3 minutes, then cast polyimide film onto the wafer and transfer sample to a hot plate which is preheated to  $\approx 100 \text{ }^\circ\text{C}$ . Cover sample with an evaporating dish, introduce an argon purge, and hold for 1 hour. Remove the sample from the hot plate and place in a high temperature vacuum oven for 12 hours. The wafer was then glued to an aluminum disk etc., as described for BPADA/ODA. A sample prepared using the patch technique is presented in Figure 3.6. A small discontinuity in the cast film is visible due to the underlying patch.



**Figure 3.6. BPADA/ODA:DoDDA, 50:50-4 prepared using the patch technique.**

Samples prepared by the patch technique worked well within the SLBT. As an after thought, for a few samples, the patch was precracked using the same method described for BPADA/ODA. This proved much more effective in initiating the blister growth for the room temperature experiments. As a consequence, samples prepared for the high temperature measurements were precracked.

### 3.3.7 Additional Comments on SLBT Sample Preparation

The final sample preparation technique for the blister specimens trivializes the effort to prepare successful blister samples. The next few paragraphs describe several preparation techniques attempted and the lessons learned from their failures. All preparation techniques began with the drilled wafer.

Attempt 1. The wafer was cleaned by immersion in a 70/30 v/v solution of concentrated  $\text{H}_2\text{SO}_4/\text{H}_2\text{O}_2$  for 90 minutes at  $90^\circ\text{C}$ . The wafer was removed, rinsed with deionized water, and then dried within a stream of nitrogen. The wafer was glued to an aluminum disk which also contained a 4 mm diameter hole. The hole in the aluminum disk was covered on the under-side with 3M Magic tape so that the wafer could be held in place by the vacuum on the spin coater. The hole on the wafer-side was covered with a circle of Teflon<sup>®</sup> tape. The wafer was then spin coated with a  $\approx 1\%$  (w/v) solution of BPADA/ODA in NMP by flooding the wafer under static conditions, then ramping to 1500 rpm and holding for 1 min. The specimen was then dried in a vacuum oven at  $200^\circ\text{C}$  to remove the casting solvent and then a Kapton<sup>®</sup> PSA reinforcement layer was adhered to the BPADA/ODA-side to prevent film puncture during the SLBT.

Result 1. The solution dewet from the wafer at the edges, the wafer surface surrounding the Teflon<sup>®</sup> circle, and from the Teflon<sup>®</sup> circle. The resulting films were not uniform in thickness. The dewetting was attributed to the solvent from the super glue, residual sulfuric acid from the cleaning step or that the acid cleaning step was not effective, and the low surface tension of Teflon<sup>®</sup>. The nonuniformity was attributed to the disruption of the spincoating process by the edge of the Teflon<sup>®</sup> circle. Since a continuous film was not prepared, the SBLT measured the adhesion of the Kapton<sup>®</sup> PSA reinforcement layer to the BPADA/ODA film, ie. the crack was not at the correct interface. Some of the wafers debonded from the aluminum and then cracked during the SLBT because the super glue had crosslinked during the vacuum oven heating step.

Lessons Learned 1. (a) A silicon wafer cleaning step needed to be added. Professor Alan Esker suggested using a 1:1:5 (v/v/v) ratio of ammonium hydroxide, hydrogen peroxide, and water at 90 °C. (b) After each cleaning step the wafers should be rinsed with 2 liters of purified water. This was also suggested by Professor Esker. (c) The Teflon<sup>®</sup> circle did not work – the hole should be covered with something else. (d) The films should be cast onto the wafer using a doctors blade – rather than by spin coating. The doctors blade will allow thicker films to be prepared, which should direct the crack to the correct interface. The technique for the preparation of free films for DMA, DEA, etc., established previously should be implemented.

Attempt 2. The wafers were cleaned with a 1:1:5 (v/v/v) mixture of hydrogen peroxide, ammonium hydroxide, and purified water, at 90 °C for 1 hour, then rinsed with 2 L of purified water. Next the wafers placed in a 2:5 (v/v) mixture of hydrogen peroxide and sulfuric acid at 100 °C for 1 hour, then rinsed with 2 L of purified water. Upon completion of the final cleaning step, water was noted to coat the entire surface. This indicated that a uniformly clean, hydrophilic silicon dioxide layer had been prepared. The wafer hole was covered with a 4 mm-diameter circle of Kapton<sup>®</sup>-PSA tape. Approximately 1 ml of 10 % (w/v) solution of BPADA/ODA in NMP was pipetted onto the wafer and a doctors blade with an 8 mil clearance was used to draw down the solution. The wafer was immediately covered and placed in an argon atmosphere. The sample was heated on a hot plate using a heating profile similar to that used for the free films. The sample was dried further in the vacuum oven and then a layer of Kapton<sup>®</sup>-PSA reinforcement was applied. The final specimen was super glued to an aluminum disk.

Result 2: The solution dewet from the wafer at the edges and the resulting film was not uniform. While the solution did not dewet at the wafer near the Kapton<sup>®</sup>-PSA circle boundary, the film thickness here was visually thinner because colors fringes were observed. In the SBLT, once the Kapton<sup>®</sup>-PSA circle delaminated, the crack again moved away from the silicon interface.

Lessons learned 2: (a) The hot plate should be preheated to  $\approx 100$  °C. When the wafer is placed on the hot plate this will cause the moisture and solvent closest to the wafer surface to evaporate, thus forcing the solution to “stick.” (b) Try casting the film directly over the hole. This should allow a film of uniform thickness over the whole surface to be prepared. (c) Do not use the Kapton<sup>®</sup>-PSA reinforcement layer.

Attempt 3. The same wafer cleaning procedure and film casting procedure as attempt 2 was employed, except the hot plate was preheated to  $\approx 100$  °C and the wafer hole was not covered. The wafer was held at  $\approx 100$  °C for 1 hour, then placed in the vacuum oven at 200 °C for 12 hours. The final specimen was super glued to an aluminum disk, and then tested using the SLBT at 1 N/mm.

Result 3. The solution did not dewet from the wafer and the resulting film was uniform. In the SLBT, the film punctured after about 2 N of force. After the test, the film was easily peeled from the wafer. The thickness of the free film was  $\approx 17$   $\mu\text{m}$  thick and the free film showed that the wafer hole had left defects (bubbles, pin-sized holes, etc).

Lessons Learned 3. (a) By casting the solution directly over the hole, solution adhered to the interior walls of the hole. Thus during the SLBT, the film must first delaminate from the interior of the hole before it can delaminate from the surface and allow the adhesion energy to be measured. A precrack should be made to prior to the SLBT. (b) Or, try “plugging” the hole with a small piece of silicon wafer. After the film has dried, remove the plug, and test within the SLBT. (c) A slower SLBT test rate should be used to prevent film puncture.

Attempt 4. The same sample preparation method as attempt 3 was employed except the hole was plugged with a small piece of silicon wafer. The plug was made by sanding down the edges of a broken chip of wafer until the plug fit within the drilled hole. The plug was made from a 300  $\mu\text{m}$  thick wafer, so that the film could be cast over a flat surface.

Result 4. The plug could not be removed from the hole without rupturing the film. In the SLBT, the shaft pressed against the plug to try and induce delamination. Non-uniformities at the plug edges caused the film to puncture.

Lessons Learned 4. The use of the plug did not seem to accomplish anything. Had the test been successful, the theory for the SLBT used to calculate the adhesion energy may have not been applicable.

Attempt 5. The same sample preparation method as attempt 3 was employed except a precrack was made by placing microliter-size drops of water at the edges of the hole to plasticize the film. After 30 min of soaking, the water was removed and the hole was blotted dry. With gentle pressure, the film adhering to the interior of the walls delaminated, thus creating a

precrack on the surface of the wafer. The sample was tested by the SLBT at 0.5 N/mm. This procedure lead to a successful SLBT and adhesion energy measurement for BPADA/ODA.

Attempt 6. The successful BPADA/ODA sample preparation method was implemented to prepare SLBT samples from the BPADA/ODA:DoDDA copolyimides. The samples could not be precracked using water due to the strong adhesion of the polyimide to the interior walls of the wafer hole.

Result 6. The SLBT samples punctured prior to any blister growth due to the strong adhesion of the polyimide to the interior walls of the wafer hole.

Lessons Learned 6. A new precrack technique was needed. Try (a) sputter coating a few angstroms of gold onto the wafer around and in the hole, (b) covering the hole with a circle of free polyimide film.

Attempt 7. The same sample preparation method as attempt 3 was employed except after the wafer cleaning, a circle of gold was sputter coated around the hole.

Result 7. The SLBT samples punctured prior to any blister growth.

Lesson Learned 7: The gold did not appear to help create a precrack.

Attempt 8. The same sample preparation method as attempt 3 was employed except just prior to film casting a circle of free film was placed over the hole. However, during the casting step, the circle of film “floated” away, and solution flowed into the hole. With this knowledge, another wafer was first preheated to a temperature near the  $T_g$  of the free film, then the circle of film was placed over the hole. The circle adhered instantly. The wafer was removed from the hot plate and cooled. Then a film was cast onto the wafer using the established procedure. The circle prevented any solution from entering the hole.

Result 8. The SLBT was successful and this preparation technique was named the “patch” technique. This technique was used for BPADA/ODA:DoDDA, 75:25, 50:50, 25:75, and BPADA/DoDDA.

### **3.3.8 SLBT Design**

The SLBT adhesion measurements were performed using a TA Instruments DMA 2980. A SLBT clamp geometry was designed and manufactured with the assistance of the Virginia Tech

Department of Physics Machine Shop. The SLBT design is based on the commercially available TA Instruments penetration clamp geometry. The custom modifications include a top crossbar for the moveable clamp, a fixed clamp platform, a hollow, cylindrical sample holder, and a penetration probe or shaft. Within the DMA, the SLBT operates in the penetration clamp geometry and in the controlled force mode. Figure 3.7 illustrates SLBT clamp geometry installed within the DMA.



**Figure 3.7. Shaft loaded blister test geometry within the TA Instruments DMA 2980.**

The designed crossbar and platform maximize the vertical displacement range of the moveable clamp to allow the adhesive debond event to be monitored over greater shaft displacements. The penetration probe, which functions as the shaft, screws into the top crossbar of the moveable clamp. The shaft tip, a 1/8 inch (3.18 mm) diameter steel ball bearing, was adhered to the shaft using J-B Weld<sup>®</sup> high temperature, high strength epoxy. Horizontal mobility of the designed crossbar allows the shaft to be positioned in the center of the substrate hole. This is an important feature which accommodates the slight sample to sample variability introduced from hand-drilling the holes in the silicon wafers. The 25.4 mm diameter and 15 mm tall sample

holder rests on the DMA platform that attaches to the fixed, furnace mounting posts. The top of the sample holder contains a lip, such that the specimen can rest securely. During the test, the film debonds uninhibited in the hollow sample holder. The front of the sample holder contains a window through which a fiber-optic borescope coupled with a video camera is inserted to monitor the progression of the debond. The borescope is interfaced with a TV/VCR and a computer to record the debond event for analysis. The window also allows the profile of the debond to be examined for plastic deformation of the film at the shaft tip.

During a SLBT experiment, the DMA measures the load,  $P$ , and the shaft displacement,  $w_o$ , variables needed for the calculation of  $G$ . The third major variable, the debond radius,  $a$ , is measured from images of the blister growth recorded using the borescope/computer.

To allow the SLBT to be performed at temperatures other than ambient, TA Instruments graciously donated an extra furnace to this research effort. This is an important capability for examining the role of polymer viscoelastic relaxations and temperature in adhesion strength. Two holes were drilled in the furnace, one for the borescope and one for a light source. The temperature was stable to  $\pm 0.2$  °C, even with the two holes. The major limitation is the temperature range in which the borescope can be safely operated; temperatures cannot exceed 80 °C.<sup>15</sup> The high temperature SLBT set-up is shown in Figure 3.8.



**Figure 3.8. TA Instruments DMA 2980 with a standard DMA furnace which was customized to accommodate the shaft loaded blister test.**

The TA Instruments DMA 2980 was selected for the SLBT versus a universal testing machine for several reasons. First, the furnace of the DMA can be closed around the SLBT clamp geometry to enable adhesion measurements at sub-ambient and higher temperatures. This is an important capability for examining the role of polymer viscoelastic relaxations and temperature in adhesion strength. Second, this DMA exhibits a vertical displacement resolution of 10 nanometers. Such resolution will allow the central shaft displacement,  $w_o$ , to be measured with greater accuracy. Third, no known adhesion studies in the literature utilize the DMA for the measurement of adhesion energies.

### **3.3.9 SLBT DMA Experimental Method**

First, the DMA was calibrated to account for the SLBT clamp geometry. The SLBT operates in the penetration clamp geometry and in the controlled force mode. The mass of the drive shaft is calibrated by installing the moveable clamp with the custom crossbar and shaft, and then following the normal TA Instruments calibration procedure. The displacement of the penetration

probe is zeroed and the clamp compliance is calibrated by placing an aluminum disk (no hole) in the sample holder.

Upon calibration, the SLBT was performed. For the ambient experiments, the DMA furnace was not closed. The laboratory temperature and relative humidity were 24-27 °C and 45-60 %, respectively. These experimental conditions were designated “high %RH.” The specimen was mounted polyimide-side down in the sample holder. The shaft was centered within the substrate hole and a 0.01 N static force was applied to bring the probe into contact with the film. Then using the “Ramp Force” segment type, the probe was displaced downward at 0.5 N/min. The 18 N load capacity of this DMA was sufficient to induce the blister growth of all the polyimides. The debond was observed via the borescope until catastrophic failure occurred or the debond grew to the substrate edge.

When testing at temperatures other than ambient, the specimen was mounted polyimide-side down in the sample holder and then the furnace was manually positioned around the SLBT clamp. The borescope and light source were inserted through the holes, and the borescope was aligned. The DMA was programmed to apply a 0.01 N static force, “Equilibrate” at the desired temperature, hold “Isothermal” for 10 minutes, and then “Ramp Force” at 0.5 N/min. During the isothermal step, the furnace temperature stabilized to  $\pm 0.2$  °C. SLBT experiments were performed at 25 °C, 38 °C, and 70 °C. Liquid nitrogen was used to mediate the 25 °C experiment. The %RH in the furnace was measured at each test temperature using a General Eastern Model 800B Humidity Indicator. At 25 °C, where liquid nitrogen was used, the %RH was  $\approx 6.5$  %RH. At 38 °C, liquid nitrogen was not used and the %RH was  $\approx 24$  %RH. At 70 °C, liquid nitrogen was not used and the %RH was  $\approx 3.5$  %RH. These experimental conditions were designated “low %RH.” The isothermal hold time was adjusted slightly for each SLBT temperature depending on the duration of the thermal equilibration step; all samples were conditioned for  $\approx 17$  minutes prior to the “Ramp Force” step. During this 17 minute period, samples are thermally equilibrated but may not have reached an equilibrium moisture content. With respect to the 38 °C and  $\approx 24$  %RH test condition, the DMA drive shaft releases a slow purge of dry air that, when the furnace is closed, fills the furnace cavity. Thus the %RH is lower than the ambient laboratory environment, but is higher than when liquid nitrogen or higher

temperatures are used. After the test ended, the borescope was not removed until the furnace returned to room temperature; thermal shock could damage the borescope components.<sup>15</sup>

### **3.3.10 The Borescope and Blister Analysis**

For the room temperature experiments, an Instrument Technology, Inc., Model 123004 rigid borescope was used to observe the blister growth. Features of this borescope include: 7.6 mm diameter, 50 cm working length, 70° field of view, and forward line of sight with a Rotary Mirror Sleeve for right angle viewing. For the high temperature experiments, an Instrument Technology, Inc., Model 123004 rigid borescope was also used to observe the blister growth. Features of this borescope include: 4 mm diameter, 28 cm working length, 70° field of view, dedicated right angle line of sight, and a heat resistant coating. For each, the borescope is equipped with a light guide which illuminates through the working length. However, due to the reflectiveness of the silicon wafers, an external light source was used to illuminate the background. A color video camera with composite video and s-video connectors attaches directly to the borescope. The composite video and s-video cables were fed to a personal computer and a TV/VCR, respectively. With caution, the borescope with the heat resistant coating can be used at temperatures up to 80 °C.<sup>15</sup> A fiber glass sleeve was also used to protect the borescope during the high temperature experiments. A tripod was used to hold the borescope in a fixed position for all experiments. One shortcoming of this model borescope for use within the SLBT is the 70° field of view. Due to the size constraints of the SLBT clamp geometry in the DMA, the 70° field of view only allows  $\approx$  14 mm of the 25.4 mm diameter silicon wafer to be observed.

To view the blister growth in real-time digitized video, an Integral<sup>®</sup> Technologies, Inc., Flash Bus<sup>™</sup> MV video frame grabber was installed. Throughout each blister experiment, an image was typically saved every 5 seconds. In a few experiments, the blister growth was so rapid that only 1 or 2 images were saved digitally. Fortunately, the blister growth was also recorded using a VCR, so for these experiments the VCR tape was played and an image was saved every 1 second. The video frame grabber was used in conjunction with Vision Gauge<sup>™</sup> software to visually inspect the blister and measure the blister radius. The blister is easily observed since the polyimide films are transparent. Each blister radius was measured five times, and the average radius was recorded. An example of a blister image and the measurement of its radius are shown in Figure 3.9.

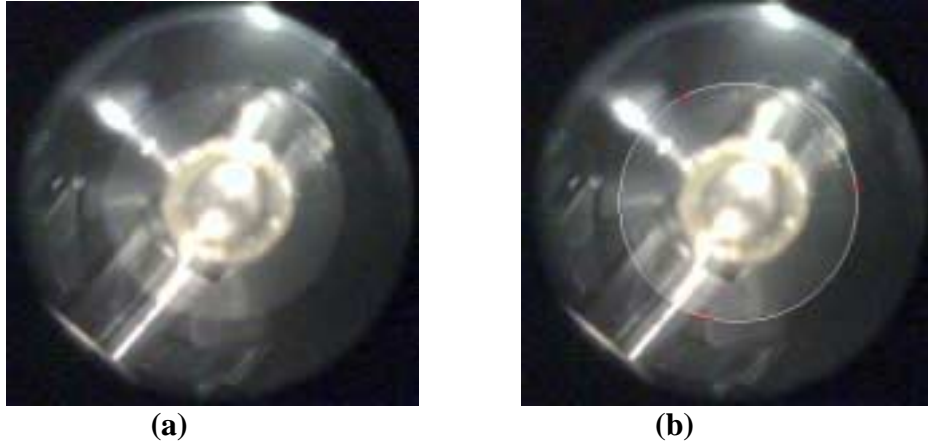


**Figure 3.9. Measurement of blister radius with Vision Gauge™ software. (a) Blister of BPADA/ODA- 2 at 3 minutes. (b) Blister radius at 3 minutes is 4.59 mm.**

The Vision Gauge™ software was calibrated for distance using a glass contact reticle purchased from Edmund Industrial Optics™. The reticle contains concentric circles 0 to 10 mm in diameter and 90° crosshairs. The linear accuracy of the concentric circles is  $\pm 2 \mu\text{m}$  and the line thickness is  $25 \mu\text{m} \pm 13 \mu\text{m}$ . The reticle was placed in the SLBT sample holder and an image of the reticle was taken using each borescope under identical conditions as for all SLBT experiments. From the image of the reticle, the horizontal distance between two cursors was then calibrated to 1 mm using the center-most circle. The curvilinear (negative) distortion, a type of optical aberration, from the borescope lens was then mapped by measuring the diameter of each concentric circle.<sup>15</sup> Curvilinear distortion does not cause the image to deteriorate, rather, the image is focused, but points are out of position.<sup>16</sup> In curvilinear distortion, image points are displaced radially inward toward the center, with the most distant points moving the greatest amount.<sup>16</sup> The curvilinear distortion of the borescope was nonlinear from the center to the edge of the reticle, but it was uniform from left to right, and top to bottom. By plotting the actual diameter versus the measured diameter (Figure 3.10), a correction equation for the distortion was determined by fitting the relationship with a second order polynomial.

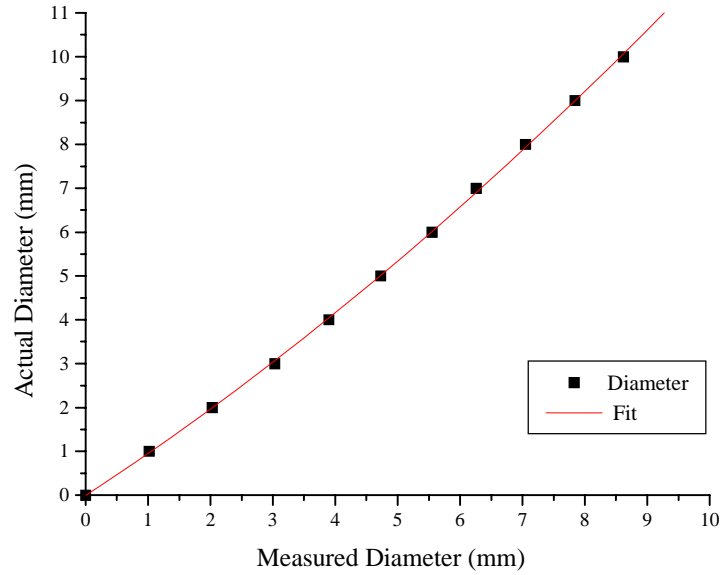


**Figure 3.10. Correction for distortion for the borescope used at room temperature.**

To convert measured blister radii to actual radii distances the correction equation 3.1, obtained from Figure 3.10, was applied:

$$y = -0.01073 + 0.93244x + 0.02755x^2$$

$$R^2 = 0.99975$$

**Equation 3.1**

where  $x$  is the measured radius and  $y$  is the actual radius. For the high temperature experiments, where the right angle dedicated borescope was used, a similar correction for distortion was mapped using the reticle. By plotting the actual diameter versus the measured diameter (Figure 3.11), a correction equation for the distortion was determined by fitting the relationship with a second order polynomial.

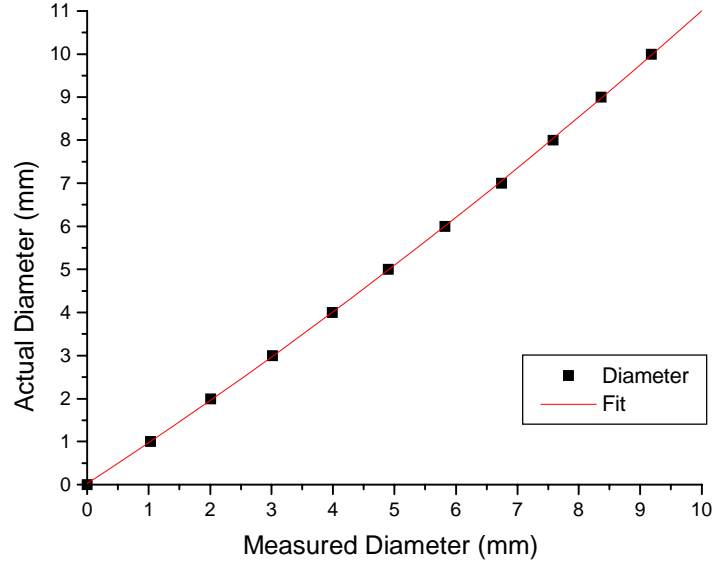


**Figure 3.11. Correction for distortion for the borescope used at high temperatures.**

To convert measured blister radii to actual radii distances the following correction equation 3.2, obtained from Figure 3.11, was applied:

$$y = 0.0284 + 0.92859x + 0.01688x^2$$

$$R^2 = 0.99992$$

**Equation 3.2**

where  $x$  is the measured radius and  $y$  is the actual radius. Comparison of Figure 3.10 and Figure 3.11, indicates that the distortion for the borescope used at high temperatures is not as pronounced, possibly because this scope is right angle dedicated. From the radii, the blister radius growth rate ( $da/dt$ ), and the adhesion energies from the load-based ( $P$  vs.  $a$ ) and the displacement-based ( $w_o$  vs.  $a$ ) equations were determined.

### **3.3.11 Surface analysis- X-Ray Photoelectron Spectroscopy**

XPS spectra of cleaned silicon wafer surfaces and the SLBT failure surfaces were obtained using a Perkin-Elmer Model 5400 XPS spectrometer with a Mg  $K\alpha$  photon source (1253.6 eV) and a hemispherical analyzer. The anode voltage and anode current were 14kV and 25mA,

respectively, and the power was 300 W. The background pressure of the analytical chamber was  $5 \times 10^{-7}$  torr. The spot size was 1 x 3 mm, and the take-off angle of the photoelectrons was  $45^\circ$  with respect to the sample surface. Photoelectron binding energies were referenced from the C-C/C-H carbon peak at 285.0 eV. Typically one spot was examined on each side of failure. A notation of “ND” (not detected) implies that less than 0.5% of that element was detected. Carbon 1s photopeaks were curve-fitted using photopeaks of Gaussian peak shape. The full width at half maximum of the curve-fitted photopeaks was typically 1.5- 1.7 eV.

The silicon wafers were characterized by XPS to determine the effectiveness of the cleaning procedure. Also, to simulate wafer conditions during typical SLBT sample preparation, wafers were examined after storage in purified water for 16 hr, and after exposure to air for 20 min and 135 min. An elemental analysis was performed for the C 1s, O 1s, N 1s, and Si 2p photopeaks. The surface concentrations of these elements for these wafer conditionings are reported in atomic percent in Table 3.3.

**Table 3.3. XPS analysis of silicon wafers.**

Sample	% C	% O	% N	% Si	SiO <sub>2</sub> :Si
Wafer-not clean <sup>a</sup>	35.6	29.1	2.2	32.2	0.3
Wafer-cleaned <sup>b</sup>	10.2	38.2	ND	51.6	0.2
Wafer-cleaned, <sup>b</sup> stored 16 hr water	15.0	40.2	ND	44.8	0.3
Wafer-cleaned, <sup>b</sup> stored 16 hr water, 20 min air	13.7	42.4	ND	43.9	0.3
Wafer-cleaned, <sup>b</sup> stored 16 hr water, 135 min air	13.8	42.7	ND	43.5	0.3

<sup>a</sup> Examined after removal from plastic packaging. Wafer from a different batch than the others tested.

<sup>b</sup> 1:1:5 mixture of H<sub>2</sub>O<sub>2</sub>/NH<sub>4</sub>OH/H<sub>2</sub>O, 90 °C, 1 hour. Rinse with 2 L of H<sub>2</sub>O. 2:5 mixture of H<sub>2</sub>O<sub>2</sub>/H<sub>2</sub>SO<sub>4</sub>, 100 °C for 1 hour. Rinse with 2 L of H<sub>2</sub>O.

Comparison of the unclean and cleaned silicon wafers indicates that the cleaning procedure is effective in substantially reducing the percentage of organic contamination. The reduction lead to an increase in the percentage of oxygen and silicon detected on the cleaned wafer surface. The silicon-to-oxygen ratio for the cleaned wafer is not 1:2, which suggests that the oxide layer on the silicon is thin and elemental silicon below the oxide layer is being detected. Thus during the SLBT, the adhesion energy of polyimide to silicon dioxide, not silicon metal, is measured. The

thickness of the oxide layer was not measured, however, it is thought to be 4-5 Å by comparison with literature values of silicon wafers with similar atomic concentrations.<sup>17</sup>

During SLBT sample preparation, after the silicon wafers were cleaned, they were stored in purified water for different durations because of the 1 hour heating step needed per wafer to remove the NMP from the cast film. For the BPADA/ODA and BPADA/ODA:DoDDA, 50:50 samples, the wafers were stored for  $\approx$  0-6 hr. However, for the BPADA/ODA:DoDDA, 75:25, 25:75, and BPADA/DoDDA samples, the wafers were stored in purified water overnight ( $\approx$  16-22 hr). To determine if storage in water introduced carbon contamination or increased the thickness of the silicon dioxide layer, XPS was performed on a wafer that was cleaned and then stored in water for 16 hr. When the wafer was removed from the water, water was noted to still wet the surface completely. The atomic concentration percentages are presented in Table 3.3. Comparison of the cleaned wafer and the wafer stored for 16 hr indicates that the carbon and oxygen have increased by  $\approx$  5 % and 2 %, respectively, and the silicon has decreased by  $\approx$  7 %. The increase in carbon is probably due to contaminants in the water. The changes in the oxygen and silicon percentages suggest that the oxide layer has grown. To explore this observation, the ratio of silicon in the form of SiO<sub>2</sub> to silicon metal was calculated using the respective peak areas. These values were 0.24 and 0.27-0.33 for the cleaned and stored wafers, respectively. The oxide layer increased in thickness by  $\approx$  3-9 %. While this change is not expected to influence the SLBT adhesion energies, it is important to consider when interpreting the XPS results for the different SLBT silicon wafer failure surfaces.

For the SLBT samples prepared using the patch technique, the cleaned wafers were exposed to air for  $\approx$  20 min during the preheat step prior to the adherence of the patch. To determine the amount of contamination, XPS was performed on two wafers that were cleaned, stored in water for 16 hr, and then exposed to air for 20 minutes or 135 minutes. The atomic concentration percentages are presented in Table 3.3. The amounts of carbon contamination are lower than for the wafer stored for 16 hr with no air exposure, but are slightly higher than the cleaned wafer. These values suggest that air exposure for short times does not cause substantial carbon contamination. The oxygen and silicon percentages further reinforce the notion that the oxide layer has grown because of their storage in water. These results will further aid the locus of failure investigations for the SLBT silicon wafer failure surfaces.

### 3.4 REFERENCES

---

- <sup>1</sup> Kreuz, J.A.; Milligan, S.N.; Sutton, R.F. "Kapton<sup>®</sup> Polyimide Film Advanced Flexible Dielectric Substrates for FPC/TAB Applications," DuPont High Performance Films Technical Paper, March 1994.
- <sup>2</sup> Handbook of Chemistry and Physics, 67<sup>th</sup> Edition, p. E-42.
- <sup>3</sup> Moy, T.M., Ph.D. Dissertation, Virginia Tech, 1993.
- <sup>4</sup> Moy, T.M.; DePorter, C.D.; McGrath, J.E. *Polymer* **1993**, *34*, 819.
- <sup>5</sup> Tan, B., Ph.D. Dissertation, Virginia Tech, 1997.
- <sup>6</sup> Tan, B.; Vasudevan, V.; Lee, Y.J.; Gardner, S.; Davis, R.M.; Bullions, T.; Loos, A.C.; Parvatareddy, H.; Dillard, D.A.; McGrath, J.E.; Cella, J. *J. Polym. Sci. Polym. Chem. Ed.* **1997**, *35*, 2943.
- <sup>7</sup> Farr, I.V.; Glass, T.E.; Ji, Q.; McGrath, J.E. *High Perform. Polym.* **1997**, *9*, 345.
- <sup>8</sup> Farr, I.V., Ph.D. Dissertation, Virginia Tech, 1999.
- <sup>9</sup> Farr, I.V.; Kratzner, D.; Glass, T.E.; Dunson, D.; Ji, Q.; McGrath, J.E. *J. Polym. Sci. Polym. Chem. Ed.* **2000**, *38*, 2840.
- <sup>10</sup> Konas, M.; Moy, T.M.; Rogers, M.E.; Schultz, A.R.; Ward, T.C.; McGrath, J.E. *J. Polym. Sci. Polym. Phys. Ed.* **1995**, *33*, 1429.
- <sup>11</sup> Konas, M.; Moy, T.M.; Rogers, M.E.; Schultz, A.R.; Ward, T.C.; McGrath, J.E. *J. Polym. Sci. Polym. Phys. Ed.* **1995**, *33*, 1441.
- <sup>12</sup> Wu, S. *Polymer Interface and Adhesion*; Marcel Dekker: New York, 1982; pp 178-180.
- <sup>13</sup> Kern, W. *J. Electrochem. Soc.* **1990**, *137*(6), 1887.
- <sup>14</sup> Higashi, G.S. In *The Physics and Chemistry of the SiO<sub>2</sub> and the Si-SiO<sub>2</sub> Interface*; Helms, C.R.; Deal, B.E., Eds.; Plenum Press: New York, 1993; pp 187-197.
- <sup>15</sup> Personal communication with Instrument Technologies, Inc.
- <sup>16</sup> Hecht, E. *Optics*, 2<sup>nd</sup> ed.; Addison-Wesley: Reading, Massachusetts, 1987; pp 220-240.
- <sup>17</sup> DiFelice, R.A., Ph.D. Dissertation, Virginia Tech, 2001.

## **4. AROMATIC POLYIMIDE VISCOELASTIC CHARACTERIZATION**

### **4.1 Introduction**

This investigation begins with an examination of the viscoelastic properties of several fully aromatic polyimides. For each, the temperature and rate dependence of the glass transition is explored by applying the principles of time-temperature superposition to generate a master curve, determining a size-scale for the relaxation by its activation energy, and estimating the scale over which intermolecular forces are being propagated by a cooperativity analysis.

Next, a case study on the influence of moisture on the mechanical and dielectric properties of Kapton<sup>®</sup>-E is presented. The experiments highlight the sub- $T_g$  relaxations and their interactions with moisture by examining their dependence on moisture content, size-scales, and distribution of relaxation times. Finally, an experimental technique is described to investigate the effect of absorbed moisture on the linear coefficient of thermal expansion of Kapton<sup>®</sup>-E.

The two investigations initiate an understanding of the tie between aromatic polyimide chemical structure and time and rate dependent properties. They also provide a standard to which the properties of partially aliphatic polyimides can later be compared.

### **4.2 Viscoelastic characterization of Kapton<sup>®</sup>-E, KB, and PI**

#### **4.2.1 Single Frequency DMA: Single Layer Films**

The storage modulus ( $E'$ ), loss modulus ( $E''$ ), and  $\tan \delta$  DMA responses of Kapton<sup>®</sup>-E and KB are presented in Figure 4.1 and Figure 4.2, respectively. Within the temperature range investigated both polyimides display three viscoelastic dispersions: the  $T_g$  or  $\alpha$  relaxation at high temperatures, and a  $\beta$  and  $\gamma$  relaxation at successively lower temperatures.

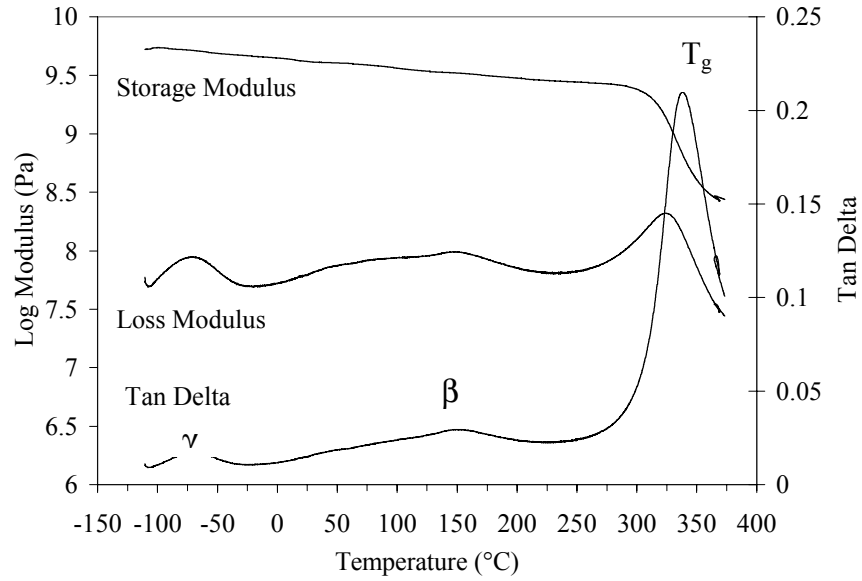


**Figure 4.1. DMA response of Kapton<sup>®</sup>-E at 1 Hz.**

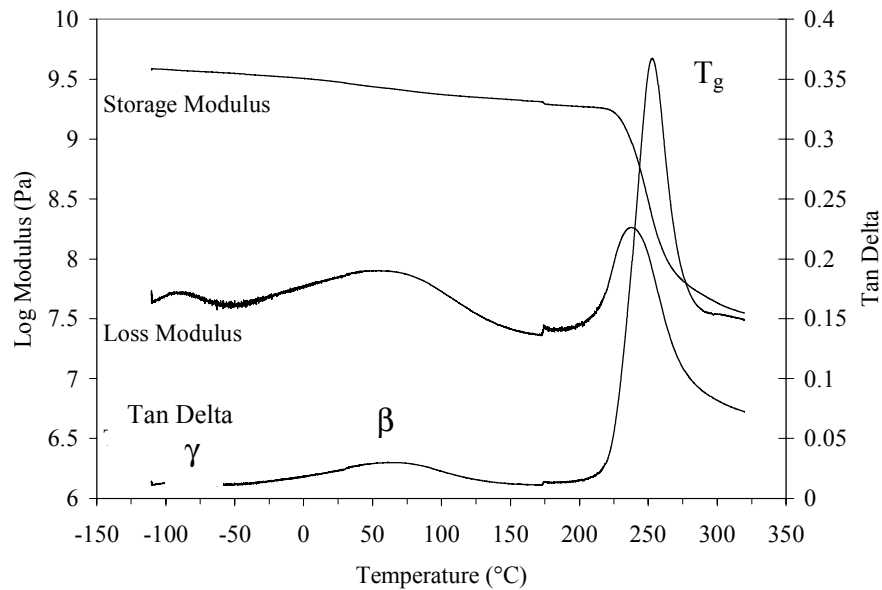


**Figure 4.2. DMA response of KB at 1 Hz.**

For Kapton<sup>®</sup>-E, the tan  $\delta$  peak maxima for the  $T_g$ ,  $\beta$ , and  $\gamma$  relaxations are 337, 147, and -70 °C, respectively. For KB, the tan  $\delta$  peak maxima for the  $T_g$ ,  $\beta$ , and  $\gamma$  relaxations are 252, 61, and -85 °C, respectively. As expected, the  $T_g$  of KB is much lower ( $\approx 84$  °C less) than that of Kapton<sup>®</sup>-E;

the BPADA monomer is considerably more flexible and nonlinear than the PMDA and p-PDA monomers found in Kapton<sup>®</sup>-E. These attributes of KB allow cooperative segmental motions associated with the  $T_g$  to initiate at lower temperatures. In addition, Kapton<sup>®</sup>-E is an oriented film - a high degree of molecular order limits cooperative segmental motions.

Figure 4.1 and Figure 4.2 also show two sub- $T_g$  local viscoelastic relaxations. As discussed in the literature review, polyimides which contain the ODA diamine display a broad sub- $T_g$  relaxation that traverses room temperature; torsional rotation of the phenyl rings within ODA has been identified as the source. Both Kapton<sup>®</sup>-E and KB contain ODA. Thus, a similar underlying molecular motion is assigned to their  $\beta$  relaxations. Also note that the  $\beta$  relaxation of Kapton<sup>®</sup>-E contains a “double peak,” but the  $\beta$  relaxation KB of does not. Fukami et al. have also measured a double peak in the  $\beta$  relaxation of a Kapton<sup>®</sup> film.<sup>1</sup> It is suspected that the orientation<sup>2</sup> of the Kapton<sup>®</sup>-E film may be related to the double peak in the  $\beta$  relaxation, and this point will be addressed later in this chapter.

At even lower temperatures, Kapton<sup>®</sup>-E and KB exhibit a further sub- $T_g$  relaxation, the  $\gamma$  relaxation, at  $-70$  and  $-85$  °C, respectively. For similar aromatic polyimides, this low temperature relaxation has been associated with absorbed moisture. Fukami et al. suggest that differences in the temperature maxima for aromatic polyimides reflects the environment of the absorbed moisture and the strength of hydrogen bonding between the moisture and the dianhydride units.<sup>1</sup> Since Kapton<sup>®</sup>-E is an oriented film and the PMDA dianhydride has a high electron affinity, reflecting strong intermolecular forces, a higher temperature is needed to initiate the  $\gamma$  relaxation than for KB.

#### 4.2.2 Single Frequency DMA: Bilayer Composite Films

The viscoelastic nature of the PI film glass transition temperature was investigated using a “supported film” technique. In tension mode in the DMA, a 20  $\mu\text{m}$  thick the single layer of PI films elongated due to softening as the temperature approached the  $T_g$ . A few degrees above the  $T_g$ , the films would elongate and break. Consequently, complete DMA results could not be obtained, regardless of the frequency, force or oscillation amplitude. By thermally bonding the PI films to either KB or Kapton<sup>®</sup>-E to prepare a “supported film,” PI elongation was prevented and complete single and multi-frequency DMA results could be attained on this composite specimen.

Figure 4.3 shows the DMA response for a KB/PI bilayer. Complete  $E'$ ,  $E''$ , and  $\tan \delta$  peaks are observed through the  $T_g$  of PI. At temperatures beyond the  $T_g$  of PI, the bilayer was also durable enough to allow the measurement of the  $T_g$  of KB.

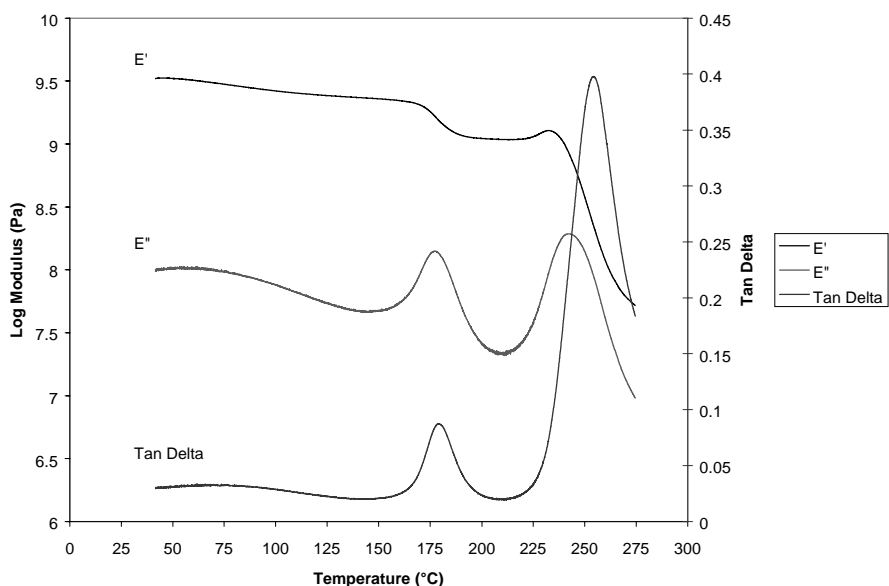


**Figure 4.3. DMA, 1 Hz for KB/PI bilayer.**

Table 4.1 lists the glass transition temperatures for the single layer (neat) KB film and for PI and KB within the bilayer. The glass transition temperature for PI is consistent with the value 179 °C noted from DSC. It appears that the KB layer does not influence the measurement of the  $T_g$  of PI by DMA. This is a significant observation for experimentalists in future investigations. The glass transition temperature values obtained from  $E'$ ,  $E''$ , and  $\tan \delta$  signals for KB in the bilayer correspond well with the values of the neat film (Figure 4.2).

**Table 4.1. Glass transition temperatures for the neat and bilayer films.**

$T_g$ (°C)	Kapton-E	KB	KB/PI Bilayer		Kapton-E/PI Bilayer	
			PI	KB	PI	Kapton-E
$E'$ <sup>a</sup>	323	236	170	239	172	n/a
$E''$ <sup>b</sup>	324	238	177	243	180	n/a
$\tan \delta$ <sup>b</sup>	337	252	179	254	181	n/a

<sup>a</sup> Values obtained from onset of rapid decrease.

<sup>b</sup> Values obtained from peak maximum.

Shown in Figure 4.3, a  $\beta$  relaxation for the bilayer was also observed. The relaxation probably contains contributions from the  $\beta$  relaxations of both PI and KB of the composite film. Also notice that the  $\beta$  relaxation and the  $T_g$  of PI are well-separated. This point is important when  $tT_{sp}$  is later applied to generate a master curve for the  $T_g$  of the PI when it is supported by KB. It is also interesting to note how small the decrease is in the  $E'$  on heating through PI's  $T_g$ , compared to the  $T_g$  of KB. The peaks in PI's  $E''$  and  $\tan \delta$  signals are also smaller in magnitude than for KB. It seems as if the relaxation is attenuated by the presence of KB.

Figure 4.4 shows the DMA response for a Kapton<sup>®</sup>-E/PI bilayer. Since PI begins to degrade around 300 °C, the experiment was terminated once the  $T_g$  of PI was exceeded. Complete  $E'$ ,  $E''$ , and  $\tan \delta$  peaks are observed for PI.

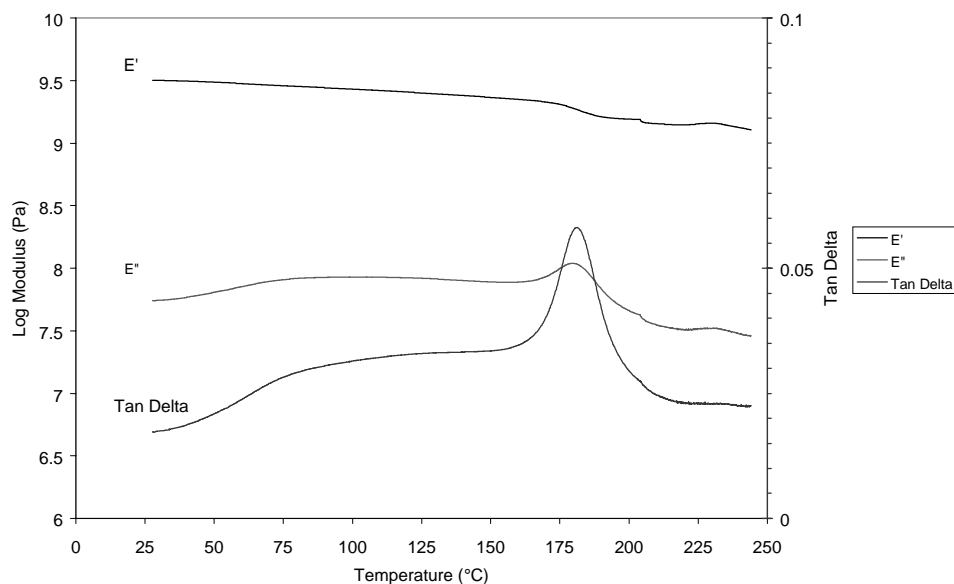


**Figure 4.4. DMA, 1 Hz for Kapton<sup>®</sup>-E/PI bilayer.**

Table 4.1 lists the glass transition temperatures for the single layer (neat) Kapton<sup>®</sup>-E film and for the PI within the bilayer composite. The  $T_g$  of PI is not influenced by the Kapton<sup>®</sup>-E layer, and the magnitude of the PI  $E''$  and  $\tan \delta$  peaks are approximately the same as that observed when supported by KB. This observation supports the conclusion above concerning the utility of the supported bilayer method of DMA experiments. However, there is one significant difference from the KB supported films: the  $\beta$  relaxation of Kapton<sup>®</sup>-E clearly overlaps with the  $T_g$  of the PI. The temperature range of the  $\beta$  relaxation for Kapton<sup>®</sup>-E (Figure 4.1) supports this observation. Due to the overlap in mechanisms,  $tT$ -sp should not be applied to generate a master curve for the  $T_g$  of PI when it is supported by Kapton<sup>®</sup>-E. This conclusion must be applied as a caveat to the supported bilayer composite DMA method in general.

It was anticipated that the sample bonding conditions for the bilayer would cause polymer-polymer interdiffusion across the interface to form an interphase region. For the KB/PI bilayer, no significant DMA relaxation suggesting an interphase region was observed. But since any interphase region would be small and DMA is not very sensitive to weak relaxations, its absence is understandable. Atomic Force Microscopy (TappingMode<sup>™</sup>) was performed in an

attempt to detect an interphase region of a KB/PI bilayer. Figure 4.5 shows a phase image for a 10 x 10- $\mu\text{m}$  region of the KB/PI bilayer.

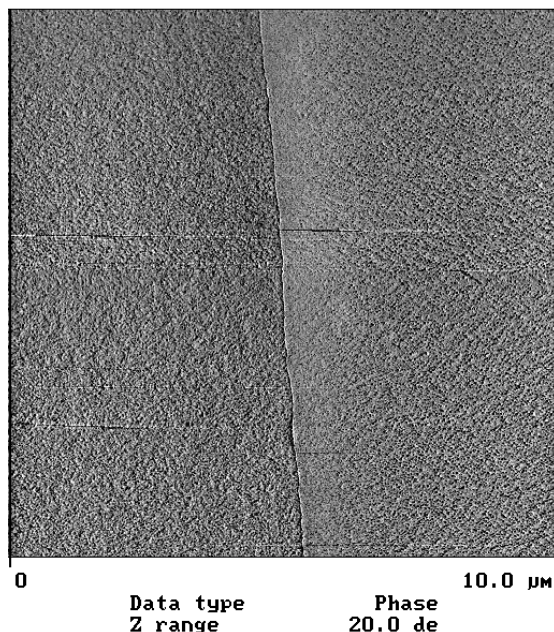


**Figure 4.5. AFM phase image of the KB/PI bilayer. With respect to the “seam” in the center of the image, KB and PI are left/right. Scale is 10 x 10- $\mu\text{m}$ .**

Figure 4.5 shows a clear “seam” where the two films join together; phase differences in the polymer on either side of the seam are not discernable. The corresponding height image (not shown) was also examined for an interphase; over the 20 nm height scale, no features near the seam were identified. The phase and height images may suggest that a true interphase region of finite width was not formed. This is not unlikely because the two polyimides are fully imidized before bonding. Also, the DMA and AFM instruments may lack the resolution to observe such phenomena.

### 4.2.3 Multi-Frequency DMA

#### 4.2.3.1 Introduction

Multi-frequency dynamic mechanical analysis can be used to explore the temperature and rate dependence of the glass transition region. Analysis of the temperature dependence of a

characteristic relaxation time is one of the best ways to study the mechanism of a relaxation and to detect the scale of the interactions involved in the viscoelastic process.<sup>3</sup> From temperature dependence data, one can calculate an activation energy for the relaxation, apply the principles of time-temperature superposition to generate a master curve, and determine the scale over which intermolecular forces are being propagated by a “cooperativity” analysis.

#### **4.2.3.2** *Time-Temperature Superposition (tT-sp)*

Based on the viscoelastic coupling of time and temperature, tT-sp was applied to generate master curves for the glass transition dispersions of Kapton<sup>®</sup>-E, KB, and PI within a KB/PI bilayer. In conjunction with a shift factor plot, the master curve can be used to predict moduli at times or temperatures that cannot be obtained experimentally.<sup>3,4,5</sup> The application of time-temperature superposition is purely empirical, but it allows accurate predictions provided that the isotherms overlap substantially and the shift factor plot is a smooth shape with no singularities.<sup>3</sup> Given such conditions, sound theoretical foundations can be constructed for tT-sp. Singularities within the shift factor plot indicate a change in the mechanism of the relaxation, such as overlap of a  $T_g$  and  $\beta$  relaxation, physical aging or degradation, during which time-temperature superposition is no longer valid.<sup>3</sup> The results for the neat Kapton<sup>®</sup>-E and KB films will be discussed first.

To construct a master curve from the “raw data” isotherms, first a reference temperature was selected. Since the master curves would be for the  $E'$ , the  $T_g$  calculated from the onset of rapid decreases in  $E'$  was chosen as the reference temperature (323 °C for Kapton<sup>®</sup>-E and 240 °C for KB). The isotherms were shifted horizontally along the frequency axis with respect to  $T_{ref}$ , beginning with the isotherms closest to the  $T_{ref}$ , to extend the modulus and construct a composite  $E'$  master curve.<sup>3,5</sup> Figure 4.6 and Figure 4.7 show the master curves and corresponding shift factor plots for Kapton<sup>®</sup>-E and KB, respectively.

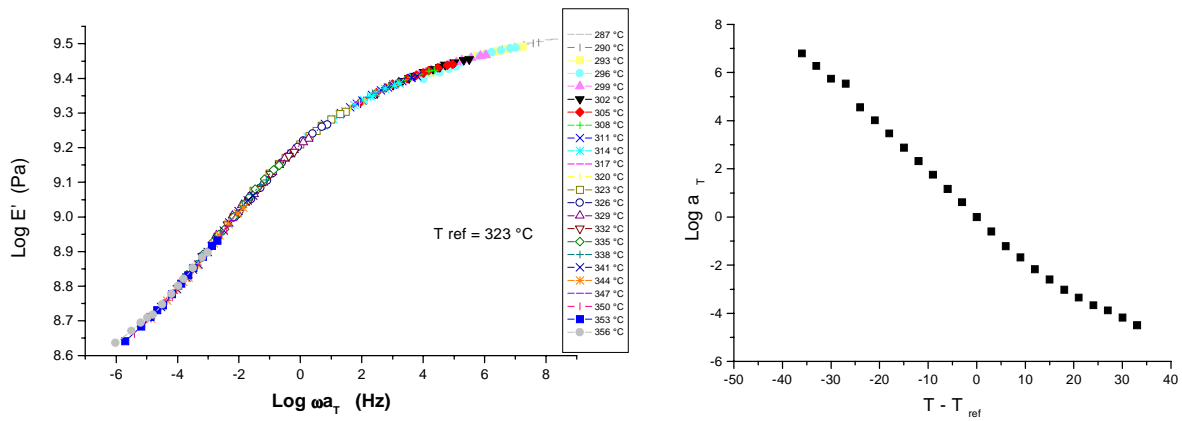


**Figure 4.6. Kapton® -E storage modulus master curve at 323 °C and shift factor plot.**

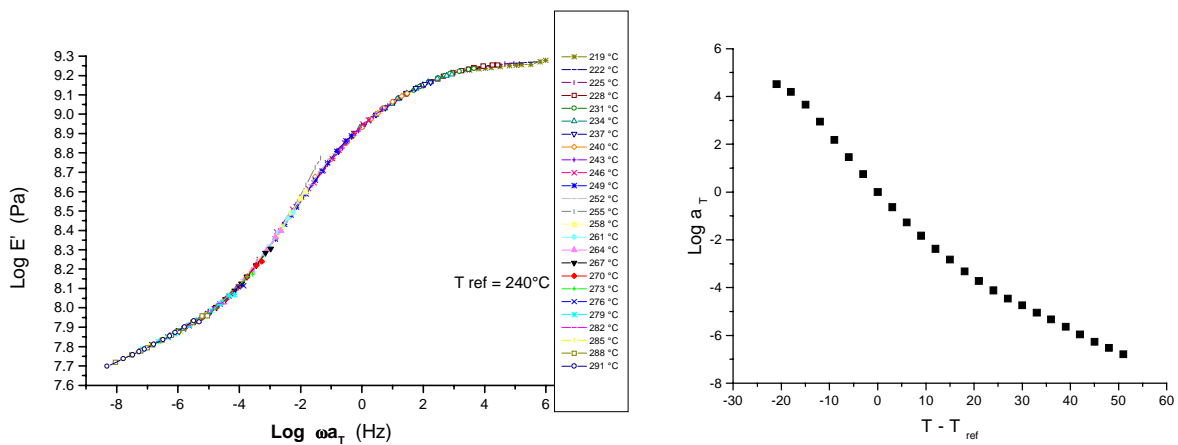


**Figure 4.7. KB storage modulus master curve at 240 °C and shift factor plot.**

The two master curves show a typical polymer response. At high frequencies, the modulus value is on the order of  $10^9$  Pa, which reflects the glassy state of the polymer. The low temperature isotherms ( $T < T_g$ ) comprise this part of the master curve. At low frequencies, the modulus is lower, for KB it is  $10^7$  Pa, which reflects the softening of the polymer as the  $T_g$  is exceeded. The high temperature isotherms ( $T > T_g$ ) comprise this part of the master curve. By executing the experiments over three decades of frequency over a 160 °C temperature range, and applying  $tT$ -sp, the modulus response was predicted for 12 decades of frequency.

The shift factor plots were created by noting the number of units an isotherm was shifted with respect to the reference isotherm in order for it to overlap and extend the modulus curve.<sup>3,5</sup> The shift factor plots both display the smooth shape and slight curvature expected in tT-sp. The equation of the shift factor curve follows the Williams-Landel-Ferry (WLF) equation:<sup>3</sup>

$$\log a_T = \frac{-C_1(T - T_g)}{C_2 + T - T_g} \quad \text{Equation 4.1}$$

where  $a_T$  is the temperature dependent shift factor,  $T$  is temperature,  $T_g$  is the glass transition temperature, and  $C_1$  and  $C_2$  are constants which vary slightly from polymer- to- polymer.<sup>14</sup>  $C_2$  is expressed in °C, however  $C_1$  is dimensionless. The  $C_1$  and  $C_2$  constants can be calculated from a linearized form of the WLF equation:<sup>3</sup>

$$\frac{1}{\log a_T} = \frac{C_2}{C_1(T - T_g)} + \frac{1}{C_1} \quad \text{Equation 4.2}$$

By plotting  $1/\log a_T$  versus  $1/(T - T_g)$ , from the slope and intercept,  $C_1$  and  $C_2$  can be determined. For Kapton<sup>®</sup>-E,  $C_1 = 48.6$  and  $C_2 = 245.7$  °C. For KB,  $C_1 = 17.7$  and  $C_2 = 78.3$  °C. Using the  $C_1$  and  $C_2$  constants for a given polymer, the master curve can be shifted to exhibit the behavior of the polymer at some other temperature. The amount of shift (on a log scale),  $\log a_T$ , is given by the WLF equation, in particular, near the  $T_g$  dispersion.<sup>3</sup>

Supported films as described above were used to explore the viscoelastic nature of the glass transition temperature region of PI films. From the single frequency DMA results, the  $T_g$  of PI supported on KB was accurately measured and interdiffusion across the interface was not detectable by DMA or AFM techniques. tT-sp is valid in regions where there is no overlap in mechanisms either in the temperature or the frequency domain. For tT-sp to be applicable for PI as a supported film, Kapton<sup>®</sup>-E's or KB's  $\beta$  transition cannot overlap with the  $T_g$  of PI in either the temperature or frequency domain. From Figure 4.1 and Figure 4.4, it is clear that the  $\beta$

transition of Kapton<sup>®</sup>-E overlaps with the  $T_g$  of PI. From Figure 4.1 and Figure 4.3, it appears that the  $\beta$  transition of KB does not overlap with the  $T_g$  of PI for a test frequency of 1 Hz. To determine the frequency dependence of the  $\beta$  transition of neat KB, multi-frequency DMA from  $-120$  to  $325$  °C was performed. Figure 4.8 indicates that the  $\beta$  transition of KB (lying  $-60$  to  $160$  °C) does not overlap with the  $T_g$  of PI in the frequency domain of interest.

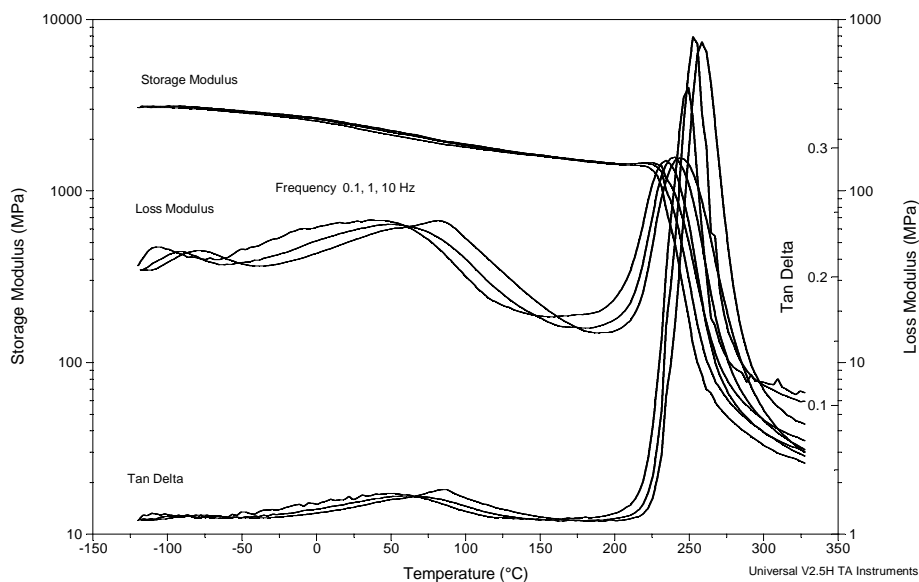


**Figure 4.8. DMA, frequency dependence of the  $\gamma$ ,  $\beta$ , and  $T_g$  relaxations of KB.**

Furthermore, the PI tan delta response measured at several frequencies within the glass transition temperature range (Figure 4.9) does not show any anomalies supporting the proposition that tT-sp is applicable. Thus, a  $E'$  master curve and shift factor plot were constructed for the  $T_g$  of PI (Figure 4.10).

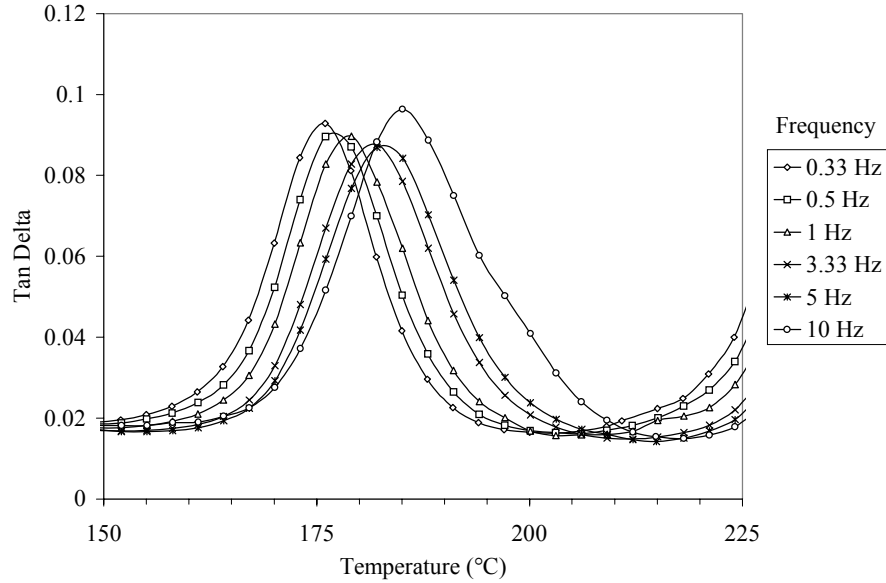


**Figure 4.9. Frequency dependence of the  $T_g$  for PI, within KB/PI bilayer.**

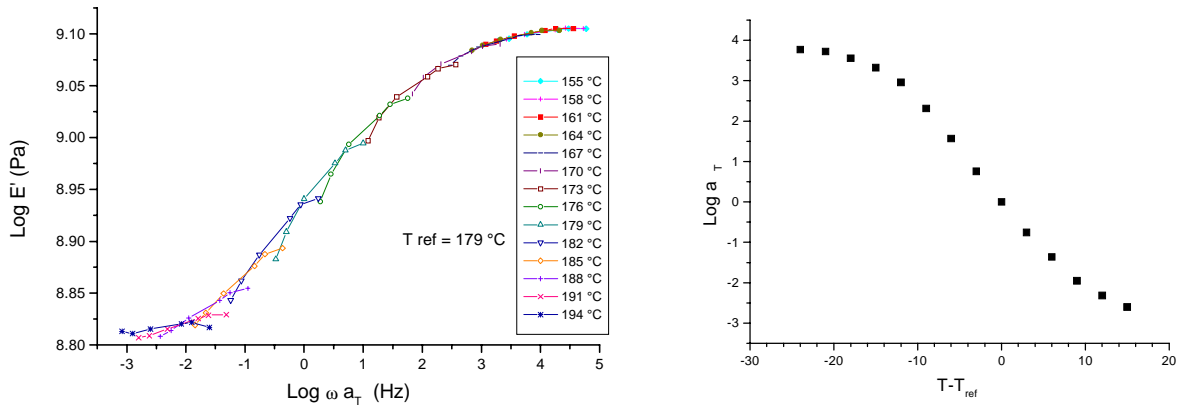


**Figure 4.10. PI storage modulus master curve for 179 °C and shift factor plot.**

The isotherms for PI do not overlap nearly as well as for Kapton<sup>®</sup>-E and KB. Some “tailing” of the isotherms at the high and low frequencies is observed, probably due to the presence of the KB. Due to the small window for analysis, the temperature range of the isotherms was limited and the modulus response could not be predicted over as many decades of frequency. Also, as observed for the  $T_g$  region of PI in the single frequency experiments, the decrease in the modulus through the transition is small, possibly due to constraints imposed by KB. For PI, the WLF

constants  $C_1$  and  $C_2$  were calculated to be 100.3 and 411.5 °C, respectively. These values differ significantly from approximate values of  $C_1 \approx 17$  and  $C_2 \approx 52$  °C for other polymers.<sup>3,4,5</sup> The deviation may arise from constraints from KB and the small window for analysis.

#### 4.2.3.3 Activation Energy

The activation energy of a relaxation depends on internal rotation potential barriers, internal friction, and the volume and environment of the moving repeat unit(s).<sup>3</sup> An activation energy for the glass transition temperature and the sub- $T_g$  relaxations was calculated for Kapton<sup>®</sup>-E, KB, and PI using an Arrhenius analysis.<sup>3,4,5</sup> The low temperature multi-frequency data for Kapton<sup>®</sup>-E are presented in Figure 4.11. Table 4.2 lists the values calculated from DMA measurements.

**Table 4.2. DMA activation energies.**

	Activation Energy (kJ/mol)		
	$\gamma$ Relaxation <sup>a</sup>	$\beta$ Relaxation	$\alpha$ Relaxation ( $T_g$ )
Kapton-E	56.6	n/a	1141.0
KB	33.9	115.5	914.0
PI	n/a	n/a	600.0

<sup>a</sup> Moisture dependent relaxation.

The different magnitudes in the  $E_a$  for the three types of relaxations reflect the sizes of their relaxation volumes. The  $\gamma$  and  $\beta$  relaxations involve small, localized chain motions, whereas the  $T_g$  involves larger scale cooperative segmental motions. Arnold et. Al. report activation energies of  $\approx 130$  kJ/mol for the  $\beta$  transitions of similar aromatic polyimides.<sup>2</sup> The cooperativity analysis indicates that the glass transition for Kapton<sup>®</sup>-E and KB involves highly cooperative motions that are very difficult to thermally activate, thus supporting a high activation energy.

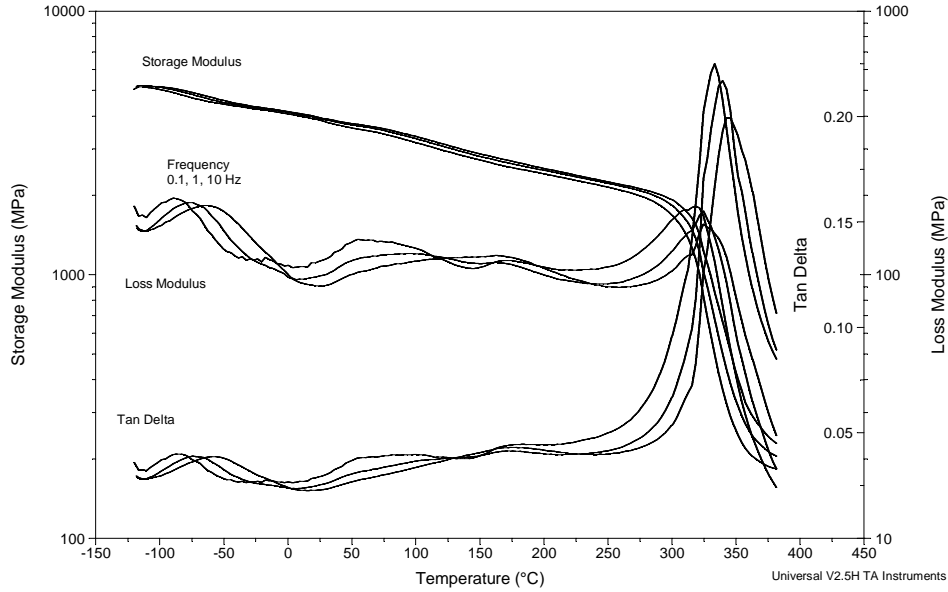


**Figure 4.11. DMA, frequency dependence of the  $\gamma$ ,  $\beta$ , and  $T_g$  of Kapton<sup>®</sup>-E.**

#### 4.2.3.4. Cooperativity Analysis

Due to their viscoelastically heterogeneous and statistical nature, polymers display non-exponential relaxation behavior; that is, they display a distribution of relaxation times. The model chosen to describe the relaxation behavior will depend on the region of the viscoelastic spectrum in question, because each region is governed by a different molecular process. In the glassy region, the KWW (Kohlrausch-Williams-Watts) function often applies. The multi-frequency dynamic mechanical results for Kapton<sup>®</sup>-E, KB, and PI surround the glass transition temperatures, so the KWW function will be used to further quantify their viscoelastic properties. The form of the KWW function is:<sup>6</sup>

$$\phi(t) = \exp(-(t/\tau_o)^\beta) \quad \text{Equation 4.3}$$

$$\beta = 1 - n$$

where  $\phi(t)$  is the distribution function,  $t$  is time,  $\tau_0$  is the characteristic relaxation time, and  $\beta$  is a fit parameter that describes the breadth of the relaxation distribution. The term  $\beta$  is conveniently reduced to  $\beta = (1 - n)$ , where  $n$  is a coupling parameter known as the “cooperativity.”

Cooperativity is a theoretical concept that describes the scale over which intermolecular forces are being propagated in a relaxation event and the strength of coordinated motions among polymer chains needed for the relaxation to occur.<sup>7,8</sup> The KWW equation is one of several equations that may be used to describe cooperativity and the distribution of relaxation times of polymers in the glassy state.<sup>6-9</sup> The value of  $\beta$  can range from 0 to 1. If  $n = 0$ , then  $\beta = 1$ , and an exponential Maxwell decay with one relaxation time occurs, corresponding to a non-cooperative relaxation. For values  $0 < n < 1$ , then  $\beta < 1$ , and a non-exponential decay process with a distribution of relaxations occurs, corresponding to a cooperative relaxation. Thus, as  $n$  increases,  $\beta$  becomes less than 1, and there is increased intermolecular coupling and a broadening of the viscoelastic spectrum.

Although “cooperativity” is associated with a particular model, researchers such as Plazek and Ngai, have applied the theory to a diverse range of polymers and correlated the cooperativity  $n$  to parameters such as chemical structure and morphology by using time-temperature superposition shift factors.<sup>7</sup> The shift factors for Kapton<sup>®</sup>-E, KB, and PI were similarly used to determine their cooperativity,  $n$ , by plotting  $\log a_T$  versus  $(T - T_g)/T_g$ . Figure 4.12 shows an overlay of the shift factors for Kapton<sup>®</sup>-E, KB, and PI.

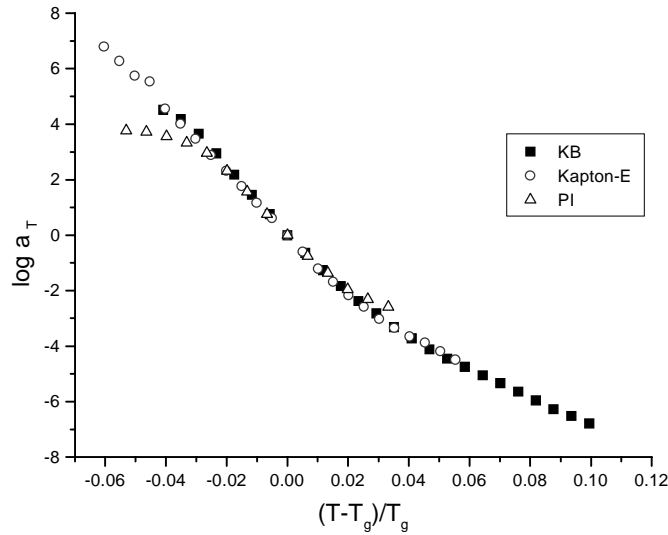


**Figure 4.12. Cooperativity plots for Kapton<sup>®</sup>-E, KB, and PI.**

The normalization of temperature with  $T_g$  will cause the two curves to meet at coordinate (0,0); however, for the whole temperature range, the curves overlap almost completely. Despite their difference in  $T_g$ , the transitions show the same temperature sensitivity and breadth in the relaxation distribution. Their molecular relaxation dispersions are thus similar.

Using a method by Plazek and Ngai, the cooperativity curves for Kapton<sup>®</sup>-E and KB, in Figure 4.12, were fitted to determine the  $n$  parameter.<sup>7</sup> The resulting equation, which resembles the WLF equation, was:<sup>7</sup>

$$(1-n)\log a_T = \frac{-C_1(T-T_g)}{C_2T_g + T - T_g} \quad \text{Equation 4.4}$$

where,  $n$  is the cooperativity parameter,  $a_T$  is the shift factor,  $C_1$  and  $C_2$  are constants obtained by Plazek and Ngai ( $C_1=5.49$  and  $C_2= 0.141$ ),  $T$  is temperature, and  $T_g$  is the glass transition temperature. Figure 4.13 shows the fit of equation 4.4 with the dynamic mechanical shift factor data.

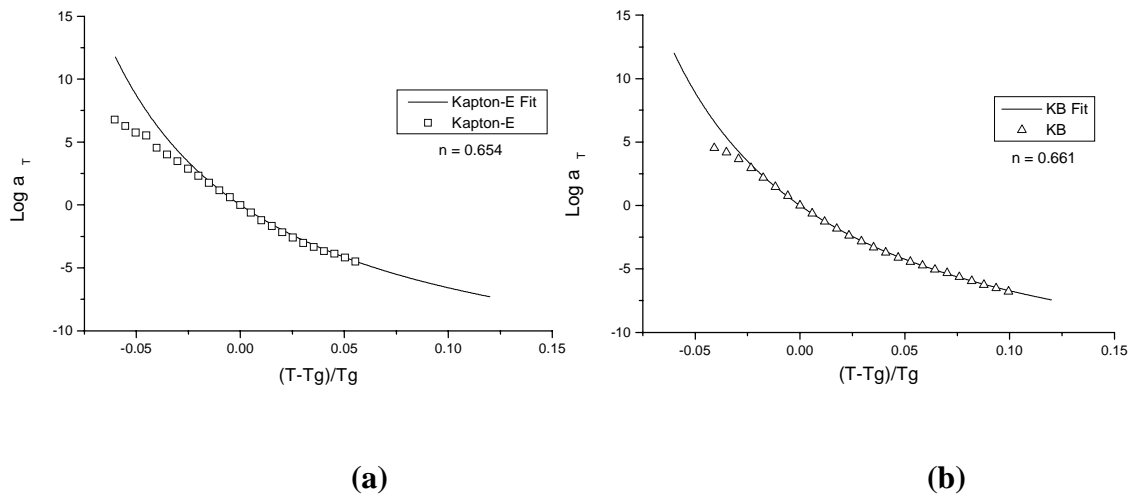


**Figure 4.13. Cooperativity data and fit-line for (a) Kapton<sup>®</sup>-E, and (b) KB.**

The analytical correlation corresponds well for most of the temperature region which allowed the cooperativity for Kapton<sup>®</sup>-E and KB to be obtained as  $n = 0.654$  for Kapton<sup>®</sup>-E and  $n = 0.661$  for KB. The two values are similar and the  $n$  values suggests that highly cooperative motions is involved in the  $T_g$  relaxation. The  $n$  values are comparable to that for an epoxy, a high modulus and crosslinked material. The high  $n$  values support the unusually high  $T_g$  activation energies of Kapton<sup>®</sup>-E and KB. The cooperativity for PI, as shown in Figure 4.12, could not be adequately described using the method of Plazek and Ngai.

#### 4.2.4. Conclusions

Dynamic mechanical analysis has been used to explore the low temperature relaxations and viscoelastic nature of the glass transition temperature for Kapton<sup>®</sup>-E, KB, and a generic polyimide called PI. In the temperature range studied, both Kapton<sup>®</sup>-E and KB exhibited three relaxations, a  $T_g$  and two sub- $T_g$  relaxations. The size scales of these relaxations were interpreted using an Arrhenius activation energy analysis. The sub- $T_g$  relaxations possessed an activation energy on the order of 100 kJ/mol or less, whereas the  $T_g$  relaxations exhibited an activation energy of  $\approx 1000$  kJ/mol. The values indicate that the glass transition is a very difficult process to

thermally activate in these systems. Storage modulus master curves for the  $T_g$  of Kapton<sup>®</sup>-E and KB were generated using  $t-T_{sp}$ .

Using the DMA, PI was characterized as a “supported film” or bilayer composite, of Kapton<sup>®</sup>-E/PI and KB/PI. With this technique, the  $T_g$  of PI is  $\approx 179^\circ\text{C}$  which is consistent with DSC results. Any sub- $T_g$  relaxations in PI could not be detected due to superposition with the sub- $T_g$  relaxations of Kapton<sup>®</sup>-E and KB. The glass transition of PI possessed an activation energy  $\approx 600$  kJ/mol. A storage modulus master curves were constructed for the  $T_g$  of PI, in a KB/PI bilayer, using  $t-T_{sp}$ . The  $E'$  isotherms showed some tailing at the high and low frequencies possibly due to constraints of the supporting film or the small temperature window for analysis. A master curve for PI when supported by Kapton<sup>®</sup>-E could not be generated due to the overlap of the  $T_g$  of PI and the  $\beta$  transition of Kapton<sup>®</sup>-E.

The master curve shift factors for the three polyimides were compared via a cooperativity analysis. All three matched for the experimental temperature range, indicating all three  $T_g$ 's were controlled by similar processes. From the cooperativity analyses, the “cooperativity” parameter,  $n$ , for both Kapton<sup>®</sup>-E and KB was  $\approx 0.66$ .

### **4.3. Effect of moisture on the mechanical and dielectric properties of Kapton<sup>®</sup>-E.**

#### **4.3.1. Introduction**

Polyimides can absorb 3-5 weight percent moisture from ambient atmospheric humidity which can significantly alter their physical properties.<sup>10-15</sup> This tendency to absorb moisture is a drawback when used within a microelectronics device because the moisture increases the dielectric constant of the polyimide, causes film dimension changes, weakens adhesive bonds, and promotes the corrosion of metal components. In this study, the effect of (1) relative humidity on the amount of absorbed moisture, the mechanical and dielectric sub- $T_g$  viscoelastic relaxations, and the tensile modulus of Kapton<sup>®</sup>-E, and (2) absorbed moisture on sample dimensions and the linear coefficient of thermal expansion of Kapton<sup>®</sup>-E, as measured using an in-situ DMA technique, were investigated. Experimental details are presented in Chapter 3.

### 4.3.2. Weight Uptakes

The Kapton<sup>®</sup>-E film samples were conditioned in seven relative humidity (%RH) environments. Figure 4.14 presents the average weight percent moisture absorbed, taken from five samples, versus the %RH. The average values are listed in Table 4.3.

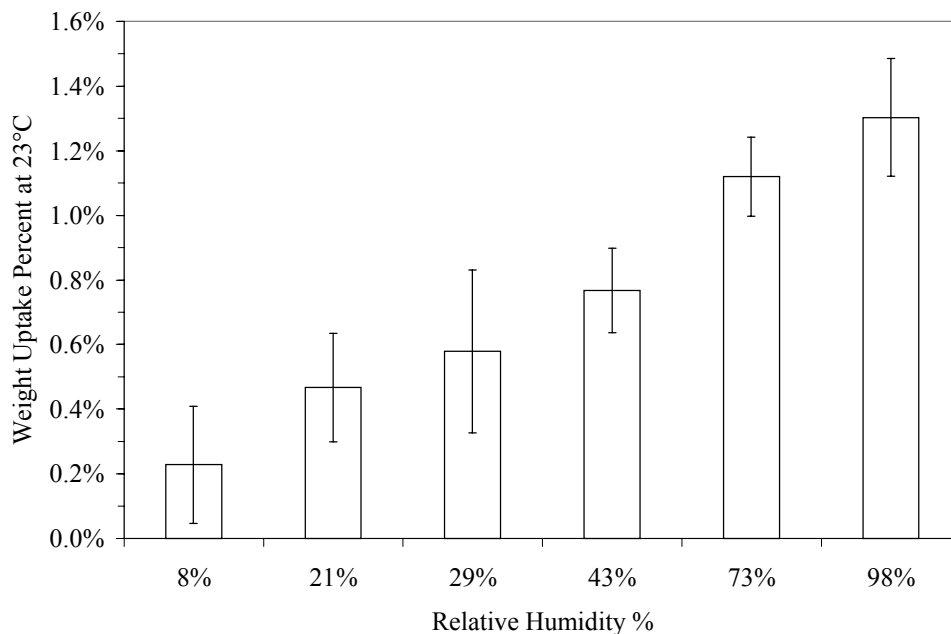


**Figure 4.14. Weight percent uptake of moisture of Kapton<sup>®</sup>-E in different percent relative humidities at 23 °C.**

While the standard deviation causes overlap at the intermediate humidities, Figure 4.14 shows a general increasing trend between the %RH and the average weight uptake percent of moisture. The weight percent moisture absorbed for several of the %RH environments was also measured by thermogravimetric analysis (TGA). The weight % change versus temperature curves are plotted in Figure 4.15. Also included in Figure 4.15 is the weight % change for a sample that had been immersed in a vial of water.

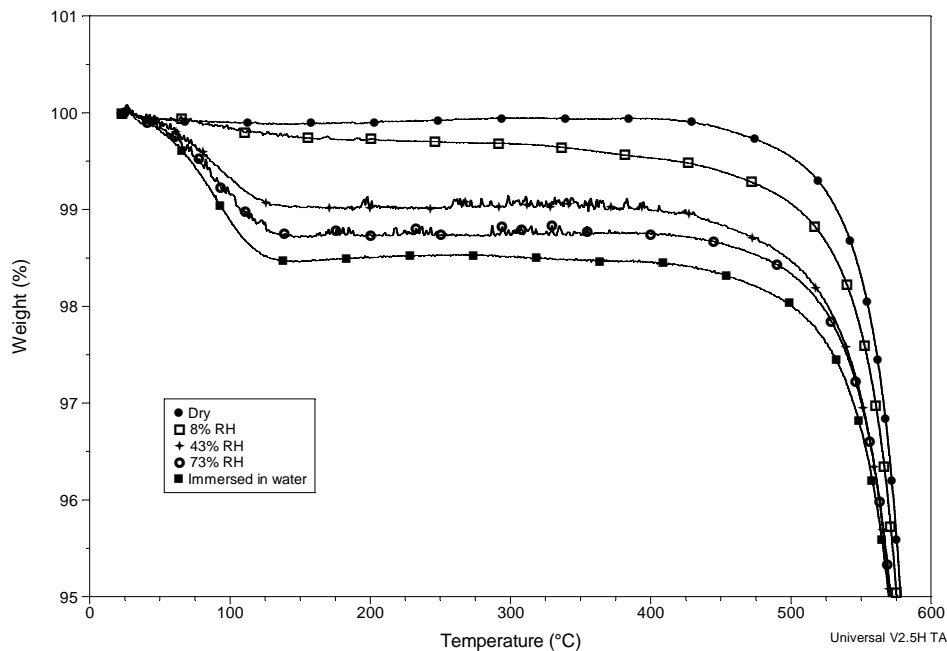


**Figure 4.15. TGA, Weight % loss in air versus temperature of Kapton<sup>®</sup>-E conditioned in different percent relative humidities.**

The TGA curves show that as the temperature increases from 25 °C, the absorbed moisture begins to evaporate immediately. By 150 °C the weight becomes constant since all the moisture has evaporated. At  $\approx$  500 °C, polymer degradation begins. The weight % loss values at 150 °C were used to calculate the % moisture absorbed by the various sample conditionings. These values are compared to the values determined gravimetrically in Table 4.3. The TGA values are based on one measurement. Reasonable correlation between the two is observed.

**Table 4.3. Moisture contents of Kapton<sup>®</sup>-E determined gravimetrically and by TGA.**

RH%	Weight Uptake % <sup>a</sup>	TGA Weight % Loss at 150 °C
Dry	-	0.11
8%	0.23 ± 0.18	0.26
21%	0.47 ± 0.17	-
29%	0.58 ± 0.25	-
43%	0.77 ± 0.13	0.98
73%	1.12 ± 0.12	1.28
98%	1.30 ± 0.18	-
Immersed <sup>b</sup>	-	1.64

<sup>a</sup> Mettler AE2000 microbalance. An average of 5 samples.

<sup>b</sup> 48 hours in water at room temperature, ≈ 25 °C.

### 4.3.3. Dynamic Mechanical Analysis

Dynamic mechanical analysis was used to probe the effect of absorbed moisture on the  $\beta$  relaxation of Kapton<sup>®</sup>-E. Figure 4.16 shows the  $\tan \delta$  response of Kapton<sup>®</sup>-E that had been dried, and then conditioned to 29, 43, 73, and 98 %RH. The  $T_g$  was unaffected by the sample history, and is therefore not shown.

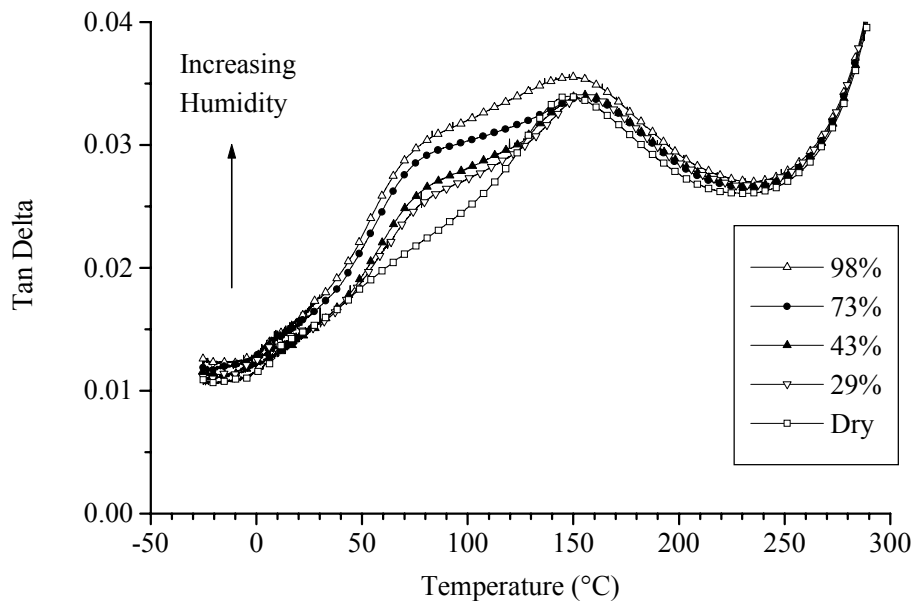


**Figure 4.16. DMA, 1 Hz. Influence of moisture content on the  $\beta$  relaxation of Kapton<sup>®</sup>-E.**

The baselines for all samples are similar and allow for a clear comparison. The  $\beta$  relaxation shows a double peak. The low temperature component,  $\approx 75$  °C, is dependent on the moisture content. The high temperature component,  $\approx 150$  °C, is not dependent on the moisture content, presumably because on heating to this temperature all the absorbed moisture has evaporated. Although the TGA results indicated that by 75 °C some water evaporation had occurred, the remaining water still has a visible enhancement effect on the molecular motion associated with the  $\beta$  relaxation. Due to the change in moisture content as the sample is heated, mechanosorptive<sup>16</sup> effects may contribute to the  $\tan \delta$  response; however, to further comment on such an effect in Kapton<sup>®</sup>-E an investigation regarding the nature of the hydrogen bonding interactions should be performed.

The absorbed moisture also affected the storage modulus, Figure 4.17, over the same temperature range.

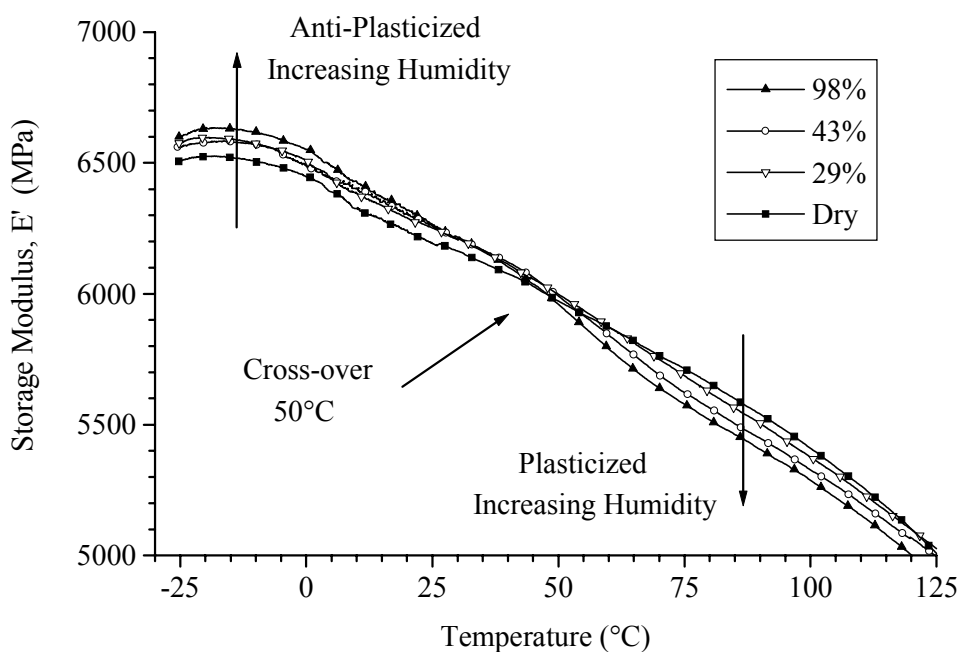


**Figure 4.17. DMA, 1 Hz. Influence of moisture content on the Storage Modulus ( $E'$ ) of Kapton<sup>®</sup>-E.**

A crossover point in the modulus behavior is observed at 50°C. At temperatures below the crossover, as the moisture content increased, the modulus increased. In this temperature range, the moisture caused an antiplasticizer effect. Whereas, at temperatures above the crossover, the opposite trend was detected and a plasticizer effect was noted. The DMA E' curves also indicate that antiplasticizer effect is most pronounced at the lowest experimental test temperature (-25 °C) and becomes less noticeable as the crossover temperature is approached. Similarly, the plasticizer effect is most pronounced for the test temperatures well above the crossover temperature. We suggest that this antiplasticizer effect at low temperatures may be caused by the absorbed water forming mechanically stable bridges between the imide carbonyl groups. As the temperature rises and the motions associated with the  $\beta$  relaxation initiate, these bridges are broken and the absorbed water enhances the relaxation. This is reflected in the crossover to a plasticizer response in the E' and in the increase in the  $\tan \delta$  magnitude relative to the “dry” sample. The concept of mechanically stable bridges formed by absorbed water has been adopted to explain similar antiplasticizer effects in nylon 6,6.<sup>17</sup>

The observations in the  $\tan \delta$  and E' signals are suggested to be related to the processing history of the oriented Kapton<sup>®</sup>-E film. The orientation creates a high degree of molecular order among the aromatic monomers which affords superior physical properties, such as high tensile modulus, high T<sub>g</sub>, and low CTE, relative to many other polymers. The mechanical properties in the plane of the film, that is, in the machine and transverse directions of the film, are particularly improved over unoriented films. Other research on Kapton<sup>®</sup>-H film (DuPont), which is a similar oriented aromatic polyimide film derived from PMDA/ODA, has determined that absorbed water resides at two types of molecular sites in the film.<sup>10,18,19</sup> The water is not strongly bound to the polyimide, rather it exists as isolated molecules or in small clusters dispersed throughout the sample.<sup>10</sup> The relative populations of the two sites is strongly dependent on film morphology, which is traceable to processing history.<sup>10</sup> Further details are provided in the literature review. In the present study on Kapton<sup>®</sup>-E, these literature examples lend credibility to our suggestion that the variations in the  $\tan \delta$  and E' signals as a function of moisture content are related to the processing history, ie. the morphology and orientation of the film.

To examine the effect of Kapton<sup>®</sup>-E film processing history on the  $\beta$  and T<sub>g</sub> relaxations, the following DMA experiments were completed: (1) perform three heating cycles, from -30 °C

to 380 °C, on a sample initially saturated with water, and (2) first condition a sample at 230 °C, 275 °C, 325 °C or 350°C for 45 min, then test in the DMA from –30 °C to 380 °C.

To address the first set of experiments, the  $\tan \delta$  responses of the  $\beta$  relaxation region of a sample initially saturated with water (1<sup>st</sup> heating) and its 2<sup>nd</sup> and 3<sup>rd</sup> heating cycles are presented in Figure 4.18.

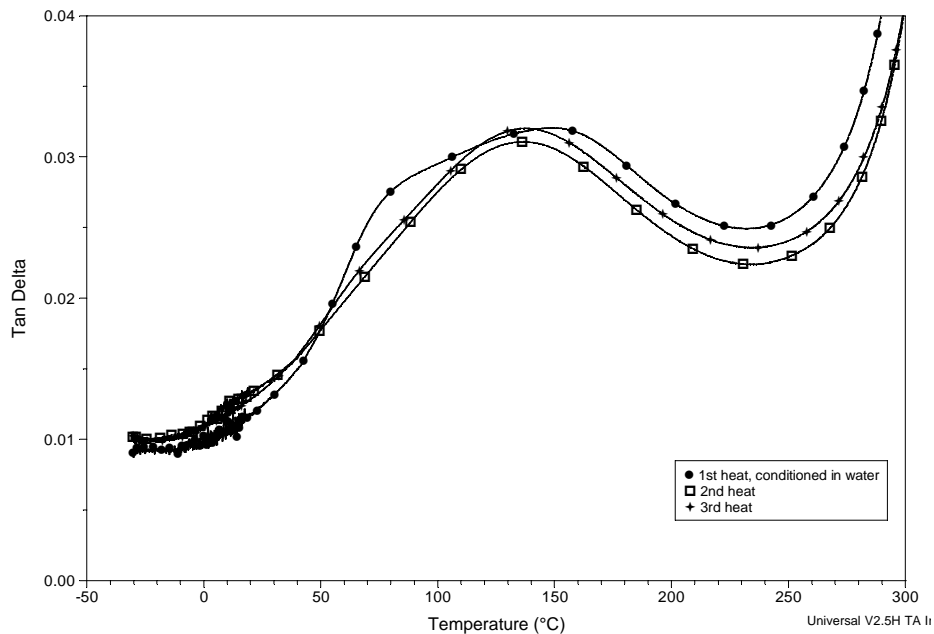


**Figure 4.18. DMA, 1 Hz. Three heating cycles of a Kapton®-E sample initially saturated with water.**

The  $\beta$  relaxation for the 2<sup>nd</sup> and 3<sup>rd</sup> heating cycles exhibit a lower  $\tan \delta$  magnitude than the initial saturated sample. Presumably, this effect arises from the evaporation of water during the first heating cycle. The shape of the  $\beta$  relaxation for the 2<sup>nd</sup> and 3<sup>rd</sup> heating cycles, however, is different from the double peak shape observed for the “dry” sample (Figure 4.16). The shape of the  $\beta$  relaxation is now similar to the  $\beta$  relaxation for KB, Figure 4.2. The  $T_g$ s for the 2<sup>nd</sup> and 3<sup>rd</sup> heating cycles exhibited a slightly lower  $\tan \delta$  value at their peak maximum,  $\approx 0.025$ , and were  $\approx 5$  °C higher. The change in the shape of the  $\beta$  relaxation lead to the second set of experiments, in which a dry sample was first thermally conditioned and then tested in the DMA.

The conditioning temperatures included two temperatures below the  $T_g$  of Kapton<sup>®</sup>-E, 230 and 275 °C, and two temperatures above the  $T_g$ , 325 and 350°C. The  $\tan \delta$  responses within the  $\beta$  relaxation region of an unconditioned sample and the 4 conditioned samples are shown in Figure 4.19.

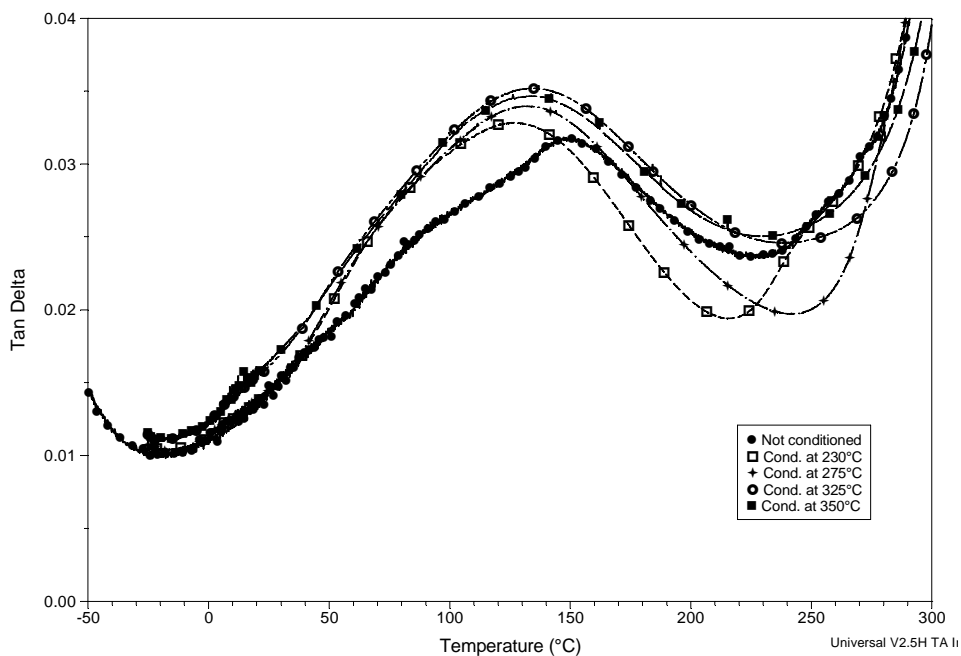


**Figure 4.19. DMA, 1 Hz. Influence of thermal conditioning on the  $\beta$  relaxation of Kapton<sup>®</sup>-E. Plot shows an unconditioned sample and 4 conditioned samples.**

The  $\beta$  relaxation  $\tan \delta$  magnitude for each type thermal conditioning was greater than the unconditioned sample; and as the conditioning temperature increases, the  $\beta$  relaxation broadens slightly on the high temperature-side of the relaxation. Similar to the results presented in Figure 4.18, the “double peak” shape is less apparent. This suggests that the thermal treatment erased some of the sample history related to its processing, which in turn influenced the local motions which give rise to the  $\beta$  relaxation. The  $\tan \delta$  responses for the  $T_g$ s overlapped very well (not presented). With these experiments in mind, it is hypothesized that the enhancement in the  $\beta$  relaxation that was observed for the 29, 43, 73, and 98 %RH environments is related to the processing history of the film. I speculate that if a sample of Kapton<sup>®</sup>-E is first thermally

conditioned near its  $T_g$ , then equilibrated within a %RH environment, and finally tested in the DMA, then there would not be a humidity effect on the  $\beta$  relaxation.

#### 4.3.4 Stress-Strain

The DMA experiments showed subtle effects of humidity on the sub- $T_g$   $\beta$  relaxation. Next, the influence of humidity on a macroscopic property, the tensile modulus, was investigated. Figure 4.20 presents the average tensile modulus, taken from five samples, as a function of % RH. Within the standard deviation, an effect of % moisture absorbed on the tensile modulus cannot be discerned. The average modulus across all samples was  $6186 \pm 85$  MPa. This value is comparable to the value of 750 kpsi, listed in the DuPont Materials Specification for Kapton<sup>®</sup>-E.<sup>20</sup> The average modulus also agrees well with the DMA storage modulus ( $E'$ ) value of  $\approx 6250$  MPa at  $\approx 25$  °C (Figure 4.17). The DMA  $E'$  curves indicate that at 25 °C, the antiplasticizer effect is less noticeable, thus it is not surprising that this effect is not observed in the stress-strain measurements.

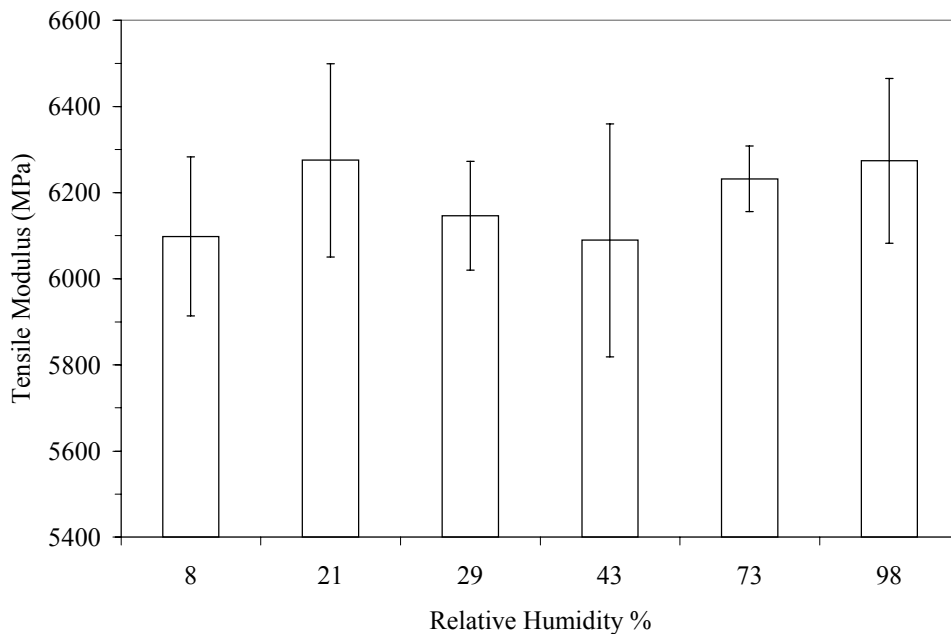


**Figure 4.20. Influence of relative humidity on the tensile modulus of Kapton<sup>®</sup>-E.**

#### 4.3.5 Dielectric Analysis (DEA)

The high frequency capability of dielectric analysis (DEA) allows smaller scale motions within the polymer, such as those associated with absorbed moisture, to be studied in greater detail than possible via DMA. Furthermore, water is a highly polar molecule which aligns easily under an applied electric field. Thus, DEA was appropriate to probe the effect of humidity on the viscoelastic relaxations of Kapton<sup>®</sup>-E. Figure 4.21 presents the  $\tan \delta$  responses for seven % RH environments at a frequency of 1000 Hz. Only the low temperature  $\tan \delta$  response is plotted in Figure 4.21 because the  $T_g$  and  $\beta$  relaxation were not observed due to contributions arising from ionic conductivity.

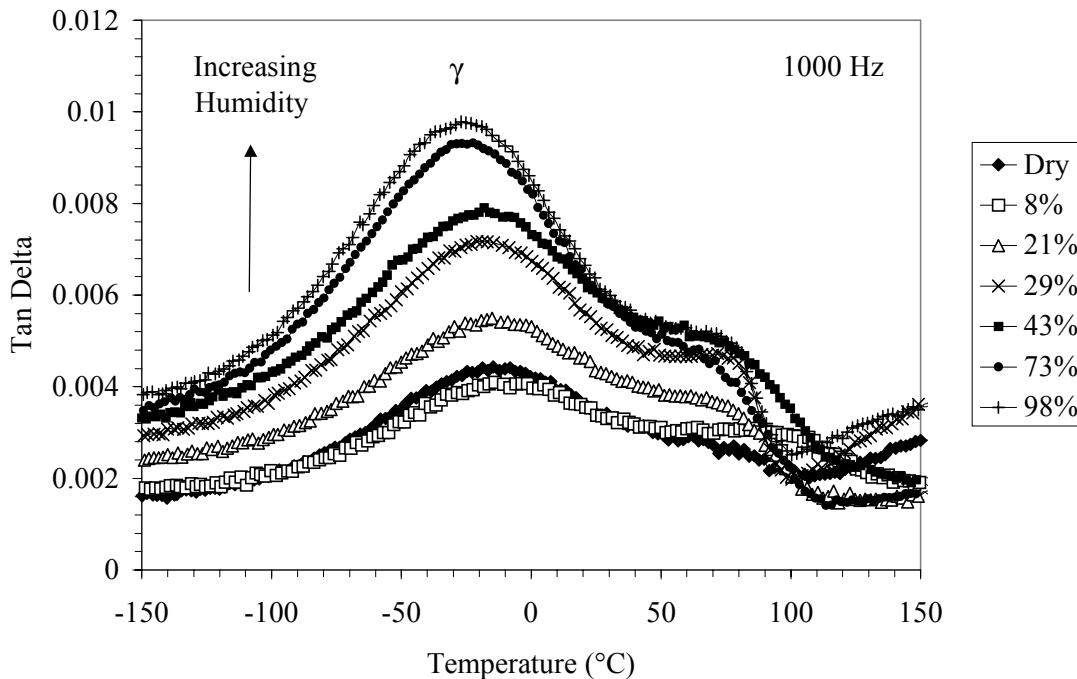


**Figure 4.21. DEA, 1000 Hz. Influence of moisture content on the  $\gamma$  relaxation of Kapton<sup>®</sup>-E.**

A moisture dependent relaxation, which is designated the  $\gamma$  relaxation, spans the temperatures from  $\approx -100$  to  $50$  °C. A shoulder on the  $\gamma$  relaxation from  $\approx 50$  to  $100$  °C exists, but this is possibly due to the evaporation of water as the temperature rises, as shown by TGA (Figure 4.15). The shoulder is not frequency dependent unlike a common viscoelastic relaxation. The sudden drop in the  $\tan \delta$  signal at  $\approx 100$  °C is associated with the evaporation of water. The

magnitude of the  $\gamma$  relaxation increases as the % RH increases. Higher amounts of absorbed moisture result in a larger dipole moment, which is then reflected in the magnitude of the  $\tan \delta$  peak. The temperature of the peak maximum ( $T_{\max}$ ) for  $\gamma$  also slightly shifts to lower temperatures as the % RH increases (Table 4.4).

**Table 4.4.  $T_{\max}$  for the  $\gamma$  component of  $\tan \delta$  at 1000 Hz as a function of % RH.**

%RH	$T_{\max}$ ( $^{\circ}\text{C}$ ) at 1000 Hz
Dry	-18.7
8%	-13.9
21%	-15.1
29%	-20.9
43%	-18.1
73%	-28.7
98%	-27.0

This plasticization effect suggests that as the % RH increases, the absorbed moisture forms clusters that have a greater internal mobility than the moisture that absorbed at low % RH. To further explore this effect, the simple or complex (noncooperative or cooperative) character of the  $\gamma$  relaxation was examined through activation energies determined from Arrhenius and Eyring methods and from its distribution of relaxation times.

#### 4.3.6. Introduction to Activation Energy Calculations

In contrast to the  $T_g$ , the temperature dependence of the mechanical or dielectric relaxation times of a sub- $T_g$  relaxation is adequately described by the Arrhenius equation. As a consequence the activation energies for secondary relaxations are typically temperature independent.<sup>21</sup> The activation energy of a relaxation can also be evaluated using Eyring's theory of absolute reaction rates in which enthalpic and entropic contributions can be determined.<sup>22</sup> Secondary relaxations often have activation entropies close to zero, thus categorizing them as simple, noncooperative relaxations.<sup>22</sup> The motions involved are localized and independent of one another. For relaxations with increasingly positive activation entropies, more cooperative, complex motions are involved.<sup>22</sup> Upon implementing the Arrhenius or Eyring methods, glass

transitions display large enthalpic energies and large, positive activation entropies. These values are often higher than the strength of a primary chemical bond; thus, it is often difficult to assign exact physical meanings.<sup>22,23</sup> The activation energy is then referred to as *apparent*.

The activation energy of the  $\gamma$  relaxation for each humidity was calculated using the Arrhenius equation and Eyring's theory of absolute reaction rates. To begin, Figure 4.22 presents the frequency dependence of the  $\tan \delta$  signal for the  $\gamma$  transition of Kapton<sup>®</sup>-E conditioned at 98 % RH.

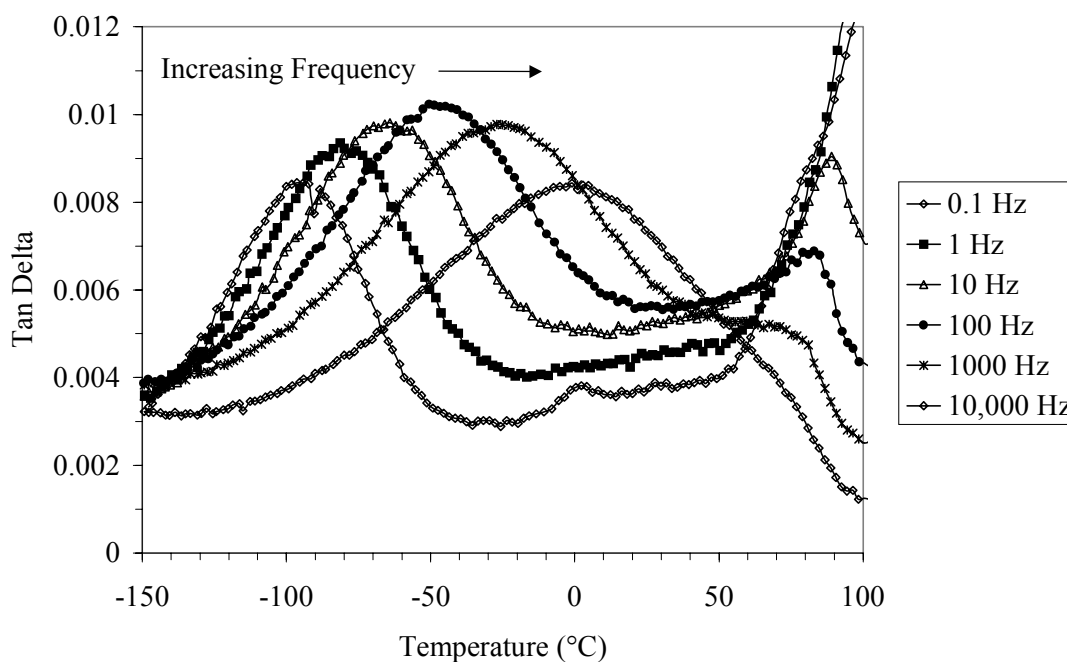


**Figure 4.22. DEA, 1<sup>st</sup> Heating. Frequency dependence of the  $\gamma$  relaxation of Kapton<sup>®</sup>-E conditioned at 98 %RH.**

As the frequency increases, the relaxation shifts to higher temperatures. Similar plots were generated for the 8%, 21%, 30%, 43%, and 73% RH samples. A coordinate pair ( $T_{\max}$ , frequency) was formed for each of the  $\tan \delta$  curves. These values are summarized in Table 4.5.

**Table 4.5. Coordinate pairs for activation energy calculations.**

Freq (Hz)	DEA, $\gamma$ Tan Delta $T_{\max}$ (°C)					
	8% RH	21% RH	29% RH	43% RH	73% RH	98% RH
0.1	-82.5	-83.8	-87.4	-89.6	-93.0	-96.4
1	-66.8	-72.5	-71.9	-76.4	-81.6	-81.3
10	-52.6	-57.9	-61.7	-56.8	-65.2	-69.8
100	-38.6	-35.7	-35.5	-39.7	-51.0	-50.5
1000	-13.9	-15.1	-20.9	-18.1	-28.7	-27.0
10000	20.8	10.0	10.4	2.1	0.4	-7.3
100000				33.1	29.1	18.4

#### 4.3.6.1. Arrhenius Activation Energy

Convenient forms of the Arrhenius equation are described in the following equations.<sup>24</sup>

$$f = \frac{kT}{h} \exp\left(\frac{-\Delta G}{RT}\right) \quad \text{Equation 4.5}$$

$$f = \frac{kT}{h} \exp\left(\frac{\Delta S}{R}\right) \exp\left(\frac{-\Delta H}{RT}\right) = f_0 \exp\left(\frac{-\Delta H}{RT}\right) \quad \text{Equation 4.6}$$

$$f = f_0 \exp\left(\frac{-E_a}{RT}\right) \quad \text{Equation 4.7}$$

$$\ln f - \ln f_0 = \frac{-E_a}{RT} \quad \text{Equation 4.8}$$

$$E_a = -2.303 \times \text{slope} \times R \quad \text{Equation 4.9}$$

$f$  = frequency  
 $f_0$  = pre-exponential factor  
 $h$  = Planck's constant  
 $k$  = Boltzmann's constant  
 $T$  = Temperature (Kelvin)

$\Delta G$  = activation free energy  
 $\Delta H = E_a$  = activation enthalpy  
 $\Delta S$  = activation entropy  
 $R$  = gas constant (8.314 J/mol-K)

Using the values from Table 4.5, log frequency versus  $1/T_{\max}$  (Kelvin<sup>-1</sup>) was plotted according to equation 4.8 for each humidity. Figure 4.23 displays the log frequency versus reciprocal temperature coordinates and their respective linear regressions.

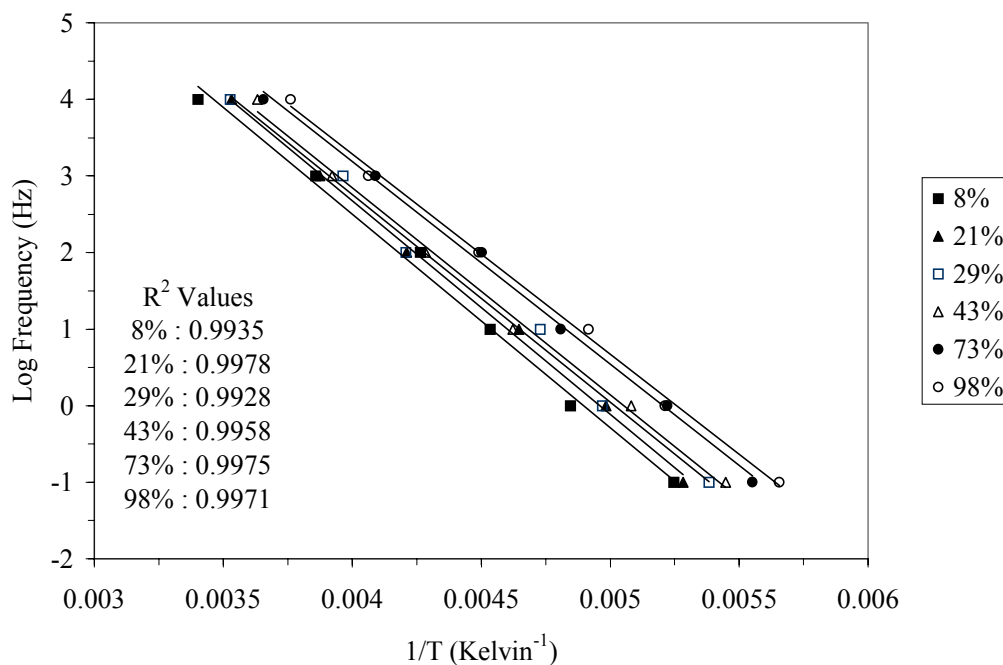


**Figure 4.23. Arrhenius activation energy plot for the  $\gamma$  relaxation of Kapton<sup>®</sup>-E as a function of % RH.**

From the slopes, the Arrhenius activation energies were calculated according to equation 4.9, and these values are listed in Table 4.6.

**Table 4.6. Arrhenius activation energies for the  $\gamma$  relaxation of Kapton<sup>®</sup>-E.**

%RH	Arrhenius $E_a$ (kJ/mol)
8%	53.5
21%	53.5
29%	51.9
43%	52.7
73%	50.6
98%	51.2

The activation energies show a general decrease as the water concentration increases. The magnitude of the activation energies is in the kJ/mol range of simple, noncooperative relaxations. The statistical  $R^2$  values indicate that the data are adequately predicted by the Arrhenius equation and the relaxation strength is independent of temperature.

#### 4.3.6.2. Starkweather-Eyring Activation Energy

The activation energies of the  $\gamma$  relaxations were also calculated using an approach developed by Starkweather, based on Eyring's theory of absolute reaction rates:<sup>25,26,27</sup>

$$f = \frac{kT}{2\pi h} \exp\left(\frac{-\Delta H}{RT}\right) \exp\left(\frac{\Delta S}{R}\right) \quad \text{Equation 4.10}$$

where the variables have the same assignment as described earlier. The activation enthalpy  $\Delta H$  is related to the Arrhenius activation energy,  $E_a$ , by:

$$E_a = \Delta H + RT \quad \text{Equation 4.11}$$

it then follows that:

$$E_a = RT \left[ 1 + \ln\left(\frac{k}{2\pi h}\right) + \ln\left(\frac{T}{f}\right) \right] + T\Delta S$$

at 1 Hz,  $\Delta S \approx 0$ , thus the equation simplifies to :

$$E_a = RT' [\ln T' + 22.922] \quad \text{Equation 4.12}$$

where in the simplified equation form,  $T'$  is the temperature of the maximum of the  $\tan \delta$  at a frequency of 1 Hz. The coordinate pairs ( $T_{\max}$ , 1 Hz) listed in Table 4.5 were substituted into the simplified Equation 4.12. Table 4.7 lists the calculated Starkweather-Eyring activation energies.

**Table 4.7. Starkweather-Eyring Activation Energies.**

% RH	E <sub>a</sub> (kJ/mol)
8%	48.5
21%	47.1
29%	47.2
43%	46.1
73%	44.9
98%	44.9

As the humidity or moisture content increases, the activation energy for the  $\gamma$  relaxation decreases by  $\approx 3.5$  kJ/mol over the range of samples. The Starkweather-Eyring energy for each humidity is lower than the corresponding Arrhenius energy. The deviation between the two represents  $T\Delta S$ . Since the deviation is small,  $\approx 5$  kJ/mol, this suggests that the entropic contribution is close to zero and that the relaxation simple and noncooperative.<sup>25</sup>

#### 4.3.6.3. Relaxation Distribution

To analyze the distribution of relaxation times from the experimental data for the  $\gamma$  relaxation of Kapton<sup>®</sup>-E, a method outlined by Starkweather was followed.<sup>27</sup> This method of analysis for secondary relaxations has been employed by several other researchers<sup>28,29</sup> and the derivations of the equations can be found in textbooks on viscoelasticity.<sup>30,31</sup>

First it is considered that  $\Phi(\ln \tau)d \ln \tau$  is the fraction of the relaxation process having relaxation times between  $\ln \tau$  and  $(\ln \tau + d \ln \tau)$ .<sup>27</sup> Thus, by normalization:

$$\int_{-\infty}^{\infty} \Phi(\ln \tau) d \ln \tau = 1$$

**Equation 4.13**

In a dielectric experiment, the permittivity  $\epsilon'$  and loss factor  $\epsilon''$  are:<sup>27</sup>

$$\varepsilon'(\omega) = \varepsilon_U + (\varepsilon_R - \varepsilon_U) \int_{-\infty}^{\infty} \frac{\Phi_{\varepsilon}(\ln \tau) d \ln \tau}{1 + \omega^2 \tau^2} \quad \text{Equation 4.14}$$

$$\varepsilon''(\omega) = (\varepsilon_R - \varepsilon_U) \int_{-\infty}^{\infty} \frac{\Phi_{\varepsilon}(\ln \tau) \omega \tau d \ln \tau}{1 + \omega^2 \tau^2} \quad \text{Equation 4.15}$$

$\varepsilon_U$  = unrelaxed dielectric modulus ( $\omega \rightarrow \infty$ )

$\varepsilon_R$  = relaxed dielectric modulus ( $\omega \rightarrow 0$ )

$\omega$  = frequency

$\tau$  = relaxation time

The expressions for  $\varepsilon'$  and  $\varepsilon''$  can be approximated to obtain the relaxation distribution from experimental data.<sup>27</sup>

$$\Phi_{\varepsilon}(1/\omega) = \frac{2 \varepsilon''(\omega)}{\pi (\varepsilon_U - \varepsilon_R)} \quad \text{Equation 4.16}$$

The factor  $2/\pi (\varepsilon_U - \varepsilon_R)$  in Equation 4.16 is essentially a normalization factor to create a dimensionless distribution. The distribution thus describes how  $\varepsilon''(\omega)$  changes with temperature and frequency.

To determine  $\varepsilon_R$  and  $\varepsilon_U$  from the experimental data for use in Equation 4.16, Argand diagrams (obtained from plotting the loss factor,  $\varepsilon''$ , versus permittivity,  $\varepsilon'$ ) were constructed for isotherms in 10 °C increments within the  $\gamma$  relaxation temperature region for each humidity.<sup>30</sup> Figure 4.24, Figure 4.26, Figure 4.28, and Figure 4.30 display the Argand diagrams for 98, 73, 43, and 30 %RH. Data for the dry, 8%, and 21% humidities exhibited ionic conductivity - Argand diagrams could not be made with accuracy. The Argand diagrams for 98, 73, 43, and 30 %RH are symmetric in shape for the  $\gamma$  relaxation; this feature is consistent with highly localized, noncooperative motions. Each point of the Argand diagram corresponds to one frequency, thus to generate a complete diagram, data spanning wide ranges of frequencies are necessary. DEA is capable of measuring the dielectric response over a sufficient frequency range for this purpose.

The points where the arc intersect the permittivity represent  $\epsilon_U$  and  $\epsilon_R$  respectively (left to right) - their difference,  $\Delta\epsilon$ , is called the oscillator strength. The oscillator strength,  $\Delta\epsilon$ , was calculated from the experimental data for each temperature isotherm for each humidity by fitting the Havriliak-Negami expression to the data using *Mathematica*.<sup>30</sup> Once  $\Delta\epsilon$  was obtained, for each combination of temperature and frequency of the  $\epsilon''(\omega)$ , the relaxation distribution  $\Phi$  (Equation 4.16) could be plotted versus  $\Delta H$  (ie.  $E_a$ , Equation 4.12). For  $\Delta H$ , temperatures characterizing the entire loss factor, not just the temperature of the peak maximum, were used. Figure 4.25, Figure 4.27, Figure 4.29, and Figure 4.31 display the distribution for the various relative humidity cases. The data form a common pattern for part of the enthalpy range, indicative of a simple and noncooperative relaxation for this range and  $\Delta S \approx 0$ . The maxima represent concentrations of relaxation processes for that enthalpy region.<sup>31</sup> This result supports the Arrhenius and Starkweather-Eyring activation energy calculations. Regions where deviations occur suggest error in the experiment or failure of the theory to accurately describe the behavior.

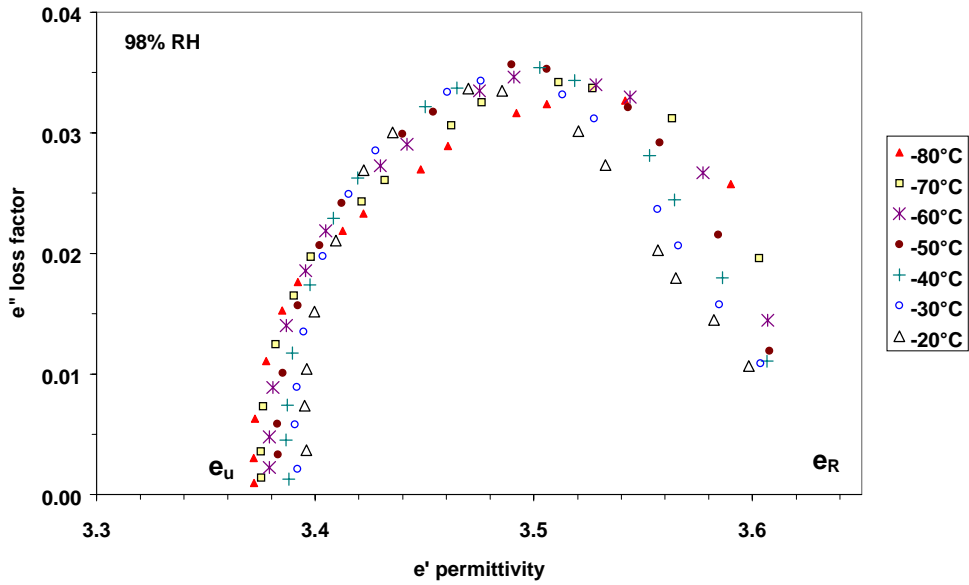


Figure 4.24. Argand diagram, Kapton<sup>®</sup>-E 98 %RH  $\gamma$  relaxation.

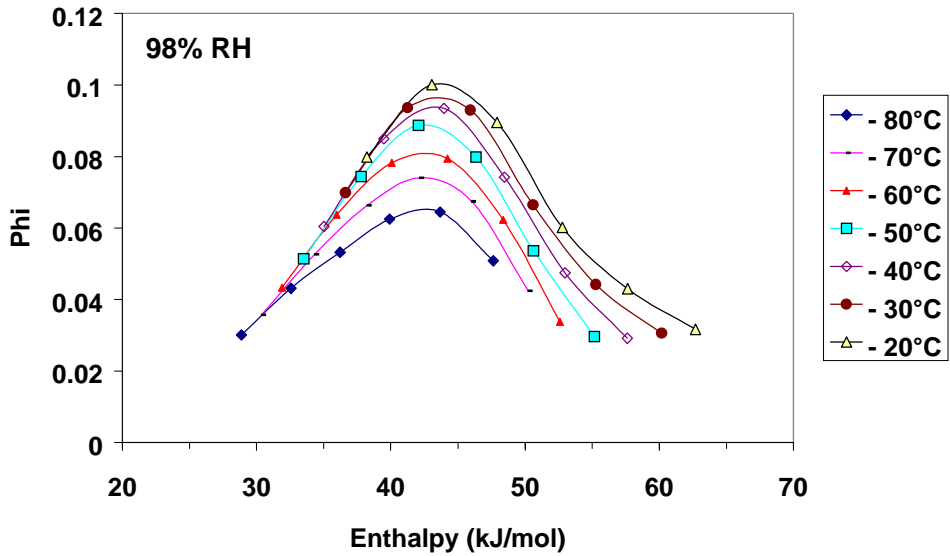


Figure 4.25. Relaxation distribution, Kapton<sup>®</sup>-E 98 %RH  $\gamma$  relaxation.

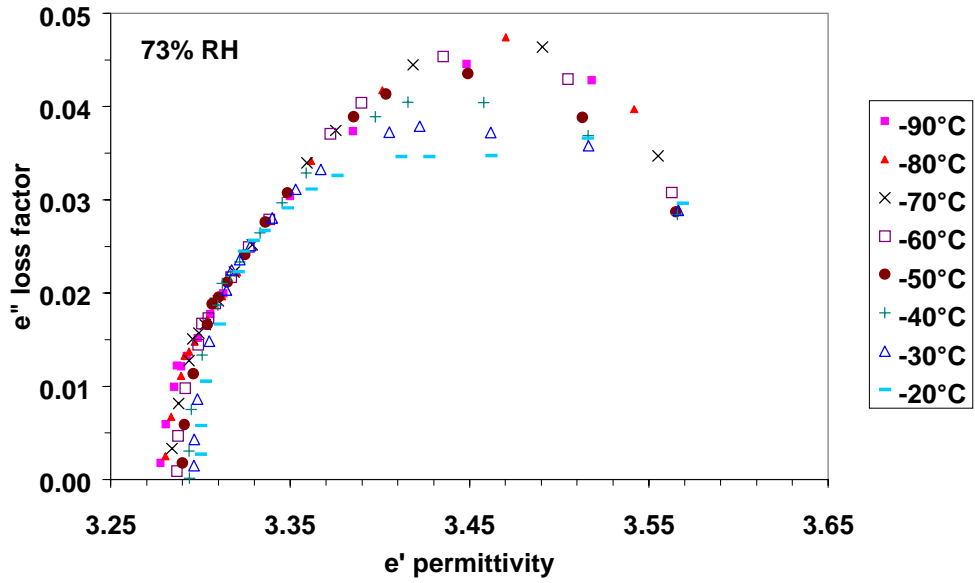


Figure 4.26. Argand diagram, Kapton<sup>®</sup>-E 73 %RH  $\gamma$  relaxation.

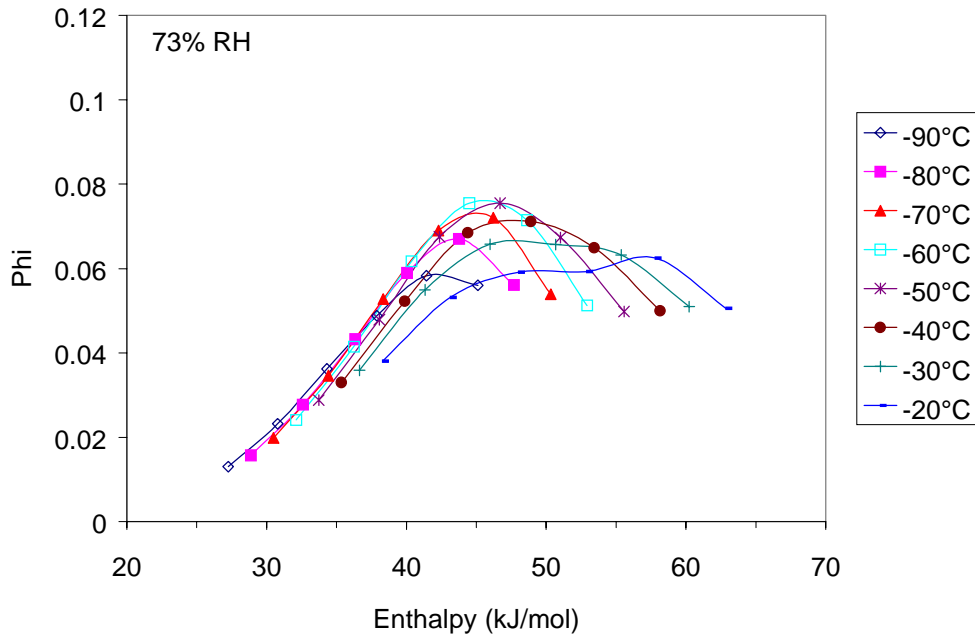


Figure 4.27. Relaxation distribution, Kapton<sup>®</sup>-E 73 %RH  $\gamma$  relaxation

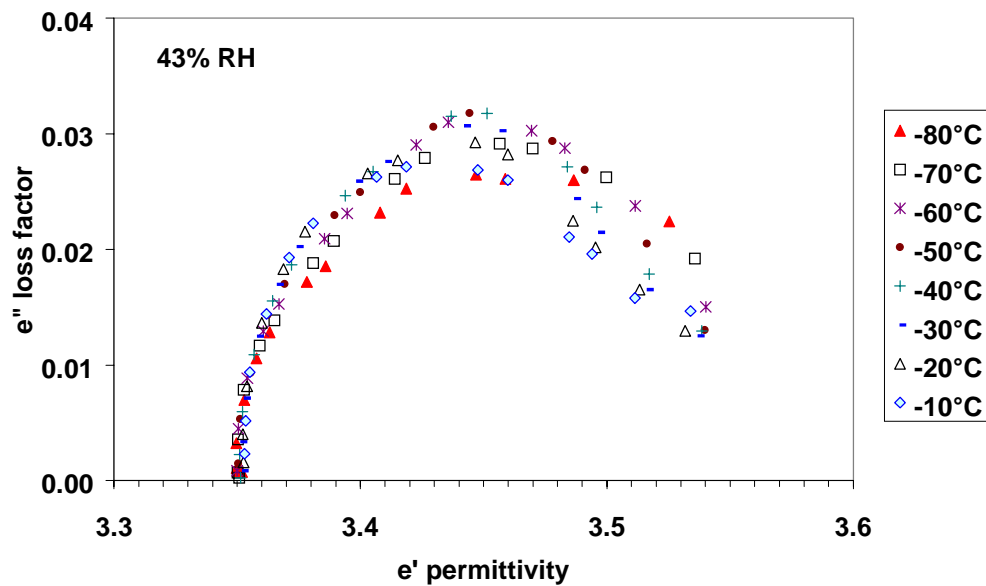


Figure 4.28. Argand diagram, Kapton<sup>®</sup>-E 43 %RH  $\gamma$  relaxation

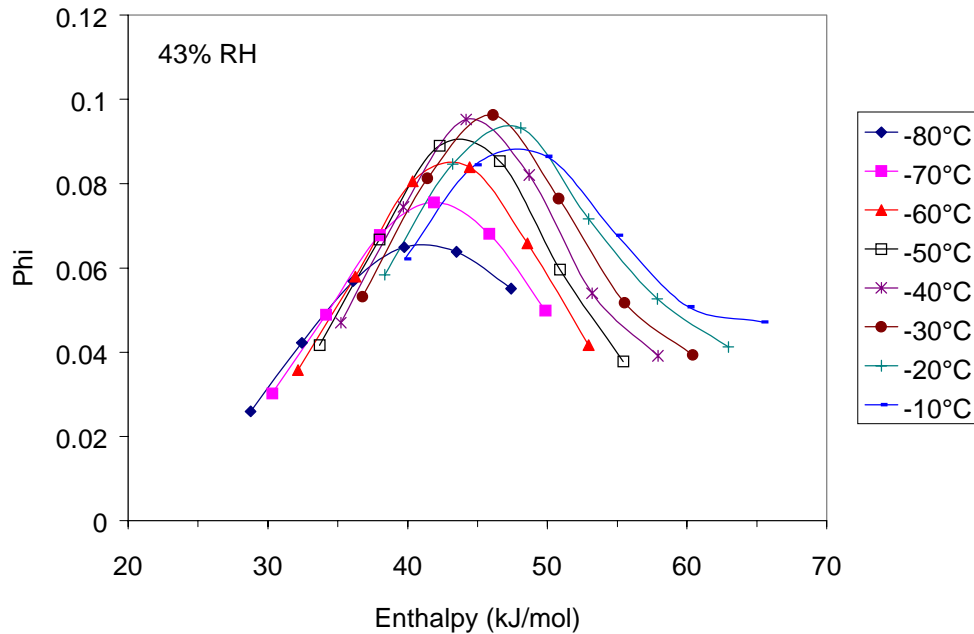


Figure 4.29. Relaxation distribution, Kapton<sup>®</sup>-E 43 %RH  $\gamma$  relaxation.

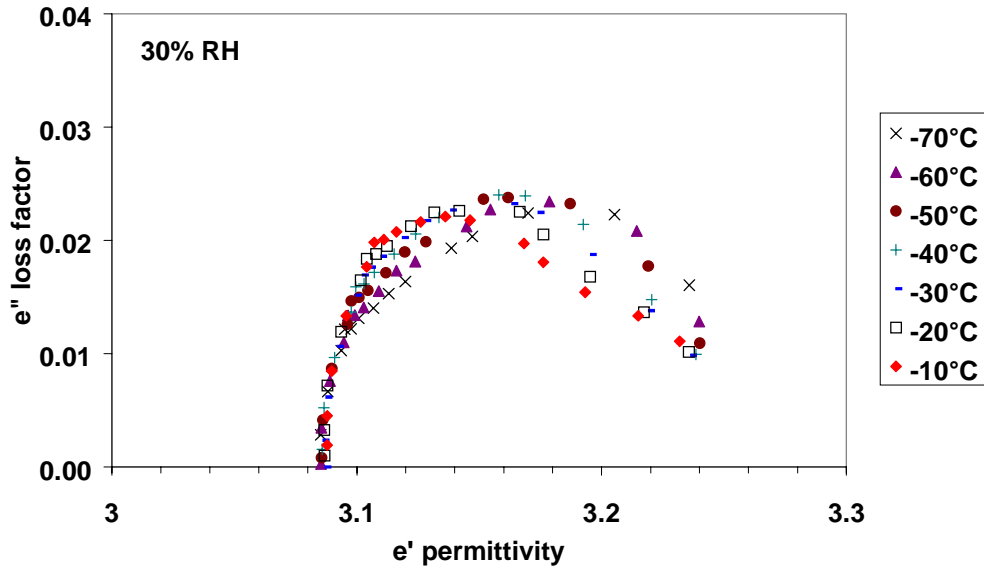


Figure 4.30. Argand diagram, Kapton<sup>®</sup>-E 29 %RH  $\gamma$  relaxation.

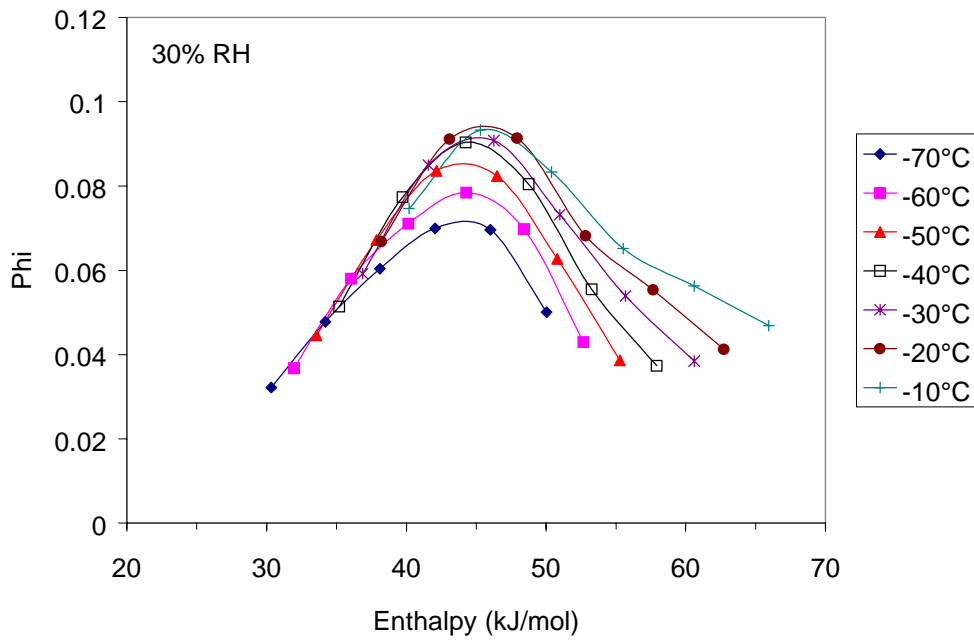
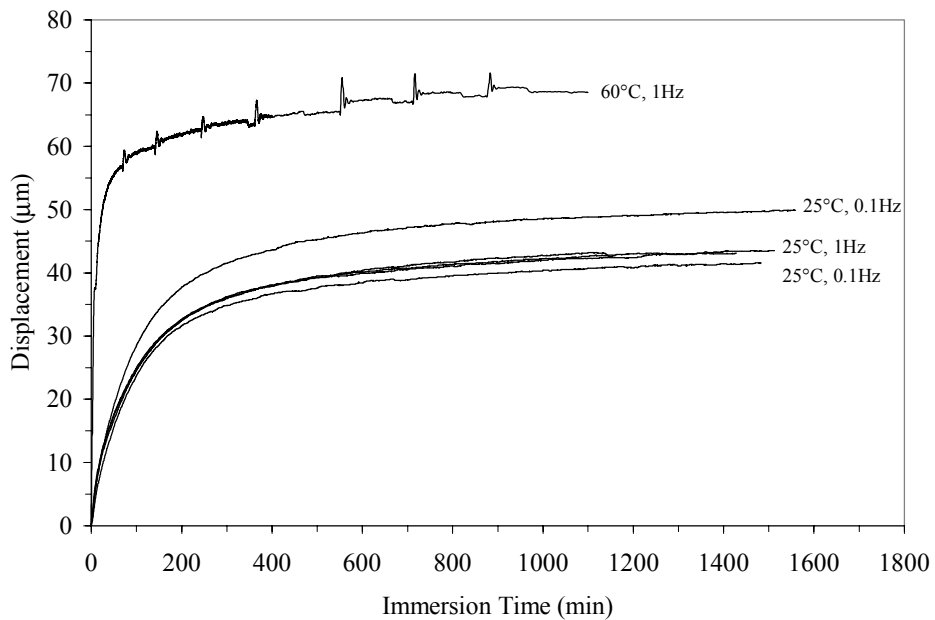


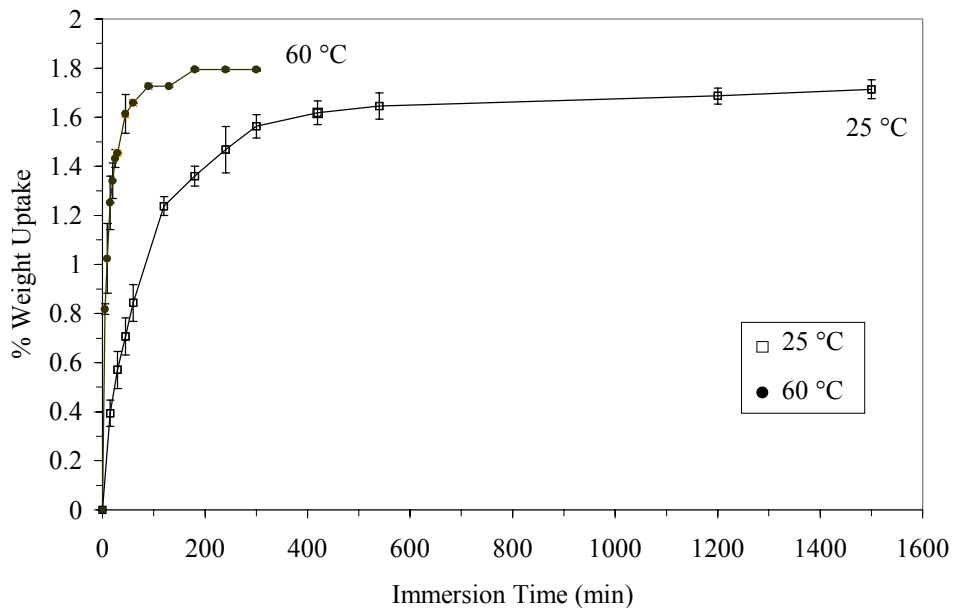
Figure 4.31. Relaxation distribution, Kapton<sup>®</sup>-E 29 %RH  $\gamma$  relaxation.

#### 4.3.7. In situ Dynamic Mechanical Analysis

An in situ DMA technique was adopted to study sample dimension changes of Kapton<sup>®</sup>-E upon exposure to water. Results in Figure 4.32 show that the sample displacements ie. sample length increase as water is absorbed by Kapton<sup>®</sup>-E. The displacements increase rapidly at short times, but at longer times, the displacements appear to reach an equilibrium value. The three samples tested at 1 Hz and a water temperature of 25 °C coincide almost exactly. Their average increase in displacement is  $\approx 43 \mu\text{m}$ . The displacements for the samples tested at 0.1 Hz and a water temperature of 25 °C, were slightly different, 49  $\mu\text{m}$  and 41  $\mu\text{m}$ . For the 60 °C sample, the initial increase in displacement is steeper than for the 25 °C samples. Presumably this arises from the faster absorption rate at the higher temperature. The 60 °C sample appears to reach an equilibrium displacement at  $\approx 69 \mu\text{m}$ . The noise in the 60 °C curve is a result of the addition of water to the fluid container. The observation that Kapton<sup>®</sup>-E increases in length upon absorption of water is supported by Popelar et al. who measured the hygral coefficient of expansion for several grades of Kapton<sup>®</sup>-H film.<sup>32</sup> The shapes of the in situ DMA curves are similar to those for the weight uptake of water by Kapton<sup>®</sup>-E measured as a function of time, shown in Figure 4.33.



**Figure 4.32. In situ DMA, Kapton®-E in water. Displacement versus immersion time for (a) 3 samples at 25 °C, 1 Hz, note that the curves overlay almost exactly, (b) 2 samples at 25 °C, 0.1 Hz, and (c) 1 sample at 60 °C, 1 Hz.**



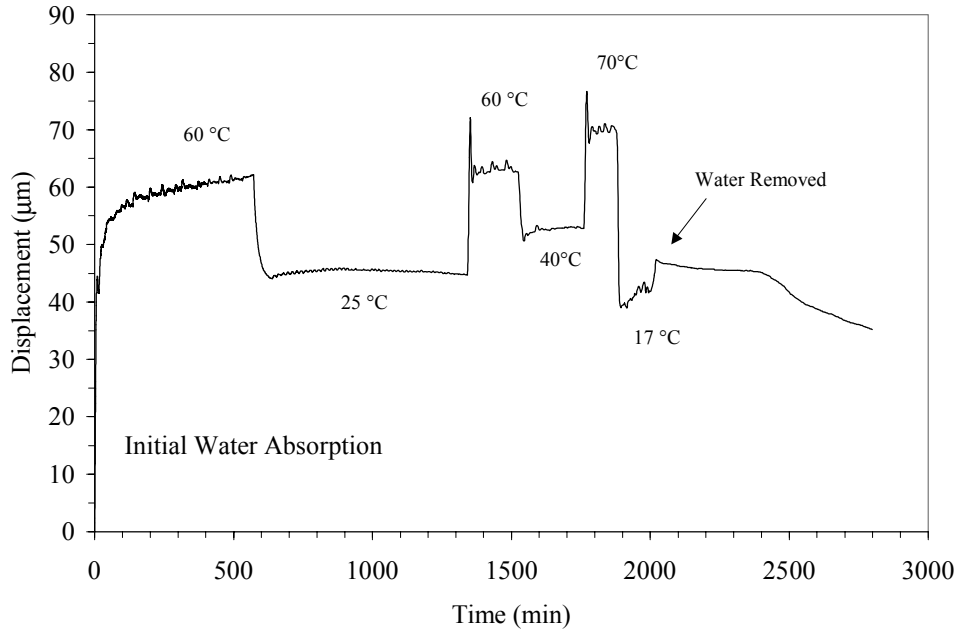
**Figure 4.33. Weight % uptake of water by Kapton®-E at 25 °C and 60 °C.**

Figure 4.33 shows that water is absorbed by Kapton<sup>®</sup>-E faster at 60 °C than for 25 °C. Both ultimately absorbed similar amounts of water, 1.7-1.8 wt.%. Repeated handling of the specimen may have led to the disagreement between the two temperatures. TGA of several saturated samples provided more conclusive evidence that both environments afforded the same water contents. Simple comparison of the shapes of the curves in Figure 4.32 and Figure 4.33 initially suggests that the change in displacement can be used to monitor diffusion in films. However, the displacement for the 60 °C is  $\approx 20 \mu\text{m}$  greater than the 25 °C samples, yet they both absorb approximately the same amount of water. This suggests that thermal expansion of the film is adding to the overall measured displacement. The contribution to the displacement from thermal expansion could not be easily separated from the displacement change due to water absorption. Thus the parameters needed for the application of Fick's second law, such as the initial displacement, could not be readily determined.

#### **4.3.7.1. Coefficient of thermal expansion**

Once a sample has reached an equilibrium water content when loaded in the in situ DMA configuration, the dimension change over an increment change in temperature can be used to determine a linear coefficient of thermal expansion. A distinction is made that a linear CTE measured by this means is for a saturated sample, as opposed to a dry sample. Since the sample is immersed in the water environment, it is assumed that any change in the equilibrium water content, which could affect the displacement value, is small.

Figure 4.34 illustrates the influence of water temperature on the displacement, ie. length change, of a Kapton<sup>®</sup>-E sample. The dry sample was initially exposed to 60 °C water. Once saturation was reached, the water temperature was changed, 60-25-60-40-70-17 °C using an TA Instruments external temperature controller. To reach  $\approx 17 \text{ }^\circ\text{C}$ , small pieces of ice were added to the fluid container; however, a constant isotherm was difficult to maintain. For 60 and 70 °C, the temperature initially overshoot the set-point which resulted in the large initial change in the displacement. The small fluctuations in the plateaus for 60 and 70 °C resulted from the addition of water to the fluid container.



**Figure 4.34. In situ DMA, 1 Hz. Influence of water temperature on the displacement of Kapton<sup>®</sup>-E. Initial water temperature is 60 °C.**

Figure 4.34 shows that as the temperature increased or decreased, the sample length correspondingly changed. The displacement jumps for the 60-25-60°C step were approximately the same, suggesting that the effect is attributable to temperature. A linear CTE was calculated using equation 4.17:

$$\alpha = \frac{1}{d_o} \left( \frac{\Delta d}{\Delta T} \right) \quad \text{Equation 4.17}$$

where  $\alpha$  is the linear CTE,  $d_o$  is the initial displacement,  $\Delta d$  is the change in displacement, and  $\Delta T$  is the change in temperature. The average linear  $\alpha$  for the saturated Kapton<sup>®</sup>-E sample was then calculated as  $49.4 \pm 4.9$  ppm/°C. Since a constant displacement plateau was not reached for 17°C, the 70 to 17 °C step was not included in the average. The linear CTE of the saturated sample is much higher than reported for dry Kapton<sup>®</sup>-E (12 ppm/°C).<sup>20</sup> This suggests that the dimensions of the swollen polymer are more easily changed by temperature. The polymer chains

of the saturated sample possibly have greater mobility due to the disruption of intermolecular forces among neighbor polyimide chains. The displacement vs. time response of saturated Kapton<sup>®</sup>-E to temperatures changes, shown in Figure 4.34, is similar to the weight percent uptake vs. time response for saturated epoxy networks to temperature changes.<sup>33,34,35</sup> For the epoxy networks, the behavior is explained by a reverse thermal effect. To associate such an effect to the Kapton<sup>®</sup>-E behavior, investigations which further elucidate the relationship between displacement at weight uptake of water and the nature of the hydrogen bonding interactions should be initiated.

#### 4.3.8. Conclusions

Exposure of dried Kapton<sup>®</sup>-E films to 8, 21, 29, 43, 73, and 98% relative humidity environments resulted in successively greater amounts of absorbed moisture. The values increased from 0.23 wt % to 1.30 wt. %, for the 8 and 98% RH environments, respectively. By DMA, relative to the  $\tan \delta$  signal for the dry sample, the absorbed moisture increased the  $\tan \delta$  magnitude of the low temperature component of the  $\beta$  transition. Thermal conditioning of Kapton<sup>®</sup>-E at various temperatures revealed changes in the  $\tan \delta$  magnitude and “double peak” shape of the  $\beta$  relaxation, relative to a dry, untreated sample. Both the humidity and thermal effects are suggested to be related to the processing history of the oriented Kapton<sup>®</sup>-E film. The DMA storage modulus was also influenced by the absorbed moisture. At temperatures below 50 °C, an anti-plasticizer effect was observed, but at temperatures above 50 °C a plasticizer effect was noted. The absorbed moisture, however, did not influence the tensile modulus of Kapton<sup>®</sup>-E, as measured by Instron mechanical testing.

Dielectrically, the absorbed moisture resulted in a low temperature relaxation whose  $\tan \delta$  magnitude increased as the moisture content increased. Analysis of the  $E_a$  by Arrhenius and Starkweather-Eyring methods indicated that the  $E_a$  of the relaxation decreased slightly (by  $\approx$  kJ/mol) as the moisture content increased. According to the theory of the Starkweather-Eyring method, the close agreement between the two types of calculations suggests that the entropic contribution,  $\Delta S$ , to the  $E_a$  is  $\approx 0$ , which allows the relaxation to be classified as “simple.” The simple nature of the relaxation was also viewed from the analysis of the distribution of relaxation

times, in which from the relationship between  $\Phi$  versus  $\Delta H$  a common pattern over all temperature isotherms was observed.

Considering the suggested processing history effect on the Kapton<sup>®</sup>-E film, it would be interesting to investigate whether thermally conditioning a sample prior to %RH exposure would have the same influence on the sub- $T_g$  relaxations. In particular, are the dielectric properties improved when some sample processing history is erased?

An in situ DMA technique was adopted to monitor the dimensional changes of Kapton<sup>®</sup>-E upon exposure to water. In addition, the average linear CTE of  $49.4 \pm 4.9$  ppm/ $^{\circ}$ C for a saturated Kapton<sup>®</sup>-E sample was measured. The application of in situ DMA in this way could provide valuable insight to the dimension changes with temperature of a polymer thin film or coating that is saturated by an aggressive fluid. Such information could assist in understanding the durability of adhesive joints in fluid environments.

#### 4.4 References

- 
- <sup>1</sup> Fukami, A.; Isaka, S.; Kubota, S.; Etoh, S. *J. Appl. Polym. Sci.* **1991**, *42*, 3065.
  - <sup>2</sup> Arnold, F.E.; Harris, F.W.; Cheng, S.Z.D. *Thermochimica Acta* **1993**, *226*, 15.
  - <sup>3</sup> Aklonis, J.J.; MacKnight, W. J., *Introduction to Polymer Viscoelasticity*, 2nd Ed; John Wiley & Sons: New York, 1983; Chapters 3 and 4.
  - <sup>4</sup> McCrum, N.G.; Read, B.E.; Williams, G. *Anelastic and Dielectric Effects in Polymeric Solids*; Dover: New York, 1991; Chapters 4 and 5.
  - <sup>5</sup> Cowie, J.M.G, *Polymers: Chemistry & Physics of Modern Materials*, 2<sup>nd</sup> Ed.; Blackie Academic & Professional: London, 1991; pp 298-300.
  - <sup>6</sup> Roland, C.M.; Ngai, K.L. *Macromolecules* **1992**, *25*, 363.
  - <sup>7</sup> Plazek, D.J.; Ngai, K.L. *Macromolecules* **1991**, *24*(5), 1222.
  - <sup>8</sup> Ngai, K.L.; Roland, C.M. *Macromolecules* **1993**, *26*, 2688.
  - <sup>9</sup> Connolly, M.; Karasz, F.; Trimmer, M. *Macromolecules* **1995**, *28*, 1872.
  - <sup>10</sup> Li, S.Z.; Chen, R.S.; Greenbaum, S.G. *J. Polym Sci Part B. Polym. Phys.* **1995**, *33*, 403.
  - <sup>11</sup> Dlubek, G.; Buchhold, R.; Hubner, Ch.; Nakladal, A. *Macromolecules* **1999**, *32*(7), 2348.
  - <sup>12</sup> Yang, D.K.; Koros, W.J.; Hopfenberg, H.B.; Stannett, V.T. *J. Appl. Polym. Sci.* **1985**, *30*, 1035.
  - <sup>13</sup> Yang, D.K.; Koros, W.J.; Hopfenberg, H.B.; Stannett, V.T. *J. Appl. Polym. Sci.* **1986**, *31*, 1619.
  - <sup>14</sup> Bernier, G.A.; Kline, D.E. *J. Appl. Polym. Sci.* **1968**, *12*, 593.
  - <sup>15</sup> Lim, T.; Frosini, V.; Zaleckas, V.; Morrow, D.; Sauer, J.A. *Polym. Eng. Sci.* **1973**, *13*(1), 51.
  - <sup>16</sup> Wang, J.Z.; Dillard, D.A.; Ward, T.C. *J. Polym. Sci. Polym. Phys. Ed.* **1992**, *30*(12), 1391.

- 
- <sup>17</sup> Starkweather, H.W., Jr. In *Water in Polymers*; Rowland, S.P., Ed.; ACS Symposium Series 127; American Chemical Society: Washington, D.C., 1980; pp 433-440.
- <sup>18</sup> Waters, J.F.; Likavec, W.R.; Ritchey, W.M. *J. Appl. Polym. Sci.* **1994**, *53*, 59.
- <sup>19</sup> Gu, X.; Gryte, C.C.; Nowick, A.S.; Li, S.Z.; Pak, Y.S.; Greenbaum, S.G. *J. Appl. Phys.* **1989**, *66(11)*, 5290.
- <sup>20</sup> Kreuz, J.A., S.N. Milligan, and R.F. Sutton, "Kapton Polyimide Film Advanced Flexible Dielectric Substrates for FPC/TAB Applications," DuPont technical paper H-54504, product specifications, 1994.
- <sup>21</sup> Hedvig, P., *Dielectric Spectroscopy of Polymers*, Adam Hilger Publishers: Bristol, UK, 1977.
- <sup>22</sup> Starkweather, H.W. *Macromolecules* **1981**, *14*, 1277.
- <sup>23</sup> David, L.; Etienne, S. *Macromolecules* **1992**, *25*, 4302.
- <sup>24</sup> Ward, I.M., *Mechanical Properties of Solid Polymers, Second Edition*, John Wiley & Sons: New York, 1983.
- <sup>25</sup> Starkweather, H.W. *Macromolecules* **1981**, *14*, 1277.
- <sup>26</sup> Starkweather, H.W. *Macromolecules* **1988**, *21*, 1798.
- <sup>27</sup> Starkweather, H.W. *Macromolecules* **1990**, *23*, 328.
- <sup>28</sup> Bas, C.; Alberola, N.D. *Polym. Eng. Sci.* **1996**, *36(2)*, 244.
- <sup>29</sup> David, L.; Etienne, S. *Macromolecules* **1992**, *25*, 4302.
- <sup>30</sup> McCrum, N.G., B.E. Read, and G. Williams, *Anelastic and Dielectric Effects in Polymeric Solids*, Dover Publications, Inc.: New York, 1967 (1991 Reprint used).
- <sup>31</sup> Ferry, J.D., *Viscoelastic Properties of Polymers*, John Wiley & Sons: New York, 1961.
- <sup>32</sup> Popelar, S.F., M.K. Chengalva, C.H. Popelar, and V.H. Kenner, AMD-Vol.155, *ASME*, (1992) 15.
- <sup>33</sup> Adamson, M.J. *J. Mater. Sci.* **1980**, *15*, 1736.
- <sup>34</sup> El Sa'ad, L.; Darby, M.I.; Yates, B. *J. Mater. Sci.* **1990**, *25*, 3577.
- <sup>35</sup> Verghese, K.N.E.; Hayes, M.D.; Garcia, K.; Carrier, C.; Wood, J.; Riffle, J.R.; Lesko, J.J. *J. Composite Materials* **1999**, *33(20)* 1918.

## 5. Characterization of Amorphous Partially Aliphatic Polyimides Based on Bisphenol-A Dianhydride

### 5.1. INTRODUCTION

The chapter discusses the physical property characterization of partially aliphatic copolyimides derived from bis[4-(3,4-dicarboxyphenoxy)phenyl]propane dianhydride, or Bisphenol A dianhydride (BPADA), and four diamines: 4,4'-oxydianiline (ODA), 4,4'-diaminodicyclohexyl-methane (DCHM), hexamethylenediamine (HMDA), and dodecyldiamine (DoDDA). Specifically, this chapter presents molecular weight, thermal, dielectric, and mechanical data to establish structure-property relationships, and discusses the molecular origins of the  $\gamma$  and  $\beta$  sub- $T_g$  viscoelastic relaxations.

The selection of aliphatic diamine monomers for this study was based on the anticipated structure-property relations for each type of aliphatic group. Cycloaliphatic diamines impart rigidity to the polymer backbone similar to that of aromatic diamines, but offer improvements in polymer transparency and dielectric constant partially due to the reduced formation of charge transfer complexes.<sup>1,2,3,4</sup> The linear aliphatic diamines are more flexible - the number of methylene units can determine the magnitude of the glass transition temperature, as well as the crystalline/amorphous morphology of the polyimide. Copolymerization of rigid plus flexible monomers (aromatic, cycloaliphatic, aliphatic) allows control of the polyimide thermal and mechanical properties in order to meet specific processing and property requirements.

### 5.2. MATERIALS

Three BPADA-based copolyimides with the following combination of diamine molar ratios: HMDA:ODA, 75:25, HMDA:DoDDA, 50:50, and HMDA:DoDDA, 25:75 were characterized in addition to the homopolymers BPADA/ODA and BPADA/DCHM. The monomer chemical structures are presented in Chapter 3.

### 5.3. RESULTS AND DISCUSSION

The solubility of the fully-cyclized polyimides allowed accurate molecular weight characterization of the entire series using GPC. Table 5.1 lists the molecular weights and

polydispersities ( $\langle M_w \rangle / \langle M_n \rangle$ ) for the different polyimide compositions. The data show that the ester-acid solution imidization produced high molecular weight polyimides, with the exception of BPADA/DCMH. The polydispersity values were around 2.2 for the series, which is typical for polycondensation reactions. Despite the low molecular weight of BPADA/DCHM, tough creasable films were easily prepared for property characterization. Wholly aromatic polyimides synthesized by the traditional two-step method are relatively insoluble; thus, the polyimide molecular weight has been typically estimated from the molecular weight data obtained for the soluble poly(amic acid) precursor.<sup>5,6,7</sup> In contrast, using GPC, molecular weight data for our fully-cyclized soluble polyimides were relatively easy to determine and more accurate.

**Table 5.1. Molecular Weight and Thermal Characterization of BPADA-based Polyimides.**

Polyimide	Diamine	$\langle M_n \rangle$	$\langle M_w \rangle / \langle M_n \rangle$	$T_g$ (°C)	$T_{deg}$ (°C)
	Molar Ratio	kg/mol		DSC*	TGA**
BPADA / ODA	1	54	2.9	224	514
BPADA / HMDA:ODA, 75:25	0.75 : 0.25	81	2.3	150	458
BPADA / HMDA:DoDDA, 50:50	0.50 : 0.50	27.3	1.9	103	465
BPADA / HMDA:DoDDA, 25:75	0.25 : 0.75	36.7	2.2	88	452
BPADA / DCHM	1	6.6	1.9	205	450

\*  $T_g$  reported from second heating cycle in nitrogen.

\*\* 5% weight loss degradation temperature in air.

Table 5.1 also lists the glass transition temperatures and thermal degradation temperatures (5% weight loss in air) for the BPADA-based polyimides. The fully aromatic BPADA/ODA possessed the highest  $T_g$  and best thermal stability, as expected. The high glass transition temperature of BPADA/ODA is attributed to the rigid, predominantly aromatic, backbone structure and the formation of strong intermolecular complexes. The high thermal stability of BPADA/ODA is due to the high content of strong aromatic covalent bonds. Table 5.1 shows that as the aliphatic content increases, the  $T_g$  and thermal stability decrease. The linear methylene groups of HMDA and DoDDA impart flexibility to the backbone and allow cooperative segmental motions associated with the  $T_g$  to initiate at lower temperatures. While, the thermal stability for these polyimides decreased due to the susceptibility of the methylene units to oxidative degradation, the lower  $T_g$  should facilitate melt processing.

The cycloaliphatic diamine, DCHM, is more rigid than HMDA and DoDDA; the increased main-chain rigidity is reflected in the high  $T_g$  of 205 °C, which is comparable to the  $T_g$  of the

fully aromatic BPADA/ODA. Glass transition temperatures of  $\approx 200$  °C have been reported for similar aromatic dianhydride-based polyimides containing DCHM.<sup>3,7</sup> Table 5.1 also shows that the 5% weight loss temperature of BPADA/DCHM is 450 °C, which is comparable to the thermal stability of the other partially aliphatic polyimides. It is noted that the DCHM methylene units are incorporated within a ring structure, such that a single C-C bond scission would not lead to an immediate significant decrease in molecular weight.<sup>1,8</sup> Conversely, for HMDA or DoDDA, methylene C-C bond scission would directly decrease the molecular weight. Thus, for limited extents of degradation, BPADA/DCHM mechanical properties may not be compromised at elevated temperatures.

The linear CTE is defined as the relative change in length divided by the change in temperature:

$$\alpha = \frac{1}{l_o} \left( \frac{\Delta l}{\Delta T} \right) \quad \text{Equation 5.1}$$

where  $\alpha$  is the linear CTE,  $l_o$  is the initial sample length,  $\Delta l$  is the change in sample length, and  $\Delta T$  is the change in temperature. From an atomistic perspective, the CTE reflects an increase in the average distance between atoms with increasing temperature.<sup>9</sup> The greater the atomic bonding energy, the less the interatomic distance will increase with temperature. Relative to aromatic covalent bonds, aliphatic covalent bonds have a lower average bond enthalpy and are thus expected to lengthen more with increasing temperature. Intermolecular interactions also act to resist dimension changes with increasing temperature with high cohesive energy densities leading to a lower CTE.<sup>10</sup> Figure 5.1 illustrates the change in sample dimension with temperature for BPADA/DCHM. The results shown in Figure 5.1 are representative of the BPADA-based polyimides. Three heating cycles and two cooling cycles are plotted. The first heating cycle is marked.

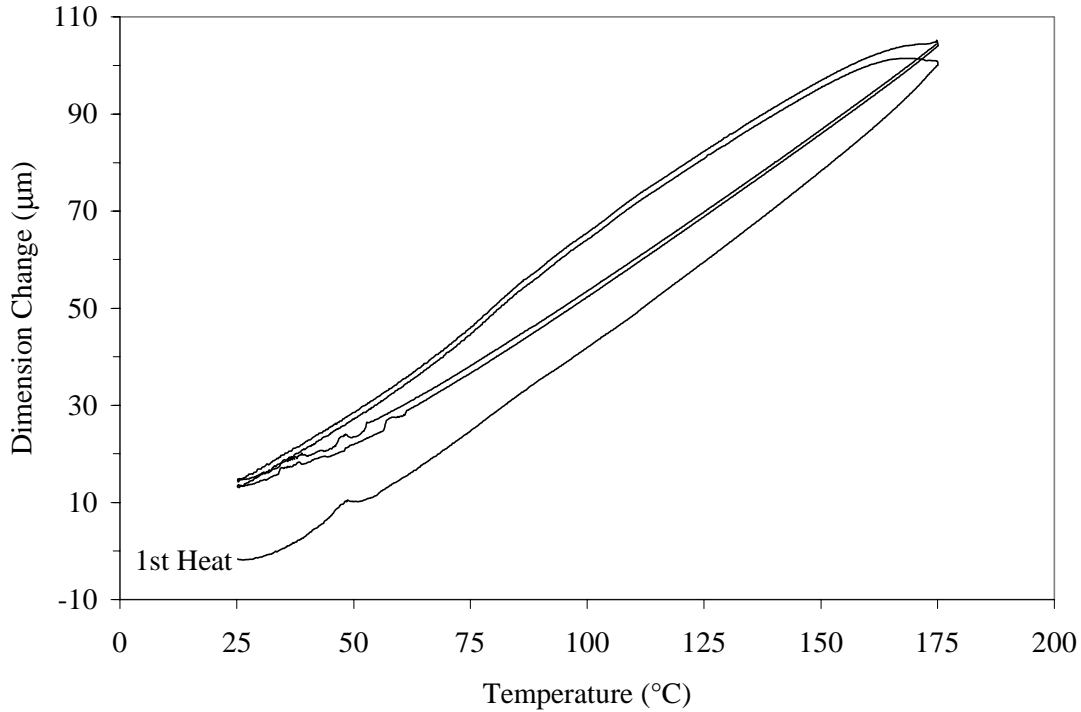


**Figure 5.1. Dimension change versus temperature for BPADA/DCHM.**

The dimension change with temperature for the first heating cycle differs from the subsequent heating cycles and reflects the sample preparation history. During the first heating cycle, absorbed moisture and residual stresses were released. Figure 5.1 shows that the cooling curves do not overlay with the heating curves. This is due to thermal lag within the DMA furnace; if the heating/cooling rates are decreased, the envelope size will decrease. Using the initial sample length and slopes of the second and third heating cycles the linear CTEs were calculated according to equation 5.1. The average linear CTE values are presented in Table 5.2.

**Table 5.2. Linear Coefficients of Thermal Expansion.**

Polyimide	CTE (ppm/°C) <sup>a</sup>
BPADA / ODA	31.0
BPADA / HMDA:ODA, 75:25	45.3
BPADA / HMDA:DoDDA, 50:50	51.5
BPADA / HMDA:DoDDA, 25:75	52.5
BPADA / DCHM	42.3

<sup>a</sup>  $l_0 \approx 15$  mm

Table 5.2 shows that as the aliphatic content increases, the CTE increases. The low CTE of BPADA/ODA is rationalized as due to the aromatic covalent bonds within its backbone and the intermolecular interactions between ODA and BPADA units on neighbor polyimide chains.<sup>10,11</sup> As the aliphatic content increases, the CTE increases because weaker covalent bonds within the polymer backbone are present and also weaker intermolecular interactions contribute. BPADA/DCHM possesses a CTE value slightly lower than that of BPADA/HMDA:ODA, 75:25. The cycloaliphatic DCHM units add rigidity to the main-chain which may facilitate the alignment of the segmental units, but they also participate in weaker, van der Waals intermolecular interactions. The aromatic ODA units add rigidity to the main-chain and add stronger, intermolecular charge transfer interactions with the BPADA units; however, since only 25% of the ODA is present in this copolyimide, its CTE is comparable to that of BPADA/DCHM. Table 5.2 shows that the CTE values for BPADA/HMDA:DoDDA, 50:50 and 25:75 are 51.5 and 52.5 ppm/°C, respectively. The CTE values are similar as expected from the similarity in chemical composition and structure. These CTE values are higher than the other polyimides investigated due to the flexibility of the aliphatic units which adds free volume thus lowering intermolecular forces.

The viscoelastic relaxations of the BPADA-based polyimides were studied using DMA. A strong correlation was observed between the glass transition temperature and the percent aliphatic content. These data were consistent with those determined from DSC. Figure 5.2 displays an overlay of log storage modulus ( $E'$ ) versus temperature for the five polyimides.

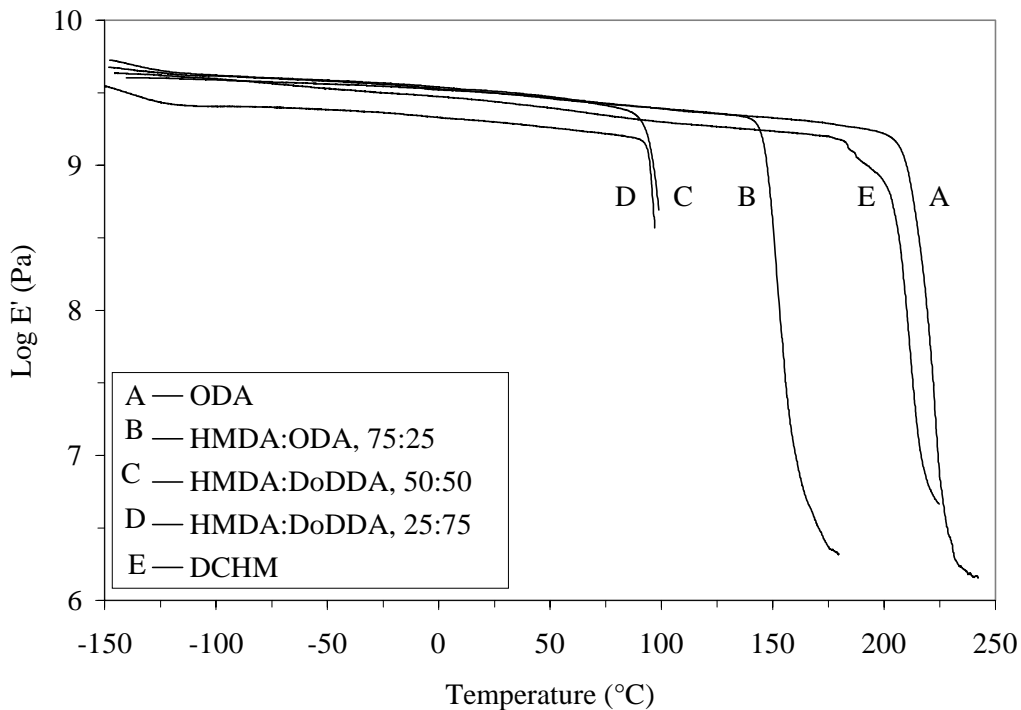


**Figure 5.2. The dependence of the storage modulus on the percent aliphatic diamine. DMA, 1 Hz.**

In Figure 5.2, the  $E'$  curve for BPADA/DCHM shows as small decrease just prior to the glass transition. Recall that BPADA/DCHM possesses a low  $M_n$  of 6.6 kg/mol. Thus, at temperatures near the glass transition, film elongation is likely. The magnitude of  $E'$  for the polyimides is typical of glassy polymers,  $10^9$  Pa, and the  $E'$  for the polyimides containing ODA units are higher than for the predominately aliphatic polyimides. BPADA/HMDA:DoDDA, 50:50 showed a  $E'$  value comparable to the ODA containing polymers, which was unexpected.

Table 5.3 lists the glass transition temperatures calculated from the onset of rapid decrease in the storage modulus ( $E'$ ) and also from the tan delta measurements. Sample elongation within the  $T_g$  for the 50:50 and 25:75 HMDA:DoDDA diamine samples prevented the acquisition of a complete tan delta peak.

**Table 5.3. DMA Glass Transition Temperatures, 1 Hz.**

Polyimide	$T_g$ (°C)	$T_g$ (°C)
	Storage Modulus*	Tan Delta**
BPADA / ODA	201	222
BPADA / HMDA:ODA, 75:25	143	156
BPADA / HMDA:DoDDA, 50:50	90	n/a
BPADA / HMDA:DoDDA, 25:75	91	n/a
BPADA / DCHM	199	215

\* Onset Temperature.

\*\* Peak Maximum.

DMA also revealed several sub- $T_g$ , local viscoelastic relaxations (Figure 5.3 and Figure 5.4). The variations in chemical composition are reflected in the tan delta signal.

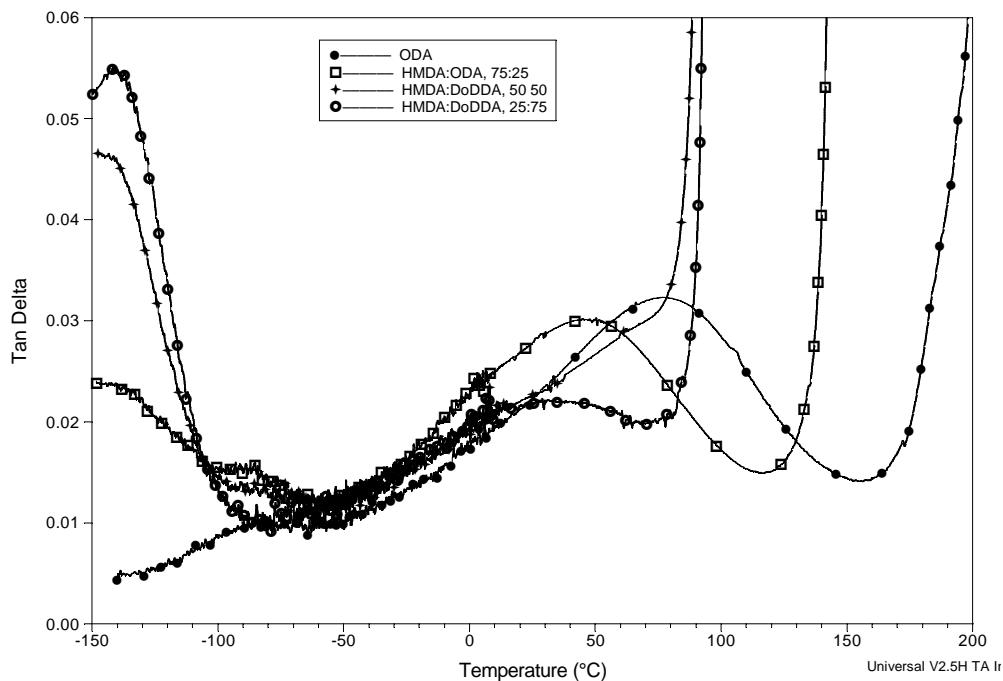


**Figure 5.3. Sub- $T_g$  DMA responses at 1 Hz for BPADA/ODA, BPADA/HMDA:ODA, 75:25, BPADA/HMDA:DoDDA, 50:50, and BPADA/HMDA:DoDDA, 25:75.**

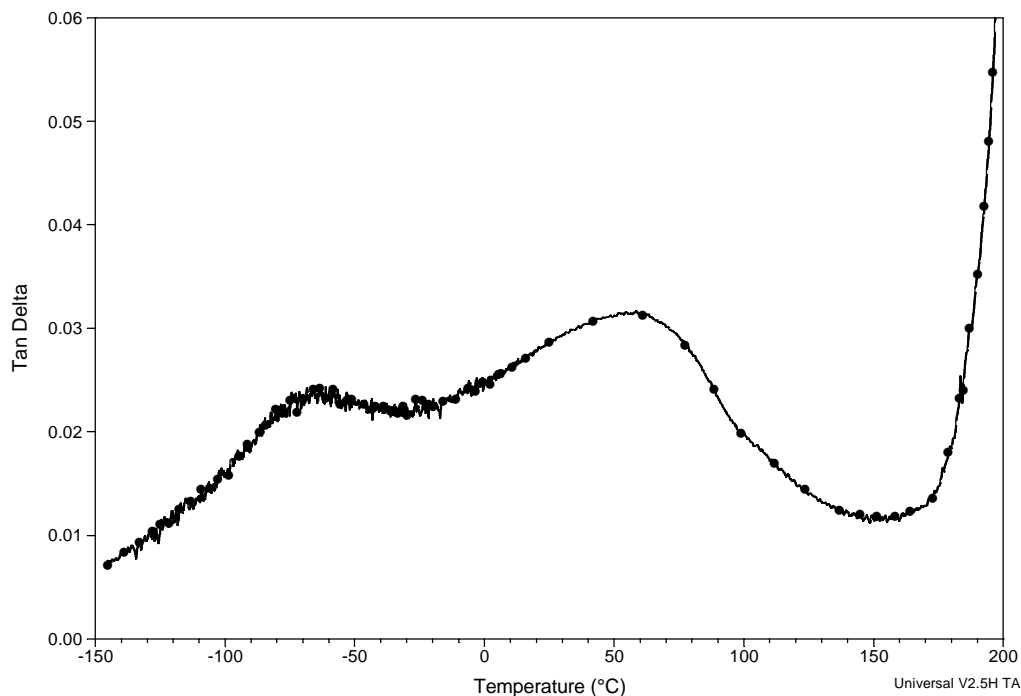


**Figure 5.4. Sub-T<sub>g</sub> DMA response at 1 Hz for BPADA/DCHM.**

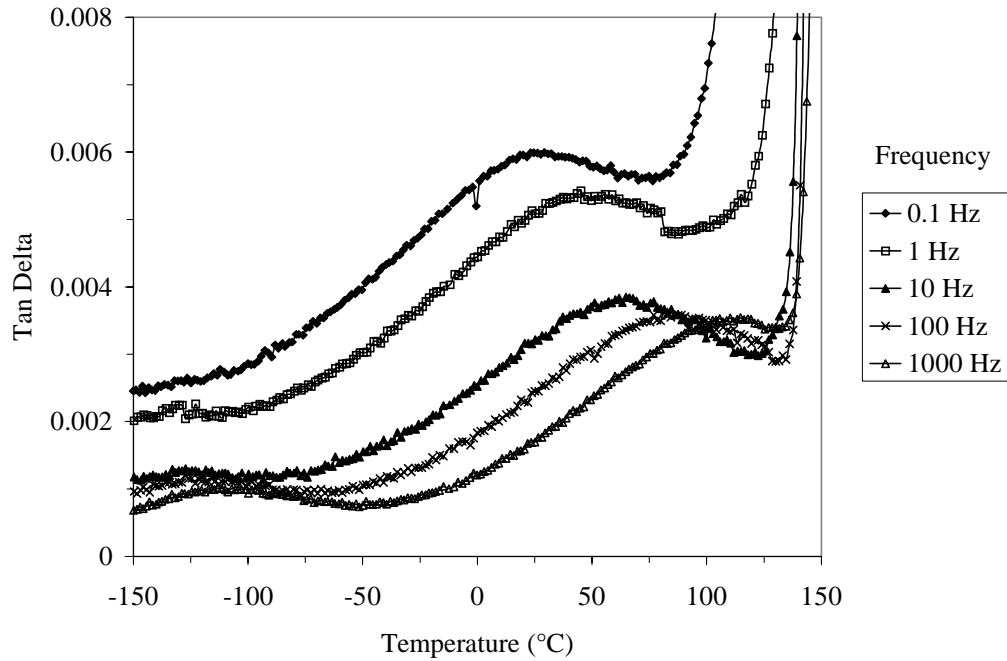
A crankshaft motion ( $\gamma$  relaxation) attributed to the DoDDA and HMDA units is observed at  $\approx -140$  °C (Figure 5.3). This assignment was made by comparison to prior viscoelastic studies of polyethylene.<sup>12</sup> The methylene unit cooperative crankshaft motions have also been observed in nylon-6,6, in polyesters, and in oxide polymers which contain linear  $(\text{CH}_2)_{n \geq 4}$  sequences that are separated by immobile groups.<sup>12</sup> While the tan delta magnitude assigned to a crankshaft motion is comprised of motions from both DoDDA and HMDA, the longer DoDDA sequences appear to be more influential. BPADA/ODA and BPADA/DCHM do not contain linear aliphatic diamines - no relaxation is observed at  $\approx -140$ °C. The molecular source for the small relaxation at  $\approx -90$  °C for BPADA/ODA and BPADA/HMDA:ODA, 75:25 has not been identified; however, the relaxation may arise from residual NMP in the film. This relaxation is not observed in the dielectric experiments in which two heating cycles were performed.

BPADA/ODA and BPADA/HMDA:ODA, 75:25 both exhibit sub-T<sub>g</sub> viscoelastic relaxations ( $\beta$  relaxations) which heating initiates at  $\approx -47$  °C, but display peak maximums at  $\approx 75$  °C and 50 °C, respectively. A phenyl ring torsional rotation within the ODA units is assigned as the underlying molecular motion. This association was made by comparison to prior viscoelastic

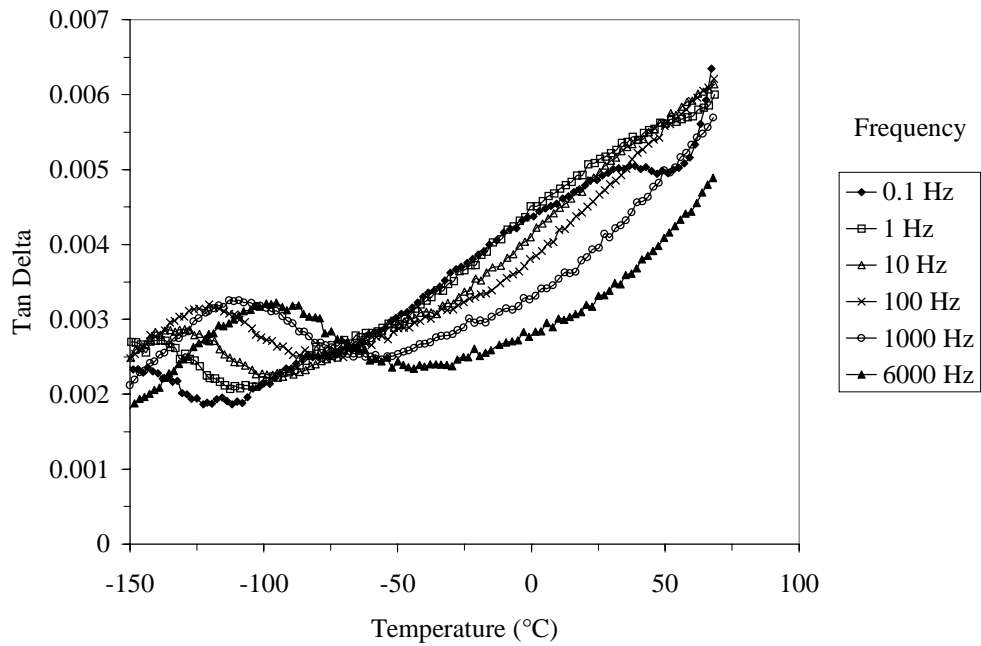
studies of partially aliphatic<sup>13</sup> and aromatic polyimides.<sup>14,15,16,17</sup> Also, it is noted that the peak maximum for BPADA/ODA is  $\approx 25$  °C higher than for BPADA/HMDA:ODA, 75:25. This effect arises from the broadening of the distribution of relaxation times as the ODA content and the backbone rigidity increase. Similar observations are reported for the  $\beta$  relaxation of polycarbonate.<sup>12</sup> A relaxation within this temperature range is also observed within BPADA/HMDA:DoDDA, 25:75, but not BPADA/HMDA:DoDDA, 50:50. This observation is peculiar because their chemical structures are so similar. Obviously the molecular source cannot be ODA units, so perhaps the flexibility arising from the higher DoDDA content allows ordering or packing during film formation which is then detected in the DMA tan delta response.

Figure 5.4 shows that BPADA/DCHM exhibits sub- $T_g$  viscoelastic relaxations at  $\approx -78$  °C and 60 °C. The relaxation at  $-78$  °C is suspected to arise from internal friction due to isomer changes within the cyclohexyl ring. Low temperature mechanical and dielectric relaxations have been observed in polycyclohexyl alkylacrylate derivatives and an axial-equatorial (chair-chair) isomer mechanism, or ring inversion, has been assigned the molecular origin.<sup>12,18</sup> A major difference between these literature examples and this study is that the BPADA/DCHM cyclohexyl ring is within the polyimide backbone, rather than on a side group. Thus, the assignment is preliminary. The location of the cyclohexyl maximum, however, is remarkably insensitive to the molecular environment.<sup>18</sup> The molecular source of the BPDAD/DCHM relaxation at  $\approx 60$  °C is not clear.

Examination of the viscoelastic properties by DEA also revealed two sub- $T_g$ , local viscoelastic relaxations. A  $\beta$  relaxation for the polyimides containing ODA was observed at  $\approx 50$  °C (1 Hz). A  $\gamma$  relaxation for the polyimides containing HMDA and DoDDA was observed at  $\approx -140$  °C (1 Hz). Figure 5.5 and Figure 5.6 present the dielectric tan delta signal frequency dependence of the sub- $T_g$  relaxations for BPADA/HMDA:ODA, 75:25 and BPADA/HMDA:DoDDA, 25:75 respectively. For each polyimide, as the frequency increases, the relaxations shift to higher temperatures. Figure 5.7 shows the dielectric response of BPADA/DCHM; the shoulder  $\approx -75$  °C (0.1 Hz) is suspected to be due to isomer conformation changes within the cyclohexyl groups. At higher frequencies, the shoulder disappears due to overlap with the higher temperature secondary relaxation.



**Figure 5.5. DEA, 2<sup>nd</sup> Heating. The frequency dependence of the  $\gamma$  and  $\beta$  relaxations for BPADA/HMDA:ODA, 75:25.**



**Figure 5.6. DEA, 2<sup>nd</sup> Heating. The frequency dependence of the  $\gamma$  relaxation for BPADA/HMDA:DoDDA, 25:75.**

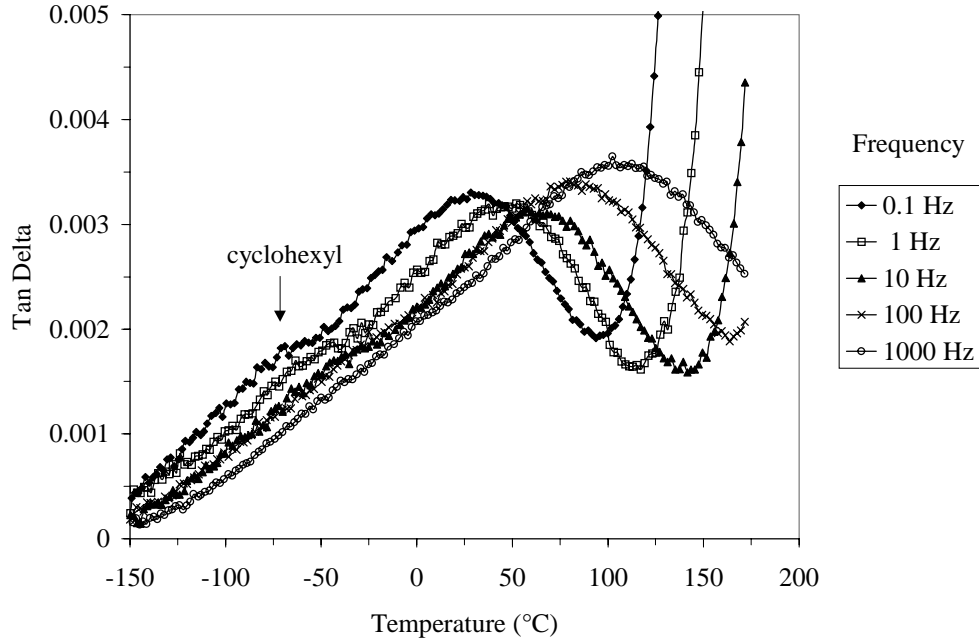


**Figure 5.7. DEA, 2<sup>nd</sup> Heating. The frequency dependence of the sub-T<sub>g</sub> relaxations for BPADA/DCHM.**

The molecular origins identified with the DMA sub-T<sub>g</sub> relaxations are clarified by using data from the DEA sub-T<sub>g</sub> relaxations in an Arrhenius activation energy analysis. The magnitude of an activation energy of a relaxation depends on rotation potential energy barriers, internal friction, and the volume and environment of the moving repeat unit(s). An activation energy of a relaxation calculated from dielectric data is generally lower than the activation energy calculated for the same relaxation from mechanical data.<sup>19</sup> The activation energy for the glass transition, the β relaxation, and the γ relaxation for each of the polyimides was calculated by applying the Arrhenius equation:

$$\omega = \omega_o \exp(-E_a / RT) \quad \text{Equation 5.2}$$

where  $\omega$  is frequency,  $\omega_o$  is the exponential pre-factor,  $E_a$  is the activation energy,  $R$  is the gas constant, and  $T$  is peak-maximum temperature. Figure 5.8 illustrates the log frequency versus  $1/T$  relationships and the best fit lines distinguish the three types of relaxations.

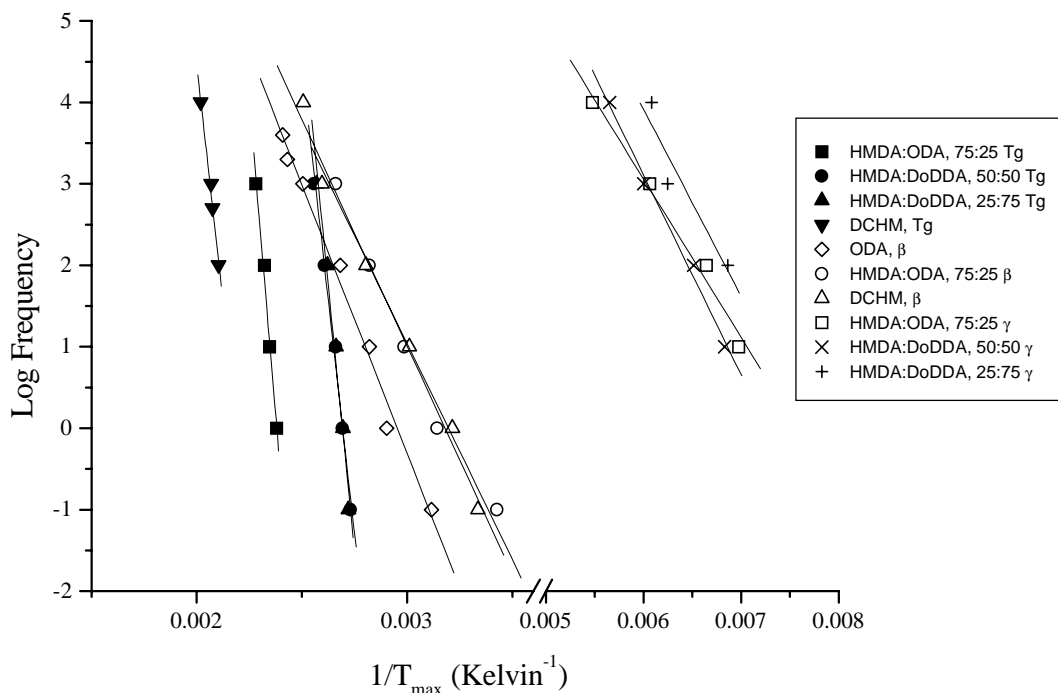


**Figure 5.8. Log frequency versus  $1/T$  for the DEA  $\gamma$ ,  $\beta$ , and  $T_g$  relaxations of several BPADA-based polyimides. Note: the curves for the  $T_g$  of HMDA/DoDDA, 50:50 and HMDA:DoDDA, 25:75 overlay almost exactly.**

In Figure 5.8 note that the slopes of the lines for the glass transition temperatures are steeper than those for the  $\beta$  and  $\gamma$  relaxations. The high slope indicates a much higher activation energy and a different volume and environment of the moving segments. Table 5.4 presents the DEA Arrhenius activation energies calculated using the slopes of the best fit lines.

**Table 5.4. DEA Arrhenius Activation Energies.**

Polyimide	Activation Energy (kJ/mol)		
	$\gamma$ Relaxation	$\beta$ Relaxation	$\alpha$ Relaxation ( $T_g$ )
BPADA / ODA	-	126.2	-
BPADA / HMDA:ODA, 75:25	44.0	101.4	591.8
BPADA / HMDA:DoDDA, 50:50	46.9	-	440.5
BPADA / HMDA:DoDDA, 25:75	37.1	-	499.4
BPADA / DCHM	-	106.7	443.6

a) relaxation not present; b) cyclohexane relaxation- a shoulder on the  $\beta$ ; c) ionic conductivity obscured the  $T_g$

The similarity in the activation energy for the  $\gamma$  relaxations suggests a common molecular origin. The  $\gamma$  relaxation  $E_a$  of  $\approx 43$  kJ/mol ( $\approx 10$  kcal/mol) agrees reasonably well with the value of 11 kcal/mol reported for polyethylene and further confirms the assignment of a crankshaft motion.<sup>12</sup> The  $E_a$  values for the  $\beta$  relaxation are the same order of magnitude and although the molecular origin for the BPADA/DCHM  $\beta$  relaxation differs from the ODA containing polyimides, their relaxation volume element size scales are similar. Mechanical and dielectric activation energies for the  $\beta$  relaxation of aromatic polyimides are in the range 95-150 kJ/mol.<sup>14,15,13</sup> Table 5.4 also shows that the activation energies for the  $T_g$  are much higher than for the local, sub- $T_g$  relaxations. This is characteristic of the thermal energy needed to activate the highly cooperative chain motions involved in the glass transition.<sup>20</sup>

Structure-property relationships for the refractive index and dielectric constant were also investigated. Polyimides with low dielectric constants are desirable to increase the efficiency at which a microelectronics device transmits signals. Polyimides containing more polarizable atoms or functional groups display a higher relative dielectric constant,  $\epsilon_r$ , in all frequency ranges than polyimides with fewer polarizable groups. Table 5.5 lists the refractive indices and estimated relative dielectric constants ( $\epsilon_r$ ) for the BPADA-based polyimides. The  $\epsilon_r$  values were estimated from the refractive indices using a relation deduced from Maxwell's equations:<sup>21</sup>

$$n^2 = \epsilon_r \quad \text{Equation 5.3}$$

where  $n$  is the refractive index and  $\epsilon_r$  is the relative dielectric constant. This relation is applicable at optical frequencies ( $10^{15}$ -  $10^{16}$  Hz) where only electronic polarization occurs.

**Table 5.5. Refractive Index and Dielectric Constant.**

Polyimide	Refractive Index	Dielectric Constant via Refractive Index
BPADA / ODA	1.662	2.763
BPADA / HMDA:ODA, 75:25	1.633	2.667
BPADA / HMDA:DoDDA, 50:50	1.612	2.599
BPADA / HMDA:DoDDA, 25:75	1.607	2.582
BPADA / DCHM	1.598	2.554

Table 5.5 shows that as the aromatic diamine content (ODA) decreases the refractive index also decreases; that is, the materials become more transparent. The increased transparency is attributed to the reduction of charge transfer complexes between neighbor polyimide chains and the reduction of extended conjugation along the polyimide backbone.<sup>5,22</sup> The polyimides with aliphatic and cycloaliphatic diamines possess comparable refractive index values. The low refractive index for BPADA/DCHM agrees well with literature examples. There, DCHM was suggested to prevent the occurrence of both inter- and intramolecular charge transfer complexes in polyimide films due to its weak electron donating property.<sup>1,2,3</sup> Similar findings were reported for polyimides containing alkyl groups.<sup>23</sup> Table 5.5 also shows that the  $\epsilon_r$  decreases with increasing aliphatic diamine content due to the presence of fewer polarizable functional groups. The decrease in chain linearity is also expected to contribute to the decrease in  $\epsilon_r$ .<sup>24,25</sup>

The temperature dependence of the dielectric constant was examined from the DEA permittivity ( $\epsilon'$ ) response. The permittivity response for BPADA/HDMA:ODA, 75:25 is illustrated in Figure 5.9.

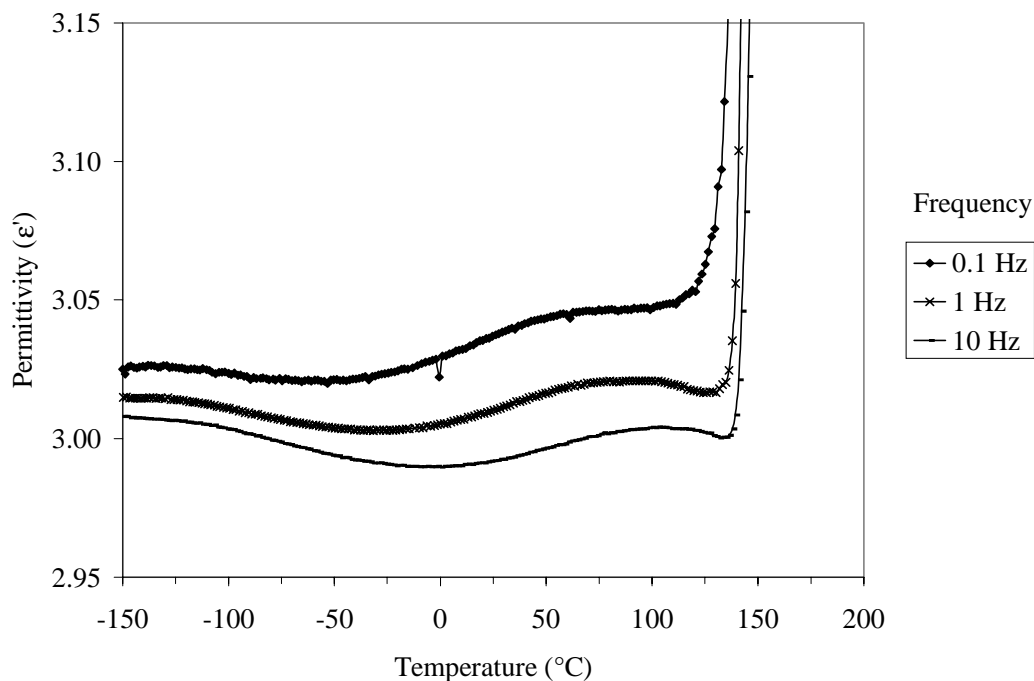


**Figure 5.9. DEA, 2<sup>nd</sup> Heating. Permittivity response for BPADA/HDMA:ODA, 75:25.**

Figure 5.9 shows a step-increase in the dielectric permittivity at the temperatures of the  $\gamma$  and  $\beta$  relaxations. The segmental mobility allows for alignment of the dipoles which results in an increase in the permittivity and causes the material to become less insulative. The permittivity increase at the  $\gamma$  relaxation is  $\approx 0.015$ . The increase in the permittivity at the  $\beta$  relaxation is  $\approx 0.025$ . The difference in step-increase values reflects the difference in the molecular origin of the  $\gamma$  and  $\beta$  relaxations. The dipoles which align due to the crankshaft motion are very weak and some dipolar contribution is thought to be from its near environment. Stronger dipoles are present in the ODA units, thus leading to a larger step-increase. BPADA/ODA displayed a step-increase of  $\approx 0.05$  at the  $\beta$  relaxation, which reflects the greater number of ODA units. A step-increase,  $\approx 0.015$ , at the temperature of the  $\gamma$  relaxation was similarly observed for the polyimides containing the diamines HMDA and DoDDA; for these polyimides no correlation between the step-increase value and the diamine content was noted. Figure 5.10 presents the temperature dependence of the permittivity response of BPADA/DCHM. The permittivity step-increase is  $\approx 0.07$ ; however, this increase contains contributions from the cyclohexyl and  $\beta$  relaxations.

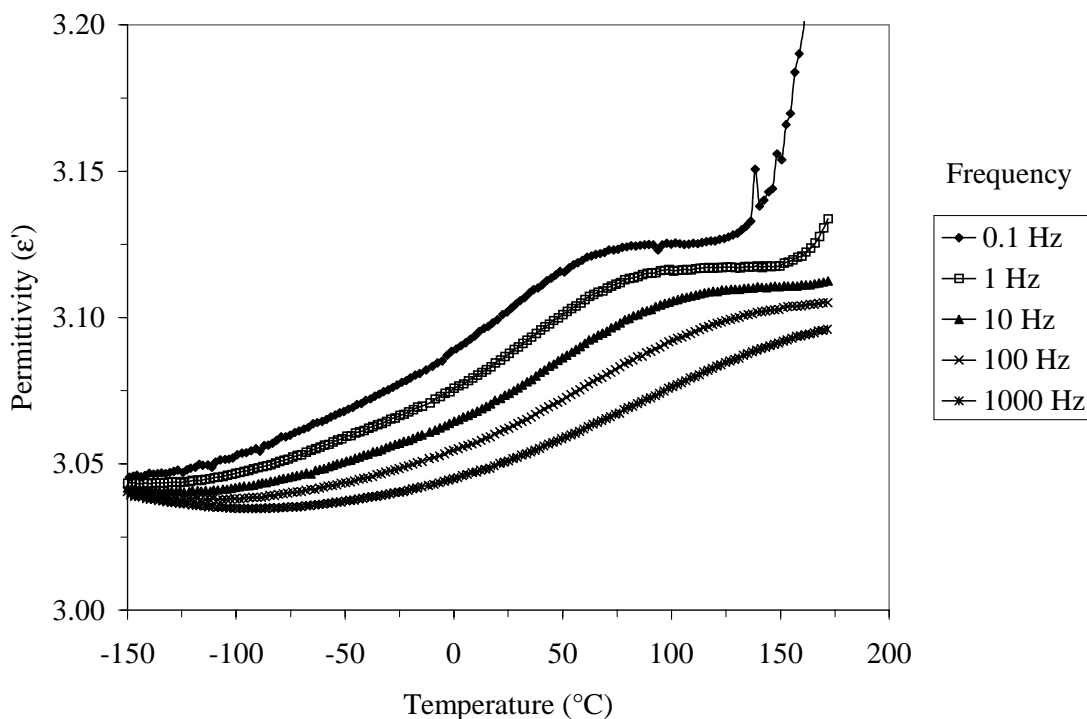


**Figure 5.10. DEA, 2<sup>nd</sup> Heating. Permittivity response of BPADA/DCHM.**

Also, note that the permittivity values in Figures 5.11-5.12 are slightly higher than the room temperature dielectric constants that were estimated from the refractive index (Table 5.5). The refractive index is measured at optical frequencies where only polarized electrons contribute to the dielectric constant; in contrast, the DEA values are measured at lower frequencies where the polarization of dipoles and electrons contribute. In addition, the thin films (0.03  $\mu\text{m}$ ) analyzed showed a tendency towards static charge, which could possibly contribute to the DEA permittivity response.

In this study, it has been demonstrated that the incorporation of the HMDA and DoDDA aliphatic diamines lower (ie. improve) the refractive index and dielectric constant relative to a fully aromatic polyimide. Next, the effect of relative humidity (RH) on the percent moisture absorption and dielectric properties are examined. It is desirable to reduce the moisture absorption of polyimides used in microelectronics applications because moisture can increase electrical conductivity, promote metal corrosion, and weaken polyimide adhesion strength to ceramics.<sup>5</sup> As a case study, the properties for BPADA/ HMDA:DoDDA, 25:75 are examined. Due to their similarity in chemical structure, the properties of this composition should be representative of BPADA/HMDA:DoDDA, 50:50 and the homopolymer, BPADA/DoDDA.

BPADA/HMDA:DoDDA, 25:75 films were conditioned in 8, 21, 29, 43, 73, and 98% RH environments and then TGA was used to determine the amount of water absorbed. The weight percent changes as a function of temperature for each RH are plotted in Figure 5.11 and the weight percent loss values at 100 °C are listed in Table 5.6. Please note the magnified y-axis scale in Figure 5.11.

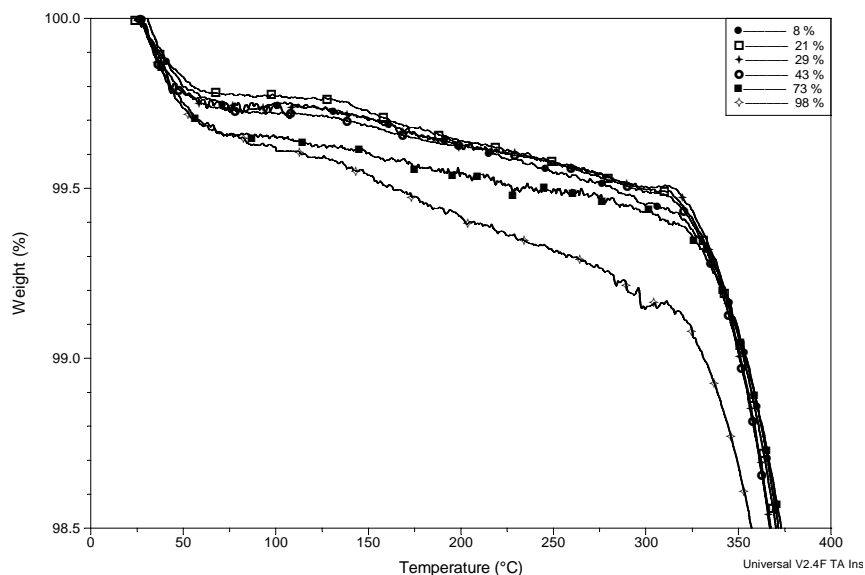


**Figure 5.11. TGA. The weight percent versus temperature for BPADA/HMDA:DoDDA, 25:75 conditioned at different relative humidities.**

**Table 5.6. TGA. Percent weight loss of BPADA/HMDA:DoDDA, 25:75 at 100 °C.**

% Relative Humidity	% Weight Loss at 100 °C <sup>a</sup>
8	0.25
21	0.23
29	0.26
43	0.28
73	0.35
98	0.39

<sup>a</sup> 10 °C/min to 600 °C in air.

The TGA experiments indicate that the films absorbed very small amounts of moisture (less than 0.4 wt%). As the RH increased from 8 to 98%, an increase in the amount of moisture absorption was detected, with the exception of the 21% RH environment; however, the absorbed moisture content may not be statistically different. The amount absorbed by BPADA/HMDA:DoDDA, 25:75 is lower than by Kapton<sup>®</sup>-E, 0.23 to 1.3 wt%, over the same range of RH (Chapter 4). The difference is attributed to the hydrophobic nature of the aliphatic HMDA and DoDDA sequences.

The effect of absorbed moisture on the dielectric properties of BPADA/HMDA:DoDDA, 25:75 was also investigated. Films were conditioned in the RH environments and then studied by

DEA. A comparison of the DEA  $\tan \delta$  curves for dry 25:75, Figure 5.6, and the DEA  $\tan \delta$  response at 1000 Hz for 25:75 conditioned by RH, Figure 5.12, reveals a moisture dependent relaxation at  $\approx -45^\circ\text{C}$ . A relaxation attributed to a crankshaft motion is detected at  $\approx -115^\circ\text{C}$ .

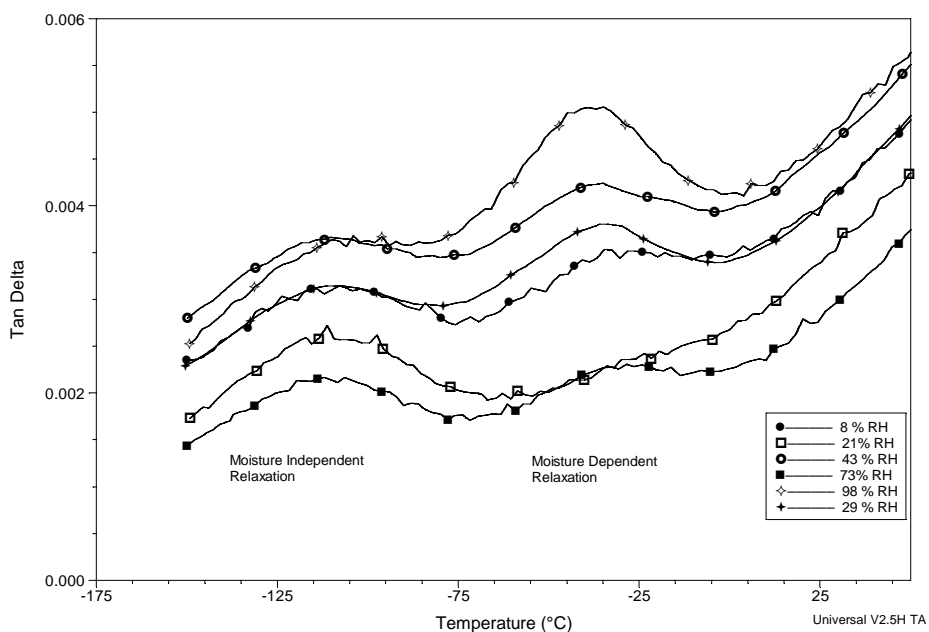


**Figure 5.12. DEA, 1<sup>st</sup> Heating, 1000 Hz. The effect of absorbed moisture on the low temperature  $\tan \delta$  response of BPADA/HMDA:DoDDA, 25:75.**

The moisture dependent relaxation for the 98% RH sample is the most pronounced and had the highest peak area. The peak areas for the remaining RH samples were similar, but a correlation between RH and peak area was not observed. Upon heating the sample a second time in the DEA, the moisture dependent relaxation disappeared. The DEA experiments suggest that although the aliphatic segments are effective in lowering the amount of moisture absorbed, the moisture could still be detrimental to device performance.

#### 5.4. CONCLUSIONS

High molecular weight, soluble, amorphous partially aliphatic polyimides were synthesized via ester-acid high temperature solution imidization. Chemical structure-physical property relationships were established. For the three polyimides, BPADA/ODA, BPADA/HMDA:ODA, 75:25, and BPADA/HMDA:DoDDA, 50:50, as the aliphatic content increased, the glass

transition temperature, thermal stability, refractive index, and dielectric constant decreased; however, the CTE increased. The physical properties of BPADA/HMDA:DoDDA, 50:50, and BPADA/HMDA:DoDDA, 25:75, did not differ appreciably due to the similarity in chemical structure and aliphatic content. The molecular origins of the sub- $T_g$   $\beta$  and  $\gamma$  viscoelastic relaxations were investigated. A crankshaft motion within the HMDA and DoDDA unit was assigned to the  $\gamma$  relaxation and a phenyl ring rotation in the ODA unit was assigned to the  $\beta$  relaxation.

Relative to BPADA/ODA, BPADA/DCHM showed a decrease in thermal stability, refractive index, and dielectric constant, and an increase in CTE; however, due to the rigidity of the DCHM, a comparable  $T_g$  value was observed. Two sub- $T_g$  viscoelastic relaxations were detected. The relaxation at  $-78$  °C is suggested to arise from isomer changes within the cyclohexyl ring. A molecular origin to the relaxation at  $60$  °C could not be assigned.

## 5.5. REFERENCES

- <sup>1</sup> Volksen, W.; Cha, H.J.; Sanchez, M.I.; Yoon, D.Y. *Reactive Functional Polymers* **1996**, 30, 61.
- <sup>2</sup> Jin, Q.; Yamahita, T.; Horie, K. *J. Polym. Sci. Polym. Chem. Ed.* **1994**, 32, 503.
- <sup>3</sup> Li, Q.; Horie, K.; Yokota, R. *Polym. J.* **1998**, 30(10), 805.
- <sup>4</sup> Chern, Y.T.; Shiue, H.C. *Macromolecules* **1997**, 30, 5766.
- <sup>5</sup> *Polyimides*; Wilson, D.; Stenzenberger, H.D.; Hergenrother, P.M., Eds.; Blackie: London, 1990; pp 57-78.
- <sup>6</sup> Kreuz, J.A.; Hsiao, B.S.; Renner, C.A.; Goff, D.L. *Macromolecules* **1995**, 28, 6926.
- <sup>7</sup> Jin, Q.; Yamahita, T.; Horie, K.; Yokota, R.; Mita, I. *J. Polym. Sci. Polym. Chem. Ed.* **1993**, 31, 2345.
- <sup>8</sup> Matsumoto, T. *Macromolecules* **1999**, 32, 4933.
- <sup>9</sup> Callister, W.D. Jr. *Materials Science and Engineering: An Introduction*, 3rd Ed.; 1994.
- <sup>10</sup> Liou, H. C.; Ho, P.S.; Stierman, R. *Thin Solid Films* **1999**, 339, 68.
- <sup>11</sup> Numata, S.; Kinjo, N. *Polym. Eng. Sci.* **1988**, 28(14), 906.
- <sup>12</sup> McCrum, N.G.; Read, B.E.; Williams, G. *Anelastic and Dielectric Effects in Polymeric Solids*; Dover: New York, 1991.
- <sup>13</sup> Eichstadt, A.E.; Ward, T.C.; Bagwell, M.D.; Farr, I.V.; Dunson, D.L.; McGrath, J.E. *J. Polym. Sci. Polym. Phys. Ed.* **2002**, 40(15), 1503.
- <sup>14</sup> Arnold, F.E.; Bruno, K.R.; Shen, D.; Eashoo, M.; Lee, C.J.; Harris, F.W.; Cheng, S.Z.D. *Polym. Eng. Sci.* **1993**, 33(21), 1372.
- <sup>15</sup> Coburn, J.C.; Soper, P. D.; Auman, B.C. *Macromolecules* **1995**, 28, 3253.
- <sup>16</sup> Li, F.; Fang, S.; Ge, J.J.; Honigfort, P.S.; Chen, J.C.; Harris, F.W.; Cheng, S.Z.D.; *Polymer* **1999**, 40, 4987.
- <sup>17</sup> Li, F.; Fang, S.; Ge, J.J.; Honigfort, P.S.; Chen, J.C.; Harris, F.W.; Cheng, S.Z.D. *Polymer* **1999**, 40, 4571.

- 
- <sup>18</sup> Heijboer, J. In *Molecular Basis of Transitions and Relaxations*; Meier, D.J., Ed.; Gordon and Breach Science: New York, 1978; pp 75-102 and pp 297-310.
- <sup>19</sup> Starkweather, H.W., Jr.; Avakian, P. *Macromolecules* **1989**, *22*, 4060.
- <sup>20</sup> Starkweather, H.W., Jr. *Macromolecules* **1981**, *14*, 1277.
- <sup>21</sup> Atkins, P. *Physical Chemistry*, 5<sup>th</sup> ed.; Freeman: New York, 1994; pp 761-762.
- <sup>22</sup> Ando, S.; Matsuura, T.; Sasaki, S. *Polym. J.* **1997**, *29(1)*, 69.
- <sup>23</sup> St.Clair, A.K.; Slep, W.S. *SAMPE Journal* **1985**, *21(4)*, 28.
- <sup>24</sup> Eftekhari, A.; St. Clair, A.K.; Stoakley, D.M.; Sprinkle, D. R.; Singh, J.J. In *Polymers for Microelectronics: Resists and Dielectrics*; Thompson, L.F.; Wilson, C.G.; Tagawa S., Eds.; ACS Symposium Series 537; American Chemical Society: Washington, D.C., 1994; pp 535-545.
- <sup>25</sup> Simpson, J.O.; St. Clair, A.K. *Thin Solid Films* **1997**, *308-309*, 480.

## 6. STRUCTURE - PROPERTY RELATIONSHIPS FOR THE BPADA/ODA:DoDDA SERIES

### 6.1. Introduction

This chapter discusses the physical property characterization of a series of partially aliphatic polyimides obtained from bis[4-(3,4-dicarboxyphenoxy)phenyl]propane dianhydride, or Bisphenol A dianhydride (BPADA), and the diamines, 4,4'-oxydianiline (ODA) and dodecyl diamine (DoDDA). Incorporation of both rigid aromatic and flexible aliphatic diamines allowed the thermal and mechanical properties to be tailored for specific adhesive applications. This chapter presents molecular weight, thermal, dielectric, and mechanical data to establish structure-property relationships, and discusses the molecular origins of the  $\gamma$  and  $\beta$  sub- $T_g$  viscoelastic relaxations. Each physical property is then interpreted to extend the molecular understanding of the adhesion strength of partially aliphatic polyimides to SiO<sub>2</sub>/Si. Chapter 7 follows with a discussion on the adhesive testing of each polyimide in the BPADA/ODA:DoDDA series to SiO<sub>2</sub>/Si.

### 6.2. Materials

The BPADA/ODA:DoDDA series of partially aliphatic polyimides included ODA:DoDDA diamine molar ratios of 100:0, 75:25, 50:50, 25:75, and 0:100. Thus, the series included both the homopolymers BPADA/ODA and BPADA/DoDDA, and random copolyimides from the intermediate molar ratios. The monomer chemical structures are presented in Chapter 3, section 3.3.

### 6.3. Results and Discussion

The solubility of the polyimides allowed accurate molecular weight characterization of all of the fully-cyclized polyimides. Table 6.1 lists the molecular weights and polydispersities for the different polyimide compositions. The ester-acid solution imidization yields high molecular weights and polydispersity values around 2.2. The accuracy and ease of this measurement contrasts with the determination of the molecular weights of many aromatic or partially aliphatic polyimides synthesized through the traditional two-step method, which are typically estimated from the molecular weight of the poly(amic acid).<sup>1,2,3</sup>

**Table 6.1. Molecular Weight and Thermal Characterization of BPADA/ODA:DoDDA Series.**

Polyimide	Diamine Molar Ratio	$\langle M_n \rangle$ (kg/mol)	$\langle M_w \rangle / \langle M_n \rangle$	T <sub>g</sub> (°C) DSC*	T <sub>deg</sub> (°C) TGA**
BPADA / ODA	1	54.0	2.9	224	514
BPADA / ODA:DoDDA, 75:25	0.75 : 0.25	48.3	2.2	186	475
BPADA / ODA:DoDDA, 50:50	0.50 : 0.50	33.6	2.3	140	461
BPADA / ODA:DoDDA, 25:75	0.25 : 0.75	29.6	2.0	112	432
BPADA / DoDDA	1	28.5	2.2	82	430

\* T<sub>g</sub> reported from second heating cycle in nitrogen.

\*\* 5% weight loss degradation temperature in air.

Table 6.1 also lists the glass transition temperatures and thermal degradation temperatures (5% weight loss) for the BPADA/ODA:DoDDA series. The fully aromatic BPADA/ODA possessed the highest T<sub>g</sub> and best thermal stability, as expected. The high glass transition temperature of BPADA/ODA is due to the rigid, predominantly aromatic, backbone structure and formation of strong intermolecular complexes. The thermal stability of BPADA/ODA is attributed to the high content of strong aromatic covalent bonds. Table 6.1 shows that as the aliphatic content increases, the T<sub>g</sub> and thermal stability decrease. The DoDDA methylene units impart flexibility to the backbone and allow cooperative segmental motions associated with the T<sub>g</sub> to initiate at lower temperatures. While, the thermal stability decreased due to the susceptibility of the methylene units to oxidative degradation, the lower T<sub>g</sub> should facilitate melt processing.

The linear coefficients of thermal expansion (CTE) were next examined for the BPADA/ODA:DoDDA series. The CTE values were calculated according to equation 5.1. Figure 6.1 illustrates the change in sample dimension with temperature for BPADA/ODA:DoDDA, 75:25. The results shown in Figure 6.1 are representative of the BPADA/ODA:DoDDA series. Three heating cycles and two cooling cycles are plotted. The first heating cycle is marked.

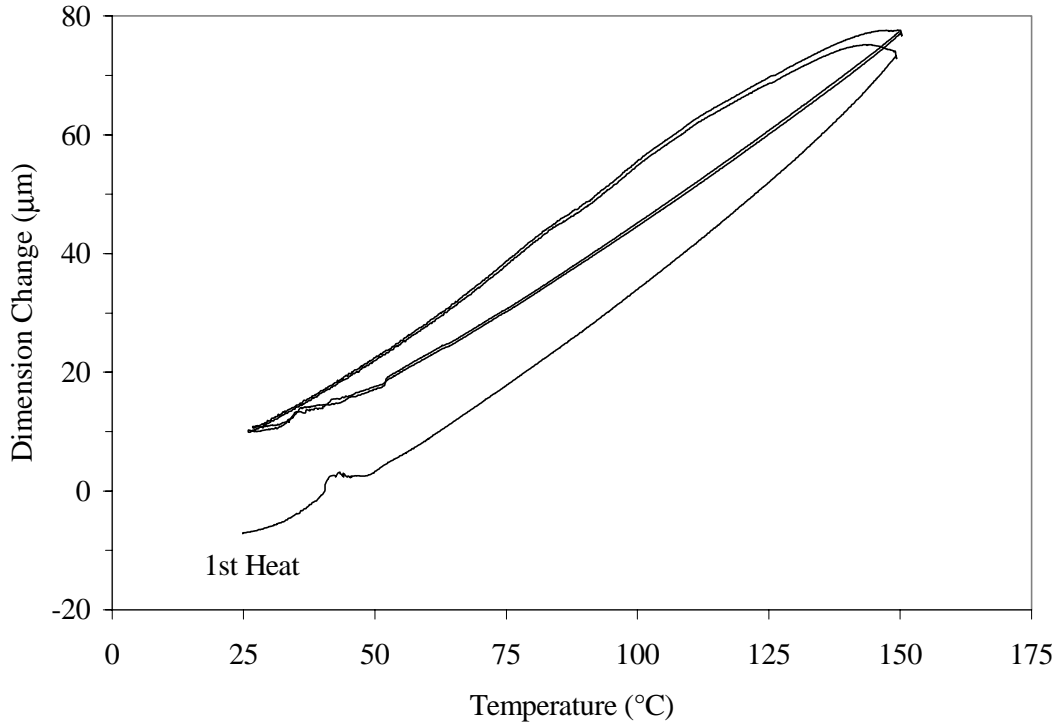


**Figure 6.1. Dimension change versus temperature for BPADA/ODA:DoDDA, 75:25.**

The dimension change with temperature for the first heating cycle differs from the subsequent heating cycles and reflects the sample preparation history. During the first heating cycle, absorbed moisture and residual stresses were released. Figure 6.1 shows that the cooling curves are different from the heating curves. This is due to thermal lag in the DMA furnace; if the heating/cooling rates are decreased, the envelope size will decrease. Using the initial sample length and slopes of the second and third heating cycles the linear CTEs were calculated according to equation 5.1. The average linear CTE values are presented in Table 6.2.

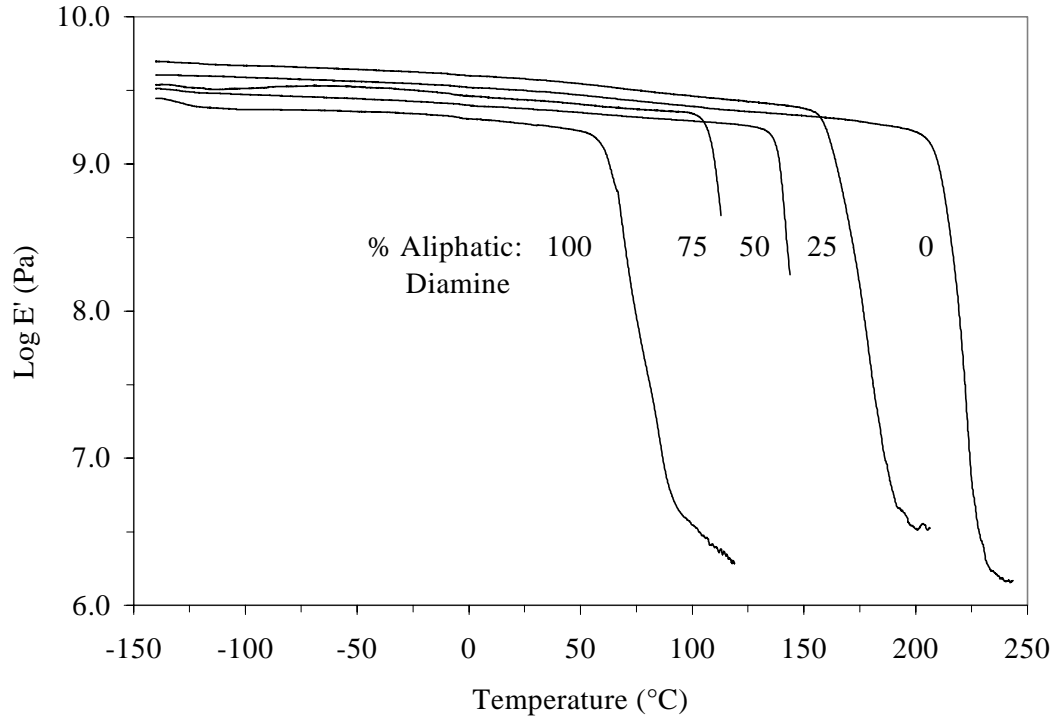
**Table 6.2. Linear Coefficients of Thermal Expansion.**

Polyimide	CTE (ppm/°C) <sup>a</sup>
BPADA / ODA	31.0
BPADA / ODA:DoDDA, 75:25	41.6
BPADA / ODA:DoDDA, 50:50	46.4
BPADA / ODA:DoDDA, 25:75	51.4
BPADA / DoDDA	59.5

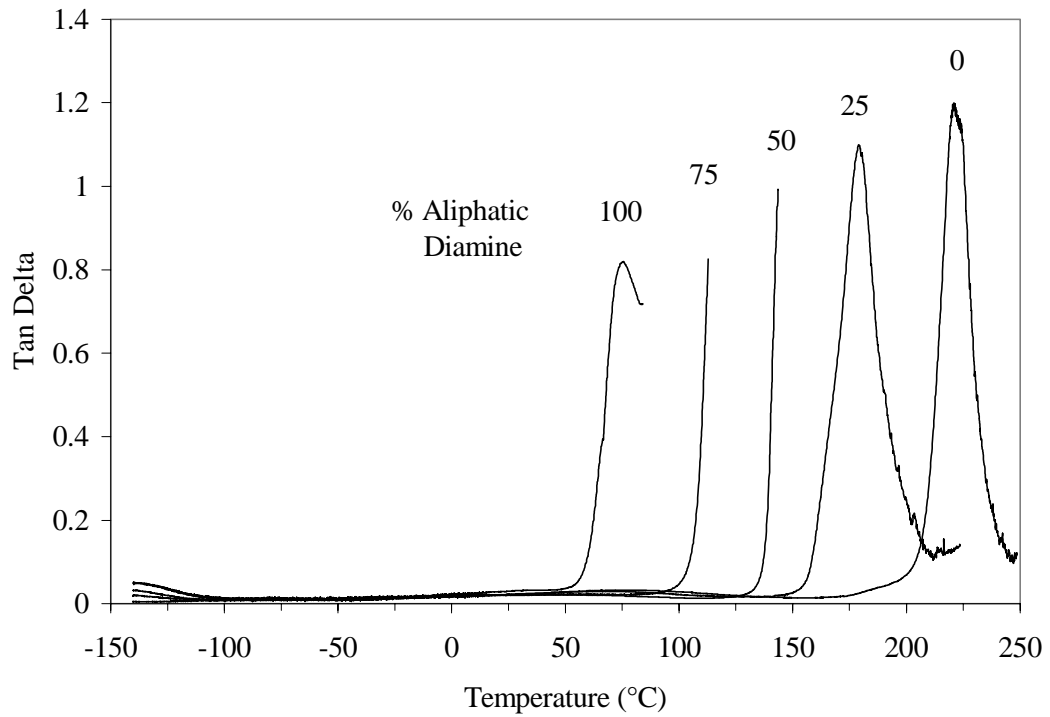
<sup>a</sup>  $l_0 \approx 14$  mm.

Table 6.2 shows that as the aliphatic content increases, the CTE increases. The low CTE of BPADA/ODA is rationalized as due to the aromatic covalent bonds within its backbone and the intermolecular interactions between ODA and BPADA units on neighbor polyimide chains.<sup>4,5</sup> As the aliphatic content increases, and correspondingly the ODA content decreases, weaker covalent bonds within the polymer backbone are present and also fewer intermolecular interactions contribute. The number of intermolecular interactions possible is further reduced by the flexibility of the aliphatic units which add free volume and thus lower intermolecular forces.

The viscoelastic relaxations of the BPADA/ODA:DoDDA series were studied using DMA. A strong correlation was observed between the glass transition temperature and the percent aliphatic content. These data were consistent with that determined from DSC; as the aliphatic content increased, the  $T_g$  decreased. Figure 6.2a and Figure 6.2b display overlays of log storage modulus ( $E'$ ) versus temperature and tan delta versus temperature, respectively, for the five polyimides.



(a)



(b)

**Figure 6.2. The dependence of the glass transition temperature on the percent aliphatic diamine. DMA, 1 Hz. (a) Storage Modulus,  $E'$  b) Tan Delta.**

Sample elongation within the  $T_g$  for the 50% and 75% aliphatic diamine samples prevented the acquisition of a complete tan delta peak. Table 6.3 lists the glass transition temperatures calculated from the onset of rapid decrease in the storage modulus ( $E'$ ) and also from the tan delta measurements.

**Table 6.3. DMA Glass Transition Temperatures, 1 Hz.**

Polyimide	$T_g$ (°C)	$T_g$ (°C)
	Storage Modulus*	Tan Delta**
BPADA / ODA	201	222
BPADA / ODA:DoDDA, 75:25	158	181
BPADA / ODA:DoDDA, 50:50	133	n/a
BPADA / ODA:DoDDA, 25:75	104	n/a
BPADA / DoDDA	56	72

\* Onset Temperature.

\*\* Peak Maximum.

An average  $E'$  value at 25 °C was determined for each polyimide from four replicate DMA experiments. These values are presented in Figure 6.3. While the average  $E'$  value shows a general decreasing trend with increasing aliphatic content, within the error, only the  $E'$  values of the homopolymers BPADA/ODA and BPADA/DoDDA significantly differ.

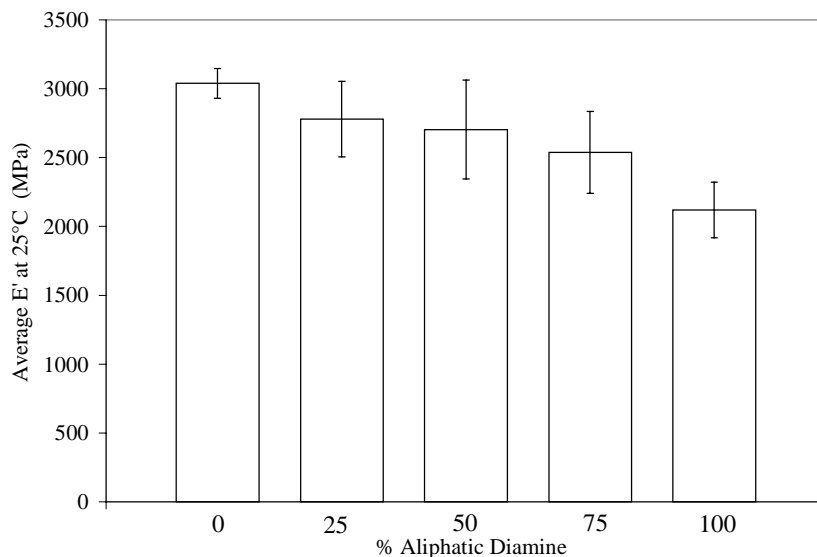


**Figure 6.3. Average Storage Modulus,  $E'$ , at 25°C.**

The average  $E'$  values are comparable to the tensile modulus value, 3140 MPa, reported for a similar partially aliphatic polyimide, BTDA/HMDA (3,3',4,4'-benzophenonetetracarboxylic dianhydride and 1,6-hexanediamine).<sup>1</sup> The average  $E'$  values are much lower, however, than measured for Kapton<sup>®</sup>-E (Chapter 4). This is not surprising given the film orientation and rigid monomers which comprise Kapton<sup>®</sup>-E.

DMA also revealed two sub- $T_g$ , local viscoelastic relaxations (Figure 6.4): (1) a crankshaft motion attributed to the DoDDA units at  $\approx -140$  °C, and (2) a phenyl ring torsional rotation attributed to the ODA units at  $\approx 50$  °C. The relaxations are termed the  $\gamma$  and  $\beta$  relaxation, respectively. These associations were made by comparison to prior viscoelastic studies of aromatic polyimides and polyethylene.<sup>6-10</sup> The methylene unit cooperative crankshaft motions have been observed within nylon 66, in polyesters, and in oxide polymers which contain linear  $(CH_2)_{n \geq 4}$  sequences that are separated by immobile groups.<sup>10</sup> Figure 6.4 also shows that some of the polyimides possessed a small relaxation in the temperature range  $-100$  to  $-50$  °C. This relaxation is thought to arise from residual NMP in the films because it was not observed in all of the replicate DMA experiments and it was not observed in the dielectric experiments, in which two heating cycles were performed.

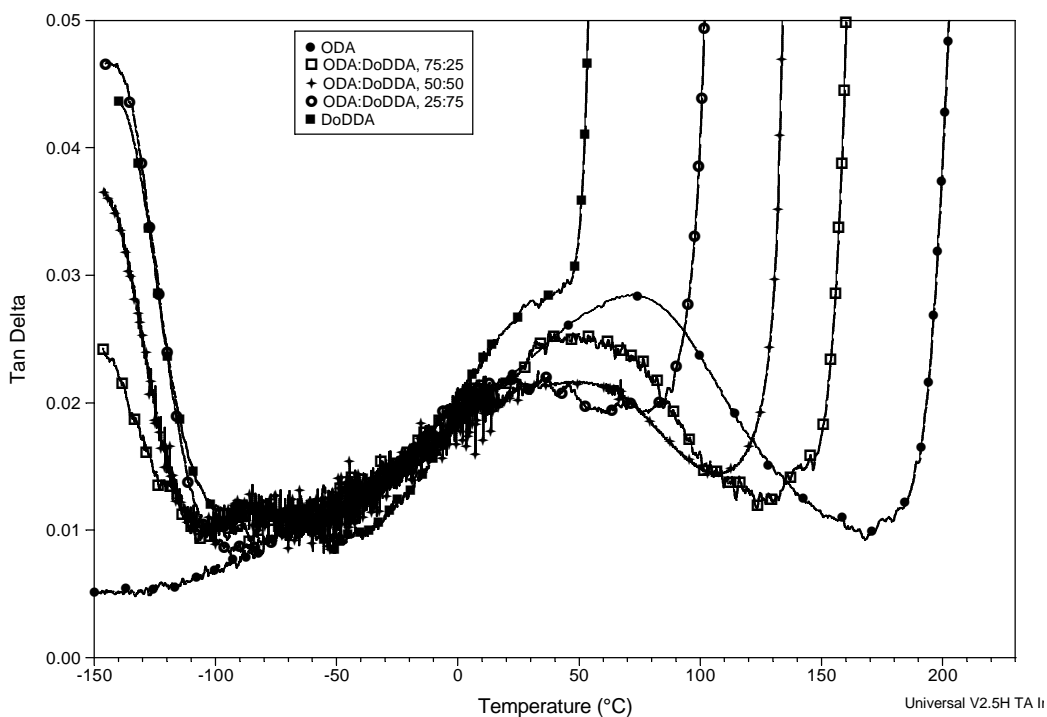


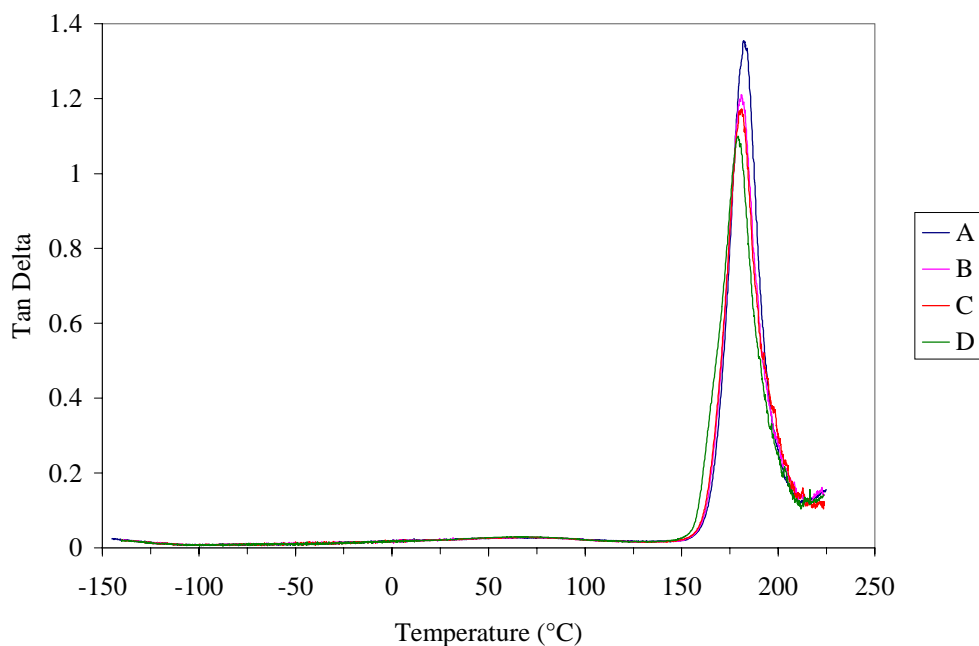
**Figure 6.4. Sub-Tg DMA responses at 1 Hz.**

The variations in polyimide chemical composition are reflected in the tan delta signal. As the DoDDA content increases, the magnitude of the  $\gamma$  relaxation increases. While an increase in DoDDA content from 75% to 100% decreases the  $T_g$  by  $\approx 40$  °C, little change in the  $\gamma$  relaxation magnitude results. For these two chemical compositions, it appears that large scale cooperative backbone motions are influenced by DoDDA, but the  $\gamma$  local motions are not.

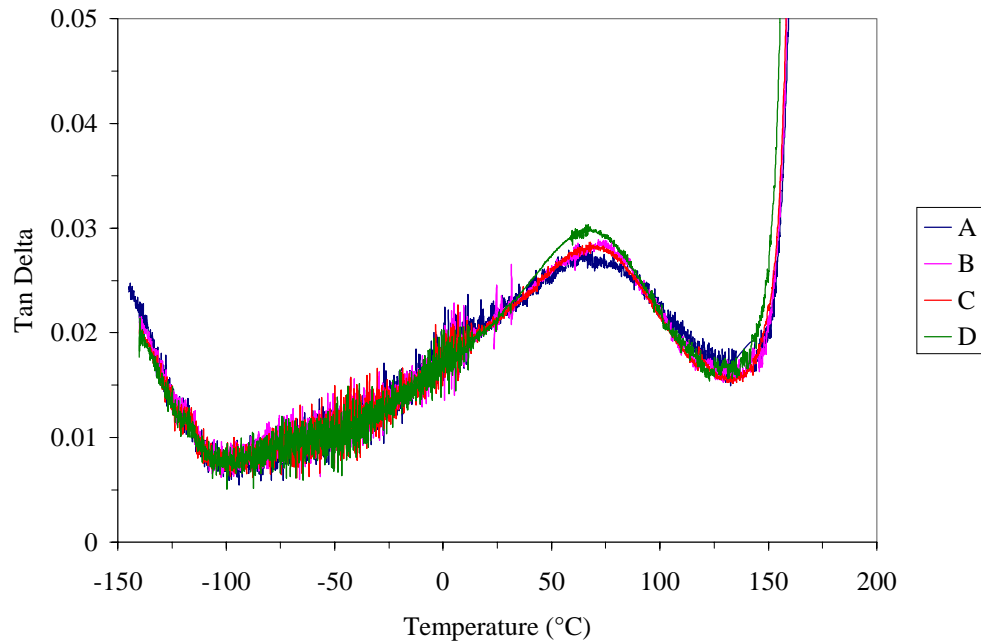
In the  $\beta$  relaxation temperature range (Figure 6.4), three key observations can be made. First, for the four polymers containing ODA, the  $\beta$  relaxation initiates at approximately  $-47$  °C; increasing the ODA content should not change the rotational potential energy of the phenyl ring. Studies on the influence of substitution of the phenyl ring with  $-\text{CH}_3$  and  $-\text{CF}_3$  on the phenyl ring rotational potential energy, and the temperature position of the  $\beta$  relaxation, support the argument.<sup>6-9</sup> Second, as the ODA content increases, the  $\beta$  relaxation peak maximum shifts to higher temperatures. Third, as the ODA content increases, the  $\beta$  relaxation peak area increases. These last two observations arise from the broadening of the distribution of relaxation times as the ODA content and the backbone rigidity increase. The temperature of the  $\beta$  peak maximum

reflects both a high average number of ODA units in motion and large internal segmental friction energy loss. Similar observations are reported for the  $\beta$  relaxation of polycarbonate.<sup>10</sup> The BPADA/DoDDA curve exhibits a shoulder around 25 °C; however, the underlying molecular motions are unknown. In summary, the polyimide backbone rigidity has a large effect on the temperature location of the  $T_g$  and the  $\beta$  relaxation, but less of an effect of the location of the  $\gamma$  relaxation. The  $\gamma$  relaxation involves a smaller volume of relaxation and is thus less influenced by its distant environment.

The  $\beta$  relaxation is of particular interest since it traverses the temperature range of practical microelectronics device operation. To quantify energy dissipation, the  $\beta$  relaxation peak area was determined as a function of percent aliphatic diamine. Four replicate DMA experiments at a frequency of 1 Hz were performed for each polyimide in the series. A random number generator was used to determine the order of the twenty experiments. Figure 6.5 and Figure 6.6 present overlays of the tan delta versus temperature responses for the four BPADA/ODA:DoDDA, 75:25 samples.

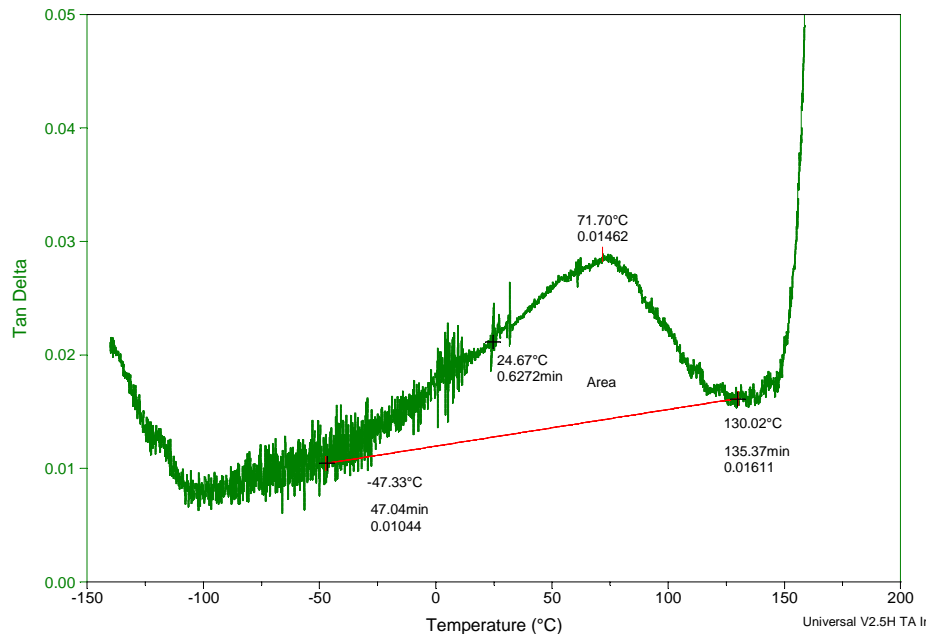


**Figure 6.5. Four replicate DMA experiments, 1 Hz, for BPADA/ODA:DoDDA, 75:25. Plot highlights the  $T_g$ .**



**Figure 6.6. Four replicate DMA experiments, 1 Hz, for BPADA/ODA:DoDDA, 75:25. Plot highlights the  $\gamma$  and  $\beta$  sub- $T_g$  relaxations.**

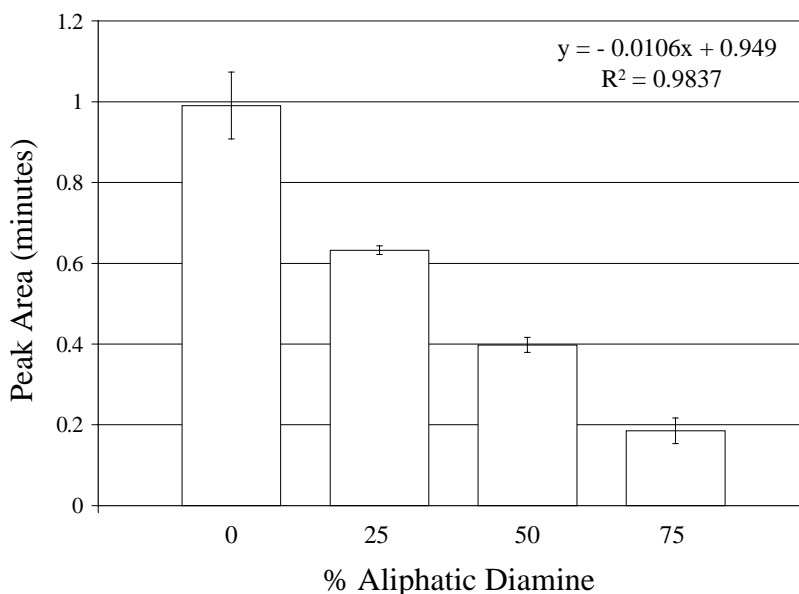
The  $\beta$  relaxation peak area was calculated from the tan delta signal for each polyimide by establishing a linear baseline and then integrating the peak with respect to time. An example calculation for BPADA/ODA:DoDDA, 75:25, sample B, is shown in Figure 6.7.



**Figure 6.7. Example calculation of the  $\beta$  relaxation peak area using a linear baseline. Sample is BPADA/ODA:DoDDA, 75:25 B.**

Figure 6.7 shows the typical values used for the  $\beta$  relaxation peak area calculation. The  $\beta$  relaxation onset temperature was  $-47.33$  °C and the tan delta value at this temperature was 0.01044. The temperature at the peak maximum was  $71.7$  °C and the peak height, defined as the difference in tan delta values for the baseline (at  $71.7$  °C) and the peak maximum, was 0.01462. The temperature at which the peak returns to the baseline was  $130.02$  °C and the tan delta value at this temperature was 0.01611. The tan delta signal was integrated with respect to time to calculate a peak area of 0.6272 minutes. The unit of the area is minutes because tan delta is dimensionless. This procedure was adopted for all the polyimides.

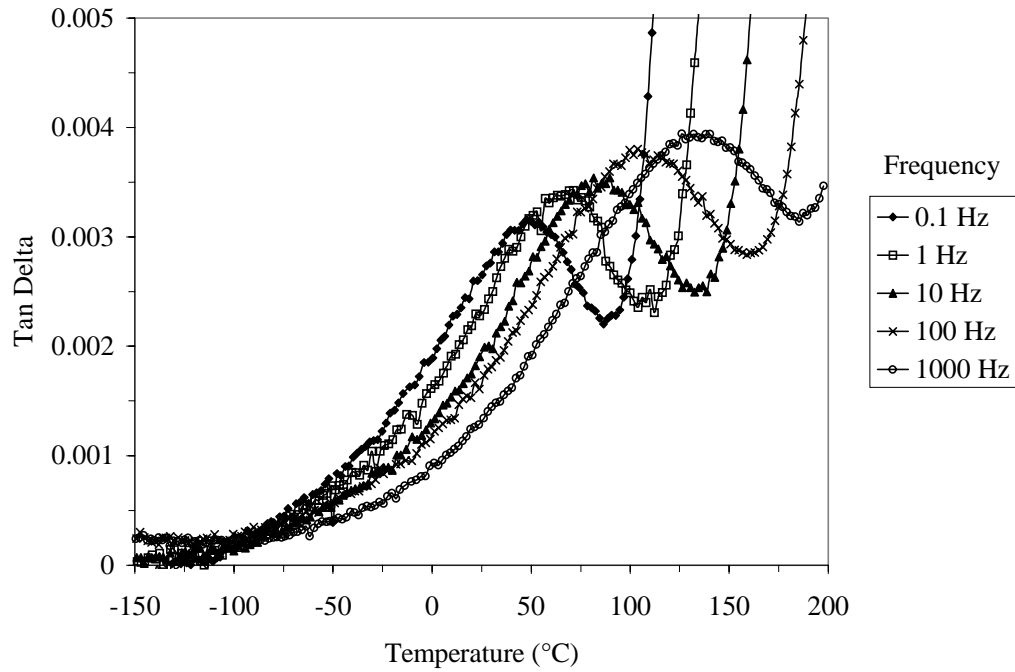
Figure 6.8 is a plot of the average  $\beta$  relaxation peak area as a function of percent aliphatic diamine. The error bars represent one standard deviation.



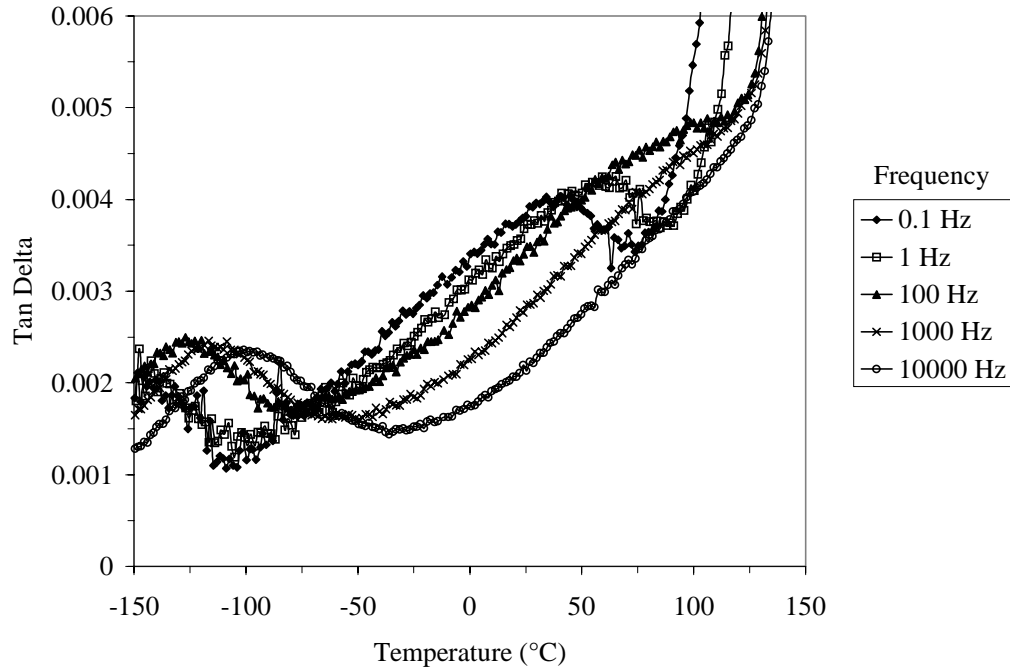
**Figure 6.8.  $\beta$  relaxation tan delta peak area.**

Figure 6.8 reveals that as the percent DoDDA increases (corresponding to a decrease in ODA content), the  $\beta$  relaxation peak area systematically decreases through a linear relationship ( $y = -0.0106x + 0.949$ , with  $R^2 = 0.9837$ ). That is, within the  $\beta$  relaxation temperature range and for a frequency of 1 Hz, as the ODA content decreases, there is less contribution to  $\phi(R,T)$  within the theory of adhesion. Figure 6.8 provides further evidence that the torsional rotation of the phenyl ring of ODA is the source of the  $\beta$  relaxation.

Examination of the viscoelastic properties by DEA also revealed two sub- $T_g$ , local viscoelastic relaxations. A  $\beta$  relaxation for the polyimides containing ODA was observed at  $\approx 50$  °C (1 Hz). A  $\gamma$  relaxation for the polyimides containing DoDDA was observed at  $\approx -140$  °C (1 Hz). Figure 6.9, Figure 6.10, and Figure 6.11 show the dielectric tan delta signal frequency dependence of the sub- $T_g$  relaxations for BPADA/ODA, BPADA/ODA:DoDDA, 50:50, and BPADA/DoDDA, respectively. Figure 6.12 and Figure 6.13 show the dielectric tan delta signal frequency dependence of the  $T_g$  relaxation for BPADA/ODA:DoDDA, 50:50 and BPADA/DoDDA, respectively. For each set of tan delta curves, as the frequency increases, the relaxations shift to higher temperatures.



**Figure 6.9. DEA, 2<sup>nd</sup> Heating. The frequency dependence of the  $\beta$  relaxation for BPADA/ODA.**



**Figure 6.10. DEA, 2<sup>nd</sup> Heating. The frequency dependence of the  $\gamma$  and  $\beta$  relaxations for BPADA/ODA:DoDDA, 50:50.**

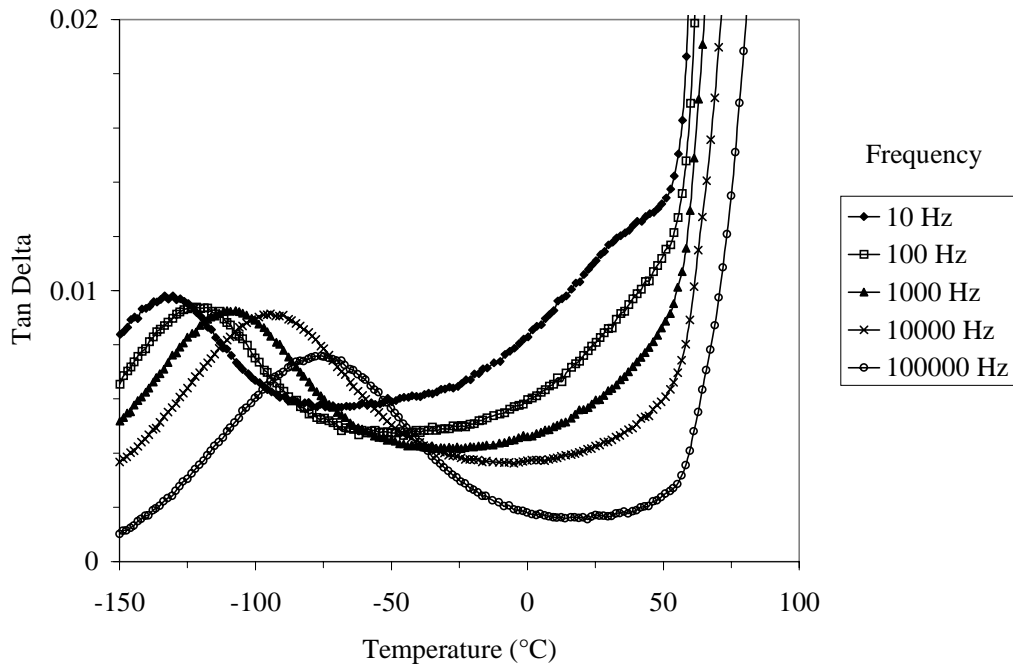


**Figure 6.11. DEA, 2<sup>nd</sup> Heating. The frequency dependence of the  $\gamma$  relaxation for BPADA/DoDDA.**

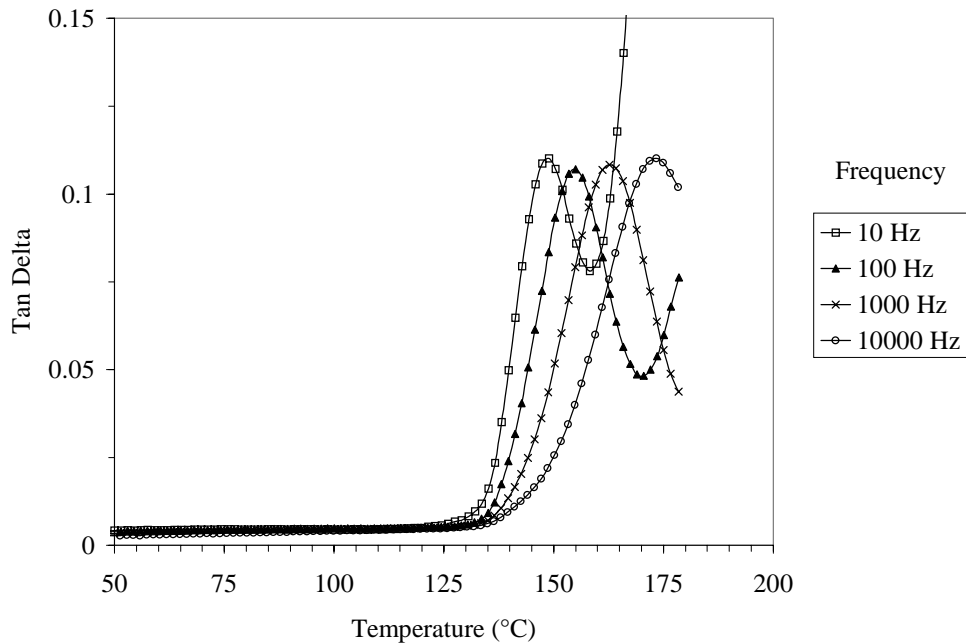


**Figure 6.12. DEA, 2<sup>nd</sup> Heating. Frequency dependence of the  $T_g$  for BPADA/ODA:DoDDA, 50:50.**

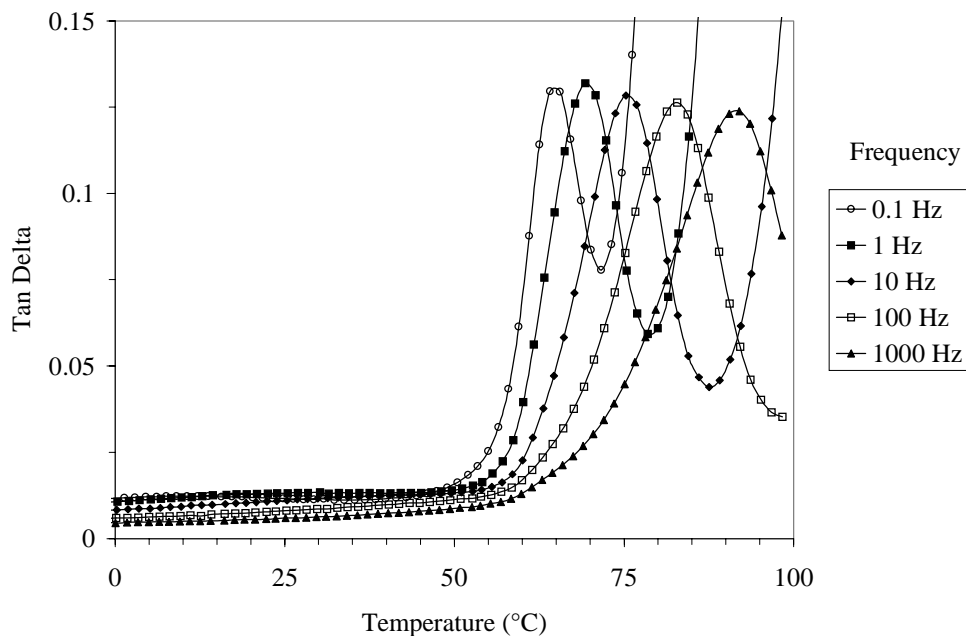


**Figure 6.13. DEA, 2<sup>nd</sup> Heating. The frequency dependence of the  $T_g$  for BPADA/DoDDA.**

The DEA sub- $T_g$  relaxation tan delta peak areas do not show the same linear variation with chemical composition as do the DMA results; however, the same molecular origins are assigned to the sub- $T_g$  relaxations based on their Arrhenius activation energy. The discussion of the Arrhenius activation energies and their calculation in Chapter 5 applies to the BPADA/ODA:DoDDA series as well. Figure 6.14 illustrates the log frequency versus  $1/T$  relationships and the best fit lines distinguish the three types of relaxations.

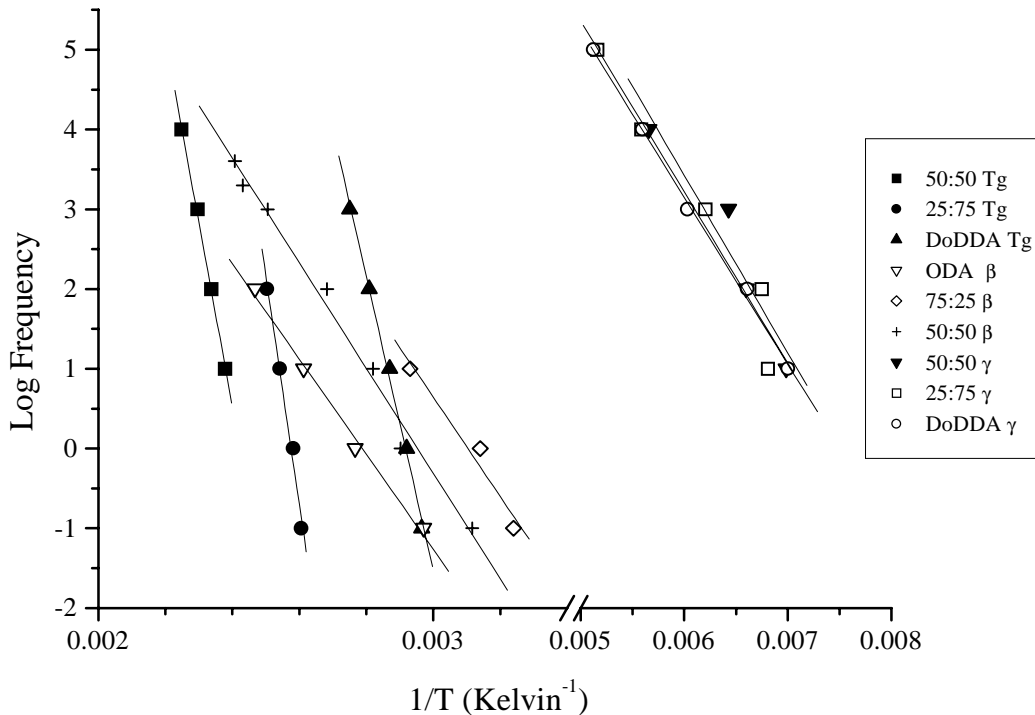


**Figure 6.14. Log frequency versus 1/T for the DEA  $\gamma$ ,  $\beta$ , and  $T_g$  relaxations of several BPADA/ODA:DoDDA polyimides.**

In Figure 6.14, note that the slopes of the lines for the glass transition temperatures are steeper than those for the  $\beta$  and  $\gamma$  relaxations. The high slope indicates a much higher activation energy and a different volume and environment of the moving segments. Table 6.4 presents the DEA Arrhenius activation energies calculated for the glass transition, the  $\beta$  relaxation, and the  $\gamma$  relaxation for each of the polyimides using the slopes of the best fit lines.

**Table 6.4. DEA Arrhenius Activation Energies.**

Polyimide	Activation Energy (kJ/mol)		
	$\gamma$ Relaxation	$\beta$ Relaxation	$\alpha$ Relaxation ( $T_g$ )
BPADA / ODA	a	126.2	c
BPADA / ODA:DoDDA, 75:25	b	114.3	c
BPADA / ODA:DoDDA, 50:50	42.6	119.2	441.2
BPADA / ODA:DoDDA, 25:75	41.5	b	548.9
BPADA / DoDDA	40.3	a	352.0

a) relaxation not present; b) relaxation observed, but the Arrhenius fit was poor; c) conductivity obscured the  $T_g$

The similarity in the activation energy for the  $\gamma$  and  $\beta$  relaxations suggests a common molecular origin. The  $\gamma$  relaxation  $E_a$  of  $\approx 41$  kJ/mol ( $\approx 9.8$  kcal/mol) agrees well with the value of 11 kcal/mol reported for polyethylene and further confirms the assignment of a crankshaft motion.<sup>10</sup> Mechanical and dielectric activation energies for the  $\beta$  relaxation of aromatic polyimides are in the range 95-150 kJ/mol.<sup>6-9</sup> The order of magnitude agrees well with the values 114-126 kJ/mol calculated for the BPADA/ODA:DoDDA polyimides. Table 6.4 also shows that the activation energies for the  $T_g$  are much higher than for the local, sub- $T_g$  relaxations. This is characteristic of the thermal energy needed to activate the highly cooperative chain motions involved in the glass transition.<sup>12</sup>

Structure-property relationships for the refractive index and dielectric constant were also investigated. The  $\epsilon_r$  were estimated from the refractive indices using a relation deduced from Maxwell's equations as described by equation 5.3. The discussion from Chapter 5 applies here as well. Table 6.5 lists the refractive indices and estimated relative dielectric constants ( $\epsilon_r$ ) for the BPADA/ODA:DoDDA series.

**Table 6.5. Refractive Index and Dielectric Constant.**

Polyimide	Refractive Index	Dielectric Constant via Refractive Index
BPADA / ODA	1.662	2.762
BPADA / ODA:DoDDA, 75:25	1.645	2.706
BPADA / ODA:DoDDA, 50:50	1.632	2.663
BPADA / ODA:DoDDA, 25:75	1.617	2.614
BPADA / DoDDA	1.600	2.560

Table 6.5 shows that as the DoDDA content increases the refractive index decreases; the materials become more “transparent.” The increased transparency is attributed to the reduction of charge transfer complexes between neighbor polyimide chains and the reduction of extended conjugation along the polyimide backbone.<sup>1,13</sup> Similar findings were reported for polyimides containing alkyl groups.<sup>14</sup> Table 6.5 also shows that the  $\epsilon_r$  decreases with increasing DoDDA content due to the presence of fewer polarizable functional groups. The decrease in chain linearity is also expected to contribute to the decrease in  $\epsilon_r$ .<sup>15,16</sup>

The temperature dependence of the dielectric constant was examined from the DEA permittivity ( $\epsilon'$ ) response. The permittivity response for BPADA/ODA is illustrated in Figure 6.15.

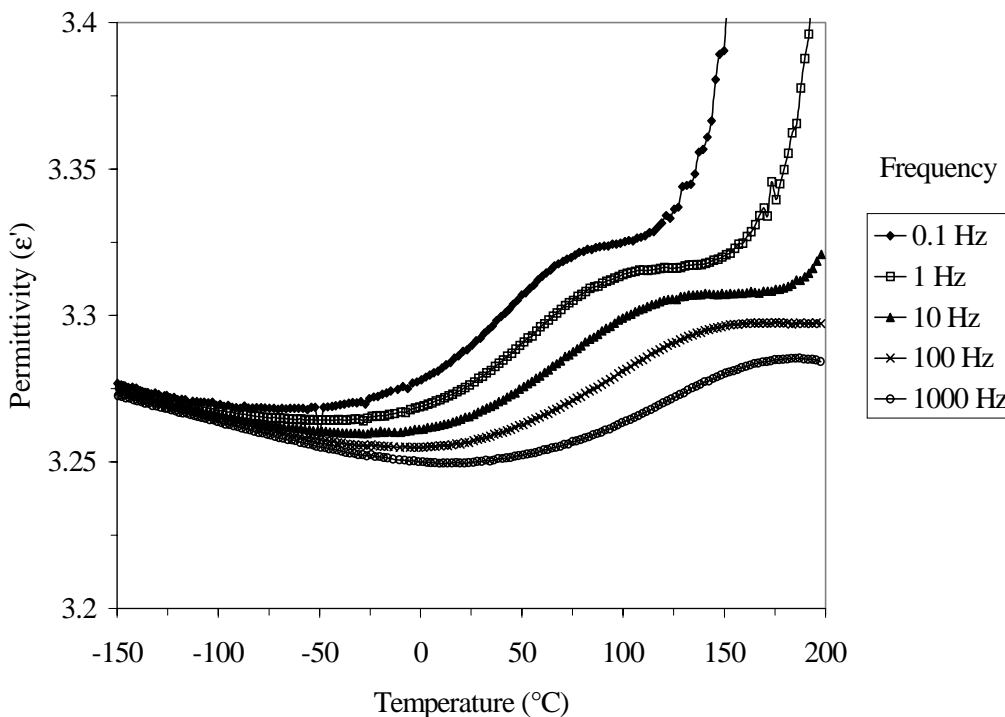


**Figure 6.15. DEA, 2<sup>nd</sup> Heating. Permittivity response for BPADA/ODA.**

Figure 6.15 shows a step-increase in the dielectric permittivity at the temperature of the  $\beta$  relaxation. The segmental mobility allows for alignment of the dipoles which results in an increase in the permittivity. The material becomes less insulative. For the polyimides containing ODA, the increase in the permittivity is  $\approx 0.05$ . A similar step-increase at the temperature at the  $\gamma$  relaxation was observed for the polyimides containing DoDDA. The permittivity increase for the  $\gamma$  relaxation is  $\approx 0.015$ . Figure 6.16 illustrates the permittivity step-increases due to the  $\gamma$  and  $\beta$  relaxations for BPADA/ODA:DoDDA, 50:50.

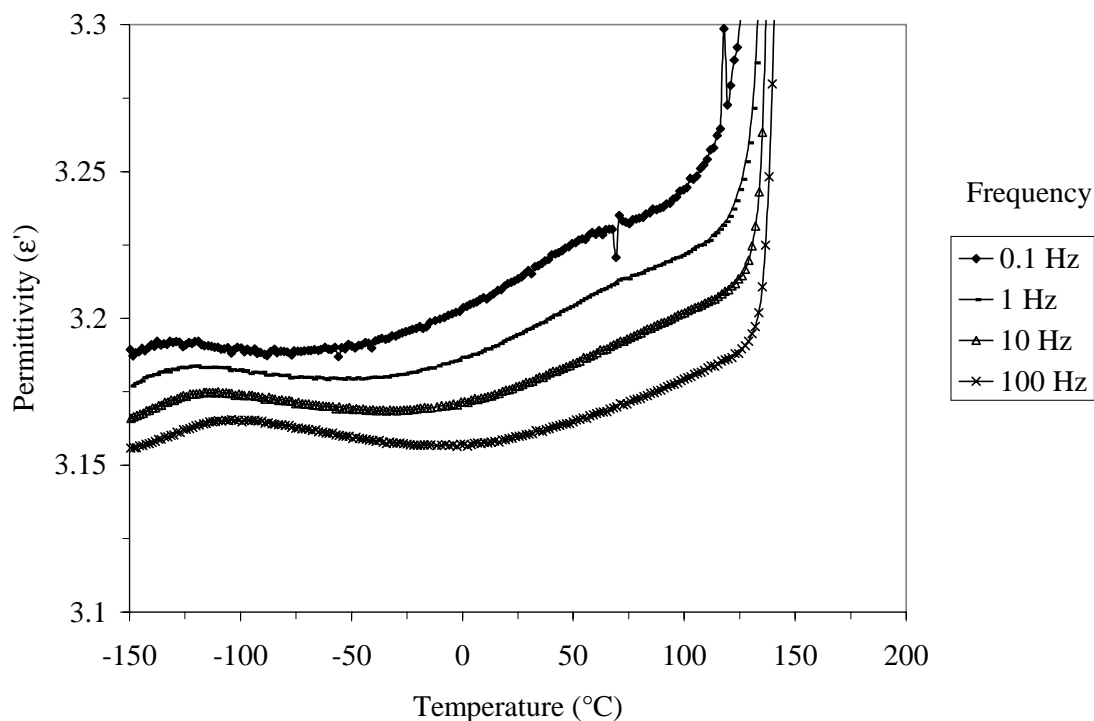


**Figure 6.16. DEA, 2<sup>nd</sup> Heating. Permittivity response for BPADA/ODA:DoDDA, 50:50.**

The difference in step-increase values reflects the difference in the molecular origin of the  $\gamma$  and  $\beta$  relaxations. The dipoles which align due to the crankshaft motion are very weak and some dipolar contribution is thought to be from its near environment. Stronger dipoles are present in the ODA units, thus leading to a larger step-increase. Also note that the permittivity values within Figure 6.15 and Figure 6.16 are slightly higher than the room temperature dielectric constants estimated from the refractive index (Table 6.5). The refractive index is measured at optical frequencies where only polarized electrons contribute to the dielectric constant; the DEA values are measured at lower frequencies where the polarization of dipoles and electrons contribute.

It was expected that as the ODA content increased, a simultaneous increase in the permittivity step-increase would occur due to the increase in the number of dipoles. A similar trend was expected with increasing DoDDA content. However, no clear trend was observed for either relaxation. The effect was possibly due to the sensitivity of the DEA to slight changes in moisture content and static charge.

The stress-strain properties of the BPADA/ODA:DoDDA series were measured to determine Young's Modulus ( $E$ ) and the yield stress ( $\sigma_y$ ) as a function of chemical composition. The stress versus strain % for BPADA/ODA is presented in Figure 6.17. As demonstrated in Figure 6.18,  $E$  was calculated from the initial linear slope (2293.5 MPa). From the point of deviation from the initial linear slope,  $\sigma_y$  (40 MPa) was taken. Figure 6.17 shows that two of the BPADA/ODA samples had a  $\sigma_{\text{uts}}$  of  $\approx 82$  MPa, and showed good ductility.

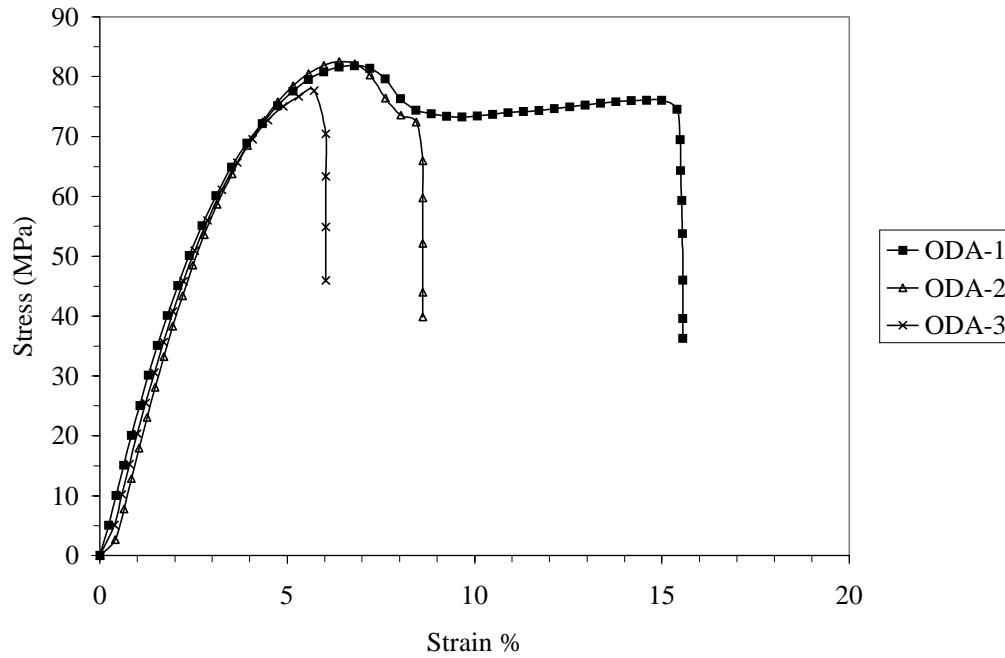


**Figure 6.17. Stress versus strain % for BPADA/ODA in tension.**

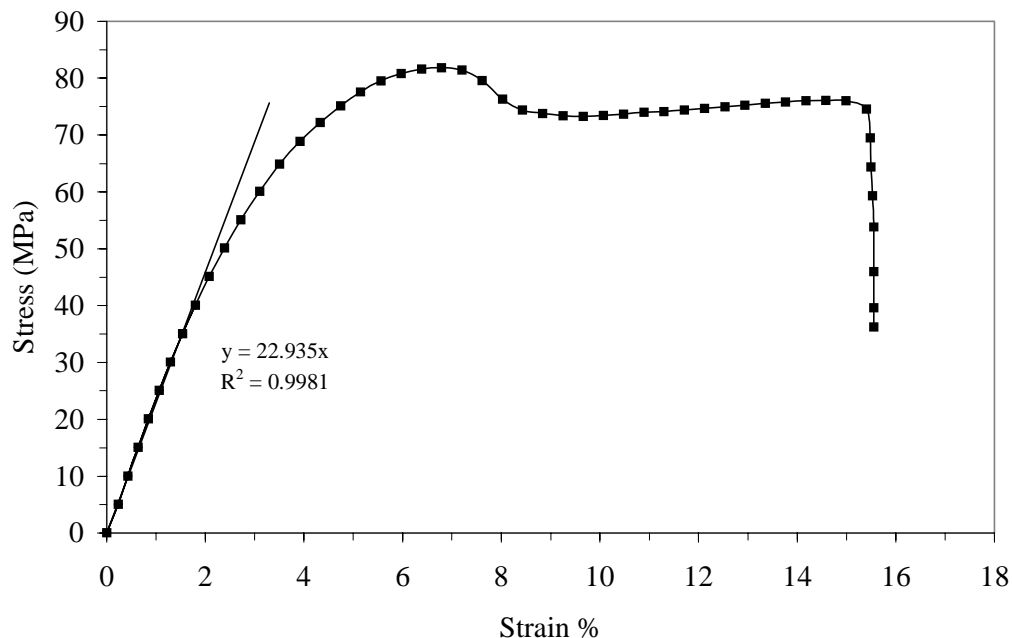


**Figure 6.18. Determination of the Young's Modulus for a BPADA/ODA sample (ODA-1).**

Figure 6.19 presents the average tensile modulus at 25 °C taken from 3 to 5 specimens of each of the polyimides. The values are on the order of  $10^9$  Pa, as expected for a glassy polymer, and generally increase from  $1577 \pm 123$  to  $2272 \pm 31.2$  MPa as the amount of the rigid aromatic diamine, ODA, increases. The trend is consistent with that measured by dynamic mechanical analysis (Figure 6.3); however, the tensile test values are lower. The difference is attributed to the sensitivity of the tensile test to film quality; anomalies increase the error in the average value. The yield stress as a function of aliphatic content is presented in Figure 6.20. The 75:25 composition exhibited the highest yield strength. Within the standard deviation the yield strengths of the other ODA containing polyimides were the same. The yield stress for BPADA/DoDDA is much lower, presumably because of its predominantly aliphatic character.

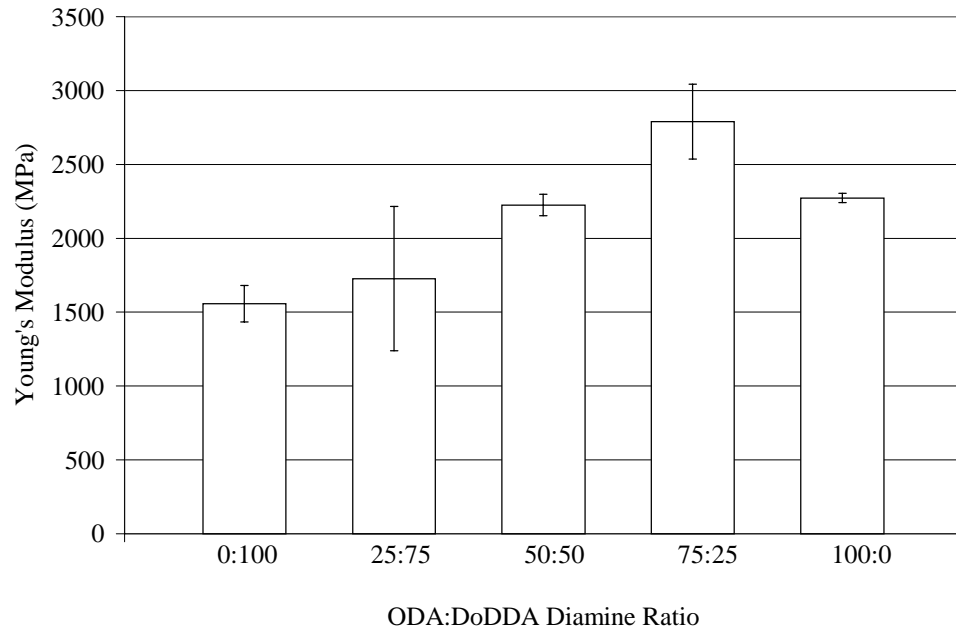


**Figure 6.19. Young's Modulus,  $E$ , as a function of chemical composition.**

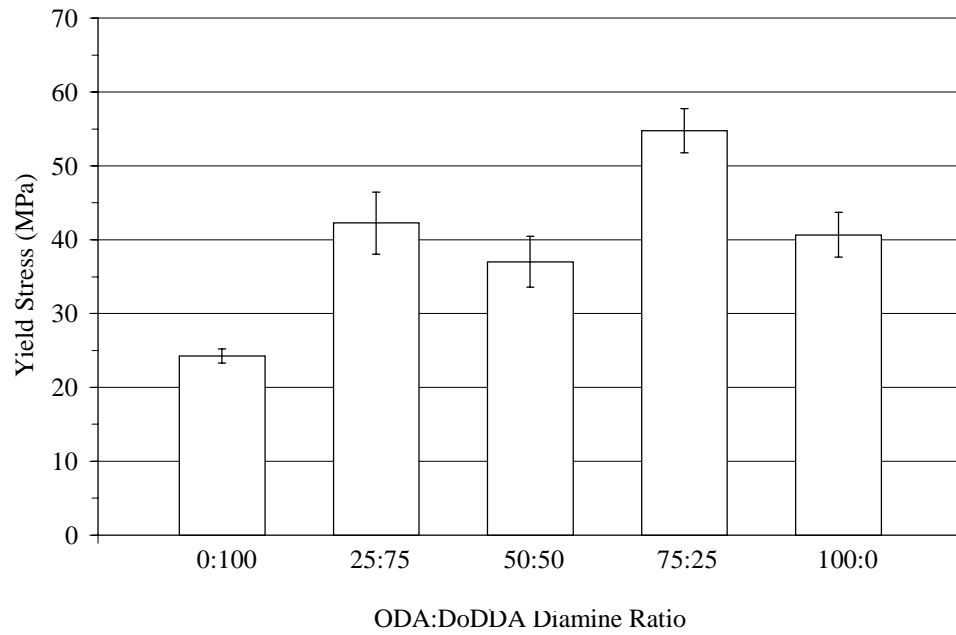


**Figure 6.20. Yield stress,  $\sigma_y$ , as a function of chemical composition.**

#### 6.4. Relevance to Adhesion

The chemical composition of a polymer influences (1) the types of physical and chemical bonding with the substrate, and (2) segmental mobility – cooperative and local viscoelastic relaxations which may dissipate energy as the adhesive is thermally or mechanically stressed. Both factors are intimately connected and contribute greatly to bulk adhesive physical properties and to practical adhesion strength. Each physical property extends our understanding of the adhesion of partially aliphatic polyimides to SiO<sub>2</sub>/Si.

The coefficient of thermal expansion (CTE), refractive index ( $n$ ), and dielectric constant ( $\epsilon_r$ ) each reflect to some extent, the intermolecular forces in the bulk polymer which also participate in intrinsic adhesion forces with the SiO<sub>2</sub>/Si substrate. Intermolecular forces resist dimension changes as the temperature increases, with high cohesive energy densities leading to lower CTE. The CTE is also a strong function of the polymer chain rigidity and linearity, since these attributes facilitate the close alignment of segments on neighbor polymer chains. The refractive index and dielectric constant reflect the polarizability of the molecules and the number of dipoles, with materials that have a greater number of polarizable atoms or functional groups displaying higher  $n$  and  $\epsilon_r$  in all frequency ranges. As the ODA content increased in the polyimide series,  $n$  and  $\epsilon_r$  increased because of the greater number of polar interactions and the formation of charge transfer complexes with the dianhydride. The opposite trend was true as the hydrophobic, aliphatic DoDDA content increased. These polar and dispersive forces contribute to the thermodynamic work of adhesion,  $W_A$ , and the intrinsic adhesive fracture energy  $G_o$ .

The glass transition is associated with the onset of large-scale cooperative segmental motions. Small-scale, local relaxations which also dissipate energy are active within the glassy state. The temperatures and magnitudes of both types of relaxations were strong functions of the diamine molar ratio. The long, flexible DoDDA segments initiated the glass transition phenomenon at lower temperatures and also enabled crankshaft-like motions at temperatures  $\approx -140$  °C. The aromatic ODA segments, while “flexible” due to the ether moiety, added rigidity to the polymer backbone and facilitated the alignment of segments and the formation of intermolecular interactions between segments on neighbor chains. Consequently, the polyimides with higher ODA contents exhibited high glass transition temperatures. The peak area of a local relaxation,  $\approx 50$  °C, was also dependent on the amount of ODA; as the ODA content increased, the peak area linearly increased. This observation in combination with literature examples, lead

to the association of a torsional rotation about the phenyl rings as the underlying molecular motion. The time–temperature dependence of the glass transition and local relaxations in conjunction with an Arrhenius activation energy analysis provided information on their volume element size scales. All observations suggest that the segmental mobility of the DoDDA and ODA units impacts both cooperative and local energy dissipative mechanisms. These same mechanisms are expected to viscoelastically dissipate energy as the PI-SiO<sub>2</sub>/Si interface is thermally or mechanically stressed.

## 6.5. Conclusions

Chemical structure-physical property relationships were established for a series of high molecular weight, soluble, amorphous partially aliphatic polyimides. As the aliphatic content increased, the glass transition temperature, thermal stability, refractive index, dielectric constant, modulus, and  $\sigma_y$  decreased; however, the coefficient of thermal expansion increased. The controlled chemical compositions of the BPADA/ODA:DoDDA series allowed the molecular origins of the local viscoelastic relaxations to be determined. A crankshaft motion within the DoDDA unit was assigned to the  $\gamma$  relaxation and a phenyl ring rotation within the ODA unit was assigned to the  $\beta$  relaxation.

## 6.6. References

- <sup>1</sup> *Polyimides*; Wilson, D.; Stenzenberger, H.D.; Hergenrother, P.M., Eds.; Blackie: London, 1990.
- <sup>2</sup> Kreuz, J.A.; Hsiao, B.S.; Renner, C.A.; Goff, D.L. *Macromolecules* **1995**, *28*, 6926.
- <sup>3</sup> Jin, Q.; Yamahita, T.; Horie, K.; Yokota, R.; Mita, I. *J. Polym. Sci. Polym. Chem. Ed.* **1993**, *31*, 2345.
- <sup>4</sup> Liou, H. C.; Ho, P.S.; Stierman, R. *Thin Solid Films* **1999**, *339*, 68.
- <sup>5</sup> Numata, S.; Kinjo, N. *Polym. Eng. Sci.* **1988**, *28(14)*, 906.
- <sup>6</sup> Arnold, F.E.; Bruno, K.R.; Shen, D.; Eashoo, M.; Lee, C.J.; Harris, F.W.; Cheng, S.Z.D. *Polym. Eng. Sci.* **1993**, *33(21)*, 1372.
- <sup>7</sup> Coburn, J.C.; Soper, P. D.; Auman, B.C. *Macromolecules* **1995**, *28*, 3253.
- <sup>8</sup> Li, F.; Fang, S.; Ge, J.J.; Honigfort, P.S.; Chen, J.C.; Harris, F.W.; Cheng, S.Z.D. *Polymer* **1999**, *40*, 4987.
- <sup>9</sup> Li, F.; Fang, S.; Ge, J.J.; Honigfort, P.S.; Chen, J.C.; Harris, F.W.; Cheng, S.Z.D. *Polymer* **1999**, *40*, 4571.
- <sup>10</sup> McCrum, N.G.; Read, B.E.; Williams, G. *Anelastic and Dielectric Effects in Polymeric Solids*; Dover: New York, 1991.

- 
- <sup>11</sup> Starkweather, H.W., Jr.; Avakian, P. *Macromolecules* **1989**, *22*, 4060.
- <sup>12</sup> Starkweather, H.W., Jr. *Macromolecules* **1981**, *14*, 1277.
- <sup>13</sup> Ando, S.; Matsuura, T.; Sasaki, S. *Polym. J.* **1997**, *29(1)*, 69.
- <sup>14</sup> St.Clair, A.K.; Slep, W.S. *SAMPE Journal* **1985**, *21(4)*, 28.
- <sup>15</sup> Eftekhari, A.; St. Clair, A.K.; Stoakley, D.M.; Sprinkle, D. R.; Singh, J.J. In *Polymers for Microelectronics: Resists and Dielectrics*; Thompson, L.F.; Wilson, C.G.; Tagawa S., Eds.; ACS Symposium Series 537; American Chemical Society: Washington, D.C., 1994; pp 535-545.
- <sup>16</sup> Simpson, J.O.; St. Clair, A.K. *Thin Solid Films* **1997**, *308-309*, 480.

## 7. ADHESION

### 7.1 Introduction

The variation of the molar ratio between the rigid aromatic and flexible aliphatic diamines within the BPADA/ODA:DoDDA series allowed thermal, dielectric, and mechanical structure-property relationships to be established as described in Chapter 6. This chapter next examines if adhesion strength is influenced by glassy polymer chemical composition. Quantitative conclusions are not obtained in the latter case due to the complexity of the adhesion tests' analysis, rather the outcomes are discussed more generally.

Furthermore, measuring the adhesion strength of the BPADA/ODA:DoDDA series to SiO<sub>2</sub>/Si required considering this problem a) molecularly, by the thermodynamic work of adhesion,  $W_A$  and b) practically, or macroscopically, by the shaft loaded blister test. The former is related to  $G_o$  and the latter describes the adhesion energy,  $G$ , stated in the general equation for adhesion energy in Equation 1.1. To interpret  $(\phi(R,T))$ , recall the structure-property relationships established in Chapter 6 for the local viscoelastic relaxations of this polyimide series. Dynamic mechanical analysis revealed that as the percent ODA increased, the  $\beta$  viscoelastic relaxation peak area systematically increased as described by a linear relationship. The peak area provides a measure of the energy dissipation,  $(\phi(R,T))$ , associated with the torsional rotation of the phenyl rings within the ODA units. The interaction of  $g(G_o)$  and  $(\phi(R,T))$  then remains. To apply these associations to an understanding of Equation 1.1, the SLBT is performed at the temperatures, 25 °C, 38 °C, and 70 °C, which lie within the  $\beta$  viscoelastic relaxation. Limitations of the SLBT for these polymer systems were recognized and detailed below. The contribution of the  $G_o$  and the  $\beta$  relaxation to the practical adhesion strength to SiO<sub>2</sub>/Si is discussed more generally. The influence of chemical composition on PI-SiO<sub>2</sub>/Si adhesion strength in high and low percent relative humidity environments is also examined.

### 7.2 Thermodynamic Work of Adhesion

The adhesion energy of the BPADA/ODA:DoDDA series to SiO<sub>2</sub>/Si was quantified molecularly by the thermodynamic work of adhesion,  $W_A$ .  $W_A$  is a measure of the secondary bonding forces across an interface and is calculated from the polar,  $\gamma^p$ , and dispersive,  $\gamma^d$ , components of the surface energy for the adhesive,  $a$ , and the substrate,  $s$ , by:<sup>1</sup>

$$W_A = 2\sqrt{\gamma_a^d \gamma_s^d} + 2\sqrt{\gamma_a^p \gamma_s^p} \quad \text{Equation 7.2}$$

If no covalent bonding occurs across the interface of an adhesive bond and adhesive bond failure is strictly interfacial, then  $W_A$  provides an estimate of the intrinsic adhesion energy,  $G_0$ .

A harmonic mean method, described in Chapter 3, was adopted to calculate the polar and dispersive components of the surface energy for the polyimide adhesive and the SiO<sub>2</sub>/Si substrate. The contact angles ( $\theta$ ) for the two probe liquids, H<sub>2</sub>O and methylene iodide, and the calculated surface energies for the polyimides and SiO<sub>2</sub>/Si (a silicon wafer) are presented in Table 7.1 and Table 7.2, respectively.

**Table 7.1. Contact angles and surface energies for the BPADA/ODA:DoDDA series.**

	ODA:DoDDA				
	0:100	25:75	50:50	75:25*	100:0
$\theta$ of H <sub>2</sub> O (°)	75.2 ± 1.1	71.1 ± 1.1	75.8 ± 1.5	-	73.5 ± 1.8
$\theta$ of CH <sub>2</sub> I <sub>2</sub> (°)	22.5 ± 2.2	19.0 ± 1.8	24.0 ± 2.0	-	19.6 ± 2.3
$\gamma_a^p$ (mJ/m <sup>2</sup> )	10.8 ± 0.5	12.7 ± 0.5	10.7 ± 0.8	-	11.5 ± 0.8
$\gamma_a^d$ (mJ/m <sup>2</sup> )	37.6 ± 0.5	37.7 ± 0.3	37.2 ± 0.3	-	38.0 ± 0.3
$\gamma_a$ (mJ/m <sup>2</sup> )	48.4 ± 0.9	50.4 ± 0.7	47.9 ± 1.0	-	49.5 ± 1.0

\*Due to impurities in the films, angles cannot be presented with confidence.

**Table 7.2. Contact angles and surface energies for a cleaned silicon wafer (SiO<sub>2</sub>/Si).**

Silicon Wafer	
$\theta$ of H <sub>2</sub> O (°)	5.1 ± 1.5
$\theta$ of CH <sub>2</sub> I <sub>2</sub> (°)	26.3 ± 1.8
$\gamma_s^p$ (mJ/m <sup>2</sup> )	43.5 ± 0.3
$\gamma_s^d$ (mJ/m <sup>2</sup> )	31.0 ± 0.6
$\gamma_s$ (mJ/m <sup>2</sup> )	74.5 ± 0.3

It was expected that the change in chemical composition in the polyimide series would create a systematic variation in  $\gamma_a^p$  and  $\gamma_a^d$ ; however, this was not the case. The differences in surface chemistry cannot be discerned within the standard deviation. The values of  $\gamma_a^p$  and  $\gamma_a^d$  are  $\approx 11 \text{ mJ/m}^2$  and  $\approx 37 \text{ mJ/m}^2$ , respectively, and the total adhesive surface energies,  $\gamma_a$ , are  $\approx 49 \text{ J/m}^2$ . The  $\gamma_a$  values are comparable to the surface energies of the aromatic polyimide PMDA/ODA ( $44.12 \text{ mJ/m}^2$ ),<sup>2</sup> polyethylene terephthalate ( $45.1 \text{ mJ/m}^2$ ),<sup>3</sup> and an amine cured epoxy ( $46.2 \text{ mJ/m}^2$ ).<sup>3</sup> The latter two, in particular, contain similar combinations of aliphatic, aromatic, and polar functional groups as the BPADA-based polyimides in the present study.

The BPADA/ODA polyimide should possess the most polar surface and exhibit the lowest  $\text{H}_2\text{O}$  contact angle and the highest methylene iodide contact angle. Conversely, BPADA/DoDDA should possess the most nonpolar surface and exhibit the highest  $\text{H}_2\text{O}$  contact angle and the lowest methylene iodide contact angle. The insensitivity of the contact angles in distinguishing among the chemical compositions could arise from the differences in the rigidity of the monomers. In the amorphous state, the flexible (low  $T_g$ ) DoDDA segments probably exist in a coiled conformation. If one assumes a random arrangement of repeating units on the surface reflecting the overall monomer volume fractions, a coiled segment will present a smaller contribution to the total surface area than the rigid segments, such as BPADA or ODA. Further, because the size of BPADA, measured by its number of aromatic groups, is greater than ODA, its properties may dominate the surface chemistry. BPADA is present in all the polyimides in the series in the highest molar amount and as a result, the total surface energies,  $\gamma_a$ , and their constitutive  $\gamma_a^p$  and  $\gamma_a^d$  values, of the polyimide adhesives are approximately the same due to this monomer.

For  $\text{SiO}_2/\text{Si}$  (Table 7.2), the low  $\theta$  of  $\text{H}_2\text{O}$ ,  $\approx 5^\circ$ , confirmed that the employed cleaning procedure created a hydrophilic surface. The  $\gamma_s^p$  value is  $\approx 13 \text{ mJ/m}^2$  greater than  $\gamma_s^d$ , which also reflects the hydrophilic nature of the surface. The total surface energy,  $\gamma_s$ , of  $\text{SiO}_2/\text{Si}$  is  $\approx 25 \text{ mJ/m}^2$  higher than that of the polyimide surfaces.

Using the surface energies in Table 7.1 and Table 7.2,  $W_A$  was calculated from equation 2. The  $W_A$  values are listed in Table 7.3.

**Table 7.3. Thermodynamic work of adhesion for PI to SiO<sub>2</sub>/Si.**

	ODA:DoDDA				
	0:100	25:75	50:50	75:25*	100:0
$W_A$ (mJ/m <sup>2</sup> )	111.7 ± 1.8	115.5 ± 1.5	111.1 ± 2.3	-	113.5 ± 2.1

\*Due to impurities in the PI,  $W_A$  value cannot be presented with confidence.

The  $W_A$  values are  $\approx 113$  mJ/m<sup>2</sup> and for reasons outlined earlier, do not appear to be a function of chemical composition.

### 7.3 The Shaft Loaded Blister Test: Background

#### 7.3.1 Introduction and Theory

When measuring the adhesion energy of a thin adhesive layer to a rigid substrate by a peel geometry, bending and tensile stresses may cause plastic yielding in the thin adhesive layer. As a result, the measured peel force will be greater and the adhesion energy will be higher than predicted for the intrinsic adhesion. The peel angle is an important parameter; typically, the larger the angle, the greater the bending stresses and resulting plastic yielding.<sup>4</sup> At small angles, where bending is minimized, tensile stresses can be high and plastic yielding can also occur.<sup>4</sup> These observations demonstrate that practical adhesion strengths depend on the intrinsic bonding forces across the interface, the mechanical properties ( $E$ ,  $\sigma_y$ ) of the adhesive, and the geometry of the adhesive joint. Furthermore, these elucidate the challenges in accurately quantifying the adhesion of thin films to rigid substrates by a peel geometry. This study of the adhesion of polyimide films to ceramic substrates for microelectronics applications falls within this category. The problem of plastic deformation in the analysis was anticipated and consequently, low expectations for quantitative results were a part of this present investigation.

The adhesion energies of aromatic polyimides to SiO<sub>2</sub>/Si have been measured by researchers using a 90° peel test, an island blister test,<sup>5,6</sup> and a pressurized blister test.<sup>7</sup> The most commonly adopted geometry was the 90° peel test. The most striking difference among the geometries is the magnitude of the adhesion energy. In most cases, the 90° peel test gave adhesion values 5-10 times greater than either blister test. Relative to the 90° peel test, plastic deformation in these blister tests is reduced due to the small debonding angle, and the value of  $G$  then more closely reflects the intrinsic adhesion energy. To characterize the adhesion energy of

the BPADA/ODA:DoDDA series to SiO<sub>2</sub>/Si for the current research, a shaft loaded blister test geometry was selected. Similar to the island and pressurized blister tests, the SLBT operates with a small debonding angle. The experimental set-up of the SLBT, however, is much simpler because the debond is driven mechanically rather than by a pressurized gas or liquid.

The theory for the shaft loaded blister test has been derived by Wan and Mai.<sup>8</sup> The key assumptions include, (1) a rigid, undeformable substrate, (2) a thin flexible membrane without bending, (3) the debond radius is much greater than the shaft radius so that the central force is point loading, (4) a debond angle less than 25°, and (5) a conical blister profile. Three equivalent solutions for the adhesion energy were derived in accordance with linear elastic fracture mechanics using an energy balance approach. The three solutions are called the load-based, hybrid, and displacement-based equations:<sup>8</sup>

$$\text{Load-Based} \quad G = \left( \frac{1}{16\pi^4 Eh} \right)^{1/3} \left( \frac{P}{a} \right)^{4/3} \quad \text{Equation 7.3}$$

$$\text{Hybrid} \quad G = \frac{1}{\pi^2 Eh} \left( \frac{P}{w_o} \right)^2 \quad \text{Equation 7.4}$$

$$\text{Displacement-Based} \quad G = \frac{Eh}{16} \left( \frac{w_o}{a} \right)^4 \quad \text{Equation 7.5}$$

where  $G$  is the adhesion energy,  $E$  is the modulus of the adhesive,  $h$  is the thickness of the adhesive,  $P$  is the applied load,  $w_o$  is the central shaft displacement, and  $a$  is the blister radius. The three solutions differ in their combination of and dependence on the experimental parameters,  $P$ ,  $w_o$ , and  $a$ , and the adhesive properties,  $E$  and  $h$ . The term  $Eh$  is called the film tensile rigidity. During stable crack growth, Equations 7.3 - 7.5 predict that  $P \propto a$ ,  $P \propto w_o$ , and  $w_o \propto a$ , respectively.

Depending on the mechanical properties of the adhesive, plastic deformation of the film at the point of contact with the shaft tip can occur. Evidence for such plastic deformation is observed by a “dimple” in the film of an evaluated specimen. Film deformation at the shaft tip

will cause the blister shape to change from a conical geometry to a double conical geometry.<sup>8</sup> The central shaft displacement,  $w_o$ , then represents the sum of the elastic displacement,  $w_e$ , and the plastic displacement,  $w_p$ .<sup>8</sup> If the blister behaves elastically at the crack tip, the theory holds; however, the change in blister shape will introduce error in the experimentally measured central shaft displacement,  $w_o$ . The value for  $w_o$  will be larger than for elastic behavior. The adhesion energies calculated by the hybrid or displacement-based equations (Equations 7.4 and 7.5), which both contain  $w_o$ , will reflect this error. The adhesion energy by the displacement-based equation will be particularly sensitive to  $w_o$ , since there, displacement is raised to the fourth power. Under such experimental circumstances, the most confidence may be placed in the adhesion energy calculated by the load-based equation (Equation 7.3).<sup>9</sup>

### 7.3.2 Experimental Parameters

The SLBT sample preparation, instrumentation, and experimental design are described in detail in Chapter 3. During a SLBT experiment, the DMA measured the load,  $P$ , and the shaft displacement,  $w_o$ , variables. The debond radius,  $a$ , was measured from images of the blister growth recorded using the borescope/computer. A few examples of blister growth are presented in Figure 7.1 and Figure 7.2.

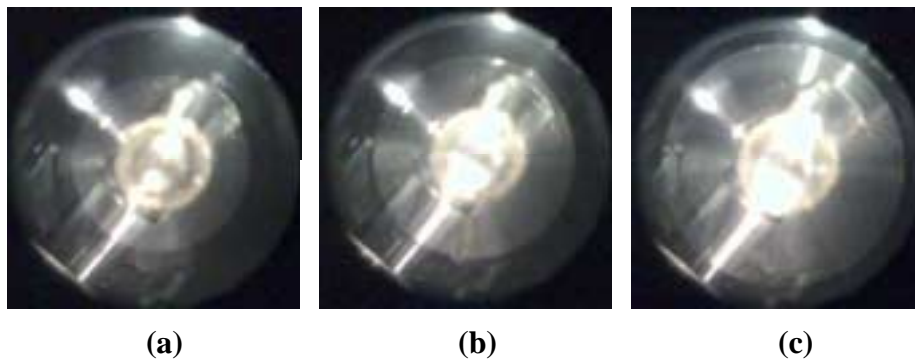


**Figure 7.1. Blister growth of BPADA/ODA-2: (a) 3 minutes, radius = 4.59 mm, (b) 6 minutes, radius = 5.52 mm, (c) 9 minutes, radius = 6.73 mm.**

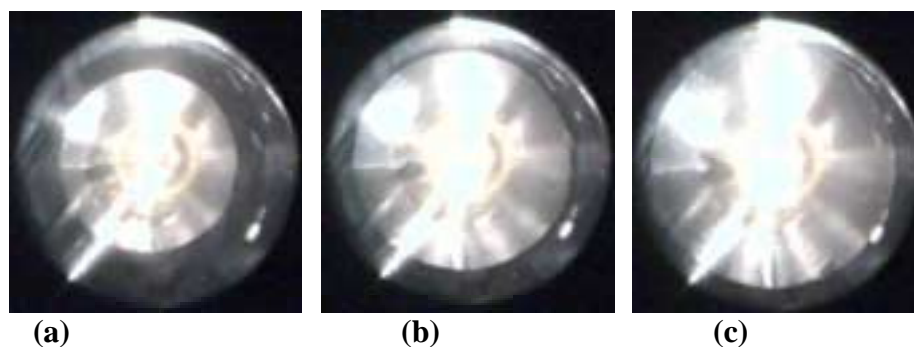


**Figure 7.2. Blister growth of BPADA/ODA:DoDDA, 25:75-1: (a) 14 minutes, radius = 4.79 mm, (b) 14.5 minutes, radius = 6.15 mm, (c) 15 minutes, radius = 6.94 mm.**

The blister shape was symmetric during crack growth and the transparency of the polyimide films simplified the measurement of the radius. The measured blister radii were corrected for the distortion of the borescope lens, as described in Chapter 3. For each polyimide in the BPADA/ODA:DoDDA series, the relationships,  $P \propto a$ ,  $P \propto w_o$ , and  $w_o \propto a$ , were examined. When these conditions were satisfied, adhesion energy values to SiO<sub>2</sub>/Si were calculated using the load-based, hybrid, and displacement-based equations.

The bulk adhesive properties,  $E$  and  $h$ , were determined independently; these values and the film tensile rigidity,  $Eh$ , are listed in Table 7.4

**Table 7.4. Film Tensile Rigidity,  $Eh$ , of the BPADA/ODA:DoDDA series.**

Polyimide	Modulus, <sup>a</sup> $E$ (MPa)	Film Thickness, <sup>b</sup> $h$ ( $\mu\text{m}$ )	Film Tensile Rigidity, $Eh$ (N/m)
BPADA / ODA	3038 $\pm$ 108	17.78	54029
BPADA / ODA:DoDDA, 75:25	2779 $\pm$ 275	15.24	42352
BPADA / ODA:DoDDA, 50:50	2704 $\pm$ 359	17.78	48081
BPADA / ODA:DoDDA, 25:75	2539 $\pm$ 298	17.78	45139
BPADA / DoDDA	2119 $\pm$ 202	17.78	37689

<sup>a</sup> Determined from the Storage Modulus of the film by Dynamic Mechanical Analysis. The average modulus is from four samples at 25 °C.

<sup>b</sup> Measured for pieces of film from the SLBT samples.

## 7.4 The Shaft Loaded Blister Test: Results and Discussion

### 7.4.1 Introduction

While the blister successfully propagated for all five polyimides adhering to SiO<sub>2</sub>/Si, for the majority, the relationships,  $P \propto a$ ,  $P \propto w_o$ , and  $w_o \propto a$ , were not observed. This section is organized to (1) address the deviations from theory, (2) present the SLBT results and corresponding locus of failure analysis for each polyimide tested at 24-27 °C at “high %RH” (45-60 %RH), (3) present the SLBT results for 25 °C, 38 °C, and 70 °C at “low %RH”, (6.5, 24, and 3.5 %RH respectively) and (4) state the conclusions.

### 7.4.2 Deviations from Theory

Four experimental factors have been identified to explain the deviations: (1) method of loading, (2) film thickness variations, (3) plastic yielding of the film, and (4) environmental effects. In this section each factor is discussed in general. In the following sections, the factors are then addressed with respect to the experimental data.

The first factor is the “load-controlled” method of operation of the DMA. Two types of mechanical testing machines are displacement-controlled, or hard, and load-controlled, or soft. Each imposes experimental limitations; in the former, the operator has no control over the load and in the latter, none over the displacement. The compliance of the machine can cause crack instabilities depending on the test material and geometry.<sup>10</sup> The compliance is viewed energetically by the amount of stored strain energy in the frame. When a crack grows, the stored strain energy adds to the strain energy of the crack. If crack propagation is stable, this extra energy may cause the crack to become unstable. Since the load-controlled machine is more compliant, it is more likely to produce an instability. The compliance of the machine also influences the deflection of the crosshead. In tension, the deflection causes the length change in a sample to be overestimated, but in compression, it is underestimated.<sup>10</sup>

The present SLBT was performed using a load-controlled machine in compression. Unstable crack growth was observed in most of the specimens prepared by the “patch” technique. The adhesion of the patch to SiO<sub>2</sub>/Si,  $G_1$ , differed from the adhesion of the film cast from solution to SiO<sub>2</sub>/Si,  $G_2$ . The transition region between the bulk patch and bulk film, in theory, possessed an intermediate adhesion energy,  $G_t$ . These are depicted schematically in Figure 7.3.

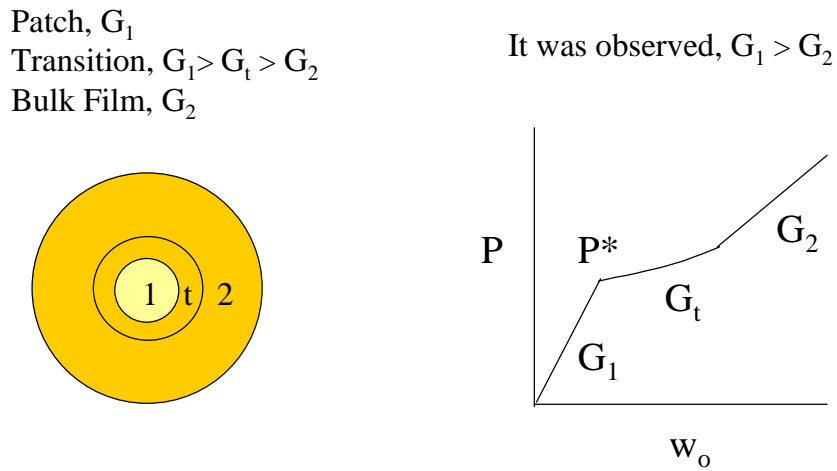


**Figure 7.3. Schematic of Sample and Change in Adhesion.**

The differences in adhesion energy were problematic because of the load-control operation of the DMA. When the load surpassed the critical load of debonding,  $P^*$ , the patch delaminated. Typically  $G_1 > G_t > G_2$ ; thus, at such a high load, the bulk film immediately delaminated. Changes in the  $P$  vs.  $w_o$  and  $P$  vs.  $a$  relationships provided evidence for the transformations in blister growth.

The second factor identified is the nonuniformity in film thickness,  $h$ , induced by the presence of the patch. The effect is shown in Chapter 3 (Figure 3.6) and is depicted schematically in Figure 7.4. The thickness of the cast film is suggested to taper down radially from the patch to the bulk cast film.

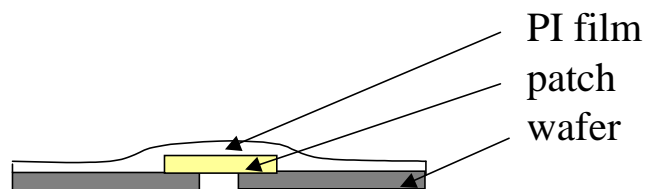


**Figure 7.4. Schematic of the variation in film thickness induced by the patch.**

The patch not only covered the hole during film casting, but also reinforced the film at the place of contact with the shaft tip during the SLBT. A discontinuity in the cast film was visible due to the underlying patch. The patch was  $\approx 10 \mu\text{m}$  thicker than the cast film, thus the discontinuity is probably of similar magnitude. The variation in the polyimide film thickness, however, was not accounted for in the film tensile rigidity,  $Eh$ , which is a term in Equations 7.3 - 7.5. The variation in thickness could also possibly cause deviations in the relationships,  $P \propto a$ ,  $P \propto w_o$ , and  $w_o \propto a$ .

The third, and major, factor leading to deviations of the SLBT data from the predictive analytical equations, is plastic yielding of the film. A large dimple, which is evidence for extensive plastic yielding, was observed in most samples at the place of contact with the shaft tip. As discussed in section 7.4.1, this causes the shaft displacement,  $w_o$ , to be overestimated and explains the deviations from  $P \propto w_o$  and  $w_o \propto a$ . Plastic yielding at the shaft tip, however, does not necessarily suggest that there is plastic yielding at the crack tip.<sup>9</sup> If there is no plastic yielding at the crack tip,  $G$  may still be determined using the load-based equation, where  $P \propto a$ . Whether or not the conditions are elastic at the crack tip may be estimated by an effective membrane stress. For the circular blister geometry, the “effective membrane stress” (in N/m),  $N_{eff}$ , of a film is described by:<sup>8</sup>

$$N_{eff} = (GEh)^{1/2} \left[ \left( \log \frac{a}{r} \right)^2 + \frac{3}{4} \right]^{1/2} \quad \text{Equation 7.6}$$

where  $r$  is the radial distance from the center of the blister. If  $N_{eff} > \sigma_y h$ , where  $\sigma_y$  is the yield strength of the adhesive, then plastic yielding is predicted to occur. At the crack tip,  $r = a$ , and Equation 7.6 simplifies to:

$$N_{eff} = \left( \frac{3GEh}{4} \right)^{1/2} \quad \text{Equation 7.7}$$

The  $N_{eff}$  at the crack tip calculated using equation 7.7 does not take into consideration the stress at the crack tip due to bending. Bending stresses at the crack tip may or may not be significant for the polyimide series in question, thus, the  $N_{eff}$  values should be interpreted with caution. The  $N_{eff}$  at the crack tip was calculated from Equation 7.7 for the BPADA-based polyimides using the adhesion energies from the load-based, hybrid, and displacement-based equations. Then, from the  $\sigma_y$  value determined from tensile tests (Chapter 6) for each polyimide in the series, and the SLBT polyimide film thickness, the criterion  $N_{eff} > \sigma_y h$  for plastic yielding was tested. For the majority of the specimens, extensive plastic yielding was predicted at the crack tip, thereby invalidating the use of Equations 7.3-7.5 to describe the adhesion energy of the BPADA-based polyimides to  $\text{SiO}_2/\text{Si}$ . The prediction further explains the deviations in the  $P \propto a$ ,  $P \propto w_o$ , and  $w_o \propto a$  relationships. Signs of plastic yielding in the post-mortem specimens where  $N_{eff} > \sigma_y h$ , included a dimple at the place of contact with the shaft tip, striations in the peeled film, and puckering of the peeled film.

The fourth factor is environmental effects that arose from the percent relative humidity (% RH) and the temperature that the SLBT experiments were performed. As discussed in section 2.9.3.3 of the literature review, humidity and temperature greatly influence the adhesion strength of PI/ $\text{SiO}_2$  and PI/silicon interfaces. The investigations by Hu et al<sup>11,12</sup> are particularly relevant and these authors' key findings are restated at this time: (1) Over the range 8 to 98 %RH, the peel strength of PI to silicon was the lowest for 55-65 %RH, and the highest for 8-20 %RH. (2) Moisture can attack the PI/silicon interface directly, via the crack tip, or indirectly, by diffusion through the polyimide film. Hu et al experimentally determined that direct attack, via the crack tip, was more important in their PI/silicon system. (3) PI to silicon peel strengths measured at high temperatures and high %RH were nearly the same as those for low temperatures and low %RH.

Each conclusion by Hu et al has implications in the present BPADA-based polyimide to  $\text{SiO}_2/\text{Si}$  investigation. The SLBT experiments were performed in high and low %RH environments that resulted as a consequence of the DMA furnace either being open or closed to the laboratory environment. The designations "high %RH" and "low %RH" will refer to the open and closed furnace experiments, respectively. When the DMA furnace was open, the ambient laboratory environment was 24-27 °C and 45-60 %RH. When the DMA furnace was

closed the SLBT experiments were performed at 25 °C, 38 °C, and 70 °C. At 25 °C, where liquid nitrogen was used, the %RH was  $\approx 6.5$  %RH. At 38 °C, liquid nitrogen was not used and the %RH was  $\approx 24$  %RH, and at 70 °C, liquid nitrogen was not used and the %RH was  $\approx 3.5$  %RH. These experimental conditions were designated “low %RH.” As described in the Experimental section, the SLBT samples were thermally equilibrated  $\approx 17$  min in the low %RH environment prior to the start of the test. The %RH in the furnace was measured at each test temperature using a General Eastern Model 800B Humidity Indicator.

In the high %RH environment, a blister was propagated in the SLBT for all five polyimides. As will be discussed later, the blister growth was probably facilitated by moisture. However, the moisture may have also contributed to deviations in the relationships,  $P \propto a$ ,  $P \propto w_o$ , and  $w_o \propto a$ . In the low %RH environment, in all cases, the film ruptured prior to any blister growth. This effect may also be related to moisture.

## 7.5 BPADA/ODA at High %RH

### 7.5.1 BPADA/ODA: SLBT Results

Blister specimens for the fully aromatic polyimide, BPADA/ODA, were identically prepared and precracked as discussed Chapter 3. The  $P$  vs.  $w_o$ ,  $P$  vs.  $a$ , and  $w_o$  vs.  $a$  relationships were examined to determine the applicability of the hybrid, load-based, and displacement-based equations, respectively. For each relationship, the proportionality between the variables was checked using a best-fit line. For  $P$  vs.  $w_o$ , the best-fit line should intersect the origin. For  $P$  vs.  $a$  and  $w_o$  vs.  $a$ , because of the finite contact zone with the shaft tip, a non-zero x-axis intercept is expected; in the present investigation, a point-load, as assumed in the derivation by Wan and Mai,<sup>8</sup> was not attainable. The finite contact zone of the film with the shaft tip causes the blister shape to resemble a cone with its tip cut off, as opposed to a true cone in a point-loading situation. Under such loading, the x-intercept should lie within the radius of the shaft tip (in this study,  $a = 1.59$  mm). When proportionality by  $P$  vs.  $w_o$ ,  $P$  vs.  $a$  or  $w_o$  vs.  $a$ , was observed, this indicated that the strain energy release rate,  $G$ , was constant, ie. blister growth was elastic, and the calculation of the adhesion energy using of Wan and Mai’s model was appropriate, provided  $N_{eff} < \sigma_y h$ . When the relationship was not proportional and  $N_{eff} > \sigma_y h$ , the blister growth was inelastic and the application of Wan and Mai’s model was not allowed. When blister growth was

inelastic, one or more of the four experimental factors described in the previous section were used to interpret the deviation. All figures are placed at the end of this section.

The  $P$  vs.  $w_o$  curves (hybrid equation) are presented in Figure 7.5. For clarity, the  $P$  vs.  $w_o$  curve for each successive sample is horizontally offset by 0.25 mm. Each  $P$  vs.  $w_o$  curve shows an initial loading region ( $P < 0.5-1$  N), followed by a linear region. The change in slope at the largest displacement for each curve indicates where the film either punctured at the contact region with the shaft tip or the blister grew to the edge of the silicon wafer. The linear region was fit to a line through the origin, as shown in Figure 7.6, to demonstrate that  $P \propto w_o$  for all samples, with the exception of ODA-1. Since this relationship does not hold for ODA-1, the blister is not elastic. For ODA-1 and ODA-2, the dimple at the place of contact with the shaft tip was large, indicating substantial plastic deformation and resulting in a much higher  $w_o$  than predicted necessary for blister growth. For ODA-3, ODA-4, and ODA-5, the dimples were very small and thus, the error in  $w_o$  should be small.

The  $P$  vs.  $a$  (load-based equation) curves for the five samples are shown in Figure 7.7. The  $P$  vs.  $a$  curves show that in all cases, blister growth was initiated by a load less than 1 N; the moisture from the high %RH has probably weakened the PI/SiO<sub>2</sub> interface. The curves also have a non-zero x-axis intercept which is greater than the radius of the shaft tip - this observation cannot be explained. In Figure 7.8,  $G$ , from the load-based equation is plotted versus the blister radius. The  $G$  for ODA-1 and ODA-2 both increase substantially during the experiment, thus it was concluded that blister growth was inelastic and that the application of Wan and Mai's model is not allowed. The  $G$  for ODA-3, ODA-4, and ODA-5 nearly double over the course of the experiment, however, these blisters are considered elastic, for reasons explained later.

The  $w_o$  vs.  $a$  (displacement-based equation) curves for the five samples are shown in Figure 7.9. All the curves have a non-zero x-axis intercept which is greater than the radius of the shaft tip, and  $G$  was not constant during the blister growth. For ODA-1 and ODA-2 which contained large dimples, error in  $w_o$  from  $w_p$  is expected.

Deviations from elastic response are now addressed. For ODA-1,  $N_{eff} > \sigma_y h$  at the crack tip, which suggests that plastic yielding occurs. This is consistent with the unproportional  $P$ ,  $w_o$ , and  $a$  relationships for this sample. In addition, the blister only grew about 2.5 mm at a growth rate,

da/dt of 0.17 mm/min. XPS, later reveals that this sample possessed the highest amount of polyimide on the SiO<sub>2</sub>/Si failure surface.

For ODA-2,  $N_{eff} < \sigma_y h$ , however within the error of  $\sigma_y$ , it could be argued that plastic yielding is predicted. The  $P$ ,  $w_o$ , and  $a$  responses for ODA-2 were intermediate of ODA-1 and ODA-3, ODA-4, and ODA-5, and showed a discontinuity. The change in slope may suggest that the debond front has moved closer to the PI/SiO<sub>2</sub> interface, at which, typically a lower load is needed to propagate. Or it may arise from plastic deformation at the shaft tip. The blister growth rate, da/dt, was 0.48 mm/min.

For ODA-3, ODA-4, and ODA-5, the calculated effective membrane stress did not predict plastic yielding,  $N_{eff} \ll \sigma_y h$ . The average blister growth rates, da/dt, were 1.19, 1.09, and 1.11 mm/min, respectively; however, as indicated in Figure 7.10, the growth rate of each slightly decreases. The blister growth rate is much higher than for ODA-1 and ODA-2, and the blisters grew to the edge of the silicon wafer. For each, the only visible sign of plastic yielding in the post-mortem specimen was a very small dimple; in fact, it was difficult to see the transparent delaminated film on the wafer. Since the dimple was very small, the average angle of debonding was estimated by  $\tan^{-1}(w_o/a)$ , to be 9.8°, 8.6°, and 6.9°, for the three samples, respectively. Figure 7.5 indicates that  $P \propto w_o$ , however, for  $P$  vs.  $a$  and  $w_o$  vs.  $a$  similar proportionality is not found. An influential experimental parameter is the high %RH. Hu et al demonstrated for a similar aromatic polyimide to silicon system, that the peel strength was weakened the most  $\approx 55$  %RH.<sup>12</sup> The blister growth for ODA-3, ODA-4, and ODA-5 was initiated by a load less than 1 N; this reflects weak adhesion. XPS later revealed that in comparison to the other BPADA-based polyimides, these three ODA samples possessed the smallest amounts of polyimide on the SiO<sub>2</sub> failure surfaces. While failure was cohesive in the polyimide, the failure probably occurred within a weak boundary layer near the interface. Thus, moisture may have followed a path of between various weak boundary layers. It is hypothesized that as the blisters grew, the locus of failure changed slightly and led to the small decreases in the blister growth rates and the non-constant  $G$  for the load-based equation. For these reasons, the blister growth for ODA-3, ODA-4, and ODA-5 is considered elastic. To calculate the adhesion energy from the  $P$  vs.  $w_o$ ,  $P$  vs.  $a$ , and  $w_o$  vs.  $a$  curves, the hybrid, load-based, and displacement-based equations were applied. The film

tensile rigidity,  $Eh$ , for BPADA/ODA is listed in Table 7.4. The adhesion energy values are presented in Table 7.5.

**Table 7.5. Adhesion Energies of BPADA/ODA to SiO<sub>2</sub> at 25 °C and high %RH.**

Sample	Adhesion Energy, $G$ (J/m <sup>2</sup> )		
	Hybrid	Load-Based	Displacement-Based
ODA-3	7.0	7.1	9.7
ODA-4	7.4	7.9	8.8
ODA-5	9.5	7.8	5.5
Average	8.0 ± 1.3	7.6 ± 0.4	8.0 ± 2.2

For ODA-3, ODA-4, and ODA-5, the adhesion energies from the three equations agree reasonably well. The average adhesion energies among the replicate samples are also in good agreement. The locus of failure analysis by XPS of the five ODA samples is discussed in the next section. As an interesting comparison, Paek et al measured the adhesion energy of a 11 μm-thick layer of PMDA/ODA to an HF-cleaned silicon substrate by a pressurized blister test.<sup>7</sup> For samples exposed to water, the adhesion energy increased from 9.84 J/m,<sup>2</sup> for an injection rate of 0.01 ml/min, to 23.05 J/m,<sup>2</sup> for an injection rate of 5 ml/min.<sup>7</sup>

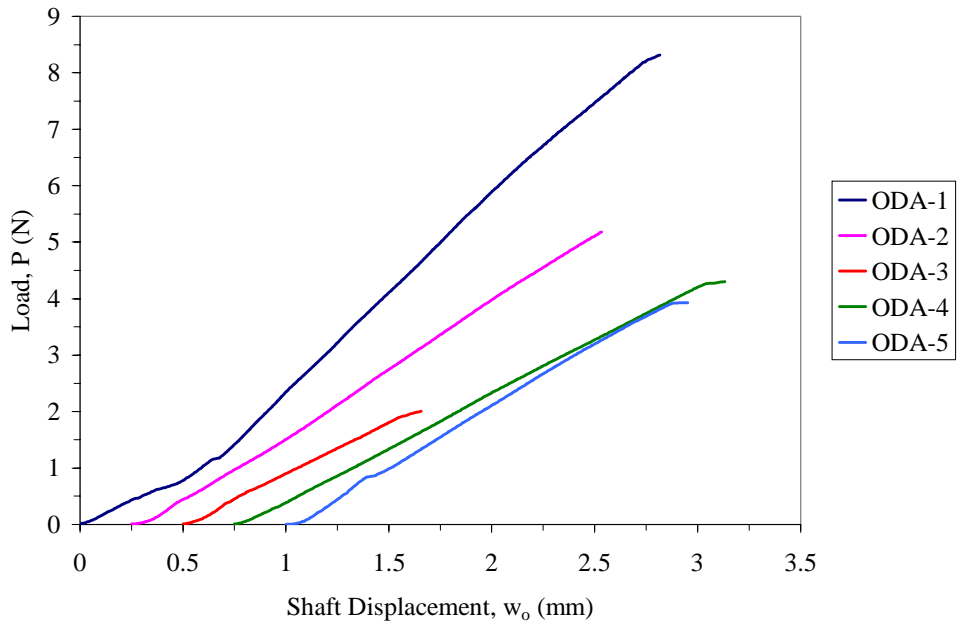


**Figure 7.5. P versus  $w_0$  for the BPADA/ODA samples. For clarity, each successive curve is horizontally offset by 0.25 mm.**

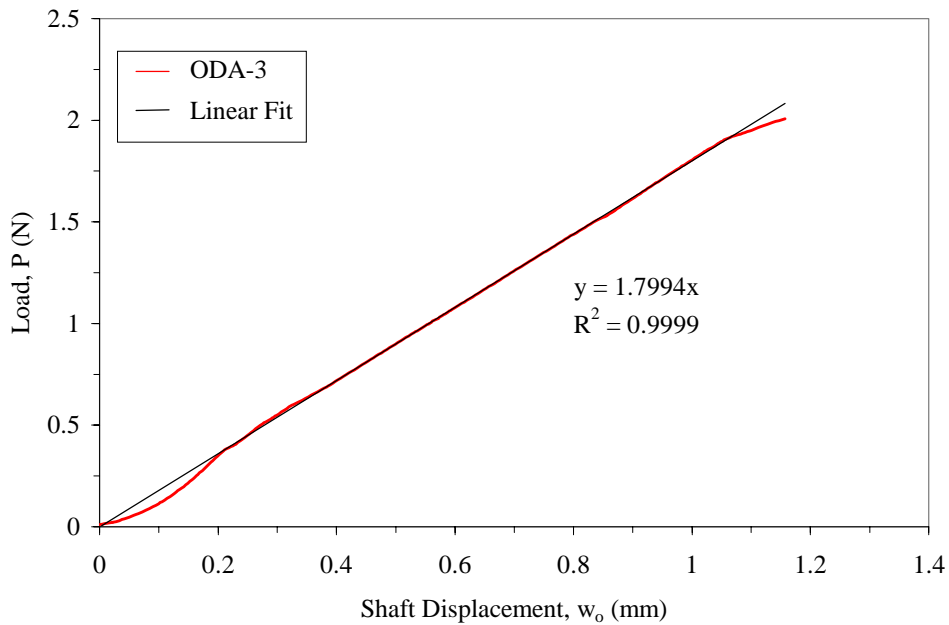


**Figure 7.6. Linear fit of P versus  $w_0$  through the origin for ODA-3.**

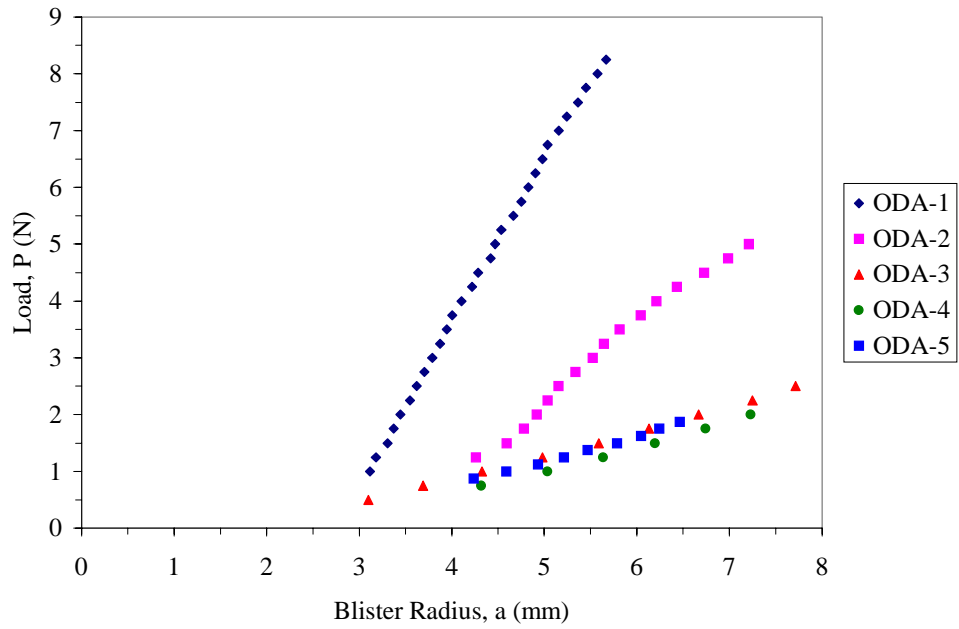


**Figure 7.7. P versus a for the BPADA/ODA samples.**

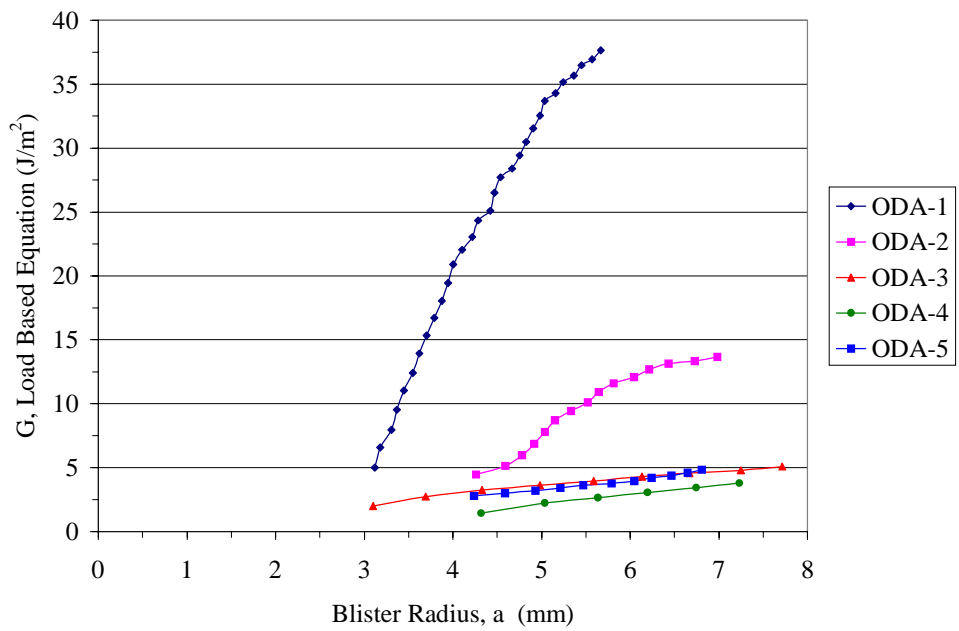


**Figure 7.8. G from the load-based equation versus a.**

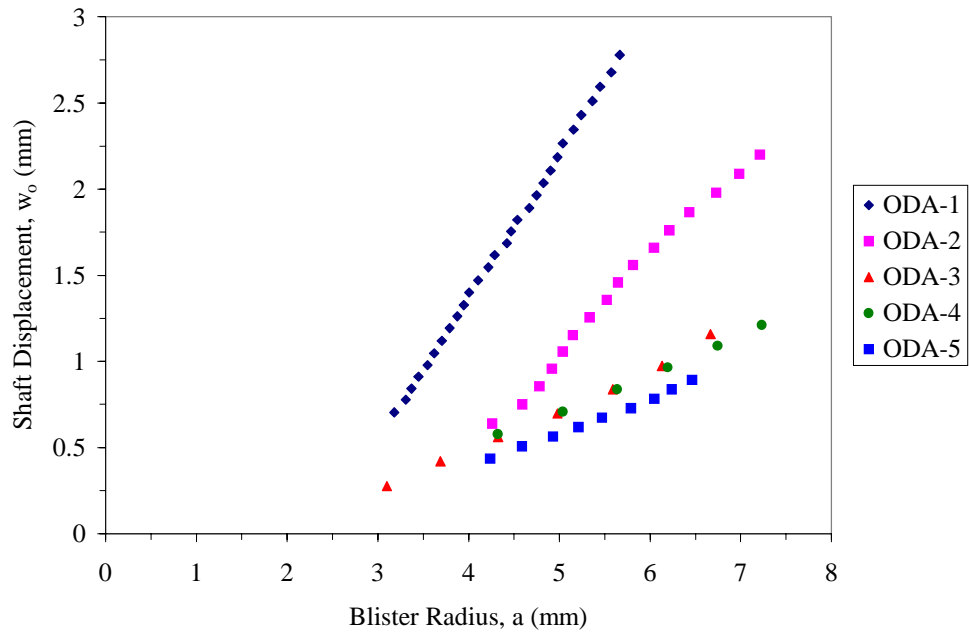


Figure 7.9.  $w_0$  versus  $a$  for the BPADA/ODA samples.

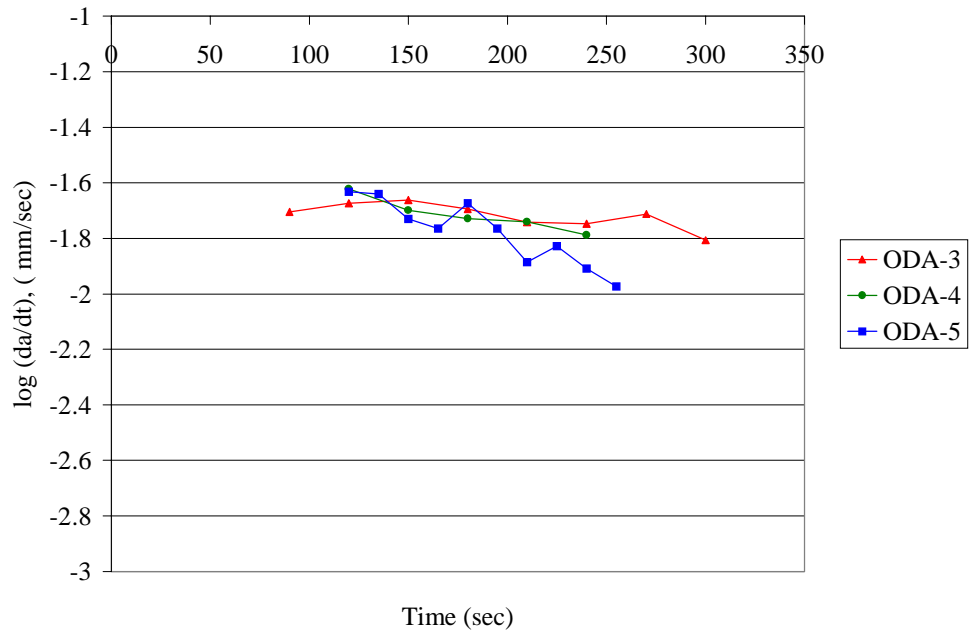
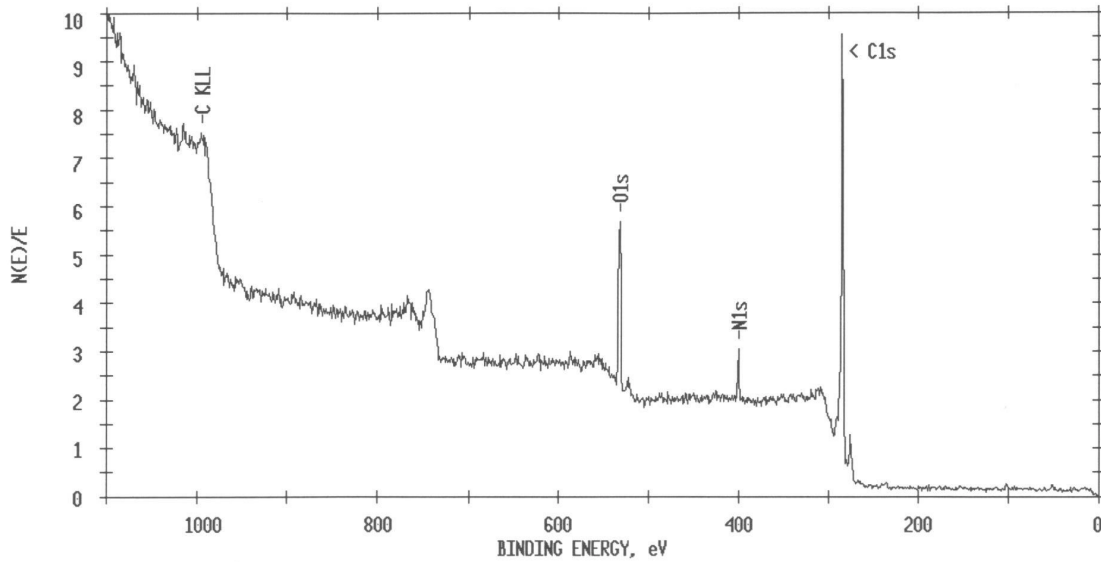


Figure 7.10.  $\log(da/dt)$  versus time for ODA-3, ODA-4, and ODA-5.

### 7.5.2 BPADA/ODA: Locus of Failure Analysis

To determine the locus of failure (LOF), the debonded polyimide film and the silicon wafer failure surface were characterized using XPS. A XPS wide-scan of the polyimide side of BPADA/ODA-2, which is representative of all the debonded polyimide films, is shown in Figure 7.11.



**Figure 7.11. XPS wide-scan of the polyimide side of BPADA/ODA-2.**

The wide-scan in Figure 7.11 shows that only carbon, oxygen, and nitrogen are on the surface - no silicon is detected. This suggests that the failure occurred within the polyimide adhesive.

A XPS wide-scan of the silicon wafer side of BPADA/ODA-2, which is representative of all the silicon wafer failure surfaces, is presented in Figure 7.12.

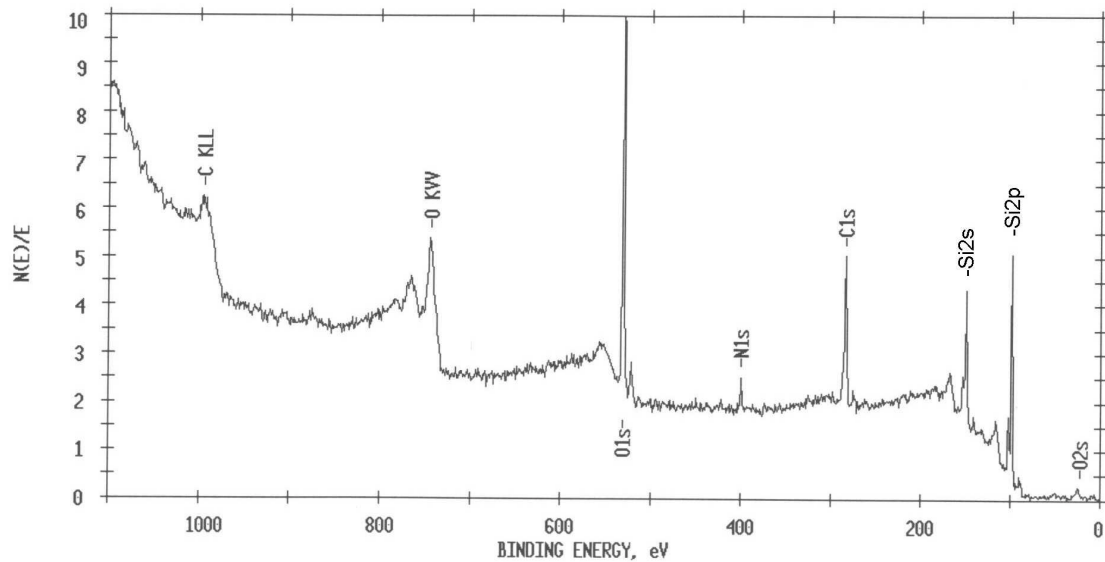


**Figure 7.12. XPS wide-scan of silicon wafer (SiO<sub>2</sub>/Si) side of BPADA/ODA-2.**

The wide-scan in Figure 7.12 shows that carbon, oxygen, nitrogen, and silicon are on the surface. Nitrogen was not detected on the cleaned silicon wafer surface (Chapter 3), thus, the N 1s photopeak in the wide-scan suggests the presence of polyimide.

For each SLBT specimen, an elemental analysis was performed for the C 1s, O 1s, and N 1s photopeaks on the polyimide side of the fracture and for the C 1s, O 1s, N 1s, and Si 2p photopeaks on the silicon wafer side of the fracture. The overall peak for each element was examined with respect to the functional groups within the polyimide chemical structure to identify the presence of polyimide on the silicon wafer surface. The C 1s photopeak for a cleaned silicon wafer, the polyimide side of SLBT BPADA/ODA-2, and the silicon wafer side of SLBT BPADA/ODA-2 are shown in Figure 7.13 to Figure 7.15. The curve fit C 1s assignments are listed in Table 7.6.

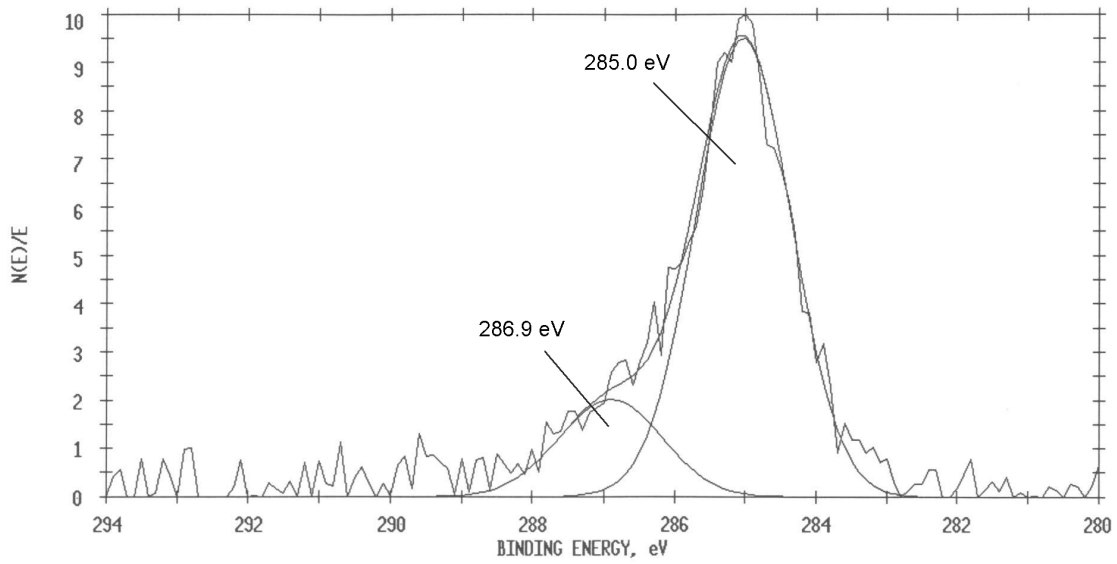


**Figure 7.13. C 1s curve-fitted photopeak of cleaned (SiO<sub>2</sub>/Si) silicon wafer (not stored in water).**

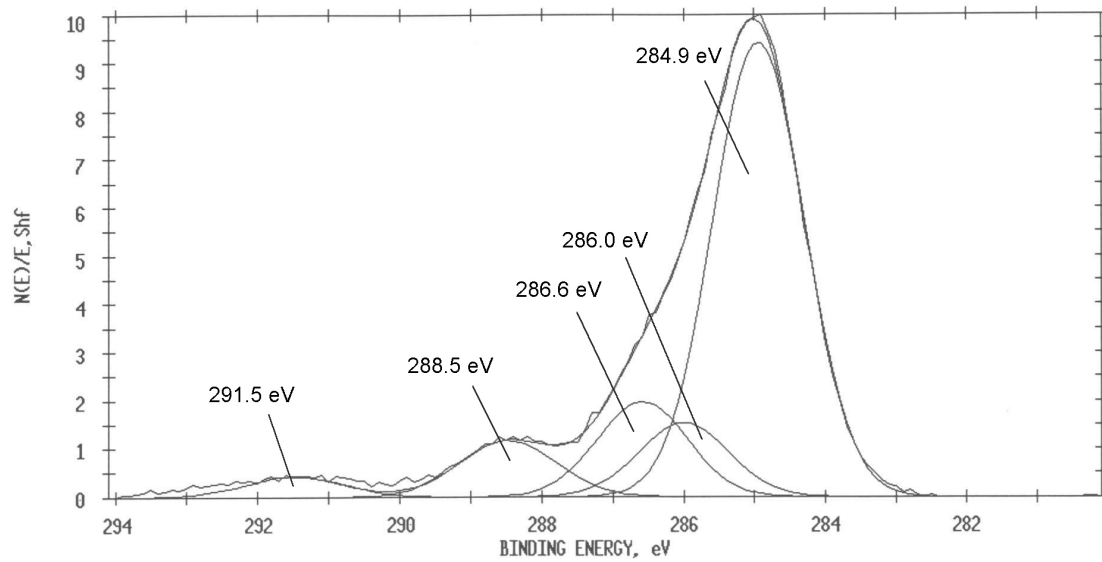


**Figure 7.14. C 1s curve-fitted photopeak of the polyimide side of BPADA/ODA-2.**

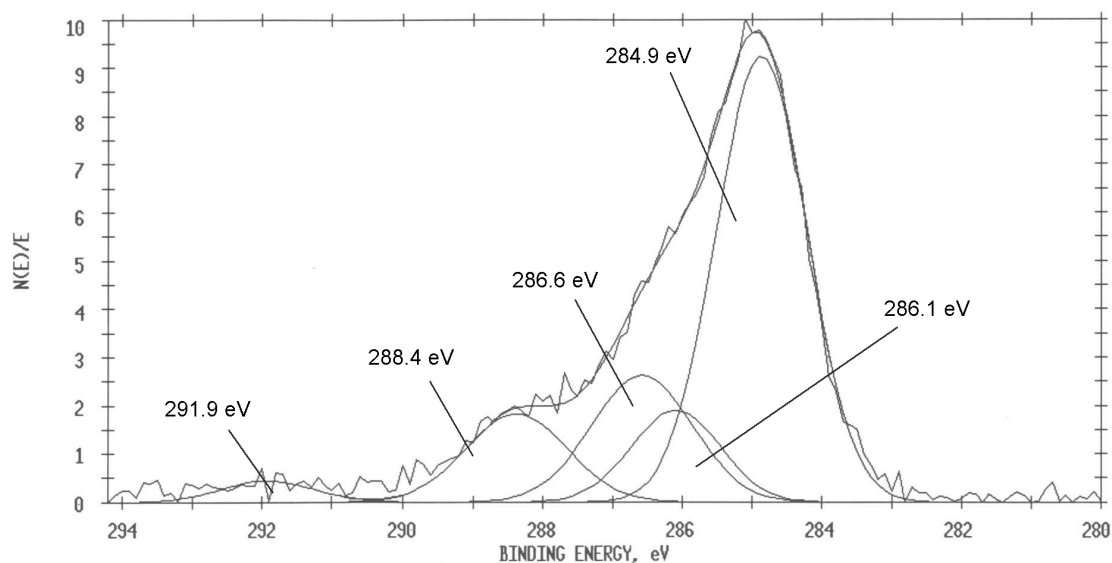


**Figure 7.15. C 1s curve-fitted photopeak of the silicon wafer side of BPADA/ODA-2.**

**Table 7.6. Curve fit C 1s assignments for cleaned silicon wafer (SiO<sub>2</sub>/Si) and failure surfaces of BPADA/ODA-2.**

Sample	% C-H/C-C	% C-N	% C-O	% C=O	$\pi-\pi^*$
Silicon Wafer-cleaned <sup>a</sup>	81.6	-	18.4	-	-
Silicon Wafer side	56.2	11.2	17.6	12.3	2.7
Polyimide side	64.9	10.4	13.3	8.4	3.1

<sup>a</sup> Wafer was not stored in water.

The C 1s photopeak of the cleaned silicon wafer (Figure 7.13) is predominantly C-H (285.0 eV) and C-O (286.9 eV) contaminants. The C 1s photopeak of the two SLBT surfaces revealed C-H/C-C (284.9 eV), C-N ( $\approx$ 286.0 eV), C-O (286.6 eV), and C=O (288.4 eV), and a  $\pi$ -to- $\pi^*$  shake-up satellite ( $\approx$ 291.5 eV). The carbonyl carbon appears at the highest binding energy because it is in the most electronegative environment.<sup>13</sup> The  $\pi$ -to- $\pi^*$  shake-up satellite arises from the aromatic carbons of the polyimide. The C1s curve-fits indicate that the same types of carbon are present on both the PI and the silicon wafer side of failure surfaces, thus the SLBT failure was in the polyimide adhesive. For the polyimide side, the percentage of the total curve-fitted area of each functional group agrees well with that expected from the BPADA/ODA chemical structure. For the silicon wafer side, the C-H/C-C and C-O contaminants on the cleaned

surface are included within the curve-fit; this leads to the small discrepancy in the area percentages with the polyimide side.

The N 1s photopeak (not shown) observed on the silicon wafer failure surface possessed a binding energy of 400.3 eV which was in agreement with the N 1s photopeak on the polyimide side. The photopeak was assigned to the N-C=O imide group. These observations verify that these blister specimens failed within the polyimide.

To determine if the polyimide on the silicon wafer side of failure was a film or existed in islands, a ratio between the intensities of the photopeaks for elemental silicon and silicon from the native oxide layer was taken. Across all SLBT specimens, the ratio was not constant, which is indicative of a film of polyimide on the silicon wafer surface.

The atomic concentration percentages for the BPADA/ODA SLBT samples are listed in Table 7.7. The N:Si ratio for the SiO<sub>2</sub>/Si failure surface, also listed in Table 7.7, is used to interpret the adhesion energies calculated from the load-based equation.

**Table 7.7. XPS results for BPADA/ODA SLBT samples.**

Sample	Failure Surface	% C	% O	% N	% Si	N:Si	Adhesion energy(J/m <sup>2</sup> ) <sup>b</sup>
Wafer-cleaned <sup>a</sup>	SiO <sub>2</sub>	10.2	38.2	ND	51.6	-	-
ODA-1	SiO <sub>2</sub>	47.7	27.2	4.5	20.6	0.22	-
	PI	82.3	14.1	3.6	ND	-	-
ODA-2	SiO <sub>2</sub>	30.3	31.2	3.2	35.4	0.09	-
	PI	82.8	13.1	4.0	ND	-	-
ODA-3	SiO <sub>2</sub>	39.2	27.6	6.1	27.2	0.22	7.1
	PI	75.4	17.1	7.5	ND	-	-
ODA-4	SiO <sub>2</sub>	22.8	36.8	2.5	37.9	0.07	7.9
	PI	83.3	12.3	4.3	ND	-	-
ODA-5	SiO <sub>2</sub>	20.3	38.0	2.3	39.4	0.06	7.8
	PI	81.5	13.7	4.8	ND	-	-

<sup>a</sup> Wafer was not stored in water.

<sup>b</sup> Adhesion energy calculated from the load-based equation.

Relative to the cleaned wafer, all the SiO<sub>2</sub>/Si SLBT failure surfaces showed an increase in the percentage of carbon and nitrogen, and a decrease in the percentage of oxygen and silicon. These findings are attributed to a layer of polyimide on the SiO<sub>2</sub>/Si surface. The failure is

probably within a weak boundary layer (WBL) in the polyimide which forms at the polyimide/SiO<sub>2</sub> interface during sample preparation. When the polyimide solution is cast onto the silicon wafer, the surface may cause the polymer chains to orient parallel to the surface.<sup>14,15</sup> Any orientation may be locked-in by the rapid heating of the silicon wafer and the evaporation of the solvent. Recalling, that the sample is placed on a hot plate that is preheated to ≈100 °C, this procedure may create a WBL between the oriented, surface-bound chains and the bulk polyimide. Adhesive bond failure could occur within the WBL or at the boundary between the surface-bound chains and the bulk polyimide.

The N:Si ratio reflects the amount of polyimide on the surface. Table 7.7 shows that ODA-1 possessed the highest N:Si ratio. For ODA-4 and ODA-5, their similar N:Si ratios are consistent with their similar adhesion energies. The atomic concentrations on the SiO<sub>2</sub> surface of ODA-4 and ODA-5 suggest nearly interfacial failure in the adhesive because although nitrogen is detected, the carbon contents are very low (≈ 21 %), the oxygen contents are comparable to the cleaned wafer (≈ 37 %), and the silicon contents are high (≈ 38 %). The adhesion energy of ODA-3 is comparable to ODA-4 and ODA-5, however, the atomic concentrations on the SiO<sub>2</sub>/Si surface of ODA-3 imply that a greater amount of polyimide is present. Table 7.7 shows that for ODA-3, the percentage of nitrogen on both the SiO<sub>2</sub>/Si and PI side is much higher (> 6 %) than for the other ODA samples. Also the PI side of ODA-3 contains a lower and higher percentage of carbon and oxygen, respectively, than for the other PI failure surfaces. The C 1s photopeak on both sides of failure revealed a very prominent C-N peak at 286.3 eV. To verify these observations for ODA-3, a second spot on a freshly exposed region of the SiO<sub>2</sub>/Si and PI failure surfaces was examined by XPS; again, a very high nitrogen percentage was detected (7.15 %). The N:Si ratio for the second spot was 0.3684. It is postulated from these observations that (1) the polyimide of ODA-3 failed at a WBL between the surface-bound polyimide chains and the bulk polyimide, (2) ODA-3 contained a high concentration of low molecular weight polyimide chains that migrated to the SiO<sub>2</sub>/Si surface during the film casting step of the sample preparation, (3) unreacted diamine monomer was present and migrated to the surface during the sample preparation or (4) the surface was contaminated with nitrogen from the ammonium hydroxide cleaning step. With respect to (4), while nitrogen contamination is possible, XPS analysis on several cleaned wafer surfaces, discussed in Chapter 3 section 3.3.11, indicated that nitrogen was not detected; thus, factors (1- 3) are probably more likely.

## 7.6 BPADA/ODA:DoDDA, 75:25 at High %RH

### 7.6.1 BPADA/ODA:DoDDA, 75:25: SLBT Results

The SLBT specimens for the ODA:DoDDA, 75:25 composition were prepared using the patch technique as described in Chapter 3. The  $P$  vs.  $w_o$ ,  $P$  vs.  $a$ , and  $w_o$  vs.  $a$  relationships were examined to determine the applicability of the hybrid, load-based, and displacement-based equations, respectively. When blister growth was inelastic, one or more of the four experimental factors described in section 7.4.2 were used to interpret the deviation. All figures are placed at the end of the section.

The  $P$  vs.  $w_o$  relationship for ODA:DoDDA, 75:25-1 is presented in Figure 7.16. Two regions are observed. The patch undergoes an initial loading in the range 0-4 N. An increase in  $w_o$  is observed at  $P \approx 2$  N where a small region of the patch debonded. At a load of  $\approx 4$  N, the patch delaminated completely and initiated blister growth. The blister growth was rapid initially, but then stabilized, as observed by the linear  $P$  vs.  $w_o$  relationship at  $w_o$  values above 2 mm. Also, the point where the blister growth exceeded the field of view of the borescope is marked. This is a typical curve for samples prepared by the patch technique. As discussed in section 7.4.2, the adhesion of the patch to SiO<sub>2</sub>/Si was usually greater than the adhesion strength of the PI film-SiO<sub>2</sub>/Si. For 75:25-1, a small region of stable crack growth was observed. In Figure 7.16, within the linear region of blister growth, the relationship  $P \propto w_o$  is not found.

The  $P$  vs.  $w_o$  relationship for ODA:DoDDA, 75:25-2 is presented in Figure 7.17. Again two regions are observed: an initial loading region, followed by a region of linear blister growth. The best-fit line from the linear blister growth region does not intersect the origin, thus the adhesion energy cannot be calculated with confidence.

The  $P$  vs.  $a$  relationships for both 75:25 samples are shown in Figure 7.18. For 75:25-1, only a small increase in load causes the blister radius to grow beyond the field of view of the borescope and the proportionality,  $P \propto a$ , is not observed. For 75:25-2, the best-fit line intersects the x-axis at 0.13 mm. This indicates that  $P \propto a$  and  $G$  is constant over the range of data by the load-based equation. The constant  $G$  for 75:25-2 is shown in Figure 7.19.

The  $w_o$  vs.  $a$  relationships for both 75:25 samples are shown in Figure 7.20 along with their best-fit lines. For 75:25-1,  $w_o$  appears to be proportional to the blister radius,  $a$ , over the whole range of data. A best-fit line through the origin was made with a statistical  $R^2$  value of

0.9965. The  $G$  values from the displacement-based equations are plotted as a function of the blister radius in Figure 7.21. Figure 7.21 shows that during the experiment  $G$  begins constant, decreases, then stabilizes. This pattern is suggested to reflect the influence of film thickness on the adhesion energy as discussed in section 7.4.2. The last six data points in Figure 7.21 reflect stable crack growth. If it is assumed that over the 0.62 N increase in load that these data are obtained that plastic deformation at the shaft tip is small, then  $w_o \propto a$ . Also presented in Figure 7.20, are the data for 75:25-2 and the equation for their best-fit line. A non-zero intercept is noted (1.50 mm), however, it lies within the radius of the shaft tip.

The results for the two samples are now summarized. For 75:25-1,  $N_{eff} < \sigma_y h$  and plastic yielding at the crack tip is not predicted. The 75:25 composition exhibited the highest  $E$  and  $\sigma_y$ , and also has a high glass transition temperature  $\approx 180$  °C, so  $N_{eff} < \sigma_y h$  is not surprising. While a large dimple at the place of contact with the shaft tip was observed, it is speculated that  $w_p$  is a constant offset during the 0.62 N increase in load that the blister radii were measured. The low  $N_{eff}$  and the speculation of a constant  $w_p$  offset are consistent with the observation that  $w_o \propto a$  and suggests that blister growth is elastic. By the displacement-based equation, the adhesion energy of BPADA/ODA:DoDDA, 75:25-1 to SiO<sub>2</sub>/Si was 22.6 J/m<sup>2</sup>.  $P \propto w_o$  and  $P \propto a$  were not observed. The blister growth rate, da/dt, was 2.46 mm/min.

For 75:25-2  $N_{eff} < \sigma_y h$  and plastic yielding at the crack tip is not predicted. This is consistent with the observation  $P \propto a$  and suggests that the application of Wan and Mai's model is allowed. By the load-based equation, the adhesion energy ODA:DoDDA, 75:25-2 to SiO<sub>2</sub> was 17.3 J/m<sup>2</sup>. A large dimple at the place of contact with the shaft tip was observed, and over the 2.5 N increase in load that the blister radii were measured. Therefore, the most confidence is placed in the  $G$  determined by the load-based equation. The blister growth rate, da/dt, was 0.65 mm/min.

The adhesion energies of BPADA/ODA:DoDDA, 75:25 to SiO<sub>2</sub>/Si are listed in Table 7.8. The adhesion energies are higher than for BPADA/ODA to SiO<sub>2</sub>/Si. This may suggest that the BPADA/ODA:DoDDA, 75:25 to SiO<sub>2</sub>/Si adhesive bond is less sensitive to moisture, possibly due to the hydrophobic aliphatic segments.

**Table 7.8. Adhesion Energy of BPADA/ODA:DoDDA 75:25 to SiO<sub>2</sub>/Si at 25 °C and high %RH.**

Sample	Adhesion Energy (J/m <sup>2</sup> )
75:25-1	22.6 <sup>a</sup>
75:25-2	17.3 <sup>b</sup>

<sup>a</sup> From the displacement-based equation.

<sup>b</sup> From the load-based equation.

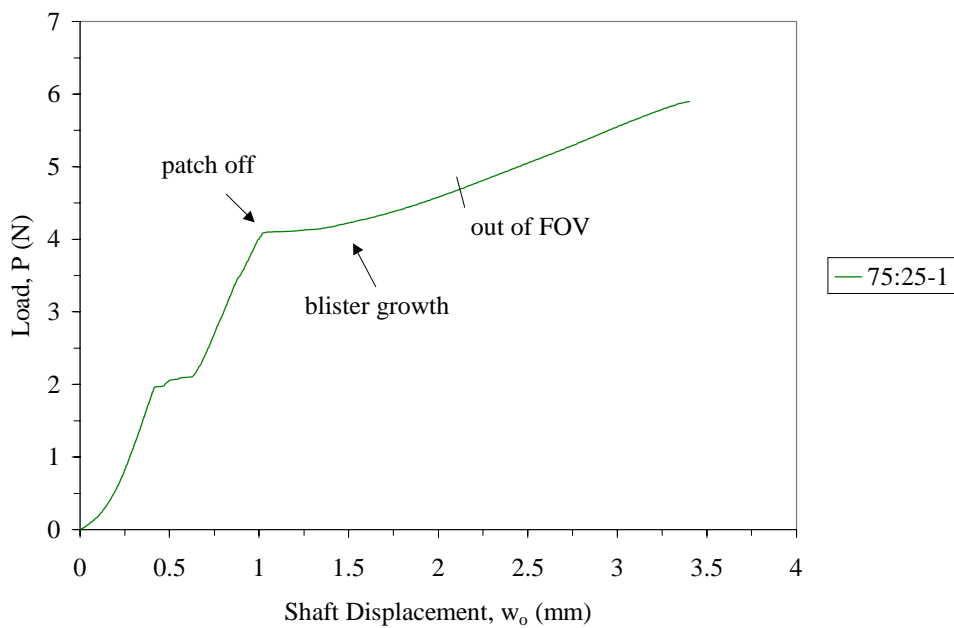


**Figure 7.16, P versus  $w_0$  for BPADA/ODA:DoDDA, 75:25-1.**

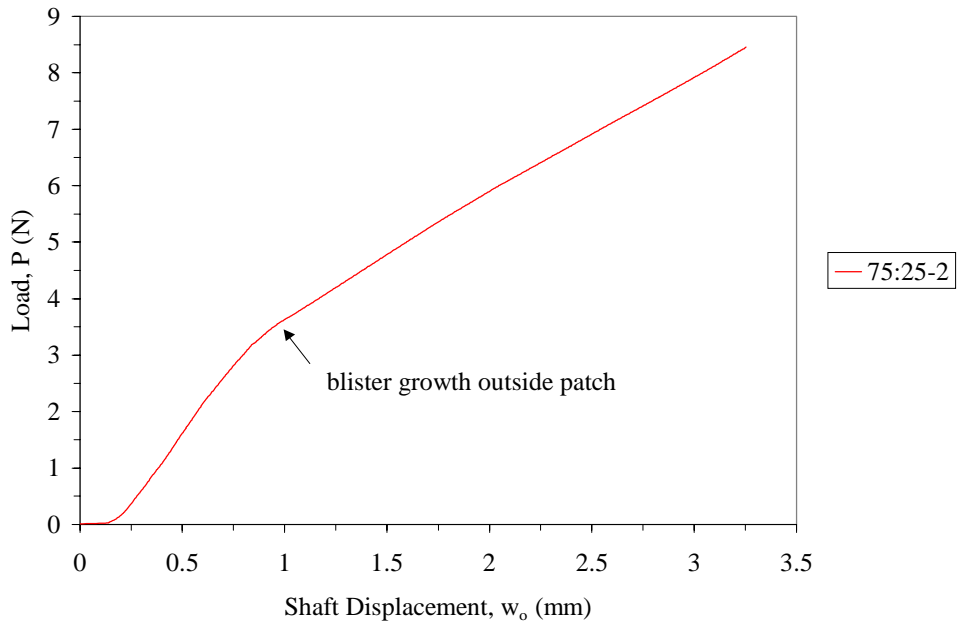


**Figure 7.17.  $P$  versus  $w_0$  for BPADA/ODA:DoDDA, 75:25-2.**

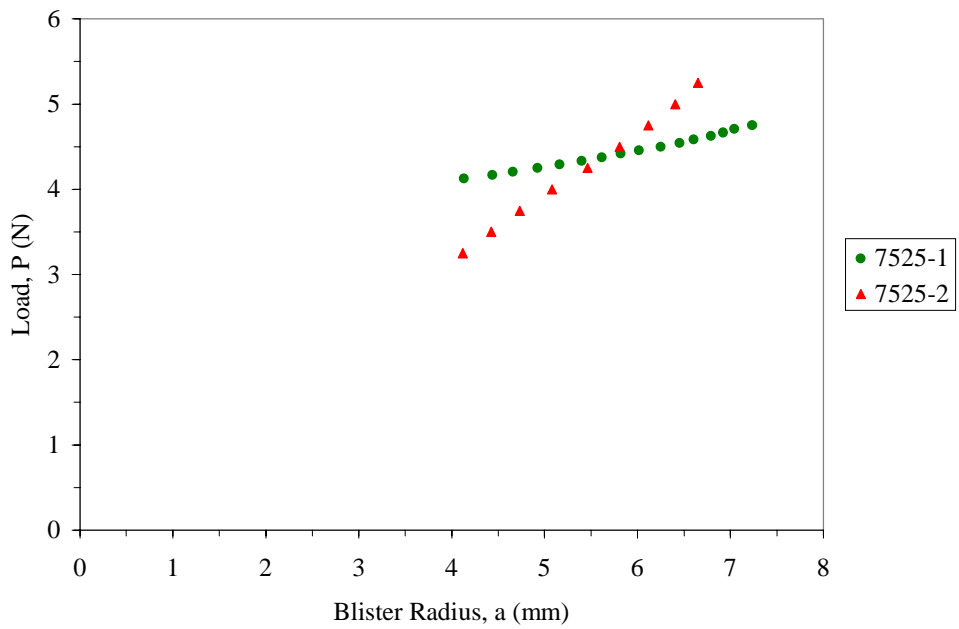


**Figure 7.18.  $P$  versus  $a$  for BPADA/ODA:DoDDA, 75:25-1 and 75:25-2.**

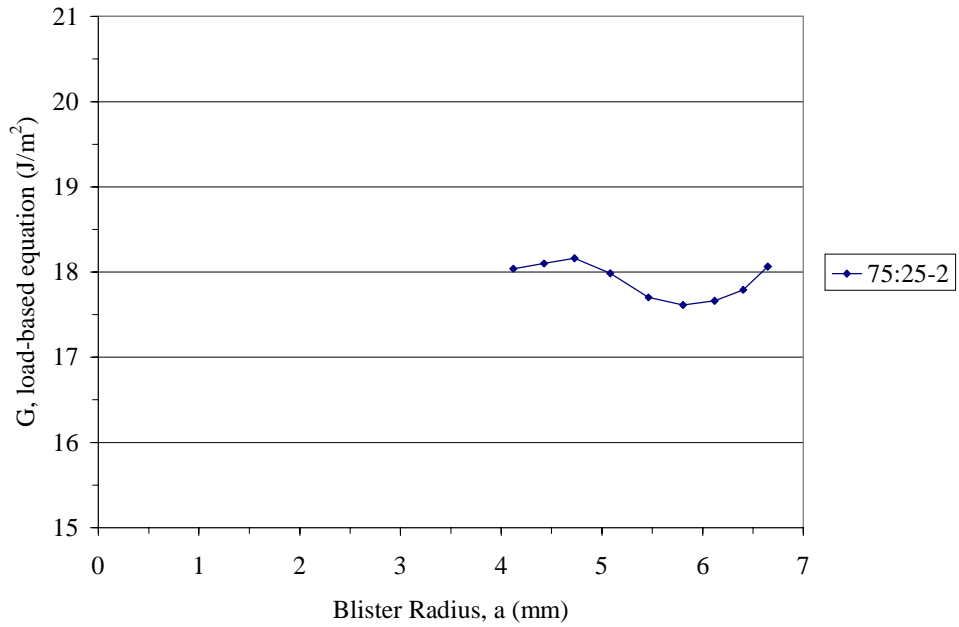


**Figure 7.19.** G from the load-based equation versus a for 75:25-2.

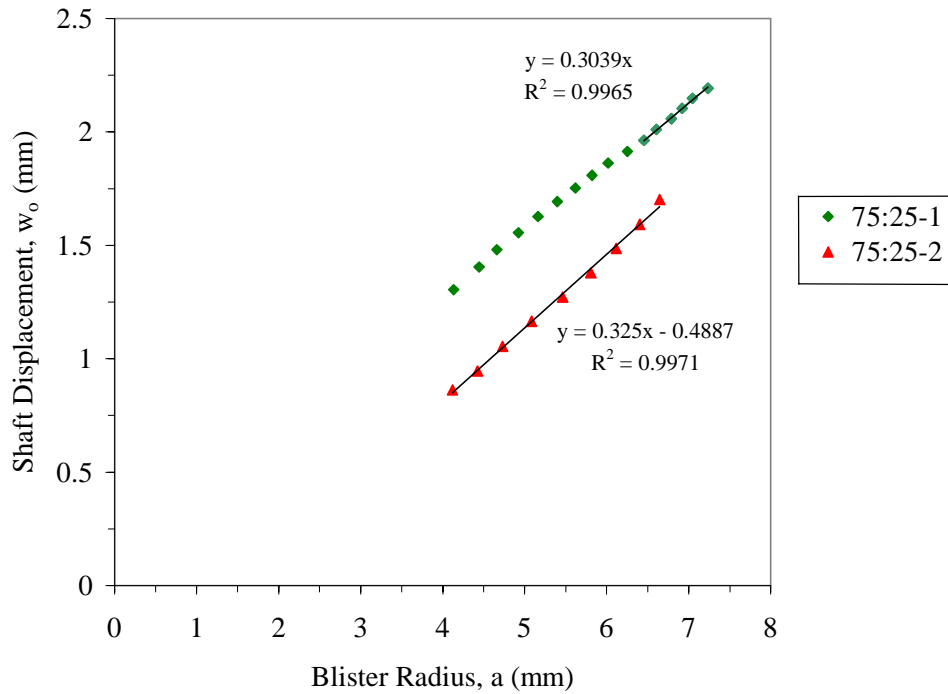


**Figure 7.20.** w<sub>0</sub> versus a for BPADA/ODA:DoDDA, 75:25-1 and 75:25-2.

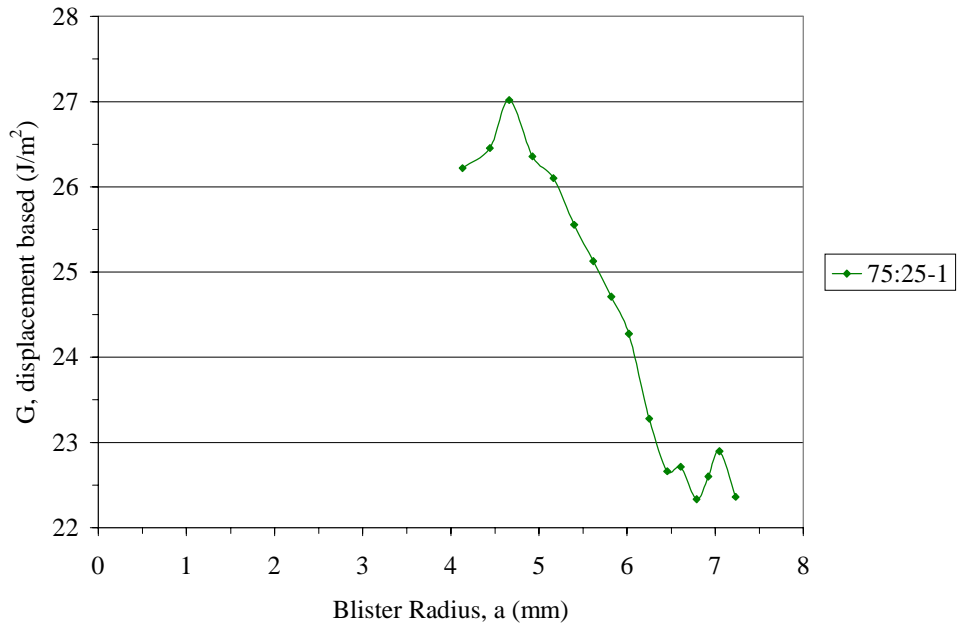


**Figure 7.21. G from the displacement-based equation versus a for 75:25-1.**

**7.6.2 BPADA/ODA:DoDDA, 75:25: Locus of Failure Analysis.**

To determine the LOF for the BPADA/ODA:DoDDA, 75:25 SLBT samples, the debonded polyimide films and the silicon wafer failure surfaces were characterized using XPS. Analogous to the BPADA/ODA samples, the wide-scans and the analysis of the photopeaks revealed that the LOF was probably within a weak boundary layer on the polyimide side. The atomic concentration percentages and N:Si ratios for the BPADA/ODA:DoDDA, 75:25 SLBT samples are listed in Table 7.9.

**Table 7.9. XPS results for BPADA/ODA:DoDDA, 75:25 SLBT samples.**

Sample	Failure Surface	% C	% O	% N	% Si	N:Si	Adhesion Energy(J/m <sup>2</sup> )
Wafer-cleaned <sup>a</sup>	SiO <sub>2</sub>	15.0	40.2	ND	44.8	-	-
75:25-1	SiO <sub>2</sub>	33.2	32.4	4.4	30.1	0.15	22.6 <sup>b</sup>
	PI	78.5	15.9	5.5	ND	-	
75:25-2	SiO <sub>2</sub>	32.5	31.1	3.3	33.0	0.10	17.3 <sup>c</sup>
	PI	81.1	14.3	4.6	ND	-	

<sup>a</sup> Wafer was stored in water for 16 hr.

<sup>b</sup> Adhesion energy calculated from the displacement-based equation.

<sup>c</sup> Adhesion energy calculated from the load-based equation.

Table 7.9 shows that for both samples, the locus of failure occurred in the polyimide. Nitrogen from the imide functional group is present on the SiO<sub>2</sub>/Si surface, but no silicon is detected on the PI side of failure. On the SiO<sub>2</sub>/Si failure surface, an increase in the percentage of carbon, and a decrease of the percentage of oxygen and silicon, relative to the cleaned wafer, is also observed. The C 1s photopeak for the SiO<sub>2</sub>/Si closely resembled that for the polyimide side of failure. All the findings are consistent with the presence of polyimide on the SiO<sub>2</sub>/Si side of failure. The N:Si ratio for 75:25-1 is slightly higher than for 75:25-2. This suggests that the locus of failure in 75:25-1 was more cohesive, which is in agreement with their estimated adhesion energies. and may explain the why its adhesion energy to SiO<sub>2</sub>/Si is  $\approx 5 \text{ J/m}^2$  greater than that of 75:25-2

## 7.7 BPADA/ODA:DoDDA, 50:50 at High %RH

### 7.7.1 BPADA/ODA:DoDDA, 50:50: SLBT Results

The BPADA/ODA:DoDDA, 50:50 samples were prepared using the patch technique. Blisters were successfully propagated using the DMA and the blister radii were measured using the borescope/computer. Analysis of the  $P$  vs.  $w_o$ ,  $P$  vs.  $a$ , and  $w_o$  vs.  $a$  relationships, the effective membrane stress, and the post-mortem specimens all lead to the conclusion that blister growth was not elastic for the five 50:50 specimens. Thus, the SLBT results are presented qualitatively and only for relative ranking.

The  $P$  vs.  $w_o$  and  $P$  vs.  $a$  curves, shown in Figure 7.23 and Figure 7.24, for 50:50-1, 50:50-2, and 50:50-3 are quite different from 50:50-4 and 50:50-5. For the latter two samples, the load-control operation of the DMA lead to rapid, crack growth over a  $P \approx 0.7 \text{ N}$  increase in

load. The blister growth rates,  $da/dt$ , were 3.41 mm/min and 56.7 mm/min for samples 50:50-4 and 50:50-5, respectively. The most confidence was placed in the  $w_o$  vs.  $a$  relationship. Figure 7.25 shows that the data for 50:50-4 can be reasonably fit to a line through the origin. For this sample, plastic yielding is not predicted because  $N_{eff} < \sigma_y h$ . The corresponding  $G$  versus  $a$  values of 50:50-4, shown in Figure 7.26, indicate that  $G$  is not constant. Therefore  $w_o$  is not proportional to  $a$ . For 50:50-5, the blister growth was so rapid that the increment of data collection by the DMA was too large to enable a  $(w_o, a)$  coordinate pair to be extracted.

The  $P$  vs.  $w_o$  curves for 50:50-1, 50:50-2, and 50:50-3 in Figure 7.23 show that after the patch debonded, rapid blister growth did not occur. For each, a second loading region is observed, followed by blister growth at a rate of 0.37, 0.22, and 0.10 mm/min for samples 50:50-1, 50:50-2, and 50:50-3, respectively. The slow rate of growth for 50:50-3 is reflected in the  $P$  vs.  $a$  curve, where the 18 N load limit of the DMA is reached, but the blister has only grown  $\approx 2$  mm. The post-mortem specimen, Figure 7.22, shows extensive plastic deformation.



**Figure 7.22. BPADA/ODA:DoDDA, 50:50-3 post-mortem specimen showing plastic yielding.**

From the  $w_o$  vs.  $a$  relationships shown in Figure 7.25, the curve for 50:50-1 appears to fit to a line through the origin reasonably well; however, plastic yielding is predicted at the crack tip by,  $N_{eff} > \sigma_y h$ . For this sample, error in  $w_o$  is expected to arise from  $w_p$ , as well. Thus, the application of Wan and Mai's model is not appropriate.

For SLBT experiments of the 50:50 composition, plastic yielding was predicted at the crack tip. This may not only be a consequence of the lower modulus and  $\sigma_y$  of the polyimide, but may also arise from stronger adhesion to  $\text{SiO}_2/\text{Si}$ . These SLBT experiments were performed at the same "high %RH" as for BPADA/ODA and the ODA:DoDDA, 75:25 composition-for which elastic blister growth was initiated. The "strong adhesion" of the 50:50 composition may indicate

that the adhesive bond is less sensitive to moisture, and as such, the tensile strength limit of the film is exceeded as it debonds.

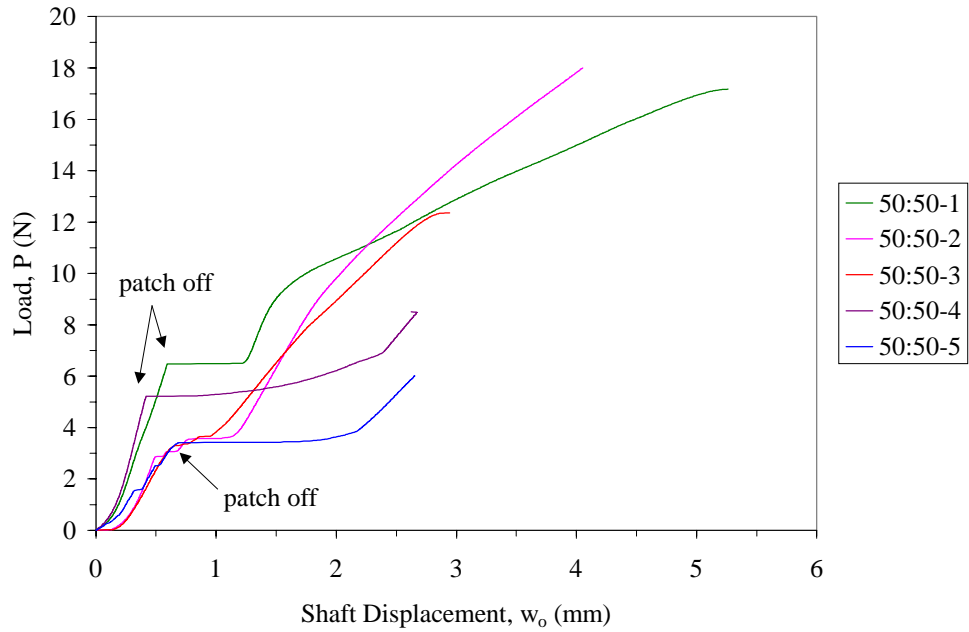


**Figure 7.23. P versus  $w_0$  for the BPADA/ODA:DoDDA, 50:50 SLBT samples.**

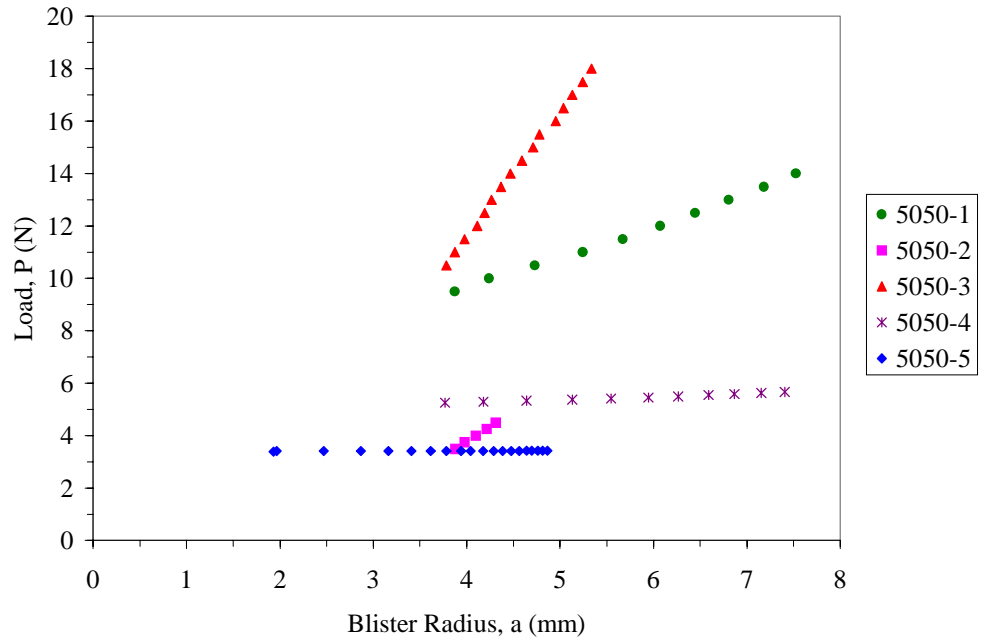


**Figure 7.24.  $P$  versus  $a$  for the BPADA/ODA:DoDDA, 50:50 SLBT samples.**

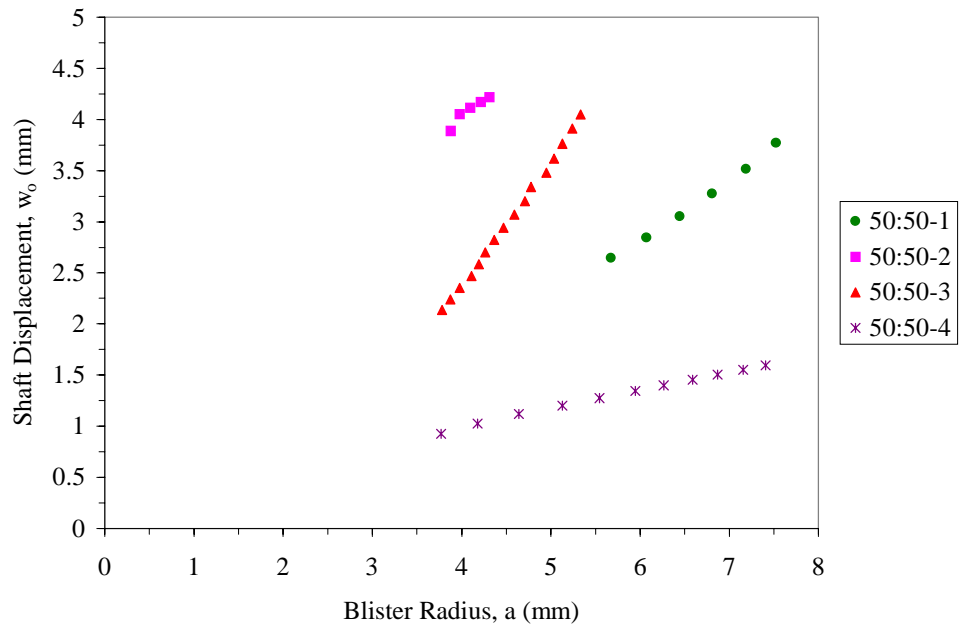


**Figure 7.25.  $w_0$  versus  $a$  for the BPADA/ODA:DoDDA, 50:50 SLBT samples.**

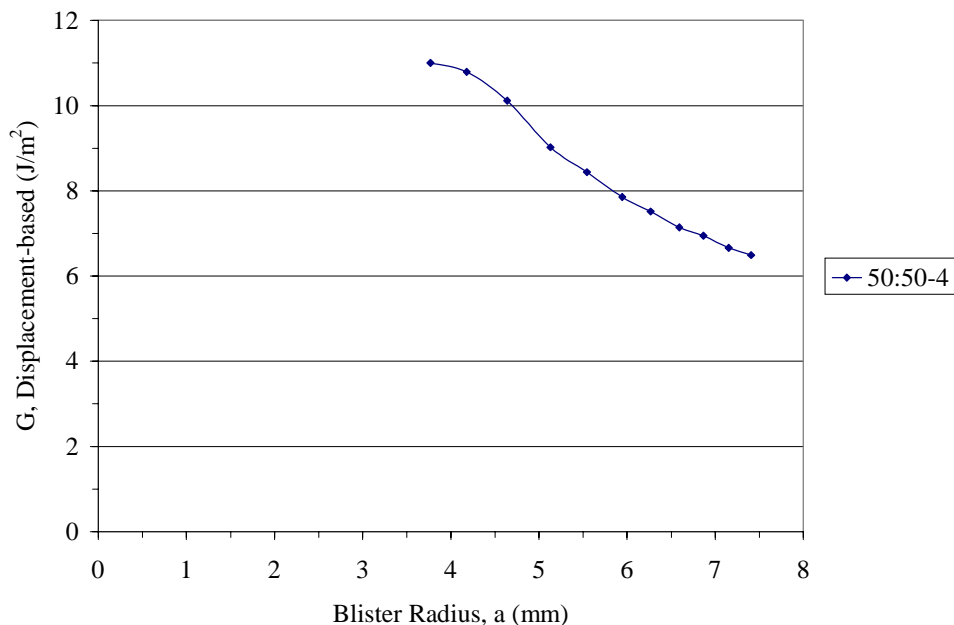


**Figure 7.26. G determined by the displacement-based equation versus a for 50:50-4.**

### 7.7.2 BPADA/ODA:DoDDA, 50:50: Locus of Failure Analysis

Although adhesion energies could not be quantified, the LOF for the BPADA/ODA:DoDDA, 50:50 SLBT samples were characterized using XPS. Analogous to the samples for the previous polyimide compositions, the wide-scans and the analysis of the photopeaks revealed that the LOF was within a weak boundary layer on the polyimide side. The atomic concentration percentages and N:Si ratios for the BPADA/ODA:DoDDA, 50:50 SLBT samples are listed in Table 7.10.

**Table 7.10. XPS results for BPADA/ODA:DoDDA, 50:50 SLBT samples.**

Sample	Failure Surface	% C	% O	% N	% Si	N:Si	Adhesion Energy(J/m <sup>2</sup> ) <sup>b</sup>
Wafer-cleaned <sup>a</sup>	SiO <sub>2</sub>	10.2	38.2	ND	51.6	-	-
50:50-1	SiO <sub>2</sub>	42.6	26.2	3.6	27.6	0.13	-
	PI	83.2	12.4	4.4	ND	-	-
50:50-2	SiO <sub>2</sub>	37.2	30.4	5.3	27.1	0.20	-
	PI	81.4	15.4	3.3	ND	-	-
50:50-3	SiO <sub>2</sub>	34.5	31.2	2.5	31.6	0.08	-
	PI	82.7	13.1	4.2	ND	-	-
50:50-4	SiO <sub>2</sub>	43.2	27.6	5.7	23.5	0.24	-
	PI	76.5	16.7	6.8	ND	-	-
50:50-5	SiO <sub>2</sub>	26.3	35.1	2.1	36.6	0.06	-
	PI	82.8	13.1	4.1	ND	-	-

<sup>a</sup> Wafer was not stored in water.

<sup>b</sup> Could not be calculated due to deviation from theory.

The high N:Si ratios for 50:50-1, 50:50-2 and 50:50-4 imply that a large amount of polyimide remains on the SiO<sub>2</sub>/Si failure surface. This is consistent with the increased percentage of carbon, relative to the cleaned wafer. The percentage of nitrogen for 50:50-4 on both sides of failure, however, is  $\approx 2$  atomic concentration % greater than observed for the other 50:50 samples. For 50:50-4, the N:Si ratio may not provide an accurate measure of the amount of polyimide on the surface for similar reasons which were outlined for sample ODA-3 in section 7.5.2. The N:Si ratios for samples 50:50-3 and 50:50-5 are much lower, which suggests that adhesive failure occurred closer to the PI interface. The carbon percentage for 50:50-5, in particular, is only 15 atomic concentration % higher than the clean SiO<sub>2</sub>/Si surface. On the polyimide side of failure, the percentages of oxygen are slightly lower than observed for the ODA and 75:25 compositions. This reflects the decrease in the ODA content, which contains an ether functional group.

## 7.8 BPADA/ODA:DoDDA, 25:75 and BPADA/DoDDA at High %RH

### 7.8.1 BPADA/ODA:DoDDA, 25:75 and BPADA/DoDDA SLBT Results

The BPADA/ODA:DoDDA, 25:75 and BPADA/DoDDA samples were prepared using the “patch” technique. Blisters were successfully propagated using the DMA and the blister radii were measured using the borescope/computer. Similar to the 50:50 composition, inelastic blister growth was observed. The effective membrane stress revealed that  $N_{eff} > \sigma_y h$ . The  $P$  vs.  $w_o$ ,  $P$  vs.

$a$ , and  $w_o$  vs.  $a$  relationships are shown in Figure 7.28, Figure 7.29, and Figure 7.30, respectively. Thus, quantitative adhesion energies for these PI-SiO<sub>2</sub> interfaces could not be determined. The further increase in the hydrophobic DoDDA content is again suggested to contribute to the apparently “stronger” adhesion to SiO<sub>2</sub> under high %RH.

Substantial plastic yielding was present in the post-mortem specimen of BPADA/DoDDA, shown in Figure 7.27.



**Figure 7.27. BPADA/DoDDA-1 post-mortem sample showing plastic yielding.**

The average  $\sigma_y$  of BPADA/DoDDA, measured by tensile tests, was  $24.3 \pm 1.0$  MPa. This average is  $\approx 13$  MPa lower than the ODA containing polyimides, reflecting the high content of the flexible DoDDA segments of this low  $T_g$  ( $\approx 80$  °C) polyimide. So it is not surprising that yielding would occur during the SLBT as well. The blister growth rate was 0.41 mm/min.

The BPADA/ODA:DoDDA 25:75 polyimide has a  $T_g \approx 112$  °C and a  $\sigma_y$  of  $42.3 \pm 4.2$  MPa. Visually, plastic deformation in the post-mortem SLBT specimens was apparent; however, it was estimated to be much less than for BPADA/DoDDA. The load-control operation of the DMA was again problematic in causing unstable crack growth once the patch debonded, as shown in Figure 7.28. Rapid blister growth occurred over a  $P \approx 1$  N increase in load. The blister growth rates,  $da/dt$ , were 1.55 mm/min and 2.91 mm/min for samples 1 and 2, respectively. Similar to the discussion for the ODA:DoDDA, 75:25 composition, the variable  $P$  was considered unreliable, and the most confidence was placed in the  $w_o$  vs.  $a$  relationship, shown in Figure 7.30. Both samples show non-zero x-intercepts. For each, the  $G$  was not constant over the range of data. From the  $G$  values of 25:75-2, it appeared that the crack was beginning to stabilize just as the blister went out of the field of view of the borescope (Figure 7.31). Regardless, plastic

yielding is predicted at the crack tip because  $N_{eff} > \sigma_y h$ , and the application of Wan and Mai's model is inappropriate.

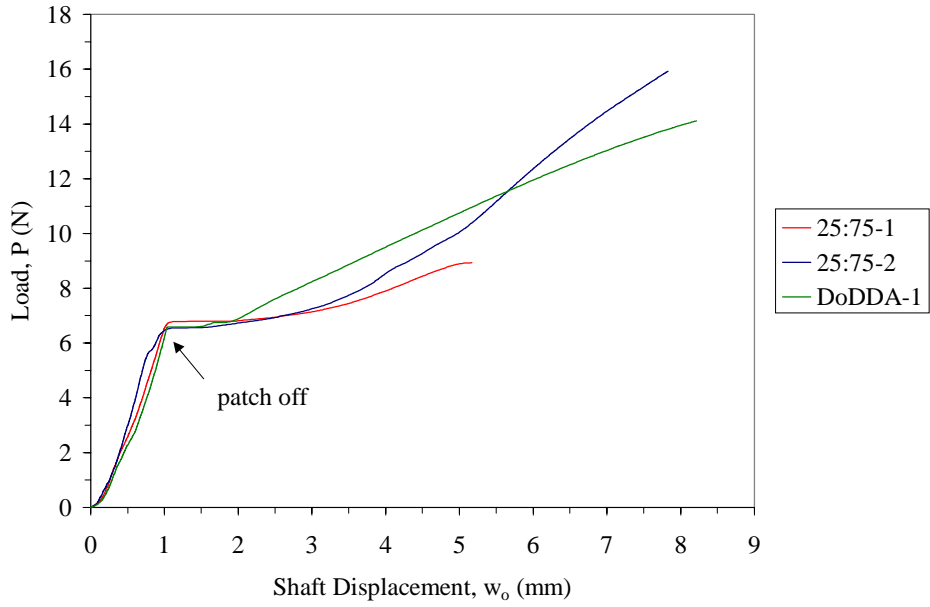


**Figure 7.28. P versus  $w_0$  for BPADA/ODA:DoDDA, 25:75 and BPADA/DoDDA.**

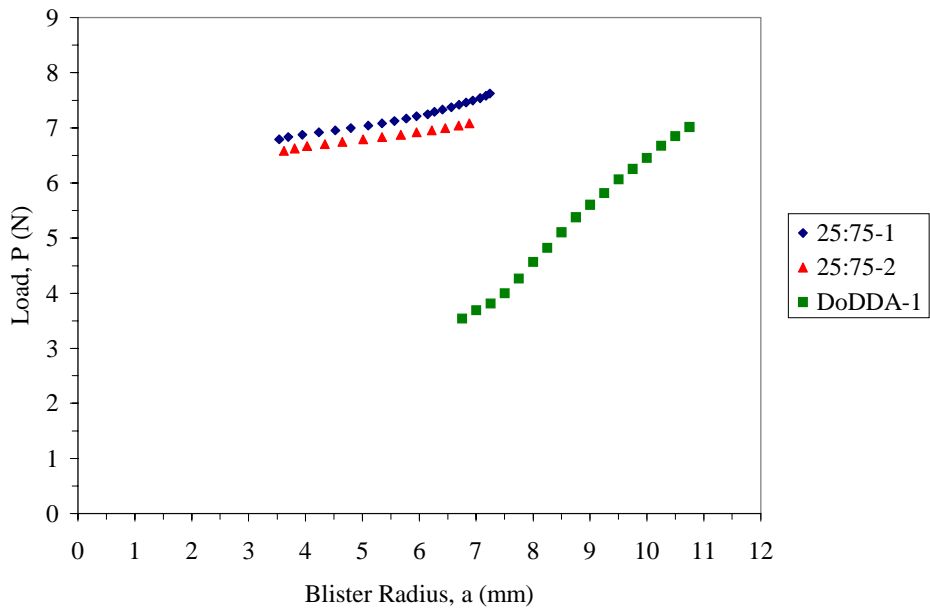


**Figure 7.29. P versus  $a$  for BPADA/ODA:DoDDA, 25:75 and BPADA/DoDDA.**

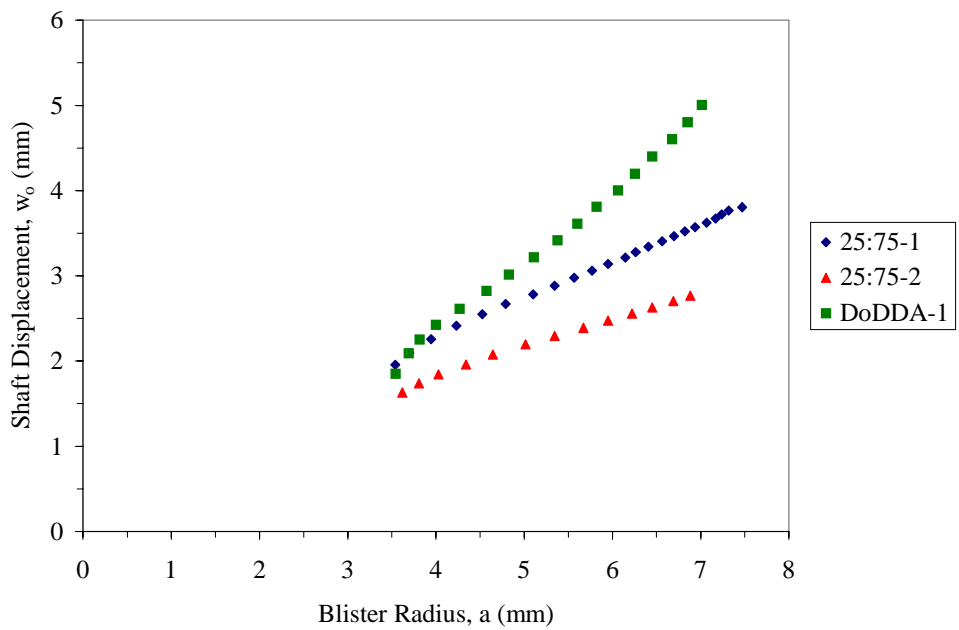


Figure 7.30.  $w_0$  versus  $a$  for BPADA/ODA:DoDDA, 25:75 and BPADA/DoDDA.

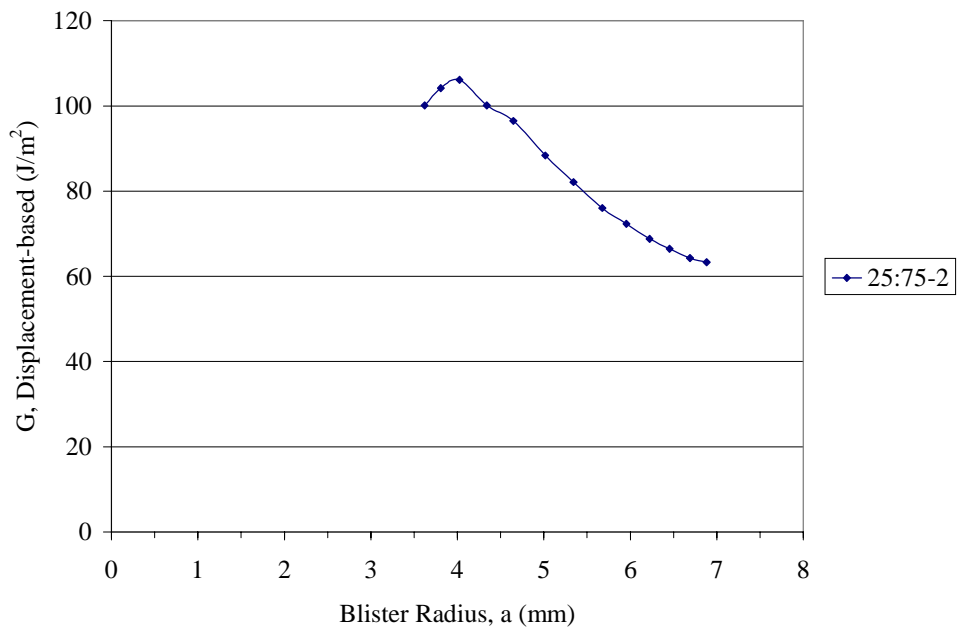


Figure 7.31.  $G$  from the displacement-based equation versus  $a$  for 25:75-2.

### 7.8.2 BPADA/ODA:DoDDA, 25:75 and BPADA/DoDDA: Locus of Failure Analysis.

Although adhesion energies could not be quantified, the LOF for the BPADA/ODA:DoDDA, 25:75 and DoDDA SLBT samples were characterized using XPS. The wide-scans and the analysis of the photopeaks confirmed that the LOF was probably within a weak boundary layer on the polyimide side. The atomic concentration percentages and N:Si ratios for the samples are listed in Table 7.11.

**Table 7.11. XPS results for BPADA/ODA:DoDDA, 25:75 and BPADA/DoDDA SLBT samples.**

Sample	Failure Surface	% C	% O	% N	% Si	N:Si	Adhesion Energy(J/m <sup>2</sup> ) <sup>b</sup>
Wafer-cleaned <sup>a</sup>	SiO <sub>2</sub>	15.0	40.2	ND	44.8	-	-
25:75-1	SiO <sub>2</sub>	31.4	31.7	3.5	33.4	0.10	-
	PI	83.6	12.4	4.1	ND	-	-
25:75-2	SiO <sub>2</sub>	38.9	32.1	4.0	25.0	0.16	-
	PI	83.3	12.3	4.4	ND	-	-
DoDDA-1	SiO <sub>2</sub>	32.3	31.8	4.2	31.7	0.13	-
	PI	83.9	11.7	4.5	ND	-	-

<sup>a</sup> Wafer was stored in water for 16 hr.

<sup>b</sup> Could not be calculated due to deviation from theory.

The N:Si ratios show that 25:75-2 contained a greater amount of polyimide on the SiO<sub>2</sub>/Si side of failure than 25:75-1. The high percentage of carbon, relative to the clean wafer, is consistent with this finding. On the polyimide side of failure, the percentage of oxygen for the DoDDA-1 sample is the lowest of the BPADA-based polyimide series because no ODA monomer, which contains an ether group, is present. For DoDDA-1 the oxygen contribution arises from the carbonyl and ether functional groups the dianhydride monomer. The C 1s photopeak for the polyimide side of failure for DoDDA-1 also reflected the change in chemical composition. The overall peak was more narrow, which indicated the increase in the C-H/C-C types of carbon and a decrease in the C-O type of carbon.

## 7.9 Low %RH SLBT Experiments

SLBT experiments for BPADA/ODA were performed in a low %RH environment at 25, 38, and 70 °C. SLBT experiments for BPADA/ODA:DoDDA, 50:50 were performed in a low %RH environment at 70 °C. The experimental details are presented in Chapter 3.

The BPADA/ODA samples all punctured at the place of contact with the shaft tip before blister growth initiated. An overlay of the load versus shaft displacement curves for the three temperatures is shown in Figure 7.32.

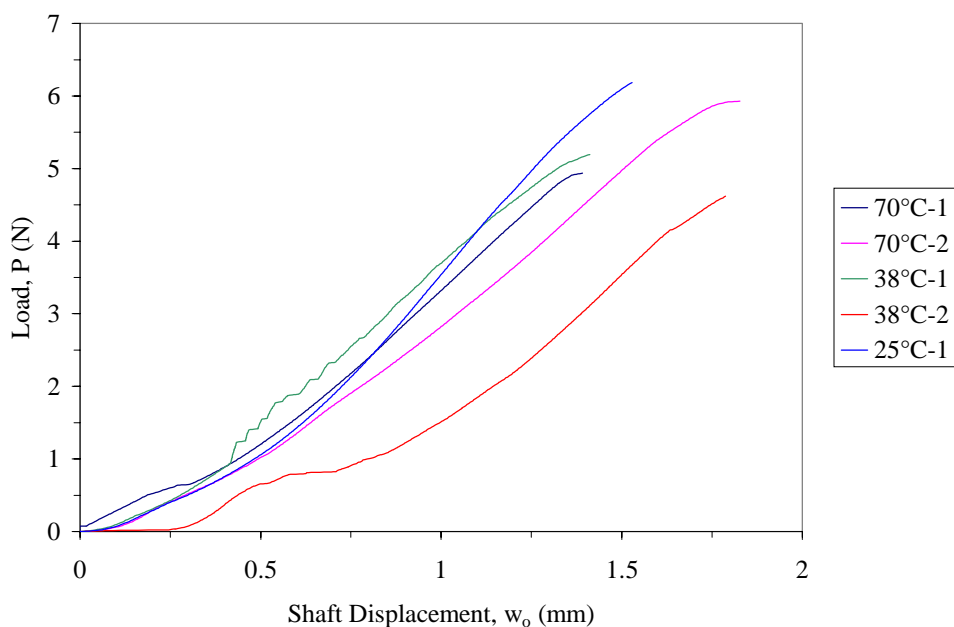


**Figure 7.32. Load versus Shaft Displacement for BPADA/ODA in a low %RH environment at 25 °C, 38 °C, and 70 °C.**

In each curve, there is an initial loading region, followed by a region of film deformation. The films punctured at a load between 4.6 – 6.2 N. For sample 38°C-2, slight blister growth was observed at  $P \approx 0.8$  N; analysis of the blister images indicated that the blister growth was fostered by a very asymmetric precrack. Once the precrack became symmetric, blister growth halted and film deformation ensued. Examination of the images of the precrack taken during the course of the experiments confirmed that true blister growth did not occur in any of the samples. This was quite surprising because at high %RH, the blister for all the ODA samples began to

propagate at load less than 1 N. It is interesting to note that the slope ( $P/w_o$ ) in the deformation region increases as the temperature decreases, with the exception of sample 70°C-1. The trend is as predicted for stress-strain relationships as a function of temperature.

For BPADA/ODA:DoDDA, 50:50, samples were prepared using the patch technique; each patch was precracked by hand to facilitate blister growth. Behavior similar to BPADA/ODA was observed. An overlay of the load versus shaft displacement curves for the samples tested at 70 °C is shown in Figure 7.33.

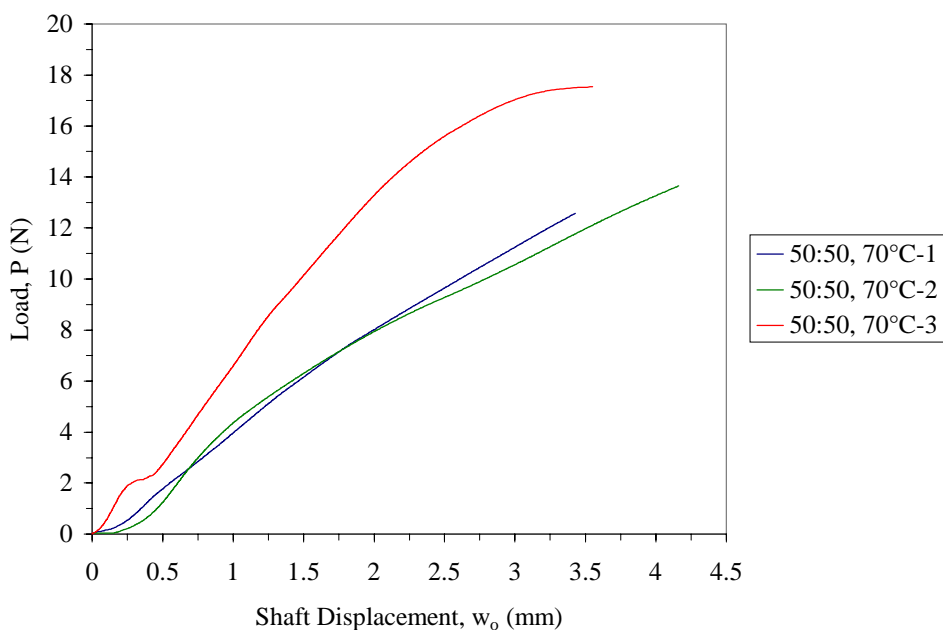


**Figure 7.33. Load versus Shaft Displacement for BPADA/ODA:DoDDA, 50:50 in a low %RH at 70°C.**

Samples 1 and 2 exhibited a small increase in the blister radius,  $\approx 0.2$  mm, before the film punctured. For both, the boundary of the blister became very white in color as the load increased. This is indicative of plastic yielding and the minimal blister growth is probably more of a consequence of the plastic yielding than true adhesive delamination. The curve of sample 3 is more similar to that of the BPADA/ODA samples; this sample also punctured prior to any measurable blister growth.

These BPADA/ODA and BPADA/ODA:DoDDA, 50:50 SLBT experiments bring several interesting points, and the comments from section 7.4.2 are referred to. First in a low %RH environment, the blisters do not propagate – even at 25 °C. This suggests that the BPADA-based polyimide to SiO<sub>2</sub>/Si adhesion is “stronger” at low %RH than it is at high %RH. For BPADA/ODA, these observations are consistent with the observations by Hu et al. for a similar fully aromatic polyimide to silicon system.<sup>12</sup> Second, the SLBT results also suggest that in a low %RH, the attack of the polyimide weak boundary layer by moisture at the crack tip and by the diffusion of moisture through the thickness of the film is less than in a high %RH – and as a result, no blister growth occurs. Third, since the blisters did not propagate at high temperatures, the specific role of the  $\beta$  relaxation in the adhesion strength and the interaction of  $g(G_o)$  and  $(\phi(R,T))$  could not be examined; however, in the absence of moisture, “stronger” adhesion was observed for the three test temperatures.

Thus with the intrinsic adhesion higher than the tensile strength limit of the material, one encounters a shortcoming of the SLBT for measuring the dry adhesion of the highly aromatic polyimides and partially aliphatic polyimides to SiO<sub>2</sub>/Si.

## 7.10 Conclusions

### 7.10.1

The adhesive fracture energies,  $G$ , measured for BPADA/ODA and BPADA/ODA:DoDDA, 75:25 by the SLBT, are 2-3 orders of magnitude larger than the corresponding values of the thermodynamic work of adhesion,  $W_A$ . It is unlikely that the differences between  $G$  and  $W_A$  arise because of covalent bonding across the interface. The polymers were fully imidized prior to adhesive bond preparation and thus, only secondary bonding forces should have been established. Agreement between  $G$  and  $W_A$  would have suggested strictly interfacial adhesive bond failure in which no energy was consumed by viscoelastic or plastic deformations of the polymer at the growing crack tip and at more remote polymer locations. XPS revealed that polyimide was on the silicon wafer-side of the failure for all SLBT specimens, and the failures were thus designated “cohesive in the polyimide.” The mechanically complex nature of these glassy polyimides made it difficult, in practice, to adopt a test rate and temperature which would provide the equilibrium conditions that would be needed to satisfy the criterion of no energy consumption at the growing crack tip in order to evaluate  $W_A$  directly.

### 7.10.2

The adhesion behavior of a novel series of polyimides to SiO<sub>2</sub>/Si was explored using a shaft loaded blister test. The shaft loaded blister test was configured using a dynamic mechanical analysis instrument, rather than the commonly used universal testing machine, to permit experiments at well-defined high temperatures ( $\pm 0.2$  °C, in the present study), an instrumental innovation.

Several factors prevented the adhesion energy of some of the polyimides from being described quantitatively from the SLBT data. These factors included the load-control operation of the DMA, sample preparation using the “patch” technique, the %RH during the experiment, and the chemical composition and physical properties of the polyimides. The chemical composition of the polyimide appeared to be important for adhesive testing at high %RH. Physical properties such as the T<sub>g</sub>, modulus, and yield strength were influential in whether the blister growth was elastic or inelastic, complicating any global interpretations of the results.

### 7.10.3

In the following paragraphs, the phrase high %RH refers to SLBT experiments that were performed at temperatures 24-27 °C and at 40-65% relative humidity, ie. an ambient laboratory environment.

At high %RH, the blister growth of BPADA/ODA to SiO<sub>2</sub>/Si was elastic and the adhesion energies were calculated using the hybrid, load-based, and displacement-based equations for the SLBT. For each specimen, the adhesion energies among the three equations agreed reasonably well. For the three specimens the average  $G$  calculated by the hybrid, load-based, and displacement-based equations are  $8.0 \pm 1.3$  J/m<sup>2</sup>,  $7.6 \pm 0.4$  J/m<sup>2</sup>, and  $8.0 \pm 2.2$  J/m<sup>2</sup>, respectively. Polyimide from the adhesive was detected on the SiO<sub>2</sub>/Si sides of the failure; however, the low N:Si ratios indicate that only small amounts were present. Failure is suggested to occur within a weak boundary layer of the polyimide. It is presumed that secondary bonds within the layer are easily displaced by moisture at the crack tip.

At high %RH, the adhesion energy for BPADA/ODA:DoDDA, 75:25 to SiO<sub>2</sub>/Si was also quantified. For each specimen, agreement among the  $G$  from the hybrid, load-based, and displacement-based equations was not observed due to error in one of the measured variables. For each specimen, the adhesion energy was then calculated from the remaining two, error-free,

variables. These adhesion energies are  $22.6 \text{ J/m}^2$  and  $17.3 \text{ J/m}^2$ . The N:Si ratios on the  $\text{SiO}_2/\text{Si}$  failure surfaces are consistent with the adhesion energies - a greater amount of polyimide remained on the  $\text{SiO}_2/\text{Si}$  surface for the  $G = 22.6 \text{ J/m}^2$  specimen than remained on the  $\text{SiO}_2/\text{Si}$  surface of the  $G = 17.3 \text{ J/m}^2$  specimen. The adhesion energies for ODA:DoDDA, 75:25 are higher and the amounts of polyimide detected on the  $\text{SiO}_2/\text{Si}$  failure surface are greater than for the fully aromatic BPADA/ODA polyimide under the high %RH environment. This observation suggests that the hydrophobic, DoDDA segments make the ODA:DoDDA, 75:25 to  $\text{SiO}_2/\text{Si}$  adhesive bond less sensitive to moisture.

At high %RH, blisters were also propagated for BPADA/ODA:DoDDA, 50:50, BPADA/ODA:DoDDA, 25:75, and BPADA/DoDDA in the SLBT. However, their adhesion energies to  $\text{SiO}_2/\text{Si}$  could not be quantified because plastic deformation at the crack tip (as predicted by  $N_{eff} > \sigma_y h$ , which suggests inelastic blister growth). The plastic yielding at the crack tip may not only arise as a consequence of the lower modulus and lower  $\sigma_y$  of the polyimide, but also from stronger polyimide adhesion to  $\text{SiO}_2/\text{Si}$ . The “strong adhesion” at high %RH conditions is suggested to be related to the polyimide chemical composition. The polyimides BPADA/ODA:DoDDA, 50:50, BPADA/ODA:DoDDA, 25:75, and BPADA/DoDDA contain increasingly larger amounts of the hydrophobic, DoDDA segments. In a high %RH environment the DoDDA segments should cause the bulk film to absorb less moisture from the atmosphere, as well as reduce the moisture-sensitivity of any weak boundary layer in the polyimide. Thus, I assume blister propagation was not facilitated by moisture at the crack tip and as a result, plastic yielding at the crack tip and “stronger adhesion” was observed. The “stronger adhesion” is further substantiated by the higher N:Si ratios, and thus higher amounts of polyimide, detected on the silicon wafer side of failure, relative to the BPADA/ODA surfaces. The high N:Si ratio, relative to BPADA/ODA, is consistent with the observations for BPADA/ODA:DoDDA, 75:25. It is therefore suggested that the incorporation of aliphatic segments into the polyimide chemical structure improves the durability of the adhesive bond to  $\text{SiO}_2/\text{Si}$  under high percent relative humidities.

#### 7.10.4

At high %RH and  $25 \text{ }^\circ\text{C}$ , the adhesion energy of BPADA/ODA to  $\text{SiO}_2/\text{Si}$  was  $\approx 8 \text{ J/m}^2$ . At low %RH and for 25, 38, and  $70 \text{ }^\circ\text{C}$  SLBT test temperatures, the adhesion energy of

BPADA/ODA to SiO<sub>2</sub>/Si could not be quantified; however, in this absence of moisture, “stronger” adhesion was observed. This is suggested to be related to intrinsic adhesion energy,  $G_o$ , differences of BPADA/ODA to SiO<sub>2</sub> associated with the two %RH environments. The role of the  $\beta$  relaxation cannot be interpreted. These observations for BPADA/ODA to SiO<sub>2</sub>/Si further reinforce the importance of moisture in the adhesion measurement of aromatic polyimides.

### 7.10.5

Plastic deformation in the strongly adhering, high aliphatic content, polyimide films was a major problem in characterizing their adhesion energy to SiO<sub>2</sub>/Si. However, for the more weakly adhering (high %RH), high aromatic content polyimide films, elastic blister growth occurred more readily. For such films, this is partially attributable to their high tensile moduli and yield strengths. These observations suggest that in a mechanically driven test such as the SLBT, higher modulus and/or thicker films may be more suited for withstanding the stresses at the crack tip and at the place of contact with the shaft tip. This experience indicates to future experimentalists that a geometry-adhesive-substrate system should be carefully selected in order to maximize results.

## 7.11 References

- <sup>1</sup> Owens, D.K.; Wendt, R.C. *J. Appl. Polym. Sci.* **1969**, *13*, 1741.
- <sup>2</sup> Qu, W.L.; Ko T.M. *J. Appl. Polym. Sci.* **2001**, *82*, 1642.
- <sup>3</sup> Kinloch, A.J. *Adhesion and Adhesives, Science and Technology*; Chapman and Hall: New York, 1987.
- <sup>4</sup> Gent, A.N.; Kaang, S.Y. *J. Adhesion* **1987**, *24*, 173.
- <sup>5</sup> Allen, M.G.; Nagarkar, P.; Surtoria, S.D. “Aspects of Adhesion Measurement of Thin Polyimide Films,” In *Polyimides: Materials, Chemistry and Characterization*; Feger, C.; Khojasteh, M.M., McGrath, J.E., Eds.; Elsevier: Amsterdam, 1989; pp 705-717.
- <sup>6</sup> Allen, M.G.; Surtoria, S.D. *J. Adhesion* **1989**, *29*, 219.
- <sup>7</sup> Paek, S.H.; Lee, K.W.; Durning, C.J. *J. Adhesion Sci. Tech.* **1999**, *13*(4), 423.
- <sup>8</sup> Wan, K.-T.; Mai, Y.-W. *Int. J. Fracture* **1996**, *74*(2), 181.
- <sup>9</sup> O’Brien, E.P.; Ward, T.C.; Guo, S.; Dillard, D.A. *J. Adhesion* **2002**, submitted.
- <sup>10</sup> Atkins, A.G.; Mai, Y.W. *Elastic and Plastic Fracture, Metals, Polymers, Ceramics, Composites, Biological Materials*; Ellis Horwood Limited: Chichester, England, 1985; Chapter 8.
- <sup>11</sup> Hu, D.C.; Chen, H.C. *J. Adhesion Sci. Technol.* **1992**, *6*(5), 527.
- <sup>12</sup> Hu, D.C.; Chen, H.C. *J. Mater. Sci.* **1992**, *27*, 5262.

---

<sup>13</sup> Riggs, W.M.; Parker, M.J. In *Methods and Phenomena Volume 1, Methods of Surface Analysis*; Czanderna, A.W., Ed.; Elsevier Science: New York, 1975; Chapter 4.

<sup>14</sup> Takahashi, N.; Yoon, D.Y.; Parrish, W. *Macromolecules* **1984**, *17*, 2583.

<sup>15</sup> Buchwalter, L.P. *J. Adhesion Sci. Technol.* **1990**, *4*(9), 697.

## 8. CONCLUSIONS

### 8.1 Aromatic Polyimides

The  $T_g$  and sub- $T_g$  viscoelastic relaxations of two aromatic polyimides, Kapton<sup>®</sup>-E and KB, were characterized by their time and dependence using dynamic mechanical analysis. The size scales of these relaxations were interpreted using an Arrhenius activation energy analysis. The sub- $T_g$  relaxations possessed an activation energy on the order of 100 kJ/mol or less, whereas the  $T_g$  relaxations exhibited an activation energy of  $\approx 1000$  kJ/mol. Storage modulus master curves for the  $T_g$  of Kapton<sup>®</sup>-E and KB were generated using t-Tsp and the master curve shift factors were compared via a cooperativity analysis. The “cooperativity” parameter,  $n$ , for both Kapton<sup>®</sup>-E and KB was  $\approx 0.66$ , which indicates that their  $T_g$ 's are controlled by similar processes.

A third polyimide, PI, was similarly characterized for the time and temperature dependence of its  $T_g$  by dynamic mechanical analysis. A unique “supported film” sample preparation method was adopted because of the small thickness,  $\approx 20$   $\mu\text{m}$ , of the PI films. The main caveat of this technique is that the  $T_g$  of PI cannot overlap with any viscoelastic relaxation ie. the  $\beta$  relaxation or  $T_g$ , of the supporting film.

Exposure of dried Kapton<sup>®</sup>-E films various %RH environments resulted in successively greater amounts of absorbed moisture. The absorbed moisture influenced the  $\tan \delta$  magnitudes of the  $\gamma$  and  $\beta$  sub- $T_g$  relaxations, as observed by dielectric and dynamic mechanical analysis. Analysis of the  $E_a$  of the  $\gamma$  relaxation by Arrhenius and Starkweather-Eyring methods indicated that the  $E_a$  of the relaxation decreased slightly ( $\approx 2$  kJ/mol) as the moisture content increased. According to the theory of the Starkweather-Eyring method, the close agreement between the two types of calculations suggests that the entropic contribution,  $\Delta S$ , to the  $E_a$  is  $\approx 0$ , which allows the relaxation to be classified as “simple.”

By DMA, relative to the  $\tan \delta$  signal for the dry sample, the absorbed moisture increased the  $\tan \delta$  magnitude of the low temperature component of the  $\beta$  transition. Thermal conditioning of Kapton<sup>®</sup>-E at various temperatures revealed changes in the  $\tan \delta$  magnitude. Both the humidity and thermal effects are suggested to be related to the processing history of the oriented

Kapton<sup>®</sup>-E film. The DMA storage modulus was also influenced by the absorbed moisture. At temperatures below 50 °C, an anti-plasticizer effect was observed, but at temperatures above 50 °C a plasticizer effect was noted. The absorbed moisture, however, did not influence the tensile modulus of Kapton<sup>®</sup>-E, as measured by Instron mechanical testing.

An in situ DMA technique was adopted to investigate the dimension changes of a saturated Kapton<sup>®</sup>-E sample with changes in temperature. An average linear CTE value of  $49.4 \pm 4.9$  ppm/°C was measured. The application of in situ DMA in this way could provide valuable insight to the dimension changes with temperature of a polymer thin film or coating that is saturated by an aggressive fluid. Such information could assist in understanding the durability of adhesive joints in fluid environments.

## 8.2 Partially Aliphatic Polyimides

### 8.2.1 Structure-Property Relationships

Chemical structure-physical property relationships were established for nine polyimides and copolyimides which were based on bisphenol A dianhydride (BPADA) and varied in their aliphatic content by their diamine molar ratio. Generally, as the aliphatic content increased, the glass transition temperature, thermal stability, refractive index, dielectric constant, modulus, and  $\sigma_y$  decreased; however, the coefficient of thermal expansion increased. The controlled chemical compositions allowed the molecular origins of the local viscoelastic relaxations to be determined. A crankshaft motion at low temperatures,  $\approx -140$  °C, was associated to the linear HMDA and DoDDA aliphatic segments. A phenyl ring rotation within the aromatic ODA unit was associated with the viscoelastic relaxation at  $\approx 50$  °C.

The BPADA-based polyimide containing the cycloaliphatic diamine, DCHM, exhibited a  $T_g$  comparable to the fully aromatic BPADA/ODA polyimide. The high  $T_g$  is associated with the rigidity the cyclohexyl functional groups add to the polymer backbone. The molecular origin of the sub- $T_g$  viscoelastic relaxation at  $\approx -78$  °C is suggested to arise from isomer changes within the cyclohexyl ring.

### 8.2.2 Adhesion

The adhesive fracture energies,  $G$ , measured for BPADA/ODA and BPADA/ODA:DoDDA, 75:25 by the SLBT, are 2-3 orders of magnitude larger than the corresponding values of the thermodynamic work of adhesion,  $W_A$ . The differences between  $G$  and  $W_A$  were attributed to cohesive failure in the polyimide and using a test rate and temperature that did not provide equilibrium conditions at the growing crack tip.

The adhesion behavior of the BPADA/ODA:DoDDA series partially aliphatic polyimides to  $\text{SiO}_2$  was explored using a shaft loaded blister test. The shaft loaded blister test was configured using a dynamic mechanical analysis instrument to permit experiments at well-defined high temperatures ( $\pm 0.2$  °C, in the present study), an instrumental innovation. Experimental details such as the load-control operation of the DMA, sample preparation methods, %RH during the test, and the chemical composition and physical properties of the polyimides were all influential in whether the blister growth was elastic or inelastic

In the following paragraphs, the phrase high %RH refers to SLBT experiments that were performed at temperatures 24-27 °C and at 40-65% relative humidity, ie. an ambient laboratory environment.

At high %RH, the blister growth of BPADA/ODA to  $\text{SiO}_2$  was elastic and the adhesion energies calculated using the hybrid, load-based, and displacement-based equations for the SLBT were  $8.0 \pm 1.3 \text{ J/m}^2$ ,  $7.6 \pm 0.4 \text{ J/m}^2$ , and  $8.0 \pm 2.2 \text{ J/m}^2$ , respectively. Polyimide from the adhesive was detected on the  $\text{SiO}_2$  sides of the failure; however, the low N:Si ratios indicate that only small amounts were present. Failure is suggested to occur within a weak boundary layer of the polyimide. It is presumed that secondary bonds within the layer are easily displaced by moisture at the crack tip.

At high %RH, the adhesion energy for BPADA/ODA:DoDDA, 75:25 to  $\text{SiO}_2$  was also quantified. The N:Si ratios on the  $\text{SiO}_2$  failure surfaces are consistent with the adhesion energies - a greater amount of polyimide remained on the  $\text{SiO}_2$  surface for the  $G = 22.6 \text{ J/m}^2$  specimen than remained on the  $\text{SiO}_2$  surface of the  $G = 17.3 \text{ J/m}^2$  specimen. The adhesion energies for ODA:DoDDA, 75:25 are higher and the amounts of polyimide detected on the  $\text{SiO}_2$  failure surface are greater than for the fully aromatic BPADA/ODA polyimide under the high %RH

environment. This observation suggests that the hydrophobic, DoDDA segments make the ODA:DoDDA, 75:25 to SiO<sub>2</sub> adhesive bond less sensitive to moisture.

At high %RH, blisters were also propagated for BPADA/ODA:DoDDA, 50:50, BPADA/ODA:DoDDA, 25:75, and BPADA/DoDDA in the SLBT. However, their adhesion energies to SiO<sub>2</sub> could not be quantified because plastic deformation at the crack tip. The plastic yielding at the crack tip may not only arise as a consequence of the lower modulus and lower  $\sigma_y$  of the polyimide, but also from stronger polyimide adhesion to SiO<sub>2</sub>. The “strong adhesion” at high %RH conditions is suggested to be related to the polyimide chemical composition. The polyimides BPADA/ODA:DoDDA, 50:50, BPADA/ODA:DoDDA, 25:75, and BPADA/DoDDA contain increasingly larger amounts of the hydrophobic, DoDDA segments. In a high %RH environment the DoDDA segments should cause the bulk film to absorb less moisture from the atmosphere, as well as reduce the moisture-sensitivity of any weak boundary layer in the polyimide. Thus, I assume blister propagation was not facilitated by moisture at the crack tip and as a result, plastic yielding at the crack tip and “stronger adhesion” was observed. The “stronger adhesion” is further substantiated by the higher N:Si ratios, and thus higher amounts of polyimide, detected on the silicon wafer side of failure, relative to the BPADA/ODA surfaces. The high N:Si ratio, relative to BPADA/ODA, is consistent with the observations for BPADA/ODA:DoDDA, 75:25. It is therefore suggested that the incorporation of aliphatic segments into the polyimide chemical structure improves the durability of the adhesive bond to SiO<sub>2</sub> under high percent relative humidities.

At high %RH and 25 °C, the adhesion energy of BPADA/ODA to SiO<sub>2</sub> was  $\approx 8 \text{ J/m}^2$ . At low %RH and for 25, 38, and 70 °C SLBT test temperatures, the adhesion energy of BPADA/ODA to SiO<sub>2</sub> could not be quantified; however, in this absence of moisture, “stronger” adhesion was observed. This is suggested to be related to intrinsic adhesion energy,  $G_o$ , differences of BPADA/ODA to SiO<sub>2</sub> associated with the two %RH environments. These observations for BPADA/ODA to SiO<sub>2</sub> further reinforce the importance of moisture in the adhesion measurement of aromatic polyimides.

## 9. SUGGESTIONS FOR FUTURE WORK

This research project offered several significant findings and these are now highlighted as suggestions for future research.

The BPADA-based partially aliphatic polyimides characterized in this dissertation were synthesized by members of Professor J.E. McGrath's research group at Virginia Tech. The ester-acid high temperature solution imidization route afforded soluble, amorphous, high molecular weight partially aliphatic polyimides, without the problem of salt formation. The success of this synthetic pathway in preparing copolyimides with controlled chemical compositions and physical properties was demonstrated. This suggests that new combinations of aromatic dianhydrides and aliphatic and cycloaliphatic diamines could easily be explored to tailor the chemical structure to meet property demands.

The polyimide containing the cycloaliphatic diamine, BPADA/DCHM, exhibited several unique properties; it possessed a  $T_g$  of  $\approx 220$  °C which is comparable to that of the aromatic polyimide, BPADA/ODA, but it exhibited a lower refractive index and dielectric constant than BPADA/ODA. These properties are desirable for microelectronics applications. Numerous researchers have prepared partially aliphatic polyimides containing DCHM; however, again, this research applied a new synthetic pathway and prompts the combination of different aromatic dianhydrides with DCHM. In addition, due to the interest in DCHM containing polyimides, an investigation regarding its adhesion strength to silicon wafers would be valuable.

This research instrumented the shaft loaded blister test in a new way- within a dynamic mechanical analyzer. While quantitative results for the partially aliphatic polyimides to silicon wafers were limited, the experimental technique was successfully demonstrated. The SLBT could be applied to study the adhesion of fully aromatic polyimides to  $\text{SiO}_2/\text{Si}$  and metals, such as Cu, Cu/Cr, Au, and Ta. The effect of humidity on aromatic polyimide adhesion to  $\text{SiO}_2/\text{Si}$  could be further explored to determine the mechanism of moisture attack within the weak boundary layer of the aromatic polyimide. Such an investigation could also provide insight towards understanding the moisture attack within the weak boundary layer within the partially aliphatic polyimides to  $\text{SiO}_2/\text{Si}$ .

This SLBT could easily be adopted to measure the adhesion of pressure sensitive adhesives to various substrates over a wide range of temperature (subambient and higher). The temperature

capability could enable adhesion energy master curves to be generated. The master curves could then be used to predict adhesion performance for experimentally unattainable times or temperatures.

## VITA

The author, Amy Elizabeth Eichstadt, was born on July 1, 1974 in Martinsville, Virginia to Drs. Francis and Karen Eichstadt. Her family moved to Parkersburg, West Virginia in 1976 and presently resides there. Throughout her youth, the author enjoyed participating in community softball, basketball, tennis, soccer, and swimming leagues. She graduated first in her class from Parkersburg Catholic High School in 1992. She attended the University of Notre Dame in South Bend, Indiana and graduated with a Bachelor's of Science degree in Chemistry in 1996. During her undergraduate studies she held two summer internships in the field of polymer science with DuPont in Wilmington, Delaware. These summer experiences prompted her to further her interests in polymer science at the graduate level at Virginia Polytechnic Institute & State University in the Materials Engineering & Science (MESc) Ph.D. program. She completed her Ph.D. degree under the direction of Professor Thomas C. Ward (Department of Chemistry) in July of 2002. The author will continue her career in the field of polymer science as a research scientist for the Corporate Research Chemical Technology Division of The Procter & Gamble Company in Cincinnati, Ohio.